

## REPORT DOCUMENTATION PAGE

AFRL-SR-BL-TR-00-

Public reporting burden for this collection of information is estimated to average 1 hour per response, including gathering and maintaining the data needed, and completing and reviewing the collection of information. Send collection of information, including suggestions for reducing this burden, to Washington Headquarters Services, Davis Highway, Suite 1204, Arlington, VA 22202-4302, and to the Office of Management and Budget, Paperwork Reduction Project 0704-0188.

0819

Washington, DC 20503.

1. AGENCY USE ONLY (Leave blank)			2. REPORT DATE 21 Dec 00	3. REPORT TYPE AND DATES COVERED Final Report: 01 Apr 95 TO 31 May 98
4. TITLE AND SUBTITLE  An Investigation Of MEMS-Based Transducers For Boundary Layer Control			5. FUNDING NUMBERS F49620-95-1-0322	
6. AUTHOR(S) Sudeep M. Kumar, William C. Reynolds and Thomas W. Kenny				
7. PERFORMING ORGANIZATION NAME(S) AND ADDRESS(ES) Stanford University 651 Serra Room 260 Stanford, CA 94305-4125			8. PERFORMING ORGANIZATION REPORT NUMBER	
9. SPONSORING/MONITORING AGENCY NAME(S) AND ADDRESS(ES) AFOSR/NA 801 N. Randolph St. Arlington VA 22203			10. SPONSORING/MONITORING AGENCY REPORT NUMBER	
11. SUPPLEMENTARY NOTES				
12a. DISTRIBUTION AVAILABILITY STATEMENT  Approved for public release: Distribution is unlimited			12b. DISTRIBUTION CODE	
13. ABSTRACT (Maximum 200 words) Using direct numerical simulations of turbulent channel flow, we present new insight into the generation of streamwise vortices near the wall, and an associated drag reduction strategy. Growth of x-dependent spanwise velocity disturbances w(x) is shown to occur via two mechanisms: (i) linear transient growth, which dominates early-time evolution, and (ii) linear normal-mode instability, dominant asymptotically at late time (for frozen base flow streaks). Approximately 25% of streaks extracted from near-wall turbulence are shown to be strong enough for linear instability (above a critical vortex line lift angle). However, due to viscous annihilation of streak normal vorticity, normal mode growth ceases after a factor of two energy growth. In contrast, the linear transient disturbance produces a 20-fold amplification, due to its rapid, early-time growth before significant viscous streak decay. Thus, linear transient growth of w(x) is revealed as a new, apparently dominant, generation mechanism of x-dependent turbulent energy near the wall.				
20010109 092				
14. SUBJECT TERMS An Investigation of MEMS-Based Transducers For Boundary Layer Control			15. NUMBER OF PAGES	
			16. PRICE CODE	
17. SECURITY CLASSIFICATION OF REPORT UNCLASSIFIED	18. SECURITY CLASSIFICATION OF THIS PAGE UNCLASSIFIED	19. SECURITY CLASSIFICATION OF ABSTRACT UNCLASSIFIED	20. LIMITATION OF ABSTRACT UL	

30 OCT 2000

# AN INVESTIGATION OF MEMS-BASED TRANSDUCERS FOR BOUNDARY LAYER CONTROL

By

Sudeep M. Kumar, William C. Reynolds and Thomas W. Kenny

Prepared with the support of the  
Air Force Office of Scientific Research  
under Grant No. F49620-95-1-0322



Report No. TF-79

Flow Physics and Computation Division  
Department of Mechanical Engineering  
Stanford University  
Stanford, California 94305-3030

May, 2000

AN INVESTIGATION OF MEMS-BASED TRANSDUCERS  
FOR BOUNDARY LAYER CONTROL

By

Sudeep M. Kumar, William C. Reynolds and Thomas W. Kenny

Prepared with the support of the  
Air Force Office of Scientific Research  
under Grant No. F49620-95-1-0322

Report No. TF-79

Flow Physics and Computation Division  
Department of Mechanical Engineering  
Stanford University  
Stanford, California 94305-3030

May 2000

© Copyright by Sudeep M. Kumar 2000  
All Rights Reserved

# Abstract

Recent experiments and simulations have demonstrated the feasibility of active boundary layer control in turbulent flows. Reduction of skin-friction drag requires the development of sensors, actuators and control algorithms to favorably modify the velocity profile close to the wall. This work describes the fabrication and characterization of modular arrays of sensors and actuators for low speed flows. These transducers provide a testbed for the evaluation and development of control strategies in a controlled environment.

The sensors are arrays of hot-films that provide snapshots of the spanwise wall shear stress distribution. The active elements are thermally isolated metal resistors embedded in polyimide diaphragms. Fabrication of modules with robust multiple backside contacts is discussed. The sensors have a frequency response of 16 kHz when operated as constant temperature hot-film anemometers at an overheat ratio of 1.5. Individual sensors have a power consumption of about 10 mW at this overheat ratio. The sensor response in a laminar flow is nearly linear with a slope of 0.3 mV/mPa.

The actuators are zero mass flux vortex generators. They are fast with millisecond rise times, have power consumption in the milliwatt range, and incur no drag penalty when not in operation. An actuator array consists of eight individually addressable PZT-silicon cantilevers with integrated cavities and unequal side gaps. Bulk micromachining of silicon is followed by mesoscale assembly of the piezoceramic in the fabrication process. Disturbance velocity fields generated by an actuator in a laminar boundary layer ( $U_\infty = 5$  m/s,  $Re_\theta = 310$ ) are reported. The disturbance is substantial, up to 25% of the free stream velocity, and is concentrated in a region of about one displacement thickness from the wall. It persists far downstream - the peak disturbance velocity is 13% of the free stream velocity 30 displacement thicknesses downstream of the actuator. The strength of the disturbance is controlled by the amplitude of the actuator drive signal. The effect of multiple actuators on the wall shear stress was determined by the sensor array.

The system was evaluated by controlling the streamwise vortex pair behind a cylinder in a laminar boundary layer. The sensors were used to optimize actuator amplitudes for reducing the skin friction in the perturbed flow. The strength of the disturbance, as

measured by the wall shear stress, was reduced by 85% at the sensor array location. This was accompanied by an 18% reduction in the drag and a 68% reduction in the spanwise standard deviation of the wall shear stress. The effect of the control persisted greater than 25 displacement thicknesses downstream of the actuator array.

## Acknowledgments

The authors gratefully acknowledge the financial support of the Air Force Office of Scientific Research under grant number F49620-95-1-0322, monitored by Dr. James McMichael and Dr. Mark Glauser. Part of this research was also supported by the National Science Foundation Instrumentation for Materials Research Program (DMR-9504099).

The authors thank Profs. J. K. Eaton, P. Bradshaw and D. M. Bloom for their valuable suggestions throughout this research project. We also thank Mr. Lakhbir Johal and Mr. Bill Sabala at the ME machine shop for their fine craftsmanship. The staff at the Center for Integrated Systems and Mr. Tom Carver at the Ginzton Microstructures Facility were very helpful in the micromachining aspects of this work.

# Contents

<b>Abstract</b>	iii
<b>Acknowledgments</b>	v
<b>Nomenclature</b>	xix
<b>1 Introduction</b>	1
1.1 Turbulent Boundary Layer Physics . . . . .	1
1.2 Boundary Layer Control Strategies . . . . .	2
1.2.1 Transition Control . . . . .	2
1.2.2 Passive Turbulence Control . . . . .	3
1.2.3 Active Turbulence Control . . . . .	4
1.2.3.1 Open Loop Strategies . . . . .	4
1.2.3.2 Closed Loop Strategies . . . . .	5
1.3 Scaling Issues . . . . .	7
1.4 Introduction to MEMS . . . . .	8
1.5 Objectives . . . . .	9
1.6 Overview of Important Results . . . . .	10
<b>2 Facility and Experimental Techniques</b>	15
2.1 Wind Tunnel . . . . .	15
2.2 Instrumentation . . . . .	16
2.2.1 Data Acquisition and Control System . . . . .	16
2.2.2 Temperature Measurement . . . . .	16
2.2.3 Pressure Measurement . . . . .	17
2.2.4 Probe Traverse . . . . .	17
2.2.5 Hot-Wire Anemometry . . . . .	18
2.3 Facility Qualification . . . . .	19

2.3.1	Uncertainty Analysis . . . . .	20
<b>3</b>	<b>Surface Shear Stress Sensors</b>	<b>25</b>
3.1	Introduction . . . . .	25
3.2	Thermal Analysis . . . . .	26
3.2.1	Analytic Solution . . . . .	27
3.2.2	Numerical Solution in Two Dimensions . . . . .	28
3.2.3	Numerical Solution in Three Dimensions . . . . .	29
3.2.4	Sensor Behavior in Water and Air . . . . .	30
3.2.5	Heat Transfer Budget for Thermally Isolated Sensors in Air . . . . .	30
3.3	Fabrication . . . . .	31
3.4	Characterization . . . . .	32
3.4.1	Evaluation of Backside Contacts . . . . .	32
3.4.2	TCR and I-V Characteristics . . . . .	33
3.4.3	Time Constants . . . . .	34
3.5	Correction for Ambient Temperature Variations . . . . .	35
3.6	Calibration . . . . .	36
3.7	Conclusions . . . . .	38
3.7.1	Design Improvements . . . . .	38
<b>4</b>	<b>Zero Mass Flux Actuators</b>	<b>59</b>
4.1	Introduction . . . . .	59
4.2	Piezoelectric Actuator Concept . . . . .	60
4.3	Actuator Design . . . . .	60
4.3.1	Optimization of Static Deflection . . . . .	60
4.3.2	Design Space . . . . .	61
4.4	Fabrication . . . . .	62
4.5	Mechanical Characterization . . . . .	63
4.5.1	Transfer Function . . . . .	63
4.5.2	Repeatability and Crosstalk . . . . .	64
4.5.3	Behavior at Resonance . . . . .	65
4.5.4	Step Response . . . . .	65
4.6	Fluid Dynamic Behavior . . . . .	66
4.6.1	Behavior in Still Air . . . . .	66
4.6.2	Behavior in Laminar Flow . . . . .	67
4.6.2.1	Velocity Perturbation Map . . . . .	67
4.6.2.2	Streamwise Evolution of Disturbance . . . . .	67

4.6.2.3	Amplitude Control . . . . .	68
4.6.2.4	Power Spectra . . . . .	68
4.6.2.5	Flow Step Response . . . . .	69
4.6.2.6	Effect of Multiple Actuators . . . . .	69
4.7	Actuator for Operation in Water . . . . .	70
4.7.1	Design . . . . .	70
4.7.2	Multi-Level Etch Process . . . . .	70
4.7.3	Fabrication . . . . .	71
4.8	Conclusions . . . . .	72
4.8.1	Design Improvements . . . . .	73
<b>5</b>	<b>Control of the Streamwise Vortex Pair Behind a Cylinder</b>	<b>97</b>
5.1	Introduction . . . . .	97
5.2	Evaluation of the Cylinder Disturbance . . . . .	98
5.3	System Identification Using Sensor Array . . . . .	99
5.4	Control Strategy . . . . .	100
5.5	Control Performance . . . . .	102
5.5.1	Spanwise Flow Maps . . . . .	102
5.5.2	Streamwise Evolution of Controlled Flow . . . . .	103
5.5.3	Figures of Merit . . . . .	103
5.6	Conclusions . . . . .	104
<b>6</b>	<b>Conclusions</b>	<b>119</b>
6.1	Sensors . . . . .	119
6.2	Actuators . . . . .	120
6.3	Control of a Streamwise Vortex Pair . . . . .	120
6.4	Recommendations . . . . .	121
<b>A</b>	<b>Common Fabrication Processes</b>	<b>125</b>
A.1	Mask Design and Fabrication . . . . .	125
A.2	Lithography . . . . .	126
A.2.1	Liftoff Process . . . . .	126
A.3	Plasma Etching . . . . .	127
A.4	Wet Anisotropic Etching . . . . .	127
A.5	Backside Contact Formation . . . . .	128

<b>B Sensor Fabrication Process</b>	<b>131</b>
B.1 Frontside Wax Protection . . . . .	133
<b>C Actuator Fabrication Process</b>	<b>137</b>
C.1 RTV Mold and Casting Fabrication . . . . .	138
C.2 PZT Bonding . . . . .	139
<b>D Uncertainty Analysis</b>	<b>143</b>
D.1 Position . . . . .	143
D.2 Velocity . . . . .	144
D.2.1 Fixed Errors . . . . .	144
D.2.2 Random Errors . . . . .	144
D.2.3 Bias Errors . . . . .	145
D.3 Wall Shear Stress Using Hot-Wire . . . . .	145
D.4 Wall Shear Stress Using Sensor Array . . . . .	146
D.4.1 Fixed Errors . . . . .	146
D.4.2 Bias Errors . . . . .	146

# List of Tables

1.1	Sizing requirements for different flows. . . . .	8
2.1	Two-axis traverse system specifications. . . . .	18
3.1	Heat transfer budget for thermally isolated sensor in air at 10 m/s. . . . .	31
A.1	Etch rate for a 30% KOH solution as a function of temperature. . . . .	128
B.1	Steps in sensor fabrication process. . . . .	132
C.1	Steps in actuator fabrication process. . . . .	138



# List of Figures

1.1	Photo of streaks in a turbulent boundary layer. . . . .	11
1.2	Schematic of turbulence generation cycle. . . . .	11
1.3	Classification of boundary layer control techniques. . . . .	12
1.4	Typical experimental control module for closed loop control. . . . .	13
1.5	Comparison of MEMS and VLSI processes. . . . .	13
2.1	Plan view of wind tunnel facility. . . . .	21
2.2	Photo of part of the test section. . . . .	22
2.3	Polynomial and King's law calibration for $2.5 \mu\text{m}$ and $5 \mu\text{m}$ hot-wires. . . . .	22
2.4	Boundary layer profiles at several spanwise locations, $x = 49.5 \text{ cm}$ , $\eta = y(U/\nu x)^{1/2}$ , $U_\infty = 4.9 \text{ m/s}$ . . . . .	23
2.5	Spanwise profiles in boundary layer and in the free stream, $x = 49.5 \text{ cm}$ , $U_\infty = 4.9 \text{ m/s}$ . . . . .	23
3.1	Illustration of the sensor concept. . . . .	39
3.2	Sensor model for heat transfer analysis. . . . .	39
3.3	Construction of unit solution from semi-infinite half plane solutions. . . . .	39
3.4	Sensor without thermal isolation in water ( $P_e = 0.41$ , $k_s/k_f = 262$ , $\alpha_s/\alpha_f = 639$ ). . . . .	40
3.5	Sensor without thermal isolation in air ( $P_e = 0.23$ , $k_s/k_f = 6039$ , $\alpha_s/\alpha_f = 4.3$ ). . . . .	41
3.6	Thermally isolated sensor in water ( $P_e = 0.41$ , $k_s/k_f = 0.04$ , $\alpha_s/\alpha_f = 149$ ). . . . .	42
3.7	Thermally isolated sensor in air ( $P_e = 0.23$ , $k_s/k_f = 1$ , $\alpha_s/\alpha_f = 1$ ). . . . .	43
3.8	Two-dimensional profiles for thermally isolated sensor in water. . . . .	44
3.9	Two-dimensional profiles for thermally isolated sensor in air. . . . .	45
3.10	Schematic showing thermal resistances for isolated sensor. . . . .	46
3.11	Sensor fabrication sequence. . . . .	46
3.12	Wafer level view of eight and sixteen sensor arrays. . . . .	47
3.13	Wafer level view of thermal isolation cavities and backside contacts. . . . .	47

3.14	Top view of part of a sixteen sensor array.	48
3.15	Tip of a single sensor.	48
3.16	Cross-section through a backside contact.	49
3.17	Leakage resistance between contacts.	49
3.18	Reduction of parasitic capacitance between contacts.	50
3.19	Temperature coefficient of resistance of sensor.	50
3.20	Current-voltage characteristics in still air.	51
3.21	Sensor resistance as a function of drive current.	51
3.22	Thermal resistance for four different sensor types.	52
3.23	Time constant determination by $3\omega$ technique.	52
3.24	Block diagram for constant temperature anemometry.	53
3.25	Photo of array of anemometers used to drive the sensor arrays.	53
3.26	Response of closed loop system to square wave input at an overheat ratio of 1.5.	54
3.27	Increase in chip temperature at two free-stream velocities.	54
3.28	Drift of two sensor outputs over a 24 hour period.	55
3.29	Crossplot of sensor output and chip temperature vs. free-stream temperature.	55
3.30	Crossplot of sensor output vs. chip temperature.	56
3.31	Temperature correction coefficient in still air and at nine free-stream velocities (0.5 m/s to 10.8 m/s in increments of 1.3 m/s).	56
3.32	Response of a sensor during calibration.	57
3.33	Calibration data for shear stress sensor array.	57
3.34	Quadratic fit to calibration data.	58
3.35	Shear stress in a laminar boundary layer with and without temperature correction.	58
4.1	Illustration of the actuator concept.	74
4.2	Dependence of tip deflection on thickness ratio.	74
4.3	Dependence of tip deflection on width ratio.	75
4.4	Design space for PZT-5H actuator in air at 10 m/s.	75
4.5	Spring constant of actuator (point load at tip).	76
4.6	Actuator fabrication sequence.	76
4.7	Top view of an actuator array.	77
4.8	Tip of a single actuator.	77
4.9	Bottom view of array.	78
4.10	Displacement transfer function of PZT-5A actuator.	78

4.39	Side section and fabrication sequence of actuator designed for operation in water. . . . .	95
4.40	Details of convex corner compensation. . . . .	95
4.41	Tip of a single actuator designed for operation in water. . . . .	96
5.1	Schematic of flow behind a cylinder. . . . .	105
5.2	Schematic of control experiment setup showing locations of cylinder, actuator array, and sensor array. . . . .	105
5.3	Disturbance profiles behind cylinder at different insertion depths as measured by sensor array ( $\Delta x_c/d = 38$ , $U_\infty = 5$ m/s). . . . .	106
5.4	Disturbance profiles behind cylinder at two free-stream velocities as measured by a hot-wire ( $y = 0.5$ mm, $\Delta x_c/d = 38$ , $z/d = 0$ ). . . . .	107
5.5	Power spectra in boundary layer behind cylinder at two free-stream velocities ( $y = 1$ mm, $\Delta x_c/d = 38$ , $z/d = 0$ ). . . . .	107
5.6	Contours of $U/U_\infty$ behind cylinder ( $\Delta x_c/d = 38$ , $U_\infty = 3$ m/s). . . . .	108
5.7	Spanwise disturbance profiles in boundary layer and wake behind cylinder ( $\Delta x_c/d = 38$ , $U_\infty = 3$ m/s). . . . .	109
5.8	Wall-normal velocity profiles in upsweep and downsweep regions behind cylinder ( $\Delta x_c/d = 38$ , $U_\infty = 3$ m/s). . . . .	110
5.9	Effect of actuators on the disturbance created by the cylinder as measured by the shear-stress sensor array. ( $\Delta x_a/d = 12.5$ , $U_\infty = 3$ m/s). . . . .	111
5.10	Effect of actuators on the disturbance created by the cylinder as measured by the shear-stress sensor array. ( $\Delta x_a/d = 12.5$ , $U_\infty = 5$ m/s). . . . .	112
5.11	Example of optimization by one dimensional search about initial guess, data from sensor array. . . . .	113
5.12	Spanwise velocity profiles in boundary layer behind cylinder with and without control ( $\Delta x_a/d = 13.1$ , $y/\delta^* = 0.17$ ). . . . .	114
5.13	Wall-normal velocity profiles behind cylinder with and without control ( $\Delta x_a/d = 13.1$ , $z/d = 0.0$ ). . . . .	114
5.14	Contours of $\Delta U/U_\infty$ behind cylinder at $\Delta x_a/d = 13.1$ . . . . .	115
5.15	Contours of $u_{rms}/U_\infty$ behind cylinder at $\Delta x_a/d = 13.1$ . . . . .	116
5.16	Spanwise velocity difference profiles for different streamwise locations ( $y/\delta^* = 0.17$ ). . . . .	117
5.17	Wall-normal velocity difference profiles for different streamwise locations ( $z/d = 0.0$ ). . . . .	117
5.18	Figures of merit as a function of streamwise location. . . . .	118

4.11	Displacement transfer functions of PZT-5A and PZT-5H actuators. . . . .	79
4.12	Transfer functions of eight different actuators. . . . .	79
4.13	Resonant frequencies and quality factors of actuators in Fig. 4.12. . . . .	80
4.14	Tip displacement repeatability when a single forcing frequency is used and crosstalk when actuator 4 is being driven. . . . .	80
4.15	Resonant frequency as a function of drive amplitude for PZT-5H actuator. .	81
4.16	PZT-5H actuator tip displacement as a function of drive amplitude. . . . .	81
4.17	Tip displacement of PZT-5A and PZT-5H actuators at 1 <sup>st</sup> resonant frequency.	82
4.18	Actuator step response. . . . .	82
4.19	Actuator response to step change in driving signal at 1 <sup>st</sup> resonant frequency.	83
4.20	Schematic showing coordinate system for actuator characterization experiments. . . . .	83
4.21	Spanwise velocity profiles in still air for different streamwise locations. . .	84
4.22	Wall-normal velocity profile in still air. . . . .	84
4.23	Spanwise velocity profiles in still air at different drive amplitudes ( $\Delta x_a = -2$ mm). . . . .	85
4.24	Spanwise velocity profiles in still air at different drive amplitudes ( $\Delta x_a = 0$ mm). . . . .	86
4.25	Time resolved velocity profiles over wide gap in still air. . . . .	87
4.26	Contours of $\Delta U/U_\infty$ at $\Delta x_a/\delta^* = 0^+$ . . . . .	87
4.27	Wall-normal velocity profile at maximum negative perturbation location compared to Blasius profile ( $\Delta x_a/\delta^* = 0^+$ , actuator drive amplitude $A = 0.9$ ). .	88
4.28	Spanwise velocity profiles at maximum negative perturbation location for different streamwise locations. . . . .	88
4.29	Spanwise velocity profiles at $y = 0.5$ mm for different streamwise locations.	89
4.30	Wall-normal disturbance profiles over narrow gap for different streamwise locations. . . . .	89
4.31	Streamwise evolution of peak disturbance amplitude. . . . .	90
4.32	Amplitude control of maximum perturbation over narrow gap. . . . .	90
4.33	Power spectra of velocity disturbance over the narrow gap. . . . .	91
4.34	Contours of $\Delta\tau/\tau_{ref}$ measured by sensor array at $U_\infty = 5$ m/s. . . . .	92
4.35	Time resolved $\Delta\tau/\tau_{ref}$ at $U_\infty = 5$ m/s. . . . .	92
4.36	Shear stress perturbations introduced by actuators in a laminar boundary layer as measured by sensor array. . . . .	93
4.37	Design space for PZT-5A actuator in water at 0.5 m/s. . . . .	94
4.38	Technique for obtaining multiple etch depths. . . . .	94

6.1	Wafer level view of 4 and 8 mm actuator arrays.	123
B.1	Sensor mount for 8 sensor die (2 mm spacing).	134
B.2	Sensor mount for 16 sensor die (1 mm spacing).	135
C.1	Actuator mount.	141
C.2	PZT bonding jig.	142
D.1	Error due to averaging over hot-wire length.	147
D.2	Error in determining the streamwise velocity gradient assuming a linear profile close to the wall.	147
D.3	Spanwise profiles behind cylinder at three different y locations from wall.	148
D.4	Schematic explaining sensor bias error.	148



# Nomenclature

## Roman Symbols

$A$	Normalized actuator drive amplitude, $A = 1$ corresponds to a drive amplitude of 20 V zero-to-peak (14.1 V <sub>rms</sub> )
$d$	Cylinder diameter (1.6 mm)
$d_{31}$	Piezoelectric coefficient (pC/N or (m/m)/(V/m))
$f$	Frequency
$OHR$	Overheat ratio, $R_{op}/R_{amb}$
$Q$	Sharpness factor of resonance peak
$R_{amb}$	Sensor resistance at ambient temperature
$R_{op}$	Sensor resistance at operating temperature
$t$	Time
$u$	Instantaneous streamwise velocity
$u'$	Fluctuating streamwise velocity . ( $u - U$ )
$u_{rms}$	$(\overline{u'u'})^{1/2}$
$u_\tau$	Wall shear velocity
$U$	Average streamwise velocity
$\Delta U$	Average streamwise velocity disturbance, difference between measurements in a disturbed and undisturbed flow
$U_{base}$	Velocity profile in undisturbed flow at $y = 0.5$ mm
$U_{ctrl}$	Velocity profile in controlled flow at $y = 0.5$ mm
$U_{cyl}$	Velocity profile in flow perturbed by cylinder at $y = 0.5$ mm
$U_\infty$	Free stream velocity
$v$	Instantaneous wall-normal velocity
$V$	Average wall-normal velocity
$V_{tob}$	Top of the bridge voltage in constant temperature anemometer
$x$	Streamwise position
$\Delta x_a$	Distance downstream of actuator cantilever tip
$\Delta x_c$	Distance downstream of cylinder centerline

*y* Wall-normal position,  $y_w = 0$

*z* Spanwise position

### Greek Symbols

$\alpha$  Temperature coefficient of resistance ( $/^{\circ}\text{C}$ )

$\delta^*$  Displacement thickness,  $\int_0^\infty (1 - u/u_\infty) dy$

$\eta$  Blasius similarity parameter ( $y\sqrt{U_\infty/\nu x}$ )

$\mu$  Dynamic viscosity

$\theta$  Momentum thickness,  $\int_0^\infty u/u_\infty (1 - u/u_\infty) dy$

$\nu$  Kinematic viscosity ( $\approx 15.1 \times 10^{-6} \text{m}^2/\text{sec}$  for air at  $20^{\circ}\text{C}$ )

$\Delta\tau$  Average wall shear disturbance,

difference between measurements in a disturbed and undisturbed flow

$\tau_{base}$  Wall shear stress in undisturbed flow measured by sensor array

$\tau_{ctrl}$  Wall shear stress in controlled flow measured by sensor array

$\tau_{cyl}$  Wall shear stress in flow perturbed by cylinder measured by sensor array

$\tau_{ref}$  Wall shear stress in undisturbed flow,

determined from hot-wire measurements 1 mm away from the wall

### Subscripts

$w$  Measurement at the wall

# Chapter 1

## Introduction

Applications of turbulence control include but are not limited to drag reduction, flow-separation control, heat-transfer augmentation/minimization and jet-noise reduction. Experiments and numerical simulations over the last few decades have shown that organized vortical structures play an important role in turbulent flows. Increased understanding of the mechanisms that generate and sustain turbulence has created considerable interest in turbulence control, especially in the areas of turbulent skin-friction drag reduction and transition control. Such control can have substantial financial benefits; the skin-friction drag constitutes about 50% of the total drag for a subsonic transport aircraft, with the wings contributing about 20% of the total (Joslin 1998). It is estimated that a 20% reduction in the skin-friction drag would translate into a yearly fuel savings of a billion dollars for the U. S. domestic airline fleet alone (Bushnell & Hefner 1990).

This chapter begins with a brief review of the physics of turbulent boundary layers. Various boundary layer control strategies are then discussed. The main focus of this work was to investigate the use of MEMS technology for boundary layer control. A brief introduction to MEMS is therefore included. This is followed by a list of objectives for this project. The chapter closes with an overview of the important results.

### 1.1 Turbulent Boundary Layer Physics

Turbulence is characterized by an instantaneous velocity field with a large range of length and time scales. The streamwise vortices that occur naturally in transitioning and turbulent boundary layers slowly build up spanwise variation of the streamwise momentum. This leads to the development of low-speed streaks in the wall region. The streaks in Fig. 1.1 were visualized using a hydrogen bubble wire in a water tunnel. They have an average spanwise spacing  $\Delta z^+ \approx 100$  (Kline *et al.* 1967) and average streamwise length  $\Delta x^+ \approx 1000$

(Blackwelder & Eckelmann 1979). These values have been nondimensionalized by the length scale  $\nu/u_\tau$ , where  $u_\tau = \sqrt{\tau_w/\rho}$  is the friction velocity and  $\nu$  is the kinematic viscosity (the superscript + indicates nondimensionalization by these inner wall variables, as is standard in the literature). The streaks are surrounded by intense shear layers both in the spanwise and in the wall-normal directions. This leads to the development of inflection points in both the streamwise and spanwise profiles (Blackwelder 1997). The inflectional surface surrounding the streaks is inviscidly unstable and the streaks go through a process of gradual lift-up, development of oscillations and then bursting and ejection. Most of the production of turbulent kinetic energy occurs during the bursting process. A schematic of the turbulence re-generation cycle is shown in Fig. 1.2. The burst frequency  $f_b^+$  (normalized by the time scale  $\nu/u_\tau^2$ ) has been measured to be constant with a value of 0.004 over the Reynolds number range  $10^3 < \text{Re}_\theta < 10^4$  (Blackwelder & Haritonidis 1983). Thus, the bursting process is intimately linked with the dynamics of the near-wall region.

In recent years, direct numerical simulation (DNS) has been used to resolve all the energy containing scales in low Reynolds number turbulent flows (Kim & Moin 1997). These simulations have provided considerable insight into the physics of turbulent boundary layers. Quantities that are difficult to measure experimentally are easily obtained from simulations. For example, conditionally averaged statistics show that high skin-friction values are associated with near-wall streamwise vortices (Kravchenko *et al.* 1993).

## 1.2 Boundary Layer Control Strategies

A classification of boundary layer control techniques is given in Fig. 1.3. This figure is not meant to be comprehensive and is included both to provide some perspective and to show where the current project fits in the general framework of boundary layer control strategies. Boundary layer control techniques can broadly be classified into methods that delay transition and methods that reduce the skin-friction drag in turbulent boundary layers. Turbulence control methods can be further divided into passive and active schemes. The following sections provide a brief overview of transition and turbulence control strategies.

### 1.2.1 Transition Control

The objective of transition control techniques is to delay the breakdown to turbulence by attenuating the growth of two-dimensional Tollmien-Schlichting (TS) waves. A control of proper phase and amplitude is introduced into the flow to cancel the instability waves. This wave superposition technique works because of the linear nature of the Orr-Sommerfeld equation that describes the TS waves. Out of phase cancellation and in phase reinforcement

of naturally occurring TS waves was demonstrated by Liepmann & Nosenchuck (1982).

An alternative approach is to use sensors and actuators to modify the flow so that the system is inherently stable. This idea has been explored numerically for the case of laminar plane Poiseuille flow. Joshi *et al.* (1997) developed a proportional controller that stabilized the unstable mode for a wide range of Reynolds numbers. Classical control theory was applied to a set of first-order ordinary differential equations obtained from the linearized Navier-Stokes equations using a Galerkin spectral method. Bewley & Liu (1998) extended this work by applying optimal and robust control theory to both supercritical ( $Re = 10000$ ) and subcritical cases ( $Re = 5000$ ). The transient energy growth in the subcritical case that can trigger nonlinear effects and cause bypass transition was reduced by a factor of 30 using a full information controller.

A number of researchers have investigated the control of three-dimensional large amplitude disturbances that can also cause bypass transition to turbulence. Breuer *et al.* (1989) used a controllable wall bump to create a three-dimensional disturbance with an initial amplitude greater than 2% of the free-stream velocity. The disturbance was counteracted downstream by a ‘traveling bump’ created by a streamwise array of eight flexible membranes. The active wall motion delayed the breakdown to a turbulent spot by about  $50 \delta^*$ , where  $\delta^*$  was the displacement thickness of the boundary layer at the location of the disturbance generator. Blackwelder *et al.* (1998) used a delta wing actuator in a transitional boundary layer with Görtler streamwise vortices. The actuator was able to delay the breakdown of the vortices into turbulence by about 25 boundary layer thicknesses.

### 1.2.2 Passive Turbulence Control

Passive control techniques do not require any energy input since they do not use sensors, controllers or actuators. These methods typically alter the flow surface to affect the structure of the near-wall turbulence. Bandyopadhyay (1986) provides an overview of a number of passive control strategies. Comprehensive reviews of riblets, large eddy breakup devices (LEBU’s) and the effect of wall curvature are presented in a series of chapters in Bushnell & Hefner (1990).

Riblets have been one of the more successful passive control schemes with drag reductions of about 6%, even though the wetted surface area is substantially increased. The low Reynolds number simulations of Choi *et al.* (1993) show that riblets reduce momentum transport by impeding the cross-flow motion. This is accompanied by a decrease in the Reynolds shear stress and a weakening of the streamwise vortices.

A different approach has been proposed recently by Sirovich & Karlsson (1997). They use an array of vees randomly aligned in the streamwise direction. The vees have a height

of 5–6 wall units and a transverse width of 200 wall units. The spanwise and streamwise period are 260 wall units and 300 wall units respectively. Experiments in a turbulent channel flow show that the drag is reduced by  $\approx 10\%$ . Their measurements suggest that the array interferes with the formation of energy-bearing roll modes.

### 1.2.3 Active Turbulence Control

The coherent structures described in Section 1.1 are quasi-random in space and have a finite lifetime, suggesting the need for an active control system. In recent years, there has been considerable interest in the area of active turbulence control and a number of reviews have been written on the subject (Bushnell & McGinley 1989, Gad-el-Hak 1994, Moin & Bewley 1994, Lumley & Blossey 1998). A number of patents for turbulence control techniques that might reduce skin-friction drag have also been issued in the past few years (Nosenchuck & Brown 1995, Keefe 1998, Sirovich *et al.* 1998). Active control methods can be further subdivided into open loop and closed loop methods, depending on whether any information about the ‘state’ of the flow is used by the control algorithm.

#### 1.2.3.1 Open Loop Strategies

Open loop techniques do not use any sensors and thus have no knowledge of the incoming flow. These strategies are attractive because they do not require embedded controllers with sophisticated logic. Control algorithms are designed offline and typically require continuous actuation. The actuation can be steady or vary periodically either in time or in the streamwise direction. These techniques achieve drag reduction by breaking the near-wall vortex regeneration cycle. Recent ideas in this area include spanwise wall oscillations, colliding wall jets, and the use of Lorentz forcing in conducting liquids.

The idea of spanwise wall oscillations as a control strategy was motivated by the observation that two-dimensional boundary layers subject to a crossflow or a spanwise pressure gradient experience temporary reductions in all turbulence quantities. Akhavan *et al.* (1993) studied the effect of spanwise oscillations by DNS of a turbulent channel flow at a Reynolds number  $Re_\tau = 200$ . The control was most effective with an oscillation period  $T^+ = 100$ , for which the drag and turbulence production were reduced by 40% and 62% respectively. The spanwise forcing disrupted the spatial coherence between streamwise vortices and low-speed streaks. Experimental studies in turbulent boundary layers by Laadhari *et al.* (1994) and Choi *et al.* (1998) have shown similar reductions. Flow visualization shows a realignment of the longitudinal vortices and a reduction in the meandering of the streaks. Large control velocities are required to obtain the reductions mentioned; typical spanwise velocities are

greater than  $10 u_\tau$ . The minimum power spent by the control is  $\int \tau_{yz,wall} w_{wall} dA$ , where  $\tau_{yz,wall}$  is the spanwise wall shear and  $w_{wall}$  is the wall velocity. This must be subtracted from the savings due to decreased skin-friction drag to get the true effectiveness. Baron & Quadrio (1996) have determined the net savings for the Akhavan simulations as a function of the control velocity amplitude. The maximum savings are about 10% and are obtained when  $w^+ < 5$ . At higher amplitudes, the power spent by the control is more than the savings obtained due to the drag reduction.

Spanwise colliding wall jets have been studied by Schoppa & Hussain (1998). They have demonstrated a 20% drag reduction in their channel flow simulations using counter-rotating vortices with a spanwise wavelength of 400 wall units. The large-scale forcing suppresses the streak instability mechanism by weakening the wall-normal vorticity flanking the streaks.

The use of Lorentz forces in conducting liquids was first investigated by Nosenchuck & Brown (1993). Experiments with their electromagnetic turbulence control (EMTC) tiles showed drag reductions of about 90%. However, recent simulations by Berger *et al.* (2000) showed that the power used to generate the Lorentz force was an order of magnitude larger than the power saved due to the reduced drag.

### 1.2.3.2 Closed Loop Strategies

Closed loop control strategies have been mainly studied by DNS. They span the range from *ad hoc* control based on physical intuition to optimal control with full field information. In particular, the ability to conduct ‘what if’ simulations allows researchers to investigate strategies that are not experimentally feasible (Jiménez 1994).

Choi *et al.* (1994) used a control opposite to the wall-normal velocity at  $y^+ = 10$  and obtained a 20% drag reduction. Hammond *et al.* (1998) showed that for this opposition control a virtual wall was established halfway between the detection plane and the wall, reducing the vertical transport of streamwise momentum. This decreased the Reynolds stress  $-\rho \overline{u'v'}$  and therefore the drag. No virtual wall was created when the detection plane was further from the wall ( $y^+ = 26$ ), and the control increased the drag significantly.

Jacobson & Reynolds (1993) studied the use of neural nets in a two-dimensional, three-component model of the near-wall region. Both adaptive inverse control and forward model control were considered. A skin-friction reduction of 8% was obtained. Lee *et al.* (1997) used neural nets to obtain a spatially invariant controller for channel flow ( $Re_\tau = 100$  and 180). Their results show a 20% drag reduction. The spanwise derivative of  $(\partial w / \partial y)_w$  was used to determine the control. It should be noted that this derivative is the leading term in the Taylor series expansion of  $v$  near the wall. This control therefore emulates that of Choi *et al.* (1994), but uses only wall information.

Koumoutsakos (1999) studied out of phase control of the spanwise wall-vorticity flux as a control technique in a turbulent channel flow ( $Re_\tau = 180$ ). The actuator strengths were limited to 5-15% of the mean bulk velocity. The control created unsteady spanwise vortical ‘rollers’ that shielded the wall from the bulk flow, reducing the drag by up to 40%. This technique requires spatial gradients of pressure at the wall, and is likely to be difficult to implement experimentally.

Recent landmark work by Bewley & Moin (1999) in an optimal control framework has demonstrated relaminarization of a low Reynolds number turbulent channel flow. Their approach is to minimize a cost functional based on the drag with the Navier-Stokes equations as the constraints. The solution procedure requires time-stepping of the adjoint equations along with the governing equations, and is computationally intensive. The algorithm also uses full field information and is therefore not realizable in a practical implementation. However, analysis of the data from these simulations is likely to yield new drag reduction mechanisms. Practical controllers based on these mechanisms can then be designed.

The field of suboptimal control, using wall information only, is currently an area of active research. Lee *et al.* (1998) obtained suboptimal control laws in closed form by neglecting nonlinear terms in the minimization process. Their procedure worked when the wall pressure gradient  $(\partial p / \partial z)_w$  or the spanwise shear stress  $(\partial w / \partial y)_w$  was included in the cost functional. For  $Re_\tau = 110$ , a reduction of 22% was obtained when spanwise shear stress information was used. However, the procedure failed when drag itself was included in the cost functional. The control law is expressed in wavenumber space and requires information over the entire spatial domain. By transforming the control into physical space, they show that a truncated control, with local support only, performs equally well. The truncated control is similar to Lee *et al.* (1997).

Experimental closed-loop control methods tend to selectively target coherent structures such as near-wall streamwise vortices. A control module might consist of an array of actuators, upstream and downstream sensors, and embedded controllers. This is schematically shown in Fig. 1.4. The upstream sensors measure the ‘state’ of the incoming boundary layer. One of the quantities that could be measured is the spanwise variation of the wall shear caused by the streamwise vortices (see Fig. 1.1). This information is used by a control algorithm to determine the appropriate actuator perturbations. The downstream sensors monitor the effect of the actuators. They can also be used to provide a feedback path to compensate for slow variations in flow conditions. Rathnasingham & Breuer (1997a) have used this setup to develop linear transfer functions for the flow between the upstream and downstream sensors. A time varying control is obtained by inverting the actuator transfer function. Their control reduces the wall shear by 7%.

### 1.3 Scaling Issues

Transducers must match coherent structure length and time scales in order to alter turbulence generation mechanisms that are most active in the inner region of a boundary layer. Estimates of these scales under flight conditions have been made by Gad-el-Hak (1994). Typical control module dimensions are estimated to be about 20 wall units in the spanwise direction and 500 wall units in the streamwise direction (a control module is assumed to consist of an actuator along with upstream and downstream sensors). The frequency response of the transducers should be an order of magnitude higher than the burst frequency. The sizing requirements for flows at different speeds are listed in Table 1.1. Smaller transducers with a higher frequency response are required as the free-stream velocity increases. The requirements at flight conditions are beyond current fabrication capabilities, but new materials and technologies currently under development might meet these stringent specifications. This project will focus on transducers for low speed flows. This is a necessary first step that enables the development of control strategies without requiring the integration of actuators, sensors and control logic. The experience gained here will also reveal potential fabrication pitfalls and areas where new technologies must be developed.

It is also important to examine the potential power savings due to skin-friction drag reduction so that the transducers can be designed within a realistic power budget. The power spent by a body moving at a velocity  $U_\infty$  in overcoming the wall shear  $\tau_w$  over an area  $A_c$  is:

$$P = \tau_w U_\infty A_c = \frac{C_f}{2} \rho U_\infty^3 A_c = \rho U_\infty \nu^2 A_c^+ \quad (1.1)$$

where  $C_f$  is the skin-friction coefficient. Note that the power consumption scales with the cube of the free-stream velocity but only linearly with the velocity when the area is expressed in wall units. Equation 1.1 can be used to compute the maximum power consumption for a given module size. This is listed in the last column of Table 1.1, and shows that the power consumption must be in the  $\mu\text{W}$ -mW range. Net savings are likely only for high speed flows. All sensing and actuation mechanisms should be evaluated in terms of their ability to meet the specifications in Table 1.1.

Finally, it is important to realize that most boundary layer control studies (experimental and numerical) have been performed at low Reynolds numbers and provide over-optimistic estimates of drag reduction in high speed flows. This can be seen by examining the velocity profile for a turbulent boundary layer at  $y = \delta$ :

$$\sqrt{\frac{2}{C_f}} = \frac{U_e}{u_\tau} = \frac{1}{\kappa} \ln \left( \frac{u_\tau \delta}{\nu} \right) + C + \frac{2\Pi}{\kappa} \quad (1.2)$$

Fluid	$U_\infty$ (m/s)	$\nu$ (m <sup>2</sup> /s)	$\nu/u_\tau$ (μm)	Burst freq (Hz)	Module size (μm × μm)	Power/module (μW)
Air (flight)	300	$3.0 \times 10^{-5}$	3	14000	$60 \times 1500$	1100
Air	30	$1.5 \times 10^{-5}$	15	380	$300 \times 7500$	80
Air	5	$1.5 \times 10^{-5}$	65	15	$1300 \times 32500$	15
Water	10	$1.0 \times 10^{-6}$	3	460	$60 \times 1500$	100
Water	0.5	$1.0 \times 10^{-6}$	45	2	$900 \times 22500$	5

Table 1.1: Sizing requirements for different flows. Data are for a flat plate turbulent boundary layer at a distance of 1 m from the leading edge.

All control techniques tend to alter the constant C. As the Reynolds number increases, the log term dominates and a given change in C has a smaller percentage effect on the skin-friction  $C_f$ .

## 1.4 Introduction to MEMS

MEMS is an acronym for Micro Electro Mechanical Systems. It refers to a range of micro-machining technologies that are used to create transducers for sensing, actuation, communication etc.

A schematic of the sequence of steps in a typical MEMS process is shown in Fig. 1.5. Silicon wafers are the primary starting material though other materials like glass and plastics are becoming more common. A mature set of technologies, borrowed from the IC industry, is available for the handling and processing of silicon wafers. These processes are parallel in nature and enable the fabrication of many devices on a single wafer. Silicon also allows for the potential integration of signal-conditioning circuitry along with the transducer.

Optical lithography is used to transfer patterns onto the surface of the wafer. A variety of deposition and etching techniques are then used to build up layers of the transducer. Materials that can be deposited include dielectrics (for e.g. silicon nitride, silicon dioxide, polyimides), polysilicon, piezoelectrics, and metals. Techniques like oxidation, chemical vapor deposition (CVD), ion implantation, evaporation, sputtering, and electroplating are used. Residual stresses and stress gradients in the individual films can dramatically affect performance and yield, and a number of recipes for low-stress films have been developed. These films are then selectively etched away using either wet or plasma etching. The etches can be either isotropic or anisotropic and a variety of shapes can be created. Sacrificial processes are used to create free-standing structures. MEMS devices tend to be planar in nature, but techniques such as LIGA, stereolithography, and wafer bonding are allowing

access to the third dimension.

The wafer is separated into individual dies after the parallel processing steps are completed. Cleaving along crystal planes and dicing using wafer saws are two commonly used techniques. Care must be taken to protect the transducers (especially the released and now freestanding structures) during this step. MEMS devices need specialized packaging techniques as the transducing element has to be exposed to the environment. This is especially true in fluid-mechanic applications where the transducer often has to be flush with the flow surface. Electrical connections must be made from the backside of the transducer so that they are robust and do not affect the flow when the transducer is not in operation.

The number of processing techniques and materials used in micromachining have exploded in recent years. A variety of MEMS processes and applications are discussed by Petersen (1982) and Kovacs (1998). McMichael (1996), Ho & Tai (1996), and Ho & Tai (1998) present overviews of MEMS devices used in fluid-mechanic applications. A description of common fabrication procedures carried out at the Stanford microfabrication facilities is presented in Appendix A.

## 1.5 Objectives

This work is a followup to the work of Jacobson & Reynolds (1995, hereafter denoted as JR). They developed a new piezoelectric actuator for boundary layer control. The actuator functioned as an on-demand, zero mass flux, streamwise vortex generator. Their experiments was performed in an unsteady boundary layer water tunnel. They were able to delay transition caused by a cylinder protruding from the wall by 40 displacement thicknesses.

The present work focused on using MEMS technology to develop modular arrays of sensors and actuators for low speed flows.

The specific objectives of this project were as follows:

- Develop a MEMS fabrication process for arrays of wall shear stress sensors. Evaluate sensor performance in low speed air flows.
- Develop a MEMS-based fabrication process for arrays of Jacobson actuators. Study the limits of miniaturization possible with state of the art micromachining techniques.
- Develop a robust backside contact technology for the sensor and actuator arrays.
- Characterize the actuator arrays in low speed air flows. Evaluate the actuators in terms of their frequency response, power consumption, and repeatability.

- Combine the sensor and actuator arrays to control a perturbed laminar boundary layer.

## 1.6 Overview of Important Results

This project consisted of three main phases - fabrication of sensor arrays, fabrication of actuator arrays, and testing of the transducer system in a perturbed flow. A brief summary of key accomplishments is listed below:

- Sensor modules that provide snapshots of the spanwise wall shear stress distribution were designed and fabricated. The sensors have a frequency response of 16 kHz when operated as constant temperature hot-film anemometers at an overheat ratio of 1.5. For low speed laminar flows, the response is nearly linear with a slope of 0.3 mV/mPa.
- Jacobson actuator modules were fabricated using a combination of micromachining techniques along with mesoscale assembly. The actuators are fast, have low power consumption, and create substantial disturbances in low speed boundary layers.
- The transducer arrays were used to control the flow behind a cylinder in a laminar boundary layer. The control reduced the strength of the disturbance by 85% and was effective for greater than 25 displacement thicknesses downstream of the actuator array.

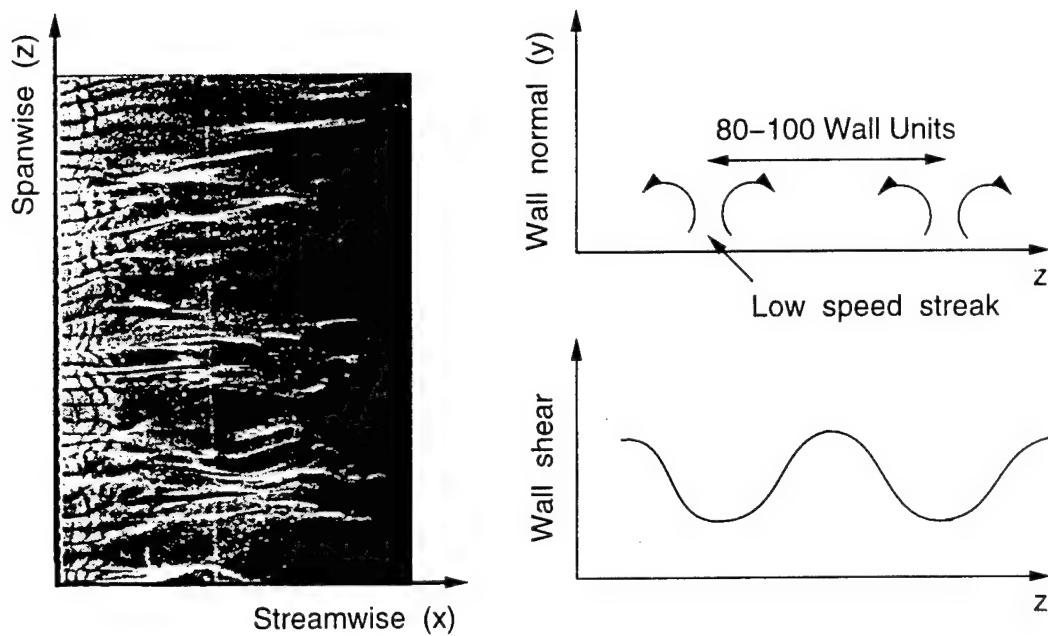


Figure 1.1: Photo of streaks in a turbulent boundary layer. The hydrogen bubble wire is 0.4 mm (2.7 wall units) above the wall. Adapted from Kline *et al.* (1967).

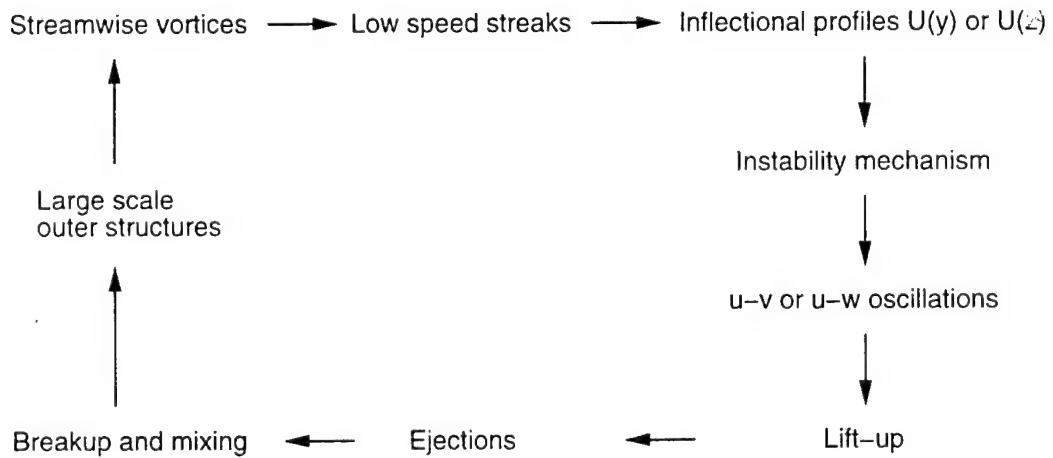


Figure 1.2: Schematic of turbulence generation cycle. Adapted from Blackwelder (1997).

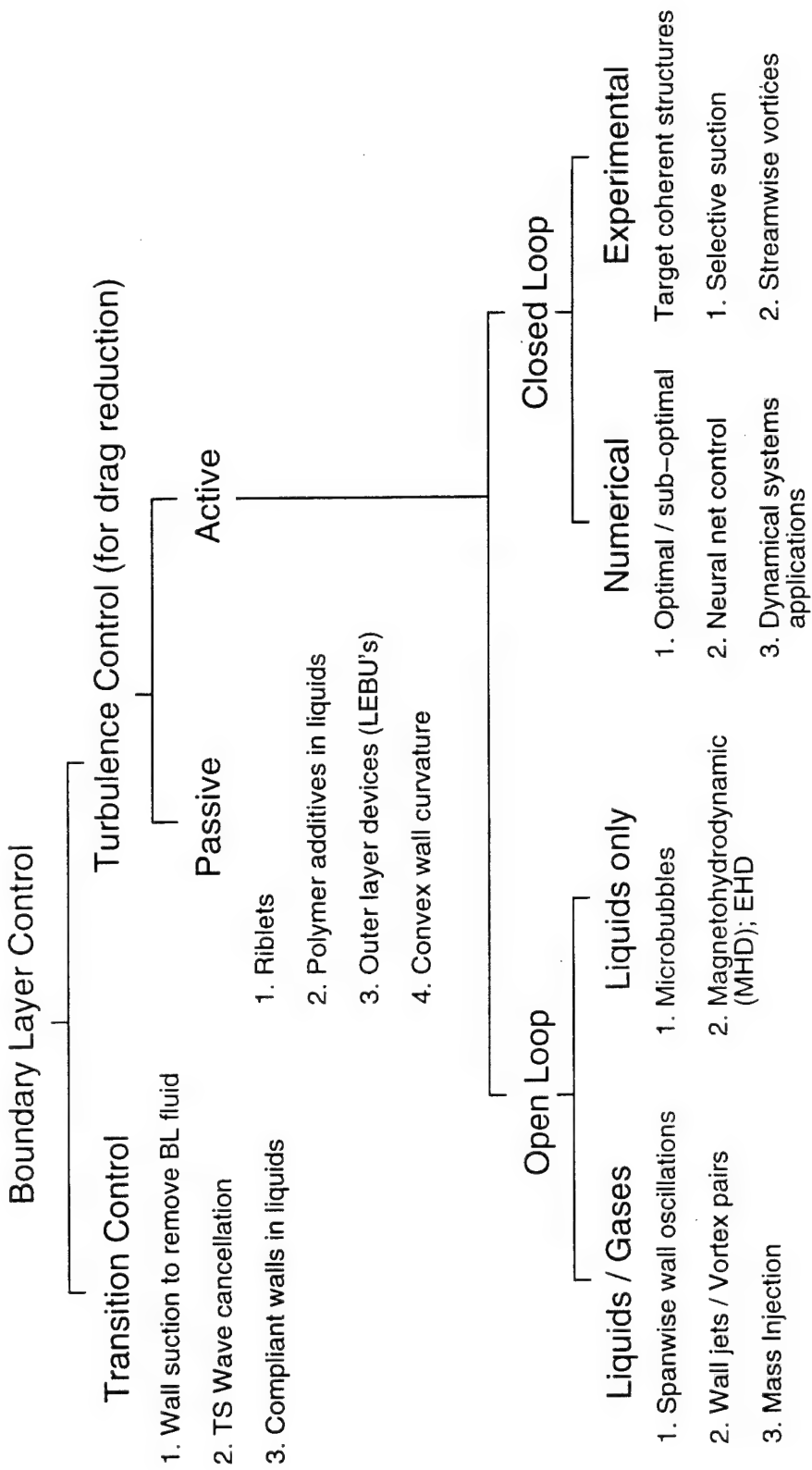


Figure 1.3: Classification of boundary layer control techniques.

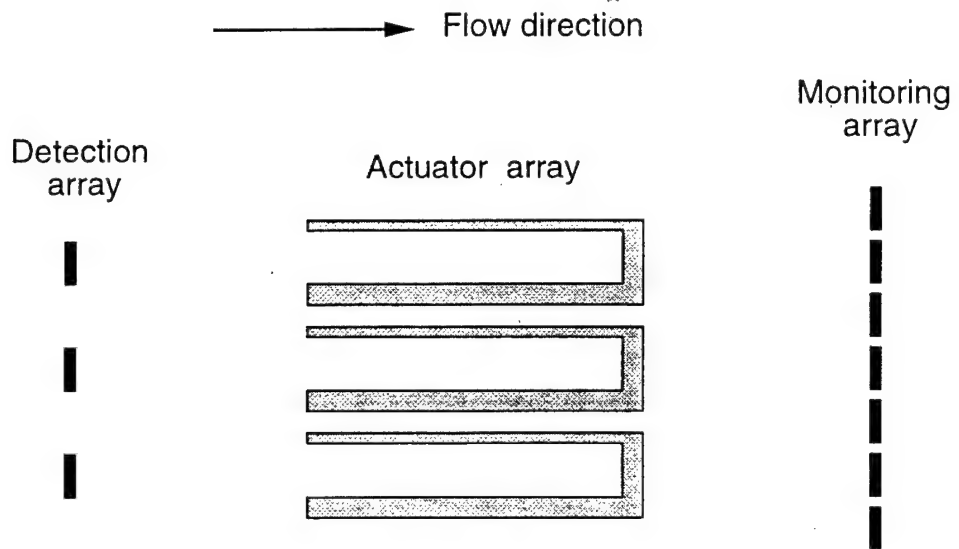


Figure 1.4: Typical experimental control module for closed loop control.

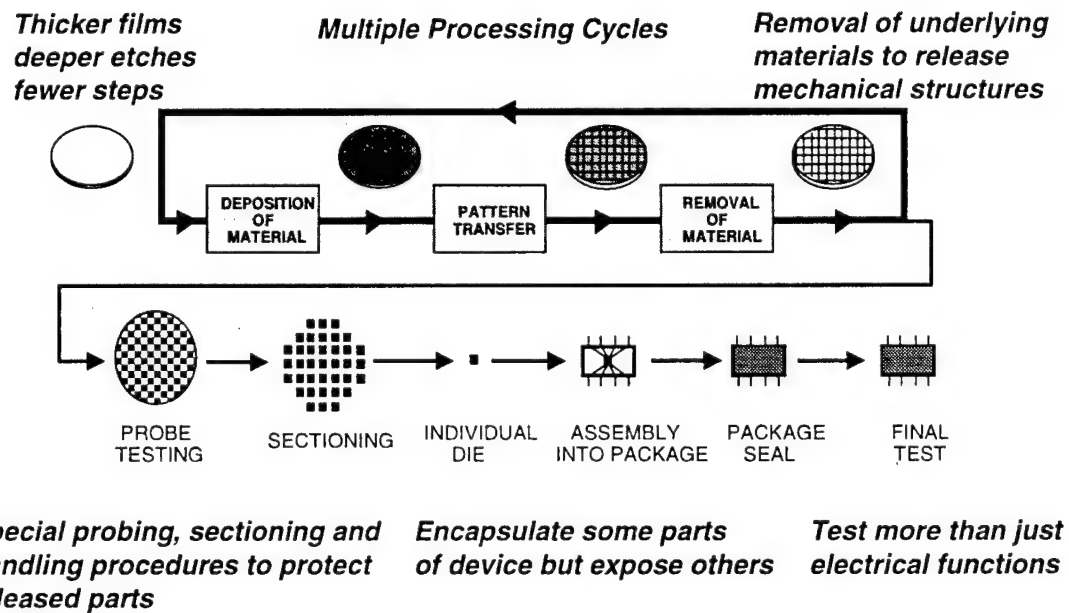


Figure 1.5: Comparison of MEMS and VLSI processes. Adapted from Pisano (1998).



## Chapter 2

# Facility and Experimental Techniques

The experiments described in this project were performed in a laminar boundary layer wind tunnel facility. The facility has been used, among others, by Westphal *et al.* (1984) and Buice & Eaton (1997), and is located in the Heat Transfer and Turbulence Mechanics Laboratory of the Mechanical Engineering Department at Stanford University. This chapter describes the main aspects of the wind tunnel, instrumentation and data acquisition equipment.

### 2.1 Wind Tunnel

A schematic of the open circuit wind tunnel used in this project is shown in Fig. 2.1. Air enters the tunnel through a large filter box ( $1.7 \text{ m} \times 1.2 \text{ m} \times 1.2 \text{ m}$ ) with a nominal filter size of  $5 \mu\text{m}$ . The blower is a New York Blower Acoustafoil size 129. It is driven by an Eaton Dynamatic 5 HP (250 V, 14 A) Ajusto-Spede-Drive with an Eaton Model 4000 controller. The blower is connected to a settling chamber with a flexible rubber coupler for vibration isolation. The settling chamber is followed by a diffuser with two additional grids. The grids enhance mixing and improve spanwise uniformity of the flow. They also decrease pressure recovery and discourage separation in the diffuser. The flow then enters a  $61 \text{ cm} \times 61 \text{ cm}$  settling chamber, passes through a honeycomb that straightens the flow, and then through a series of three small-mesh screens. Finally, the flow is accelerated through a two-sided two-dimensional 4.8:1 contraction into the test section. The cross section at the end of the contraction is  $12.7 \text{ cm} \times 61 \text{ cm}$ . A new 147 cm long test section was built for this project. The free-stream velocity in the test section can be varied from 0.5 m/s to 14 m/s.

Results are presented in a right-handed coordinate system, where  $x$  is the streamwise coordinate,  $y$  the normal coordinate, and  $z$  the spanwise coordinate. The instantaneous

velocity in the streamwise direction is denoted by  $u$ , in the normal direction by  $v$ , and in the spanwise direction by  $w$ . The wall with the transducer inserts is located at  $y = 0$ .

The actuator tips ( $\Delta x_a = 0$ ) are located 49.5 cm downstream of the contraction. A photo of the test section is shown in Fig. 2.2. The flow is from left to right. The center insert contains an array of actuators. The right insert has an array of shear stress sensors. The left insert is used for introducing a cylinder into the crossflow boundary layer. It can also be used for an upstream array of sensors. Flow diagnostics include a total pressure Kiel probe, a single component hot-wire anemometer, and a thermistor for measuring the free-stream temperature (seen in the far right of the picture).

## 2.2 Instrumentation

### 2.2.1 Data Acquisition and Control System

The main computer for data acquisition in this project was a 200 MHz Pentium Pro PC. A Data Translation DT31-EZ card was used as the primary data acquisition board. It has a throughput of 250 kHz and 16 single-ended analog to digital (A/D) inputs with 12 bit resolution. It also has 8 channels of digital input/output (DIO) and 2 channels of digital to analog output (D/A). The D/A outputs were used for controlling the tunnel velocity and for calibrating the buck and gain stage of the hot-wire anemometer. The data acquisition programs were written in the LabVIEW graphical programming environment (version 5.0).

The actuators were controlled using an Analogic DAC812 card installed in a 80486 DX2 66 MHz PC. Details about the card and the actuator drive circuitry are provided in JR. The maximum amplitude of the actuator drive signal was 20 V (14.1  $V_{rms}$ ). The drive amplitude, normalized by this maximum, is denoted by the symbol  $A$  throughout this report. The control programs were written using the Turbo C compiler (version 3.0).

### 2.2.2 Temperature Measurement

The temperature in the free stream was measured using an Omega Violet/Black thermistor (part number 44007, nominal resistance is  $5 \text{ K}\Omega$  at  $25^\circ\text{C}$ ). It was used to determine the air density and to correct the hot-wire bridge voltage for ambient temperature variations. The air temperature was not controlled and tracked ambient laboratory conditions (over a 24 hr period, the ambient temperature drifted by about  $5^\circ\text{C}$ ). The thermistor resistance was measured by a Fluke 8842A digital multimeter (DMM). A GPIB (IEEE-488) interface was used to transfer data from the DMM to the PC. The temperature was determined from

thermistor resistance using the calibration of Simonich & Moffat (1982) :

$$\frac{1}{T} = A + B \ln R + C(\ln R)^3 \quad (2.1)$$

with the following constant values:

$$A = 1.286 \times 10^{-3}$$

$$B = 2.360 \times 10^{-4}$$

$$C = 9.433 \times 10^{-8}$$

The temperature,  $T$ , is in K (kelvin) and the resistance,  $R$ , is in  $\Omega$  (ohms). This equation fits the data in Omega's datasheets to  $\pm 0.01^\circ\text{C}$  over the range of  $15\text{-}40^\circ\text{C}$ . The uncertainty in the measured temperature is  $\pm 0.2^\circ\text{C}$ .

### 2.2.3 Pressure Measurement

Pressure measurements were made using a Validyne model DP103-10 differential pressure transducer (range  $0.88 \text{ cm H}_2\text{O}$  or about  $12 \text{ m/s}$ ). The transducer was coupled to a Validyne model CD15 carrier modulator. The voltage output of the modulator varied linearly with pressure difference across the transducer diaphragm and was measured using the DT31-EZ board. The offset and gain were adjusted for maximum resolution. The pressure transducer was calibrated against a Combist micro-manometer (full scale  $1'' \text{ H}_2\text{O}$ , least count  $0.0005''$ ). The free-stream velocity was determined by measuring the dynamic pressure using a Kiel probe and a static pressure tap on the wall.

### 2.2.4 Probe Traverse

A two-axis stepper motor driven traverse was used to move the hot-wire in the wall-normal and spanwise directions. The wall-normal traverse was a Velmex Unislide Model MA1506Q1 traverse while the spanwise traverse was custom built. Details of the traverse system are summarized in Table 2.1. The stepper motors were driven in full step mode using a L/R drive. A custom driver was built for the two motors using the UCN5804B unipolar driver chip from Allegro Microsystems Inc. The DIO port of the DT31-EZ board was used to control the step and direction inputs of the UCN5804. The tunnel wall through which the flow diagnostics were introduced was made of Plexiglas strips with dimensions varying from 5 mm to 75 mm. By repositioning these strips, the entire traverse could be moved in the streamwise direction in increments of 5 mm.

Direction	Lead screw	Stepper motor details	Resolution
Wall normal	10 threads/cm	Vexta PX245-02AA, 2 phase, 6V, 0.8A/phase, 200 steps/rev	5 $\mu\text{m}/\text{step}$
Spanwise	20 threads/inch	Superior Electric M061-FC02, 2 phase, 5V, 1A/phase, 200 steps/rev	6.4 $\mu\text{m}/\text{step}$

Table 2.1: Two-axis traverse system specifications.

### 2.2.5 Hot-Wire Anemometry

A single component hot-wire anemometer was used to measure the streamwise velocity  $u$ . The hot-wire was operated in constant temperature mode for maximum frequency response. A Dantec 56C17 CTA bridge in a 56B10 main frame was used. The sensor was a TSI model 1218 single wire boundary layer probe. Both 2.5  $\mu\text{m}$  and 5  $\mu\text{m}$  diameter platinum-coated tungsten wires were used. The corresponding active lengths were 640  $\mu\text{m}$  and 1270  $\mu\text{m}$ , giving  $l/d$  ratios greater than 250. The sensor was operated at an overheat ratio  $OHR = R_{op}/R_{amb}$  of 1.8. The resistances  $R_1$  and  $R_3$  in the Wheatstone bridge were 20  $\Omega$  and 400  $\Omega$  respectively, giving a bridge ratio of 20 (see Fig. 3.24). The bridge was tuned using a square wave test signal to obtain a frequency response of 30 kHz. The bridge voltage was offset and amplified to make optimal use of the resolution of the data acquisition system.

The hot-wire was calibrated in the free stream using the Kiel probe as a reference. Calibration data were obtained by varying the free-stream velocity. The calibration data were fit to King's law:

$$V_{tob}^2 = A + BU^n \quad (2.2)$$

where  $V_{tob}$  is the mean bridge voltage and  $U$  is the mean velocity.  $A$  and  $B$  are the coefficients found by a least squares fit to the calibration data. The exponent  $n$  is often taken to be 0.45; however, in this work  $n$  was chosen to give the best least squares fit to Eqn. 2.2. The value of  $n$  was between 0.39 and 0.44. A third order polynomial fit was also used when small velocities (0–2 m/s) were being measured as in Section 4.6.1, and for calibration of the micromachined sensor arrays. Typical calibration curves for 2.5  $\mu\text{m}$  and 5  $\mu\text{m}$  wires are shown in Fig. 2.3. The 5  $\mu\text{m}$  wire has a larger response but it also averages the velocity field over a greater spanwise distance.

A Bearman temperature correction (Bearman 1971, Anderson & Eaton 1987) was used to compensate for small drifts in ambient temperature.

$$V_{corr} = V_{meas} + V_{meas} \left( \frac{\alpha}{2(OHR - 1)} (T - T_{cal}) \right) \quad (2.3)$$

where  $V_{meas}$  is the instantaneous measured voltage,  $T$  is the free-stream temperature at the time the voltage was measured, and  $T_{cal}$  is the calibration temperature. The temperature coefficient of resistance  $\alpha$  of the platinum coated tungsten wire was  $0.004/^\circ\text{C}$ . The hot-wire was recalibrated when the difference between the free-stream temperature and the calibration temperature exceeded  $1^\circ\text{C}$ .

The linearity of the Blasius profile over the first 20% of the boundary layer was used to determine the location of the wall ( $y = 0$ ). A least squares fit to the near-wall data was used to extrapolate to the zero velocity location. This offset was added to the nominal hot-wire positions to get the true wall-normal locations.

### 2.3 Facility Qualification

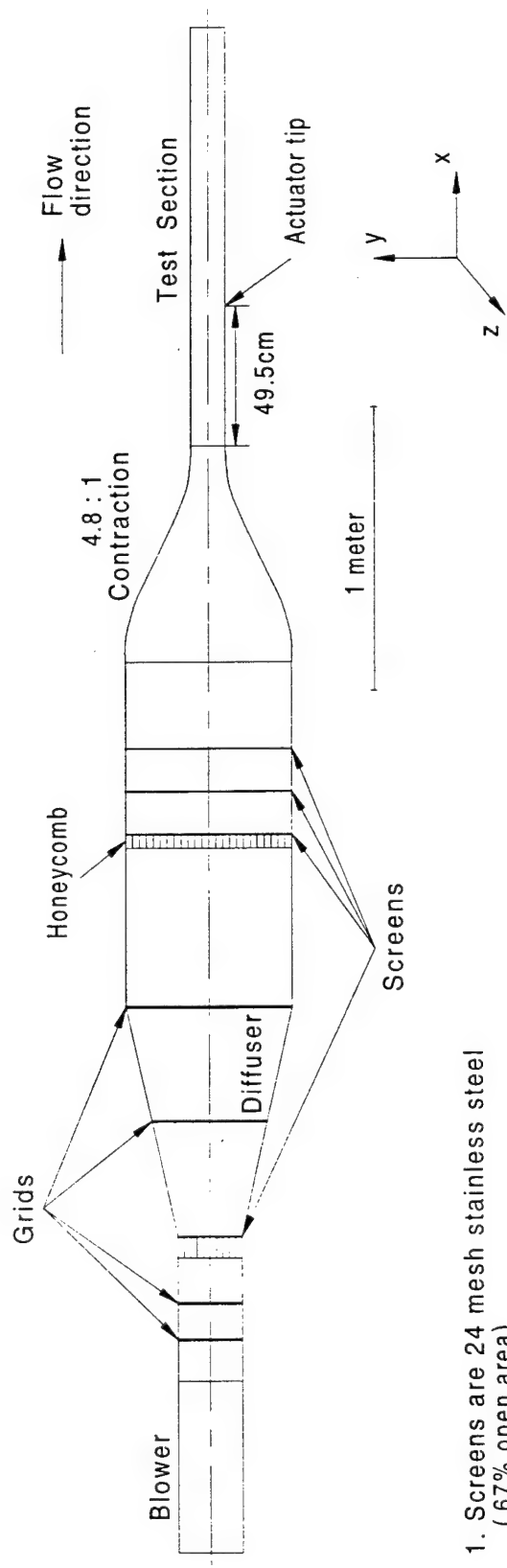
Figure 2.4 shows velocity profiles at five different spanwise locations in a laminar boundary layer at  $U_\infty = 4.9$  m/s. The data are plotted in the nondimensional Blasius coordinate  $\eta = y(U/\nu x)^{1/2}$ . A virtual origin was determined by fitting the velocity profiles to the Blasius boundary layer profile. A single origin was chosen for all the spanwise locations. The virtual origin adds an offset of 7.5 cm in the streamwise direction. The agreement with the Blasius profile is within the uncertainty of velocity and position measurements, except for the centerline profile. This is indicative of spanwise variations in the boundary layer.

Figure 2.5 shows velocity profiles at five different wall-normal locations, four in the boundary layer and one in the free stream. The maximum variation in the free-stream velocity is less than  $\pm 0.3\%$  of the mean. The rms value of the velocity fluctuations in the free-stream is about 0.35% of the mean. The maximum spanwise variation in the flow occurs at  $y/\delta^* = 1.28$  and is about  $\pm 4\%$  of the free-stream velocity. Closer to the wall at  $y/\delta^* = 0.43$  the maximum variation drops to about  $\pm 2\%$  of the free-stream velocity.

It was suspected that the grid at the diffuser exit was the cause of the spanwise non-uniformity in the boundary layer (see Fig. 2.1). This grid has 1.3 cm diameter holes on a 1.6 cm hexagonal lattice. The open area is 58% which is slightly less than the minimum 60% recommended by Tan-Atichat *et al.* (1982). The grid was removed and the spanwise runs were repeated. The non-uniformity was still present but the spanwise and wall-normal fluctuations had increased considerably. All the data presented in this report was taken with the last grid reinstalled at the diffuser exit. A systematic removal and insertion of the flow conditioning devices is required to trace the source of the spanwise non-uniformity. The spanwise uniformity in the tunnel was adequate for this project as the actuators create disturbances with magnitudes that are about 25% of the free-stream velocity.

### **2.3.1 Uncertainty Analysis**

An uncertainty analysis of experimentally measured quantities is presented in Appendix D. All uncertainty estimates are reported at a 95% confidence level. The uncertainty in the mean velocity is about  $\pm 2\%$  of the local value. The relative uncertainty in the wall shear stress determined using a hot-wire is  $\pm 6\%$ . The sensor array has an uncertainty of  $\pm 1$  mPa.



1. Screens are 24 mesh stainless steel  
(67% open area).

2. First three grids have 1.3 cm square perforations  
on 1.6 cm centers (64% open area). Last grid has  
1.3 cm dia holes on a 1.6 cm hexagonal lattice.  
(58% open area).

Figure 2.1: Plan view of wind tunnel facility.

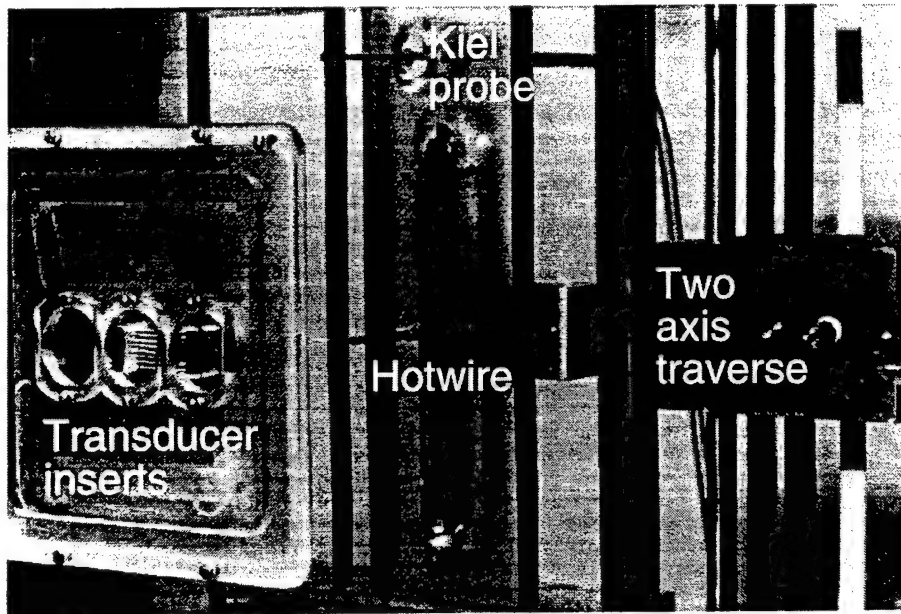


Figure 2.2: Photo of part of the test section. The transducers inserts and diagnostics are on opposite side walls but are superimposed in the picture.

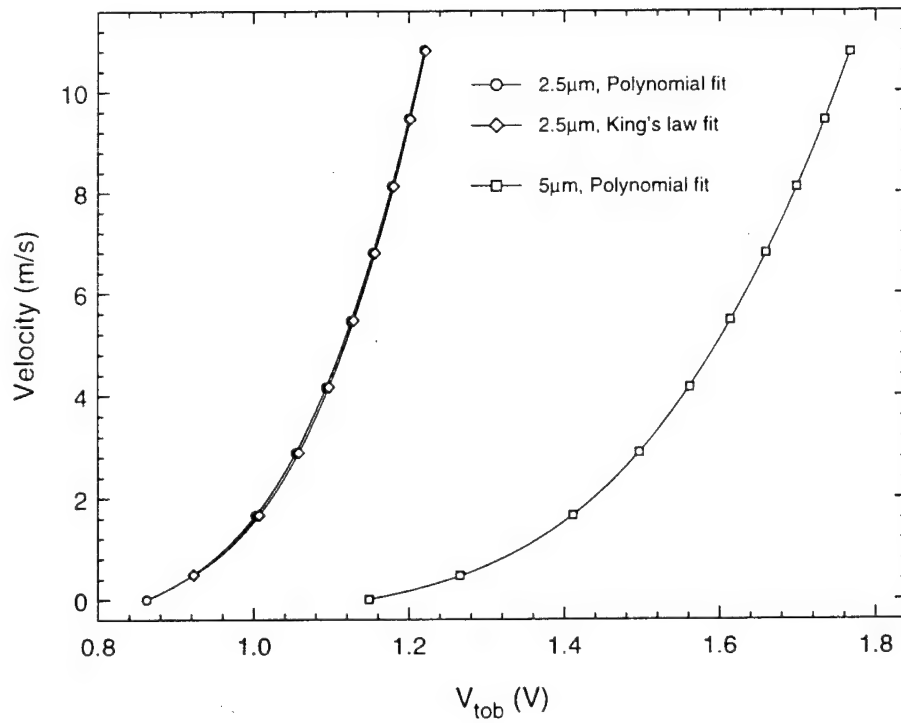


Figure 2.3: Polynomial and King's law calibration for  $2.5 \mu\text{m}$  and  $5 \mu\text{m}$  hot-wires. Note that the polynomial calibration extends to zero velocity.

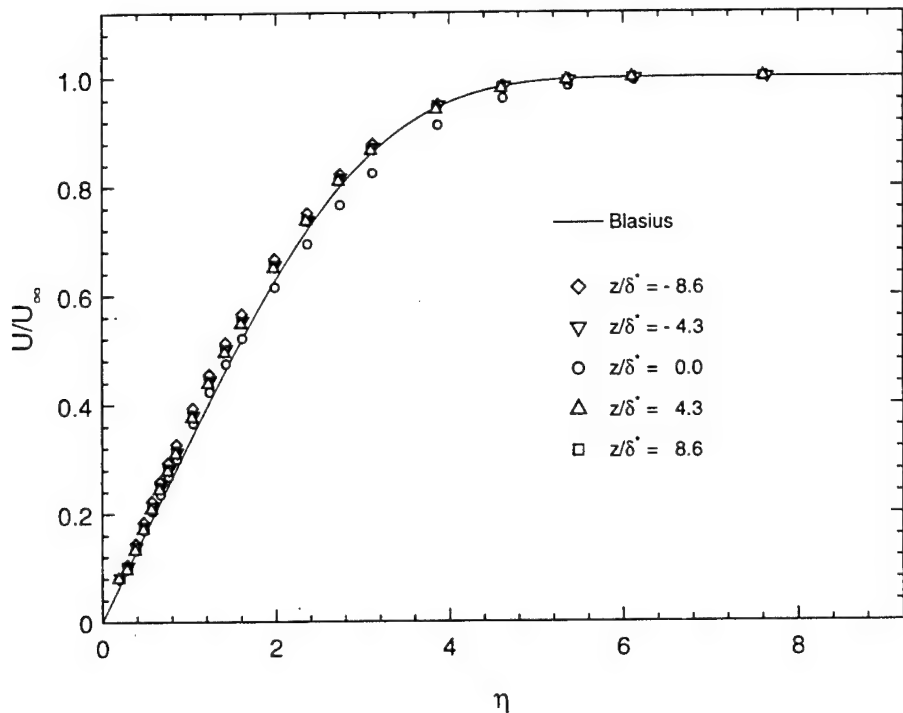


Figure 2.4: Boundary layer profiles at several spanwise locations,  $x = 49.5$  cm,  $\eta = y(U/\nu x)^{1/2}$ ,  $U_\infty = 4.9$  m/s.

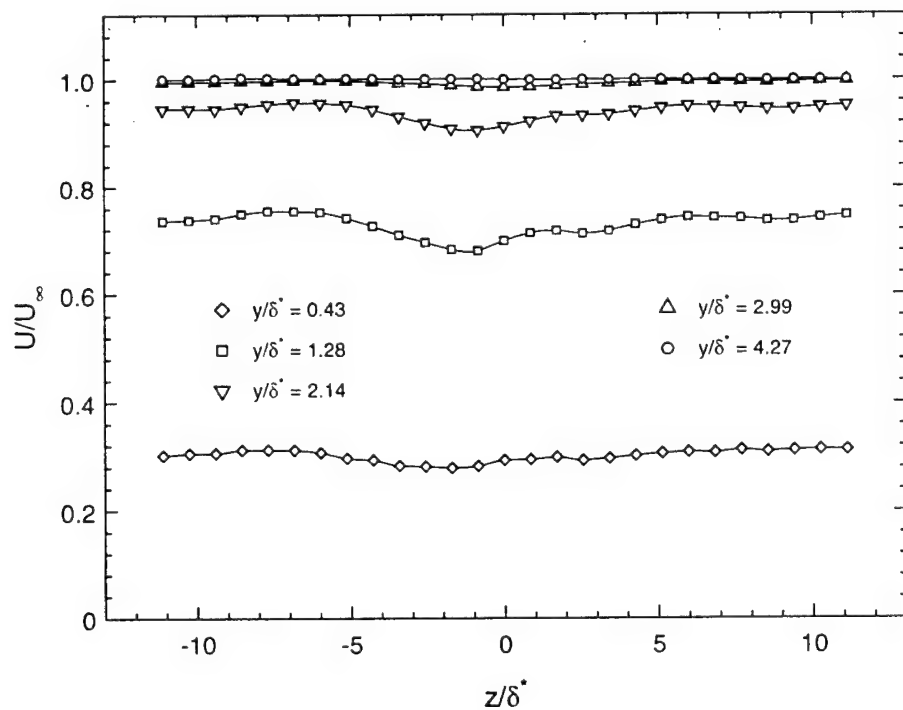


Figure 2.5: Spanwise profiles in boundary layer and in the free stream,  $x = 49.5$  cm,  $U_\infty = 4.9$  m/s.



# Chapter 3

## Surface Shear Stress Sensors

### 3.1 Introduction

Knowledge of the surface shear stress distribution is useful in analyzing flow fields and for active boundary layer control studies. Spanwise maps of the instantaneous shear stress in turbulent boundary layers can be used to predict flow details in the near-wall region (Podvin & Lumley 1998). This information can ultimately be used by an active control algorithm. Shear stress measurement techniques have been reviewed by Haritonidis (1988) and Hanratty & Campbell (1996).

*Direct methods* measure either the force or deflection caused by the wall shear stress. Floating-element sensors fall into this category and micromachined versions with capacitive, piezoresistive or position sensing readout schemes have been developed (Shajii *et al.* 1992, Padmanabhan *et al.* 1996).

*Indirect methods* can be classified as either momentum balance methods or correlation methods. Momentum balance methods involve the measurement of integral quantities like the pressure gradient in a channel flow or the momentum thickness in a boundary layer. The average shear stress is then determined by a force balance or by using the momentum integral equation. Correlation methods relate the shear stress to other measurable quantities. Examples of such sensors include the Preston tube, Stanton tube and flush mounted electrochemical or hot-film probes.

Pairs of sensors can be used to measure the magnitude and direction of the surface shear stress vector. Sirkar & Hanratty (1970) describe chevron mass transfer probes with a pair of slanted electrodes that can resolve both streamwise and spanwise wall velocity gradients. Arrays of such sensors were used to study secondary flows and identify flow patterns close to the wall in a turbulent flow (Hogenes & Hanratty 1982).

Micromachined hot-film and floating-element sensor arrays are capable of capturing both

the spatial and the temporal fluctuations of the wall shear stress (Jiang *et al.* 1996, Padmanabhan *et al.* 1997). Hot-film sensors with on-chip biasing circuitry have been recently fabricated by Wang *et al.* (1999). Hot-film sensors are simpler to fabricate and more robust than floating-element sensors and they were chosen for this project. Backside contacts that ensure planarity of the flow surface have been implemented for single sensors (Goldberg *et al.* 1994).

This chapter begins with the thermal analysis of a hot-film sensor. Next, the fabrication of sensor modules with robust multiple backside contacts is described. The sensors are characterized in terms of their I-V characteristics, power consumption and time constants. Compensation techniques for ambient temperature variations are discussed. Finally, calibration details for sensor arrays in a laminar boundary layer with a shear stress range of 0–80 mPa are presented.

## 3.2 Thermal Analysis

Figure 3.1 shows a schematic of a micromachined hot-film sensor. The heat transfer from the sensor to the fluid depends on the speed of the fluid going over it. The velocity profile is linear close to the wall and thus the heat transfer can be related to the wall velocity gradient and therefore the shear stress.

A heat transfer analysis is needed to answer issues such as the need for thermal isolation, the spacing between sensors to reduce crosstalk, and the effective sensor length seen by the flow. This requires the solution of a conjugate heat transfer problem to get accurate estimates of the wall heat flux and the surface temperature. One method for doing this is to couple a two-dimensional conduction solver with a boundary layer code like STAN7 (Kays & Crawford 1993).

However, considerable insight and scaling laws can be obtained by examining solutions for a model problem. The problem considered is that of a sensor sitting on a single material substrate, as shown in Fig. 3.2. The thermal boundary layer is assumed to be in the linear region of the velocity profile; this is normally true for micromachined sensors. Buoyancy effects are negligible (the Grashof number is estimated to be about 0.1) and heat transfer in the substrate is assumed to be by conduction. Two substrates are considered - air and silicon. These represent sensors with and without thermal isolation respectively. The solution of this model problem can also be used to estimate a spatially varying heat-transfer coefficient for a conduction solver.

In this section, analytic and numerical solutions for the model problem are developed. The need for thermal isolation is discussed. Estimates of minimum streamwise and spanwise

spacings between sensors are presented. The section concludes with a thermal budget for thermally isolated sensors in air.

### 3.2.1 Analytic Solution

An analytic solution is developed for the two-dimensional quasi-steady conjugate heat transfer problem following Mathews & Poll (1985). Longitudinal diffusion in the fluid is ignored in accord with the boundary layer approximation. Analytic solutions including this term show that this is a valid approximation (Mathews & Poll 1985). Since characteristic time scales in the fluid are much shorter than in the substrate, the problem is assumed to be quasi-steady in the fluid and unsteady in the substrate (Cole & Beck 1987). The solution is used to validate the numerical code in two dimensions. The code is then extended to three dimensions.

The governing equations are:

$$y^* \geq 0 : \quad \beta^* y^* \frac{\partial T_f^*}{\partial x^*} - \alpha_f^* \frac{\partial^2 T_f^*}{\partial y^{*2}} = 0 \quad (3.1)$$

$$y^* \leq 0 : \quad \frac{\partial^2 T_s^*}{\partial x^{*2}} + \frac{\partial^2 T_s^*}{\partial y^{*2}} = 0 \quad (3.2)$$

where  $*$  denotes dimensional quantities, and the subscripts  $f$  and  $s$  represent the fluid and the substrate respectively.  $\alpha_f^*$  is the thermal diffusivity of the fluid and a linear velocity profile  $U^* = \beta^* y^*$  is assumed.

The boundary conditions include matching the temperature and heat flux at the interface and the requirement that the temperature drop to ambient at large distances from the sensor. The equations are nondimensionalized using the length scale  $L^* = \sqrt{\alpha_f^*/\beta^*}$  and the integral of the heat flux  $q'^* = \int_{-\infty}^{+\infty} q''^*(x) dx$ .

The nondimensional equations and boundary conditions are:

$$y \geq 0 : \quad y \frac{\partial T_f}{\partial x} - \frac{\partial^2 T_f}{\partial y^2} = 0 \quad (3.3)$$

$$y \leq 0 : \quad \frac{\partial^2 T_s}{\partial x^2} + \frac{\partial^2 T_s}{\partial y^2} = 0 \quad (3.4)$$

$$T_s(x, 0) = T_f(x, 0) \quad (3.5)$$

$$K \frac{\partial T_s}{\partial y}(x, 0) - \frac{\partial T_f}{\partial y}(x, 0) = q''(x) \quad (3.6)$$

$$x \rightarrow \infty, \quad y \rightarrow \infty \quad T \rightarrow 0 \quad (3.7)$$

where  $K$  is the thermal conductivity ratio  $k_s/k_f$ .

The equations are reduced to ordinary differential equations by taking the Fourier transform in the  $x$  direction and are then solved as in Mathews & Poll (1985). The surface temperature distribution in the Fourier domain is given by:

$$\bar{T}(\alpha, 0) = \frac{\bar{q}(\alpha)C_1}{\sqrt{4\pi\alpha^2}KC_1 + (2\pi\alpha)^{1/3}\exp(-i\pi/6)C_2} \quad (3.8)$$

where  $\bar{q}(\alpha)$  is the Fourier transform of the top-hat heat flux:

$$\bar{q}(\alpha) = \frac{\sin(2\pi\sqrt{Pe}\alpha)}{2\pi\sqrt{Pe}\alpha} \quad (3.9)$$

$Pe$  is the Peclet number defined as:

$$Pe = \frac{a^{*2}}{L^{*2}} = \frac{\beta a^{*2}}{\alpha_f} \quad (3.10)$$

where  $a^*$  is the half-width of the sensor (see Fig. 3.2).

The surface temperature distribution in physical coordinates is obtained by taking the inverse Fourier transform of Equation 3.8 and is given by:

$$T(x, 0) = \int_0^\infty \bar{T}_r(\alpha) \cos(2\pi\alpha x) + \bar{T}_i(\alpha) \sin(2\pi\alpha x) d\alpha \quad (3.11)$$

where:

$$\bar{T}(\alpha, 0) = \bar{T}_r(\alpha) + i\bar{T}_i(\alpha) \quad (3.12)$$

The integration in equation 3.11 is performed using a 4<sup>th</sup> Runge Kutta routine with accuracy monitoring. Similar operations are performed for the heat flux.

### 3.2.2 Numerical Solution in Two Dimensions

The numerical solution is obtained by application of the Unsteady Surface Element (USE) method (Cole & Beck 1987, Cole & Beck 1988). The temperature in the substrate is obtained using DuHamel's theorem in terms of the heat flux at the interface:

$$T_s(x, y, t) - T_\infty = - \int_{\xi=-\infty}^{\infty} \int_{\lambda=0}^t q_s(\xi, \lambda) \frac{\partial^2 \psi_s}{\partial \xi \partial t}(x - \xi, y, t - \lambda) d\xi d\lambda \quad (3.13)$$

$\psi_s$  is the fundamental solution for unit heat flux over the half plane  $x \geq 0$ . At the surface  $y = 0$ ,  $\psi_s$  is given by:

$$\psi_s(x, 0, t) = \frac{1}{\sqrt{4\pi k_s^2 t}} [2\sqrt{\alpha_s t} \operatorname{erfc}(\frac{x}{2\sqrt{\alpha_s t}}) - \frac{x}{\sqrt{\pi}} E_1(\frac{x^2}{4\alpha_s t})] \quad (3.14)$$

where  $\text{erfc}( )$  is the complementary error function and  $E_1( )$  is the exponential integral function.

An equation similar to (3.13) holds in the fluid where the fundamental solution is:

$$\psi_f(x, 0, t) = \frac{a}{k_f} \frac{9^{1/3}}{\Gamma(2/3)Pe^{1/3}} \left(\frac{x}{a}\right)^{1/3} H(x) \quad (3.15)$$

where  $H( )$  is the Heaviside step function and  $\Gamma( )$  is the Gamma function.

The steps in the USE method are briefly summarized as:

1. Equation (3.13) is discretized both in space and time over N surface elements and M time steps. The heat flux is assumed to be constant over each surface element and each time step.

$$T_s(x, y, t) - T_\infty = - \sum_{j=1}^N \sum_{k=1}^M q_s(x_j, t_k) [\Delta\psi_s(x, x_j, y, t_M - t_k) - \Delta\psi_s(x, x_j, y, t_M - t_{k-1})] \quad (3.16)$$

where:

$$\Delta\psi_s(x, x_j, y, t) = \psi_s[x - (x_j - L_j/2), y, t] - \psi_s[x + (x_j + L_j/2), y, t] \quad (3.17)$$

$x_j$  is the streamwise coordinate of the center of element j.  $\Delta\psi_s(x, x_j, y, t)$  represents the solution for a unit heat flux over element j. It is calculated by taking the difference of two half-plane solutions, as is illustrated in Fig. 3.3. This procedure is repeated for the fluid solution.

2. The temperature at the interface is matched at each time step. This gives a matrix equation in the unknown interfacial heat flux that involves a discrete convolution in time. The equation can be solved starting from the first time step.

### 3.2.3 Numerical Solution in Three Dimensions

Spanwise diffusion in the fluid is ignored in accord with the boundary layer approximation. As a result, the two-dimensional solution is still valid in three dimensions. No such simplification can be made for the substrate. The new fundamental solution for the substrate is for unit heat flux over the quarter plane  $x \geq 0, z \geq 0$ . At the interface  $y = 0$ ,  $\psi_s$  is given by:

$$\psi_s(x, 0, z, t) = \frac{\sqrt{\alpha_s}}{4\sqrt{\pi}k_s} \int_{\lambda=0}^t \frac{1}{\sqrt{t-\lambda}} [1 + \text{erf}(\frac{x}{2\sqrt{\alpha t}})] [1 + \text{erf}(\frac{z}{2\sqrt{\alpha t}})] \quad (3.18)$$

The solution for unit heat flux over an element can be constructed by superposing four quarter plane solutions (Liang & Cole 1992). The USE method outlined in the previous section can then be applied.

### 3.2.4 Sensor Behavior in Water and Air

Results are presented for flow in water at 0.5 m/s and in air at 10 m/s. Figures 3.4 and 3.5 show the heat flux and the temperature distributions for a sensor on a silicon substrate. Silicon has a high thermal conductivity, about 150 W/m-K, and provides the dominant loss mechanism. In both cases, less than 1% of the heat flux goes into the fluid. The temperature profiles are nearly symmetric about  $x/a = 0$ , which again confirms that conduction into the substrate is much more significant than convection into the fluid. Thus, thermal isolation is critical for operation of these sensors.

Figures 3.6 and 3.7 show the corresponding profiles for a thermally isolated sensor. The pure fluid solution with no conduction into the substrate is also shown. For water, the conjugate heat transfer solution closely matches the fluid only solution. This is because water has a thermal conductivity about 25 times that of air, and provides the path with the least thermal resistance. For air, about 85% of the heat flux enters into the flow directly above the sensor. The conjugate solution has a considerably lower peak temperature than the fluid only solution and also shows that the effective sensor length is at least twice the physical size of the sensor. Note that the temperature profiles in both cases have long wakes with little upstream influence, as is expected for a flow in which convection is the dominant heat transfer mechanism. The wakes also suggest that a streamwise spacing of 50 sensor lengths is required to keep the magnitude of the crosstalk between streamwise rows of sensors below 10%.

Figures 3.8 and 3.9 show the two-dimensional heat-flux and temperature distributions for thermally isolated sensors with an aspect ratio of 8. Once again, the sensor performs better in water with a more localized heat-flux distribution and smaller lateral spreading. A minimum spanwise spacing of 10 sensor lengths is required to minimize crosstalk in the spanwise direction.

### 3.2.5 Heat Transfer Budget for Thermally Isolated Sensors in Air

While the previous analysis provided useful scaling estimates, it is not directly applicable to the micromachined sensor shown in Fig. 3.1. This is because the sensor diaphragm is bounded by high thermal conductivity silicon that comprises the bulk of the sensor chip. The silicon serves as an isothermal material and maintains the temperature at the diaphragm

Path	$R_{thermal}$ equation	$R_{thermal}$ (K/mW)	Budget %
Metal	$L_2/(8k_m t_m d)$	45	62
Polyimide	$L_1/(4k_i t_i L_2) \parallel L_2/(4k_i t_i d)$	130	21
Fluid	$1/(hdL_2)$	200	14
Back Loss	$t_{wafer}/(k_{air} d L_2)$	1100	3

Table 3.1: Heat transfer budget for thermally isolated sensor in air at 10 m/s.

boundary close to the ambient temperature. Thus, losses even from the extremely thin membrane become important and must be considered in the analysis.

A thermal resistance model accounting for the various heat-transfer paths is shown in Fig. 3.10. A parabolic temperature distribution is used to estimate the resistance for the metal as it has internal heat generation. This analysis is simplistic as it assumes linear temperature profiles and one-dimensional behavior but it should provide order of magnitude estimates. A list of the thermal resistances and their contribution to the heat transfer budget is given in Table 3.1. The spanwise conduction in the metal film is a major source of heat loss and accounts for about 60% of the heat transfer budget.

### 3.3 Fabrication

The fabrication sequence is summarized in Fig. 3.11. A layer of low-stress silicon nitride 0.2  $\mu\text{m}$  thick is deposited on <100> silicon wafers. The nitride on the wafer backside is patterned to define the thermal isolation cavity and contacts. A timed anisotropic etch in KOH solution (30% wt, 80 °C) is carried out to thin the silicon in the exposed regions (Fig. 3.11a). A two step liftoff process is then used to define the sensors on the frontside. First, a bilayer of Cr:Ni (200 Å : 2500 Å) is evaporated to define the sensor element. The thickness of the nickel layer is limited by residual stresses that can cause the nickel to delaminate from the substrate. This is followed by evaporation of Cr:Au (200 Å : 1  $\mu\text{m}$ ) to create low resistance leads to the contacts. The thickness of the gold layer was chosen so that the lead resistance is less than 10% of the total sensor resistance. A layer of low thermal conductivity polyimide 7  $\mu\text{m}$  thick is spun on to form the diaphragm in which the sensor is embedded (Fig. 3.11b). The polyimide electrically isolates the sensors in conductive environments and protects the metal leads. It also supports the metal lines over the contacts once they are released, as was first shown by Barth *et al.* (1985). A one-sided anisotropic etch is then used to etch the silicon remaining in the trenches. This is followed by a backside nitride etch that exposes the contacts and removes the nitride from under

the sensor. Next, a low temperature dielectric (photoresist AZ4620 or PECVD nitride) is deposited on the backside and patterned in a contact aligner to provide access to the metal leads on the frontside. This step reduces the parasitic capacitance between contacts but was omitted as explained in Section 3.4.1. A ribbon cable connector (8 pin, 2 rows, 2 mm spacing from Samtec Inc.) is then used to transfer conductive epoxy (H20E-PFC from Epoxy Technology Inc.) into the backside contact trenches. The process is self-aligning and multiple contacts are made simultaneously (Fig. 3.11c, see Appendix A for more details). Finally, the sensor die is epoxied into a custom designed Plexiglas mount to complete the fabrication process. A step-by-step listing of the fabrication process is given in Appendix B.

Photos of the frontside and backside of a completed sensor wafer are shown in Figs. 3.12 and 3.13 respectively. Six through wafer alignment marks are seen in both photos. Test structures for determining the resistivity of the metal films are seen in the right hand lower corner of Fig. 3.12. Figure 3.13 shows the thermal isolation cavities, backside contacts, and the dicing guides for separating the individual dies. Each sensor has its own ground contact to avoid the formation of ‘ground loops’. The sixteen sensor arrays have two staggered rows of contacts for two ribbon cable connectors. In this case, alternating sensors have longer leads. The fabrication process is quite robust and die level yields (all sensors in an array functional) are greater than 90%. Figure 3.14 is a top view of part of a sensor die. It shows the sensing element and the leads to the backside contacts. The spanwise spacing of the sensors are 2 mm and 1 mm for the eight and sixteen sensor arrays respectively. A magnified view of a single sensor is shown in Fig. 3.15. The outline of the thermal isolation cavity beneath the sensor is clearly seen. The dimension of the sensing element is  $35 \mu\text{m}$  by  $280 \mu\text{m}$ . This gives an aspect ratio of 8 and is chosen to obtain nominal resistances between 5–6  $\Omega$ . This ensures that the sensor arrays are compatible with standard constant temperature anemometry equipment.

## 3.4 Characterization

### 3.4.1 Evaluation of Backside Contacts

A cross-section through a backside contact is shown in Fig. 3.16. Cured epoxy is distributed uniformly around the connector pin. Insertion of the connector into the trenches does not cause significant bulging over the contacts on the active side. The contact resistance is estimated to be less than  $0.1 \Omega$ . The leakage resistance between adjacent contacts (without dielectric isolation) as a function of input DC voltage is shown in Fig. 3.17. The inset in the figure shows the test setup, which is a simple voltage divider. The parasitics are modeled as a resistance and a capacitance in parallel. The measurements have large error bars and

considerable scatter as the output voltage fluctuates considerably. However, the leakage resistance is always greater than  $200\text{ k}\Omega$  and is of little concern because of the small sensor resistance.

The problem of parasitic capacitances between adjacent contacts is minimized because of the small sensor resistance. Techniques for reducing this capacitance include using a thick dielectric layer, wafer thinning, and partial metallization to reduce contact area (Linder *et al.* 1994, Burger *et al.* 1995). The setup for measuring the parasitic capacitance is shown in the inset of Fig. 3.18. The capacitance is determined from the 3 dB frequency  $1/(2\pi RC)$  of the voltage divider. At the 3 dB frequency the amplitude of the output drops to 0.707 times the amplitude at DC and this is shown by a dashed line in the figure. Fig. 3.18 shows that the parasitic capacitance between contacts is reduced from  $1200\text{ pF}$  to  $220\text{ pF}$  by using a coating of AZ4620 photoresist. This increases the crossover frequency for the RC network formed by the sensor and the parasitic capacitance to  $145\text{ MHz}$  from  $27\text{ MHz}$  (assuming a sensor resistance of  $5\text{ }\Omega$ ). In the experiments in this project, the sensors are used in constant temperature mode with a maximum cut-off of  $20\text{ kHz}$ . Furthermore, they are interfaced to the anemometers using  $5\text{ m}$  BNC cable. The cable itself adds a parasitic capacitance of about  $500\text{ pF}$  to the Wheatstone bridge circuit. Thus, there is little benefit in reducing the parasitic capacitance and the dielectric coating step is omitted in order to simplify the fabrication process.

### 3.4.2 TCR and I-V Characteristics

The temperature coefficient of resistance (TCR) of the sensor is shown in Fig. 3.19. The data were obtained by placing sensor wafers without thermal isolation on a hot chuck and measuring the sensor resistance over the expected operating temperature range. The TCR of the sensors as determined from the least-squares fit is  $5.5 \times 10^{-3}/^\circ\text{C}$  and compares well with bulk values of nickel. Once the TCR has been determined, the sensor can also be used as a resistance temperature device (RTD) to measure the bulk temperature of the silicon die. This is used to correct for changes in the ambient temperature as will be discussed in Section 3.5.

Fig. 3.20 shows the current-voltage characteristics for a sixteen sensor array. As the drive current increases, the voltage drop across the sensor starts to increase exponentially. This is due to the increase in resistance caused by Joule heating of the thermally isolated sensor. The sensors with long leads have a higher lead resistance and therefore a higher offset. It should be noted that the lead resistance is thermally coupled to the silicon and therefore does not cause appreciable heating of the polyimide diaphragm and the active element. Therefore, the slopes for the sensors with short and long leads are the same, especially at

higher bias currents. The plot also shows the repeatability that can be achieved within a sensor array.

The plot of sensor resistance as a function of drive current in Fig. 3.21 clearly shows the higher lead resistance for the sensor with long leads. An overheat ratio of 1.5 is easily attainable before burnout, which occurs close to 45 mA in still air. The increase in sensor resistance can be converted to an average temperature rise using the TCR determined earlier. This can then be plotted against the power input to the sensor to extract the thermal resistance. This was carried out for four different sensor types and the results are shown in Fig. 3.22. The sensor where the thermally isolation cavity is backfilled with epoxy has the lowest thermal resistance. The nominal isolation case has a thermal resistance of about 9 K/mW. The thermal resistance increases by 11% when the 0.2  $\mu\text{m}$  thick silicon nitride membrane is etched away,. This is because the low-stress silicon nitride has a relatively high thermal conductivity of about 8 W/m-K (Kurabayashi 1999). The thermal resistance increases by 43% when the polyimide is etched so that its thickness is reduced from 7  $\mu\text{m}$  to 3.5  $\mu\text{m}$ . The sensors with the silicon nitride membrane etched were chosen for the flow experiments. This ensures that the flow surface does not see a step in the polyimide and circumvents repeatability issues associated with non-uniformity of the polyimide etch rate across the sensor die. Individual sensors have a power consumption of about 10 mW at an overheat ratio of 1.5 (about 90 °C above ambient).

### 3.4.3 Time Constants

The sensor time constant was measured using the  $3\omega$  technique as indicated in Fig. 3.23. The  $3\omega$  technique has been used previously for thermal conductivity measurements (Cahill 1990). As shown in the inset, the sensor is driven by a current source at angular frequency  $\omega$ . This causes temperature and therefore resistance oscillations at  $2\omega$  because of  $i^2R$  heating in the metal sensor. The resistance oscillation times the original driving current at frequency  $\omega$  causes a small oscillation of the voltage across the sensor at frequency  $3\omega$ . This third harmonic is picked up by a differential lock-in amplifier and the time constant is determined from the 3 dB point in the resulting Bode plot. In still air, the time constant is 2 ms. This is adequate for control experiments in low speed air flows even without any compensation.

The sensor must follow shear stress fluctuations in order to measure turbulent statistics accurately. This requires that the sensor have a frequency response that captures all the dominant energy containing fluctuations in the flow. In practice, high bandwidths are obtained using constant temperature anemometry. The key idea is to compensate electronically for the thermal inertia of the sensor. A schematic of a constant temperature anemometer (CTA) circuit is shown in Fig. 3.24. The sensor is one leg of a Wheatstone

bridge. A change in velocity (or shear stress) over the sensor causes a change in the temperature and hence the resistance of the sensor. The error signal because of the bridge imbalance is amplified and fed back to the top of the bridge. Thus, the sensor is maintained at a constant temperature and the top of the bridge voltage  $V_{tob}$  now carries information about the shear stress. The bridge voltage is offset, amplified and filtered before being digitized by the data acquisition equipment. Further details about hot wire anemometry can be found in Bruun (1995).

Figure 3.25 shows a rack of ten hot-wire anemometers from A. A. Lab Systems (Wilmington, DE 19810) used for driving the sensors. Two such racks were used. The resistances  $R_1$  and  $R_3$  were  $50 \Omega$  and  $500 \Omega$  respectively, giving a bridge ratio of 10. The gain and cut-off frequency of the de-aliasing filter for all the sensors were set at 100 and 14 kHz respectively. A linearized analysis of the governing equations shows that both electrical and velocity perturbations about an operating point have the same time constant (Perry 1982). The frequency response of the system was therefore tested by injecting a square wave signal into the bridge circuit, as shown in Fig. 3.24. The response of the system to the square wave input is shown in Fig. 3.26. The system has a frequency response of 16 kHz at an overheat ratio of 1.5.

### 3.5 Correction for Ambient Temperature Variations

Figure 3.27 shows the increase in chip temperature at two tunnel speeds determined by using one of the on-chip sensors as a RTD. At the low wind-tunnel speeds in this project, about 80% of the heat generated in the sensor flows directly into the substrate. This causes an increase in the bulk temperature of the silicon chip that depends on the number of sensors turned on. Therefore, all the sensors used during data acquisition must be turned on during calibration. The temperature rise decreases as the tunnel velocity increases. This is because the heat transfer coefficient on the entire chip surface increases with an increase in the free-stream velocity. As calibration data are obtained by varying the tunnel speed, the chip temperature cannot be used to correct for free-stream temperature variations during calibration, as will be shown in Fig. 3.32.

Figure 3.28 shows the drift of the amplifier voltage of two sensors over a 24 hour period. The chip temperature and the free-stream temperature are also shown. As the free-stream and the chip temperature drop, more energy is required to maintain the sensor at its operating temperature and therefore the bridge voltage increases. The opposite behavior is seen when the free-stream temperature rises. Hence, a crossplot of bridge voltage vs. temperature can be used to extract a temperature compensation coefficient. This is shown in

Figs. 3.29 and 3.30. The crossplot of bridge voltage vs. free-stream temperature in Fig. 3.29 shows hysteresis-like behavior. The crossplot of chip temperature vs. free-stream temperature shows the same hysteretic pattern. This is because the sensor mount acts as a thermal capacitance and causes the chip temperature to change at a different rate, especially during the cooling part of the cycle. The crossplot of bridge voltage vs. chip temperature collapses the previous data, as shown in Fig. 3.30. This shows that the bridge voltage tracks the chip temperature and hence the chip temperature must be used for temperature compensation during operation. The two slopes in the figure are different because the sensor with long leads has a larger resistance in the anemometer circuit. The temperature compensation coefficients for all sensors in the array are determined simultaneously and are used to correct the raw bridge voltages during data acquisition.

Figure 3.31 shows a crossplot of the bridge voltage vs. chip temperature at ten different speeds over the entire calibration range. The mean temperature correction coefficient is about 10 mV/C with a standard deviation of 0.5 mV/C. Thus, the slope does not change appreciably over the velocity range under consideration and a single temperature compensation coefficient can be used over the entire velocity range.

### 3.6 Calibration

Fig. 3.32 shows the response of a single sensor as the free-stream velocity is varied from 0 to 10.8 m/s. The sensor responds to changes in the free-stream temperature at the closed loop bandwidth. The chip temperature decreases as the free-stream velocity increases and so cannot be used to correct for increases in the free-stream temperature (note that the CTA circuitry keeps only the sensing elements and not the entire chip at constant temperature). The sensor output is therefore corrected using the free-stream temperature and a compensation coefficient evaluated from a crossplot of bridge voltage vs. free-stream temperature (Fig. 3.29). The plot of the amplifier voltage shows that the sensor response is composed of two parts. One is the immediate rise caused by increase in the shear stress over the sensor. The second part of the response is due to the increased heat loss to the substrate caused by a decrease in the chip temperature. The conduction response ranges from 20–40% of the total sensor response. The larger fractions occur at lower velocities due to greater decreases in the chip temperature. This implies that the sensor will always underpredict spanwise variations in wall shear as discussed in Appendix D. The plot shows that the chip temperature reaches a quasi-steady state in about 1.5 minutes. This corresponds to about two or three time constants of the entire chip depending on the flow velocity. Note that the data in the plot is only for 1.2 min after the flow velocity is changed. During

calibration, the temporal behavior of the sensor is not resolved. The amplifier voltage is sampled approximately 1.5 minutes after the free-stream velocity is changed. The 1.5 minute interval was a compromise between allowing the sensor to come to steady state and finishing the calibration in a reasonable amount of time.

The sensors are calibrated against a hot-wire placed at  $y = 1$  mm. The hot-wire itself is calibrated *in situ* and the data is fit using a third order polynomial to avoid errors at low velocities. The velocity data can be converted to wall shear  $\tau_w$  as the Blasius profile is linear over the first 20% of the boundary layer (with an error of less than 1%):

$$\tau_w = \mu \frac{\partial U}{\partial y} \Big|_w \approx \mu \frac{U}{y}. \quad (3.19)$$

The position of  $y = 1$  mm ensured that the hot-wire was in the linear region of the velocity profile and reduced absolute errors due to the uncertainty in the location of the wall.

The calibration data for 14 shear stress sensors is shown in Fig. 3.33. The sensors with long leads have higher bridge voltages because of larger resistances in the Wheatstone bridge circuit. The difference between the maximum and minimum bridge voltage is about 3% of the mean bridge voltage for the two sensor types. This can be attributed to slight differences in the bridge balance as well as minor variations between individual sensors. The sensor response is nearly linear over the narrow range of shear stresses considered here and has a slope of about 0.3 mV/mPa. The value of the slope depends on the resistance in series with the sensor in the Wheatstone bridge; a  $50 \Omega$  resistance was used here.

The sensor calibration data is fit using a quadratic polynomial as shown in Fig. 3.34. Strictly speaking, a linear fit would suffice but a quadratic fit was chosen so that the calibration could be extended to zero shear. Polynomial fits are preferred to traditional 1/3 power law fits, especially in flow fields with fluctuating wall shear stress (Haritonidis 1988, Alfredsson & Johansson 1988).

The sensor response was tested in a laminar boundary layer with a free-stream velocity of 5 m/s. The results with and without temperature correction are shown in Fig. 3.35. The shear stress increases without temperature compensation as the free-stream temperature drops. The spanwise distribution also shows a sinusoidal pattern for the cases with the largest drift. This is because the sensors with long leads have a larger compensation coefficient and so a slightly greater drift. After correction, the shear stress values lie in a tight band with a mean of 26.4 mPa and a standard deviation of 0.37 mPa. The uncertainty in the shear stress measurements for a 95% confidence interval is  $\pm 2\sigma$  and is about  $\pm 1$  mPa.

### **3.7 Conclusions**

A simple four mask process for fabricating shear stress sensor arrays with multiple back-side contacts was developed. The sensors are thermally isolated metal resistors embedded in polyimide membranes. Backside contacts are etched along with the thermal isolation cavities and do not require additional mask steps or wafer bonding. The sensors have a frequency response of 16 kHz when operated as constant temperature hot-film anemometers at an overheat ratio of 1.5. Individual sensors have a power consumption of about 10 mW at this overheat ratio. The sensor response in a laminar flow is nearly linear over the range of 0–80 mPa and has a slope of 0.3 mV/mPa. The completed devices are sufficiently robust for use in low-speed air or water tunnels without any additional packaging.

#### **3.7.1 Design Improvements**

The sensor performance could be improved by reducing conduction heat loss to the substrate. This can be done both by increasing the aspect ratio and by decreasing the thickness of the metal film. This was not pursued as both techniques increase the sensor resistance, making it incompatible with standard constant temperature anemometry equipment. Chevron sensors that can measure  $(\partial w / \partial y)_w$  should also be considered. Careful matching of the sensors will be necessary to extract both components of the wall shear stress.

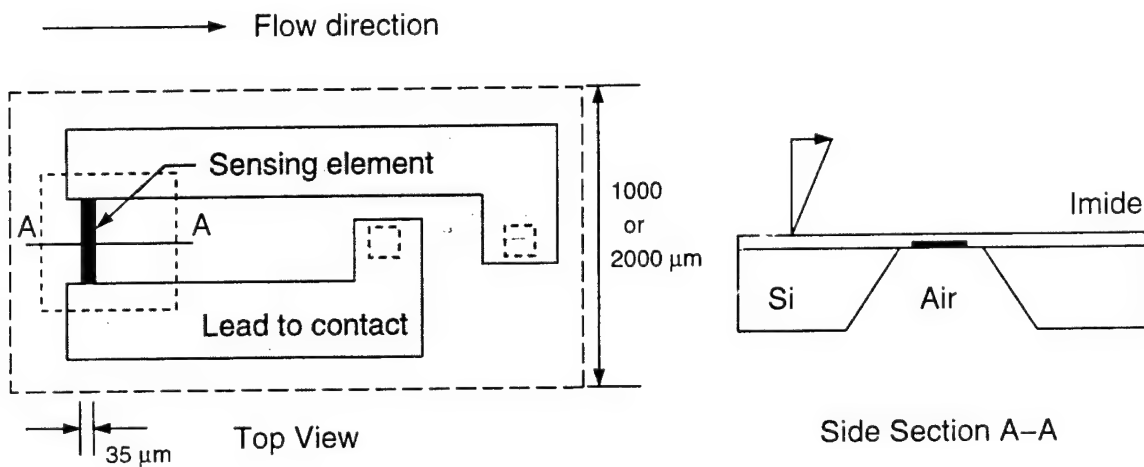


Figure 3.1: Illustration of the sensor concept.

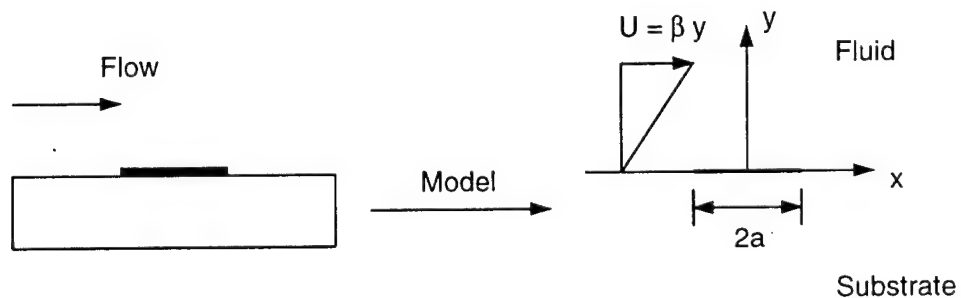


Figure 3.2: Sensor model for heat transfer analysis.

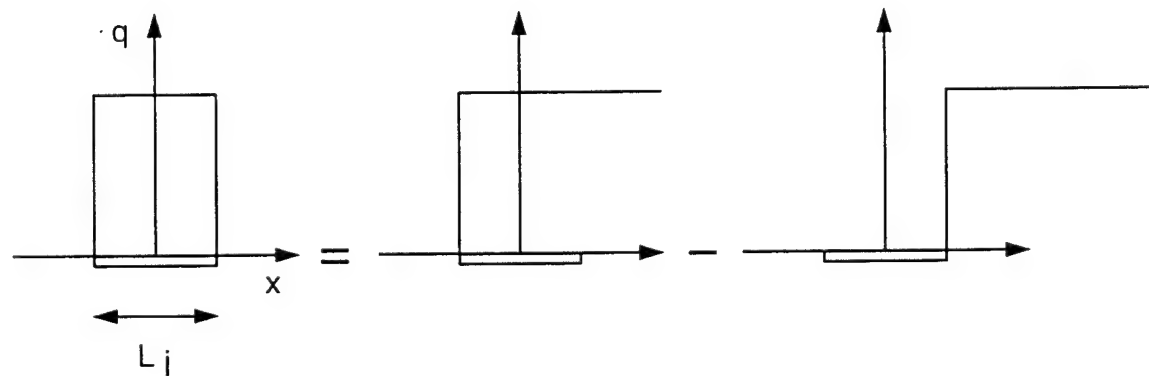
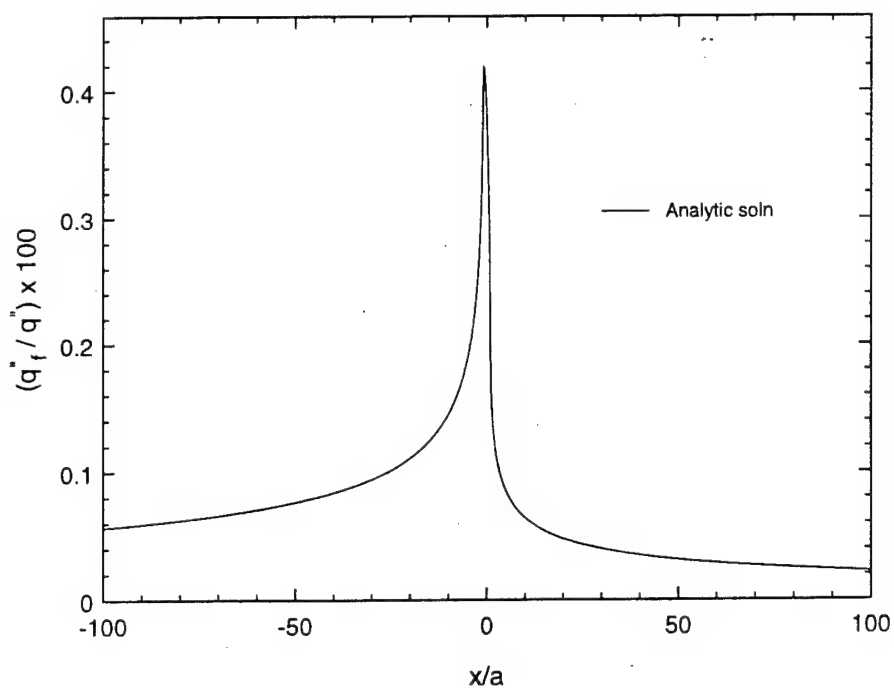
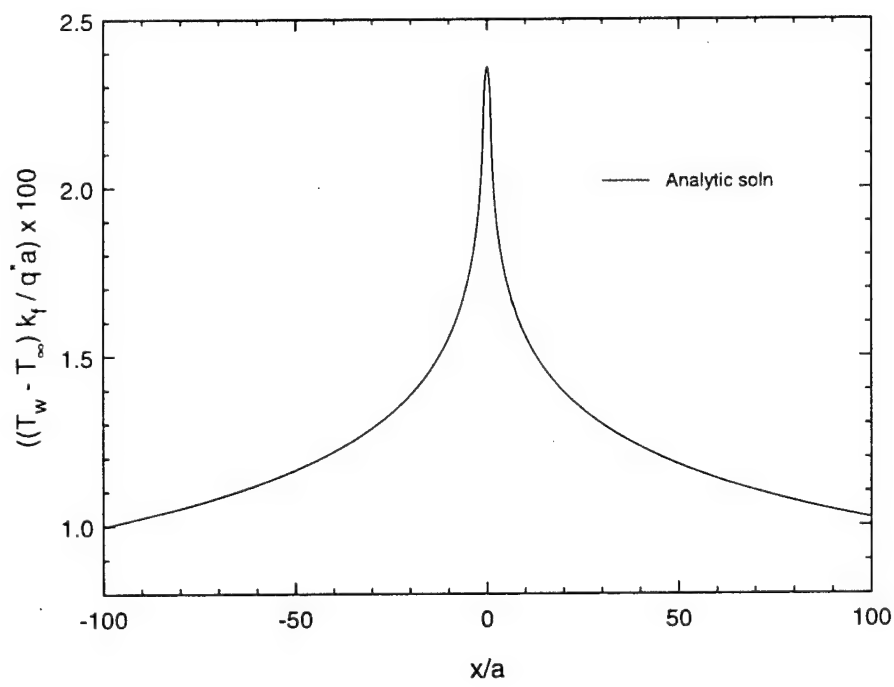


Figure 3.3: Construction of unit solution from semi-infinite half plane solutions.



(a) Heat Flux



(b) Temperature

Figure 3.4: Sensor without thermal isolation in water ( $Pe = 0.41$ ,  $k_s/k_f = 262$ ,  $\alpha_s/\alpha_f = 639$ ).

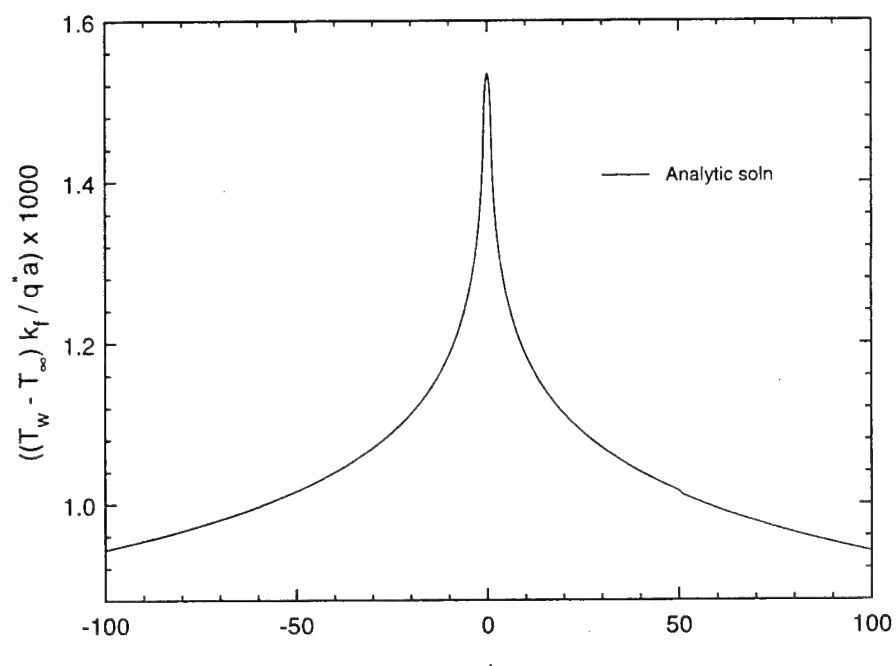
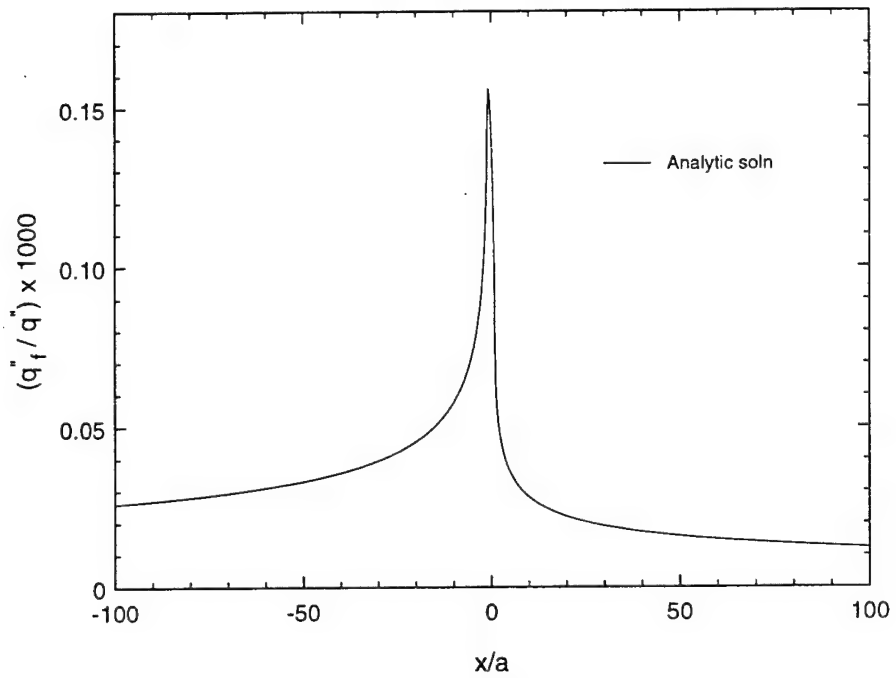
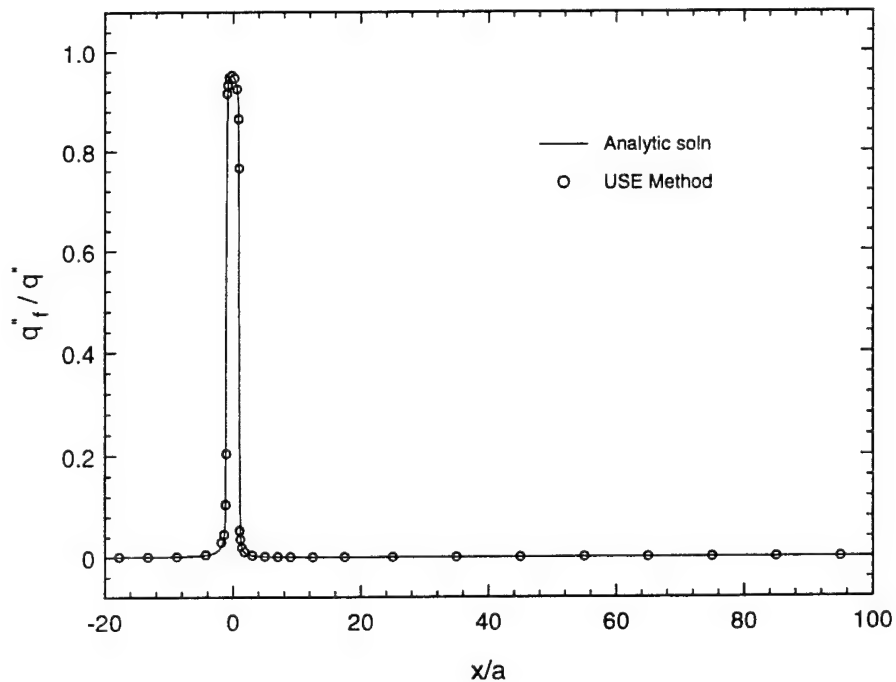
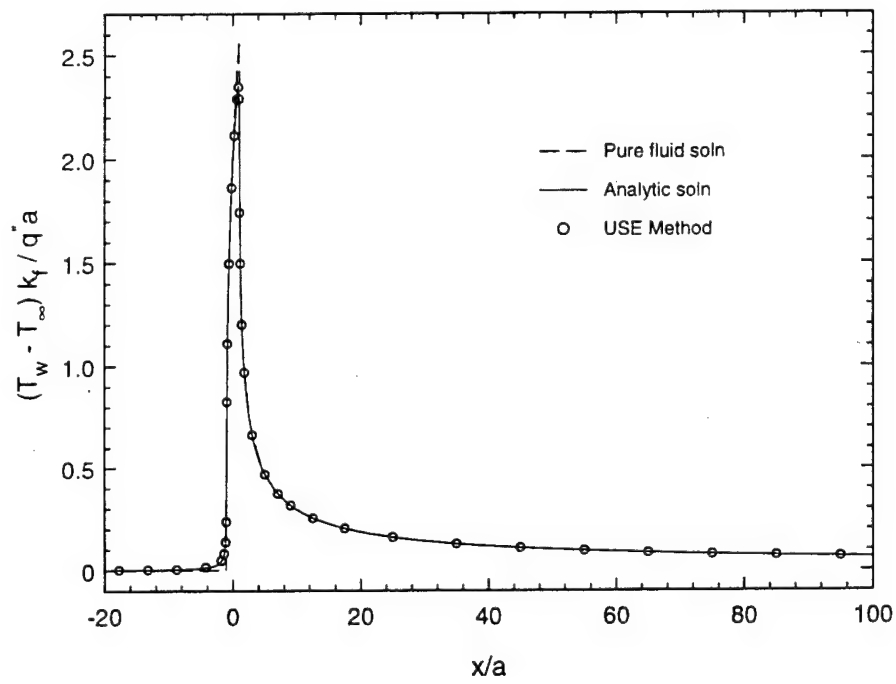


Figure 3.5: Sensor without thermal isolation in air ( $Pe = 0.23$ ,  $k_s/k_f = 6039$ ,  $\alpha_s/\alpha_f = 4.3$ ).

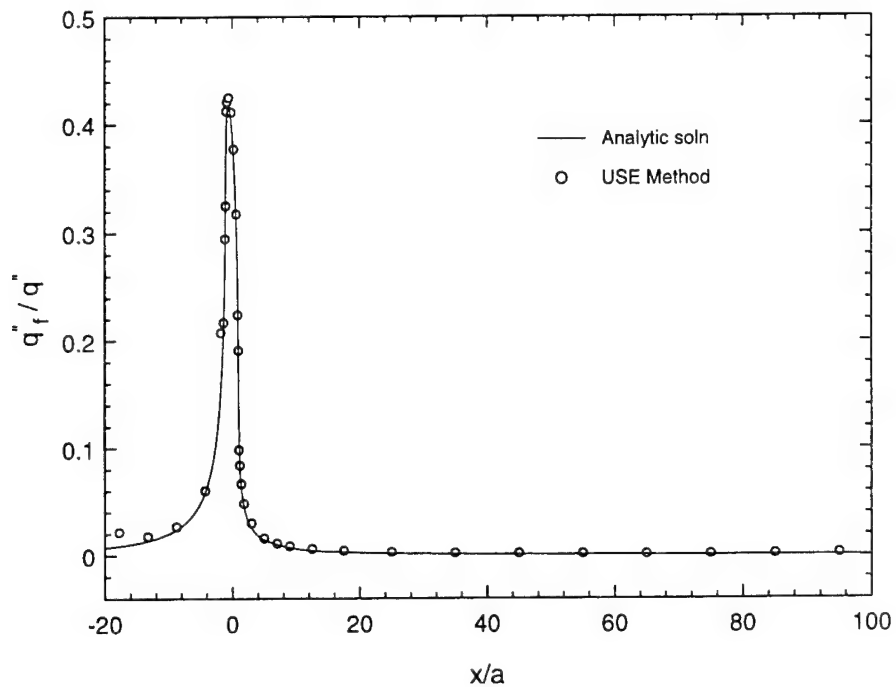


(a) Heat Flux

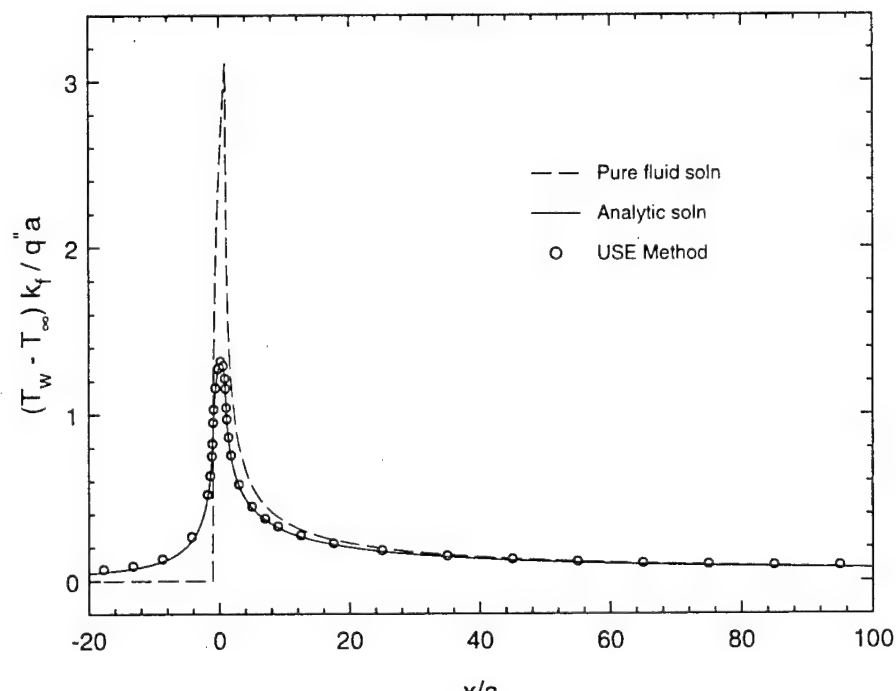


(b) Temperature

Figure 3.6: Thermally isolated sensor in water ( $Pe = 0.41$ ,  $k_s/k_f = 0.04$ ,  $\alpha_s/\alpha_f = 149$ ).

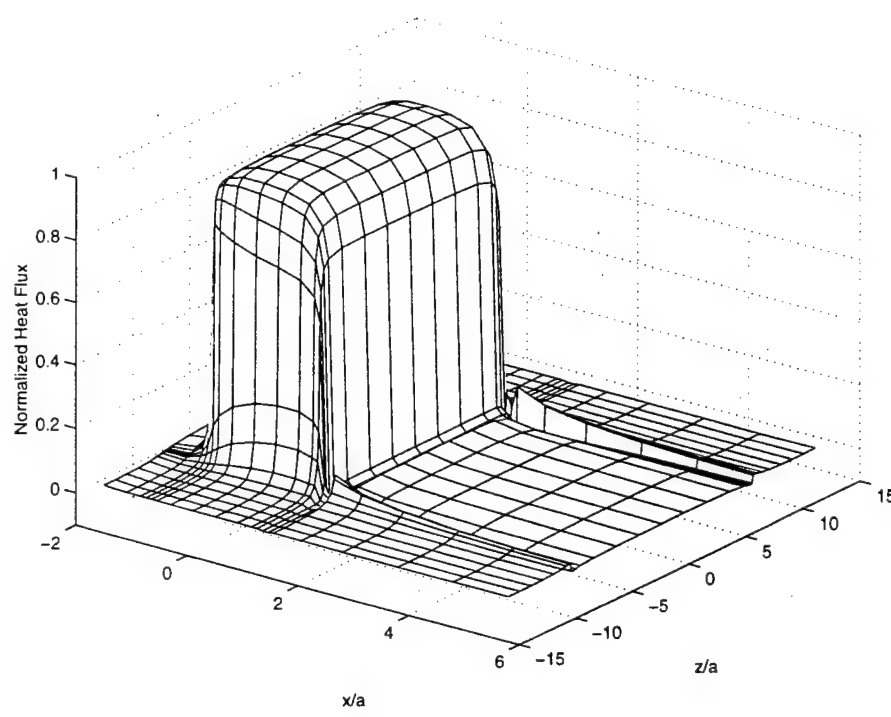


(a) Heat Flux

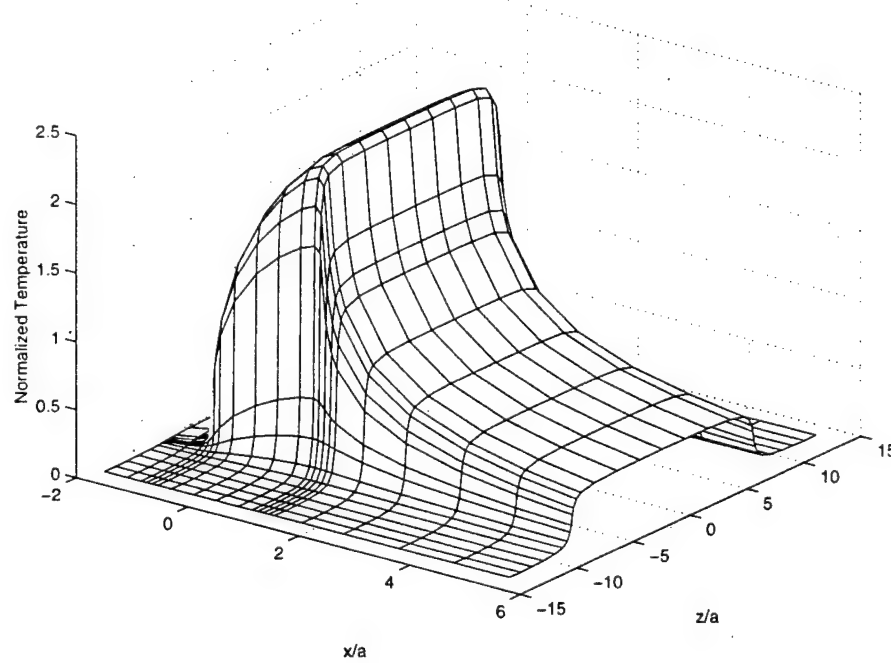


(b) Temperature

Figure 3.7: Thermally isolated sensor in air ( $Pe = 0.23$ ,  $k_s/k_f = 1$ ,  $\alpha_s/\alpha_f = 1$ ).

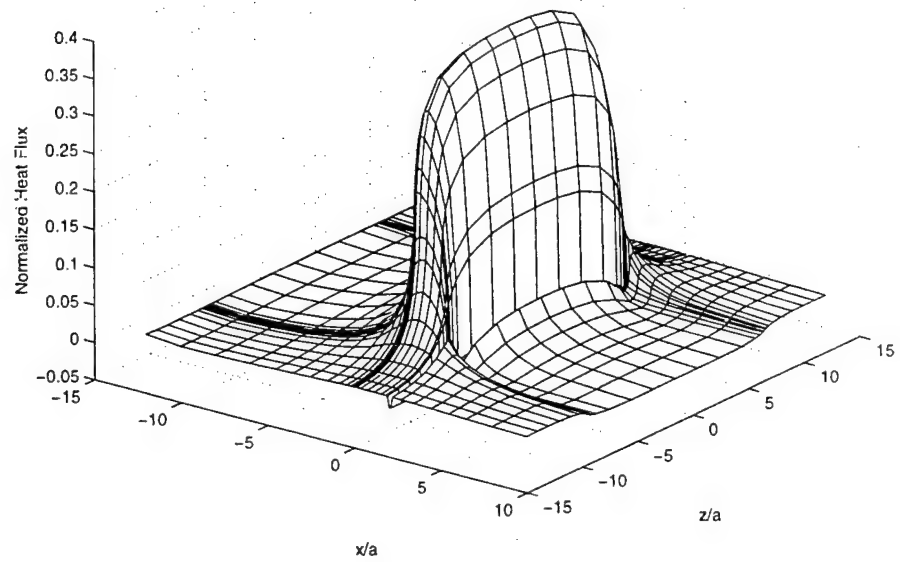


(a) Heat Flux

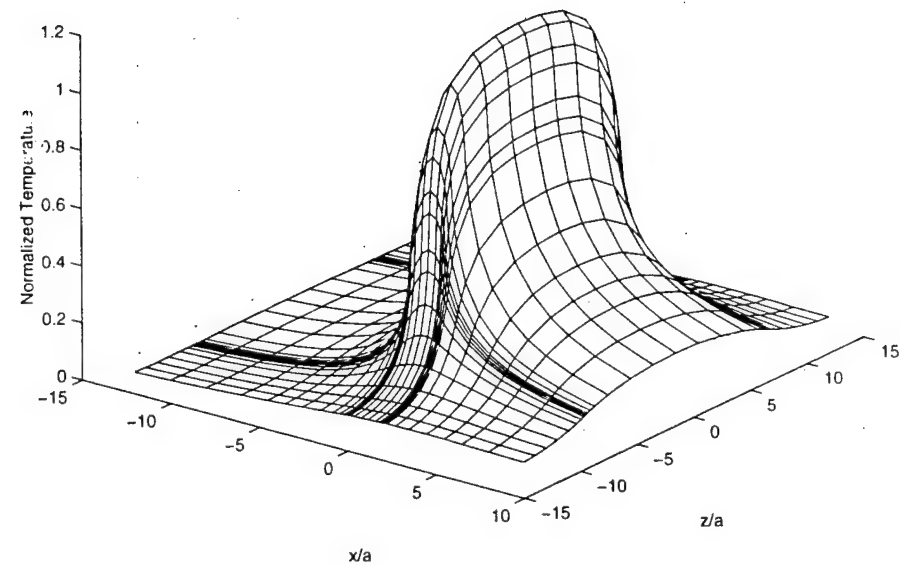


(b) Temperature

Figure 3.8: Two-dimensional profiles for thermally isolated sensor in water (sensor aspect ratio = 8).



(a) Heat Flux



(b) Temperature

Figure 3.9: Two-dimensional profiles for thermally isolated sensor in air (sensor aspect ratio = 8).

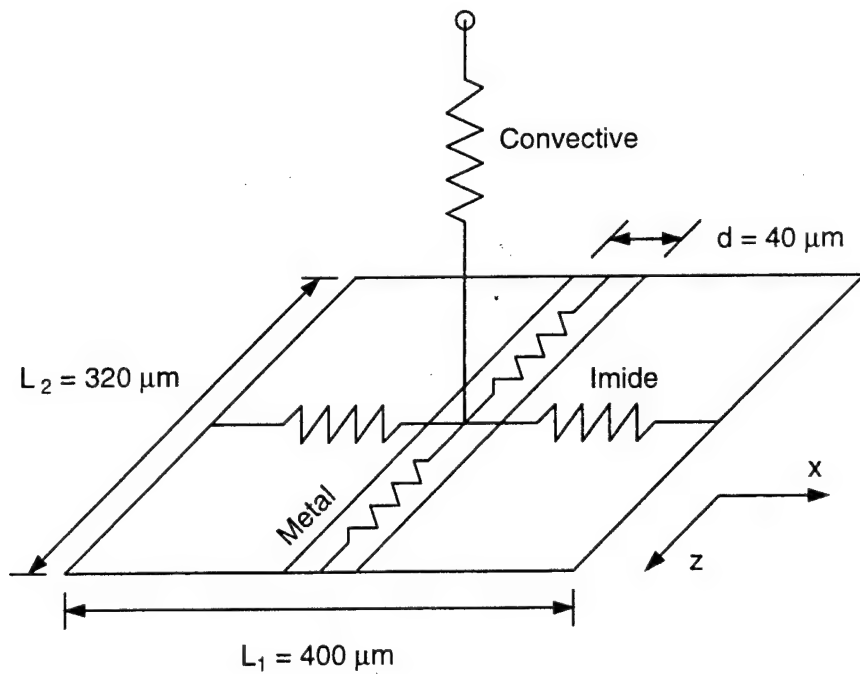


Figure 3.10: Schematic showing thermal resistances for isolated sensor.

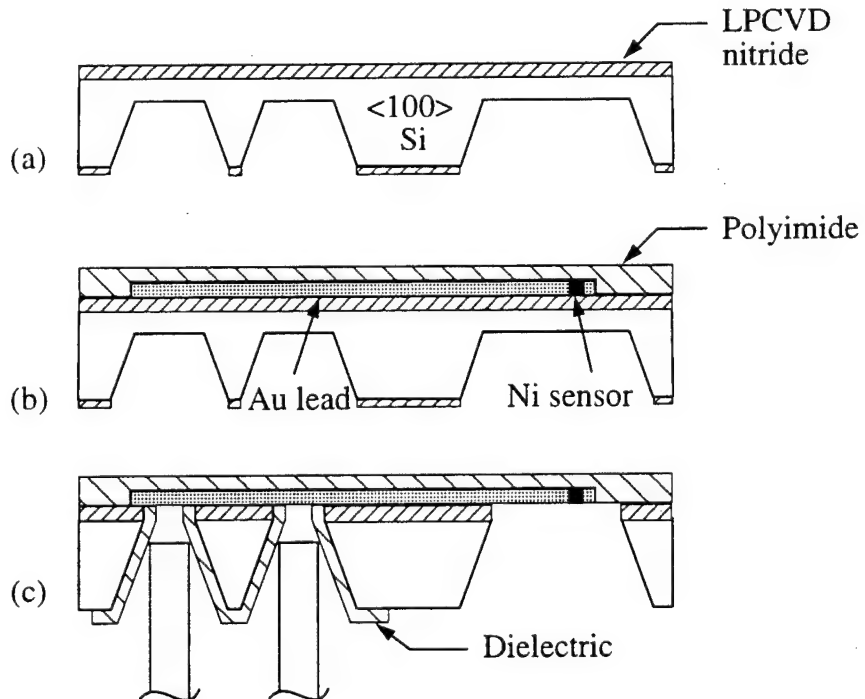


Figure 3.11: Sensor fabrication sequence (Not to scale).

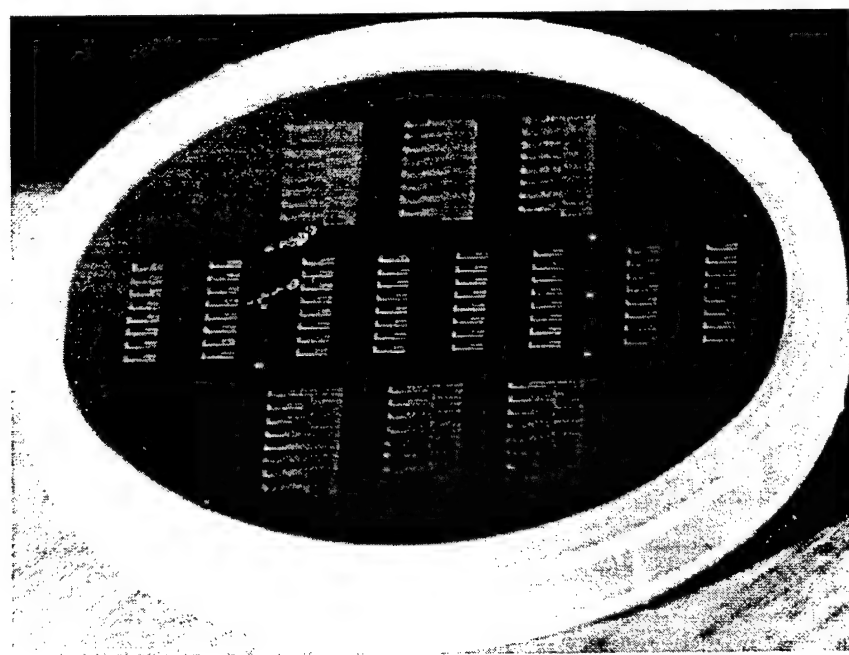


Figure 3.12: Wafer level view of eight and sixteen sensor arrays.



Figure 3.13: Wafer level view of thermal isolation cavities and backside contacts.

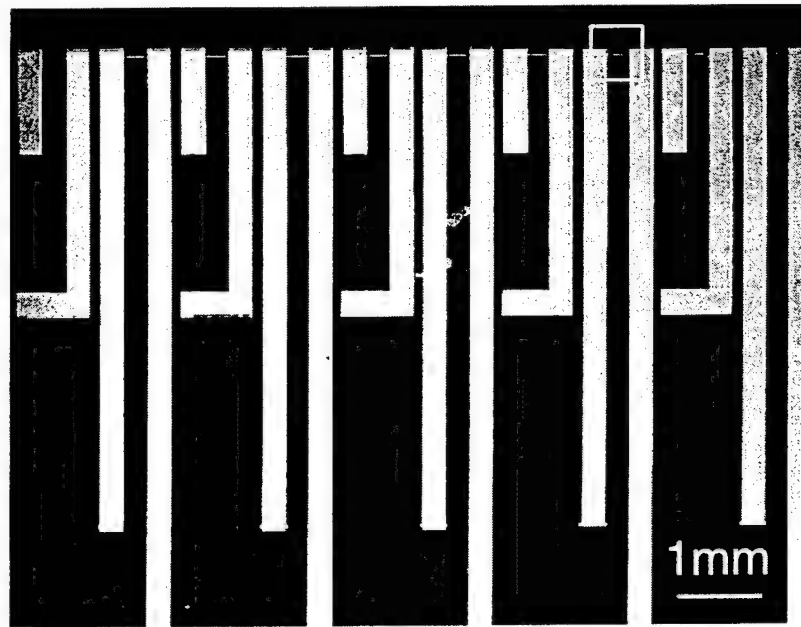


Figure 3.14: Top view of part of a sixteen sensor array. A magnified view of the image in the white square is shown in Fig. 3.15.

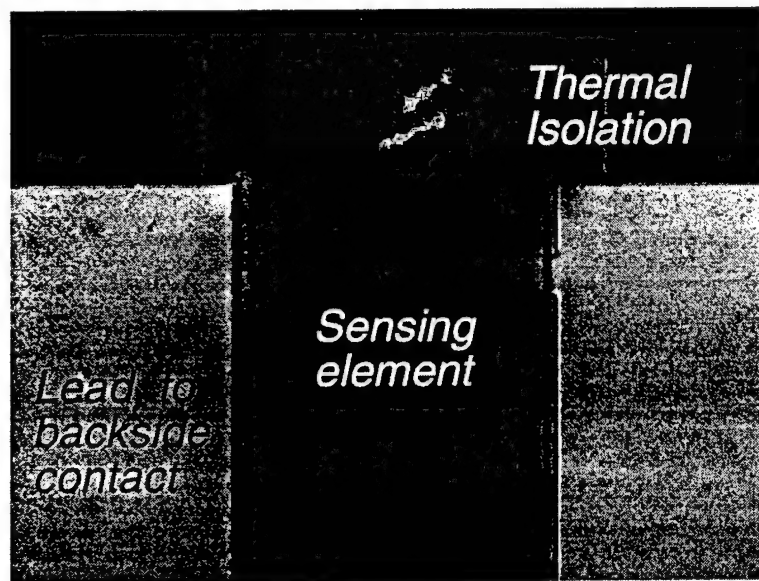


Figure 3.15: Tip of a single sensor. The sensing element is  $35 \mu\text{m} \times 280 \mu\text{m}$ .

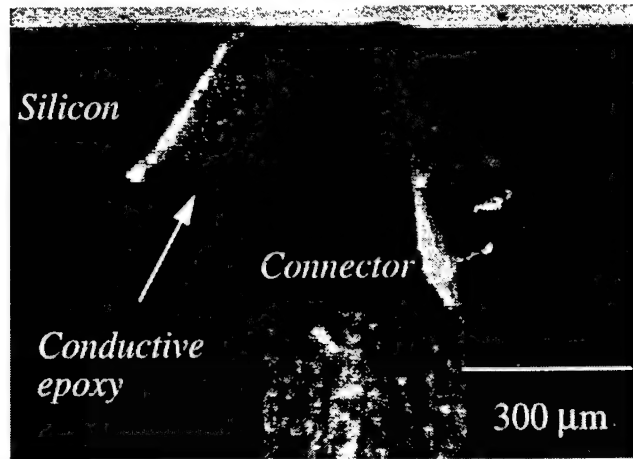


Figure 3.16: Cross-section through a backside contact.

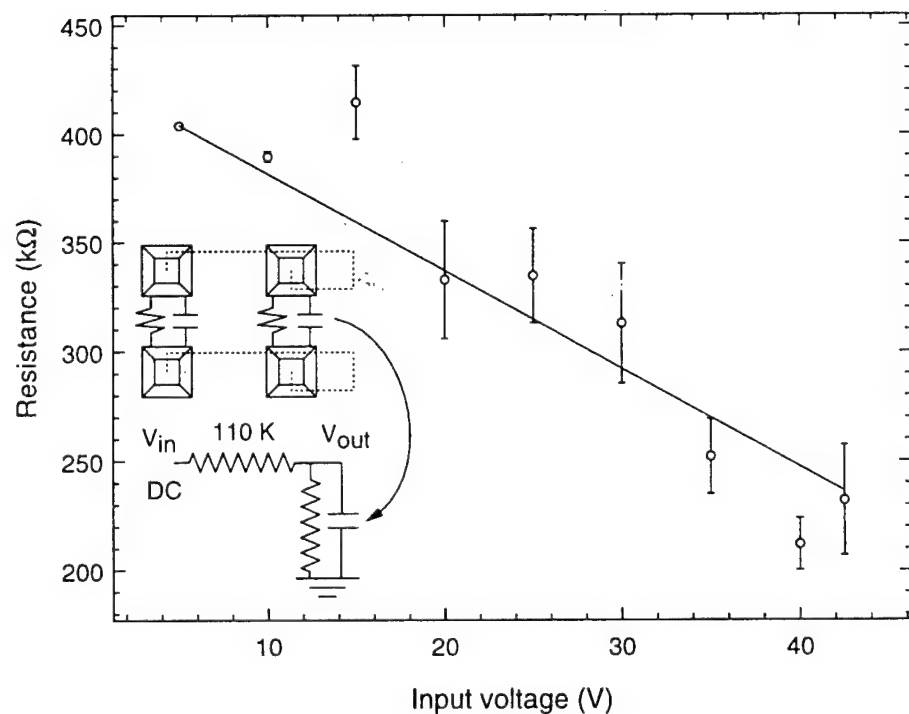


Figure 3.17: Leakage resistance between contacts.

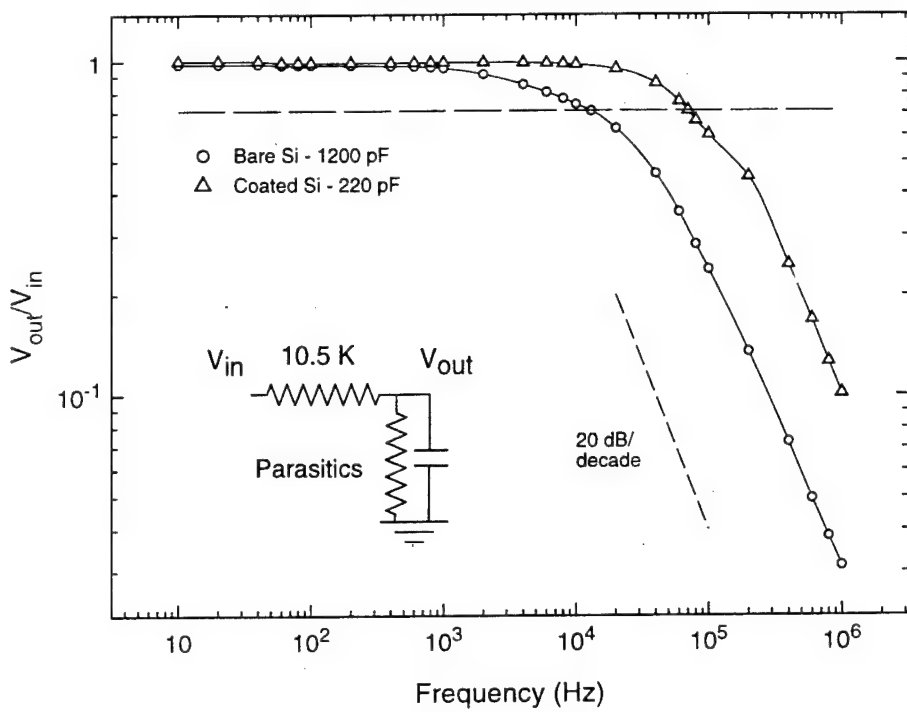


Figure 3.18: Reduction of parasitic capacitance between contacts. The magnitude of the input voltage is 1 V<sub>rms</sub>.

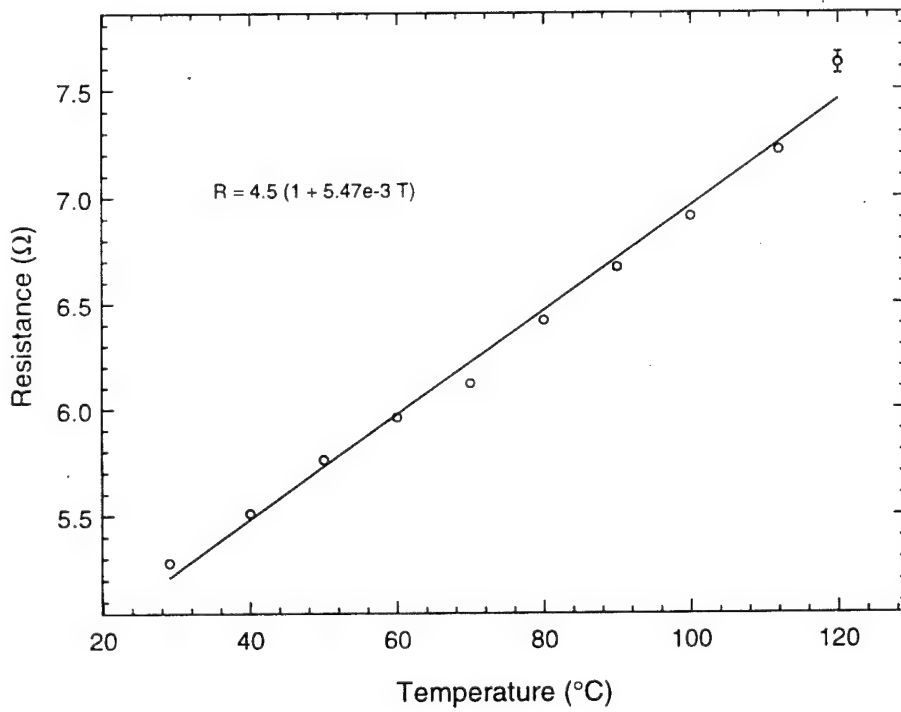


Figure 3.19: Temperature coefficient of resistance of sensor.

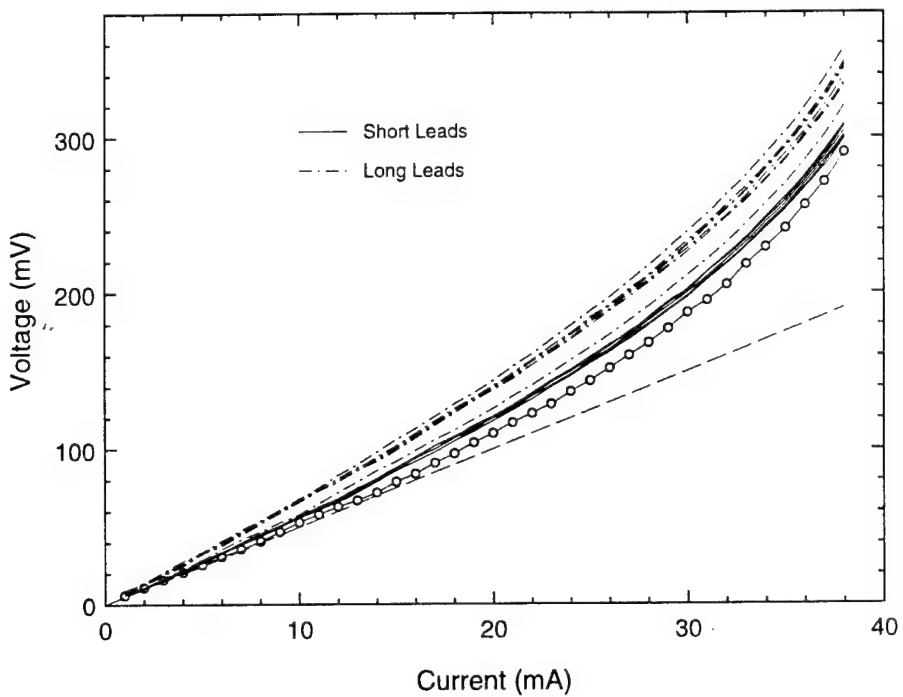


Figure 3.20: Current-voltage characteristics in still air.

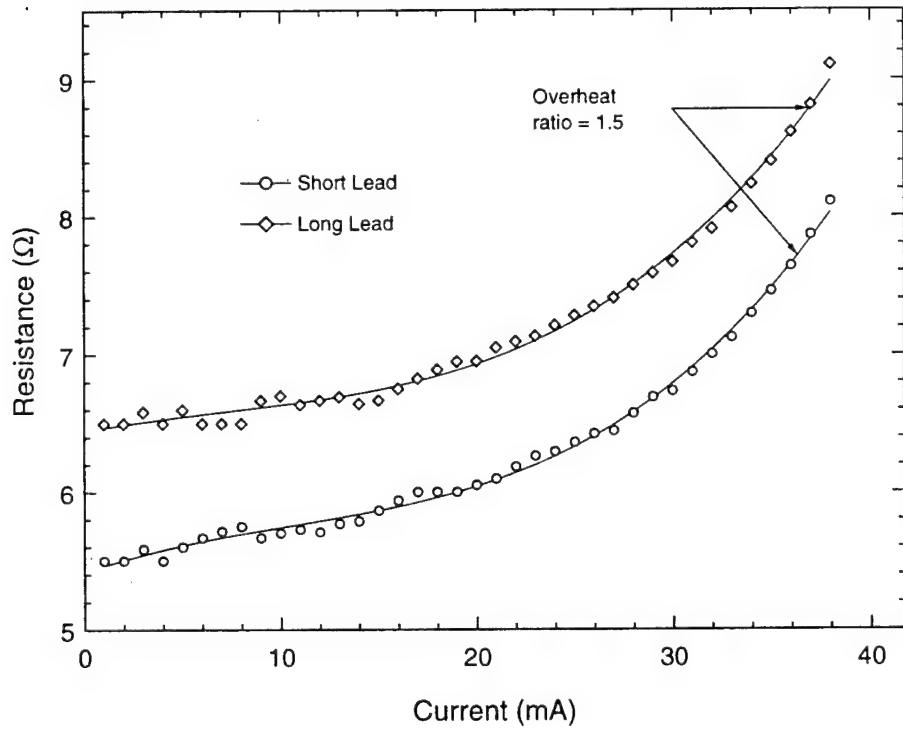


Figure 3.21: Sensor resistance as a function of bias current. An overheat ratio of 1.5 is used during shear stress measurement.

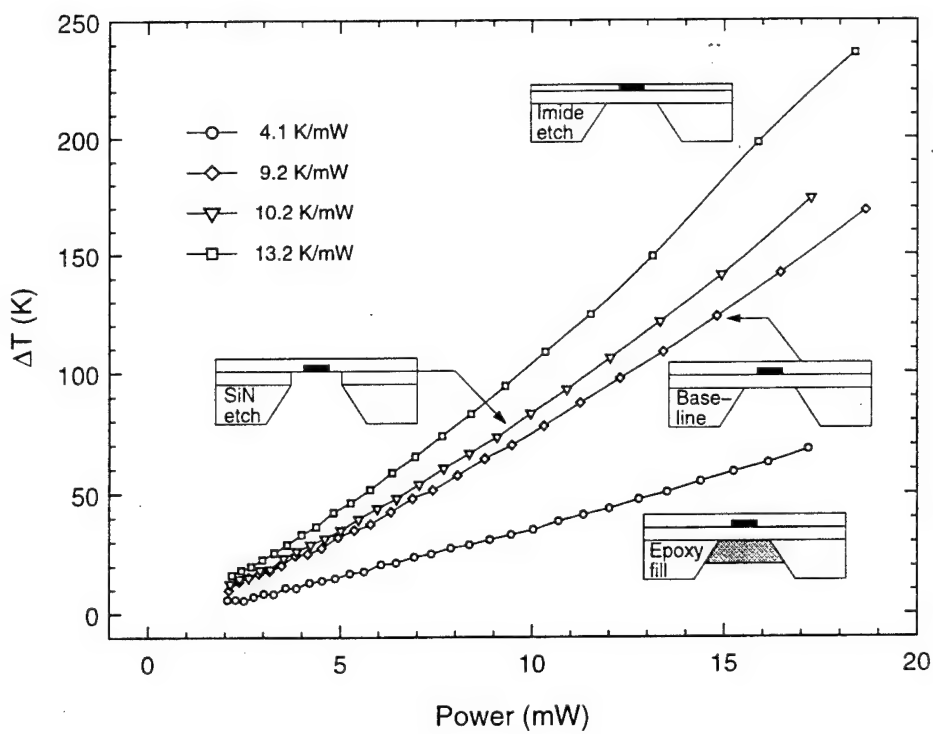


Figure 3.22: Thermal resistance for four different sensor types.

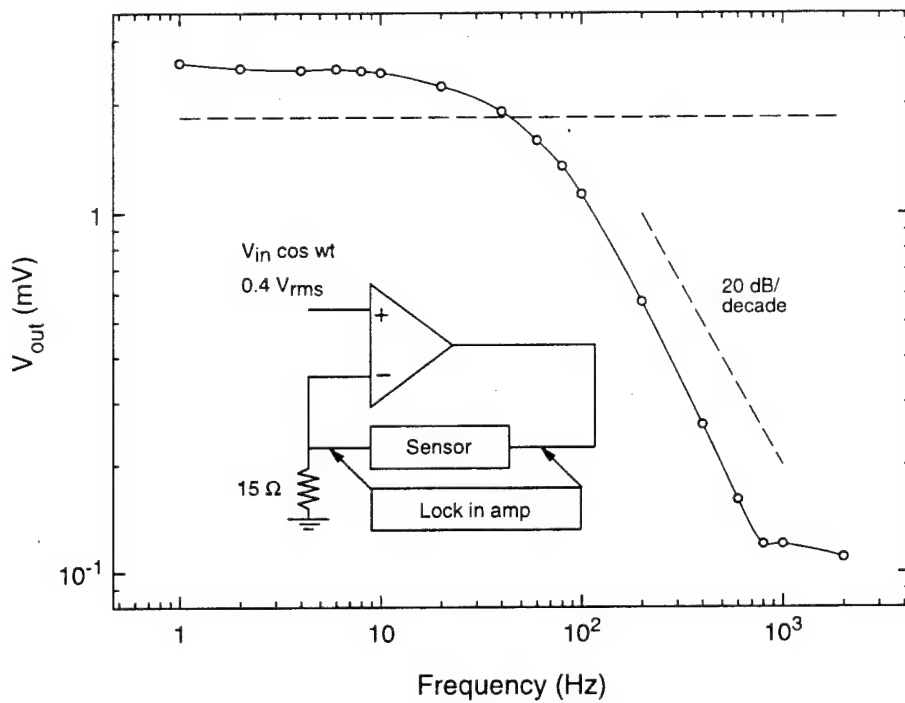


Figure 3.23: Time constant determination by  $3\omega$  technique.

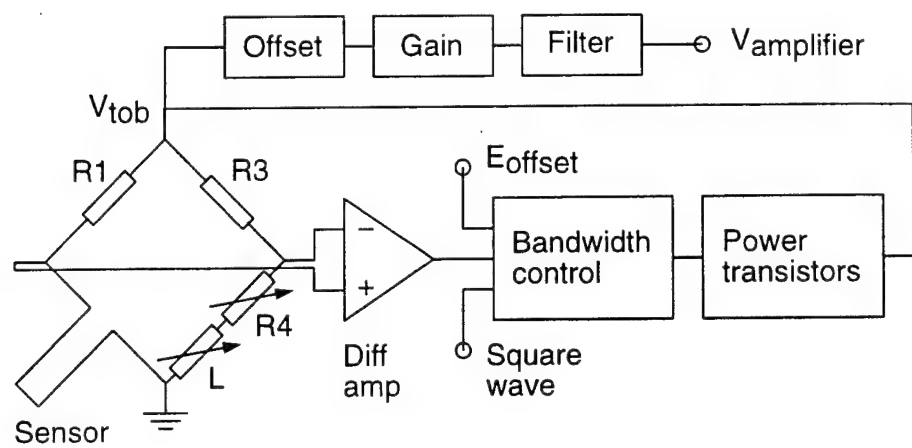


Figure 3.24: Block diagram for constant temperature anemometry.

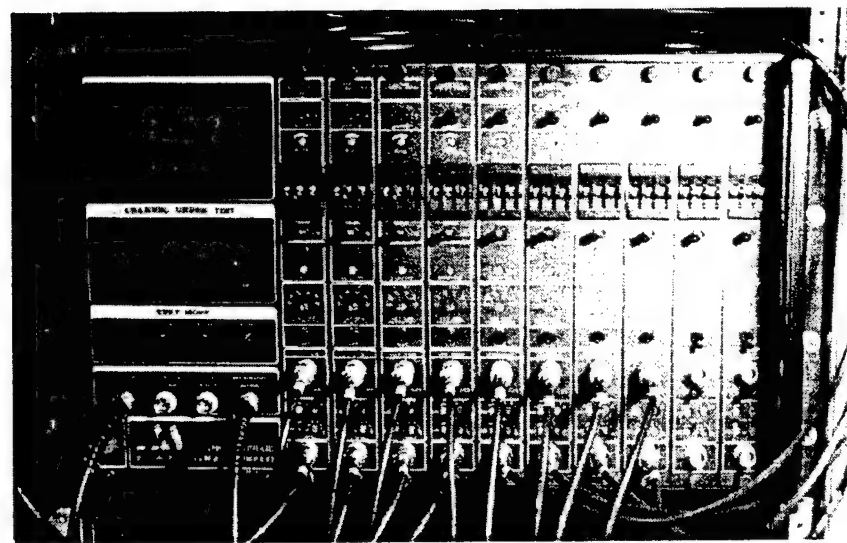


Figure 3.25: Photo of array of anemometers used to drive the sensor arrays.

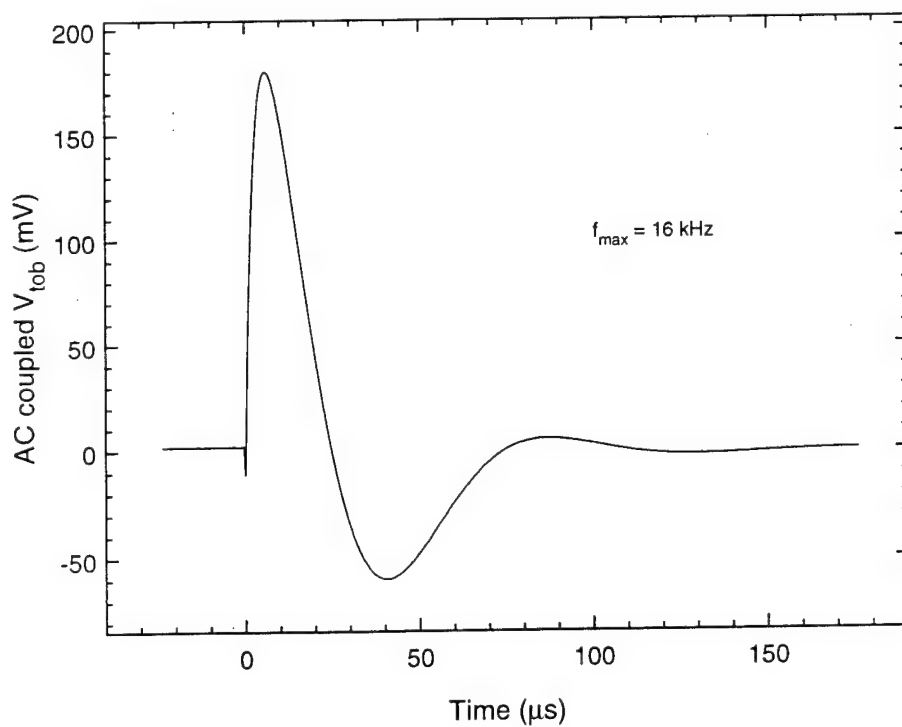


Figure 3.26: Response of closed loop system to square wave input at an overheating ratio of 1.5.

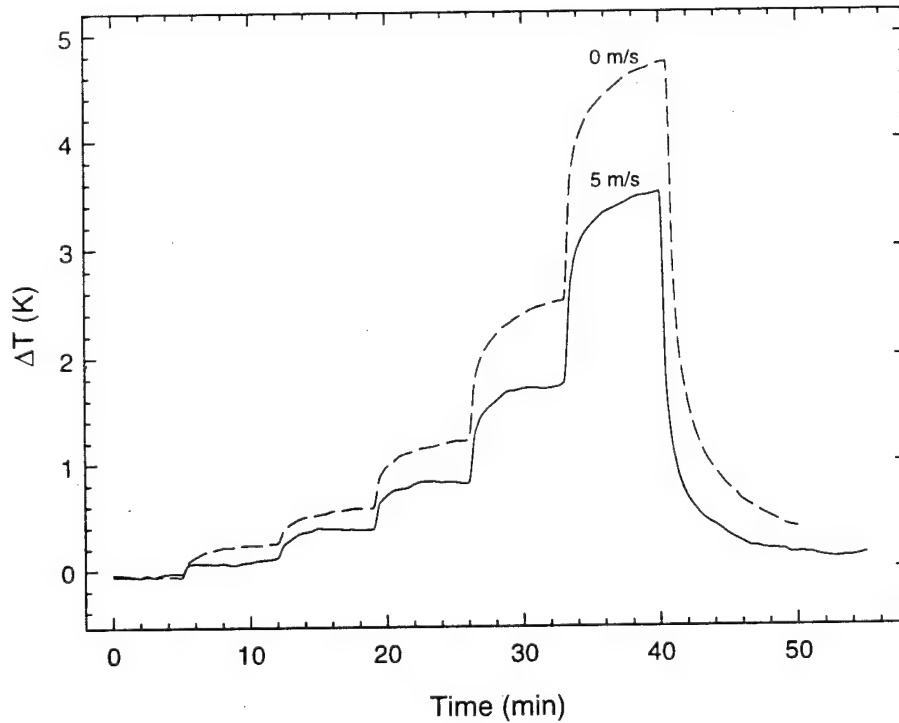


Figure 3.27: Increase in chip temperature at two free-stream velocities. The different plateaus correspond to 1, 2, 4, 8 and 14 sensors being turned on.

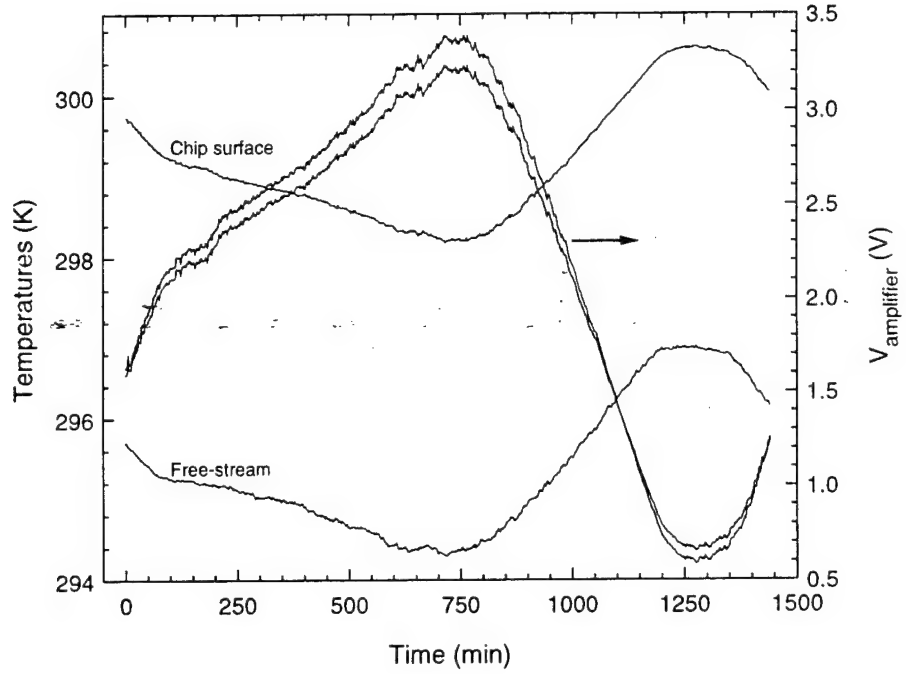


Figure 3.28: Drift of two sensor outputs over a 24 hour period. The free-stream temperature and the chip temperature are also shown. Readings were taken every 2 minutes. The free-stream velocity was 5 m/s.

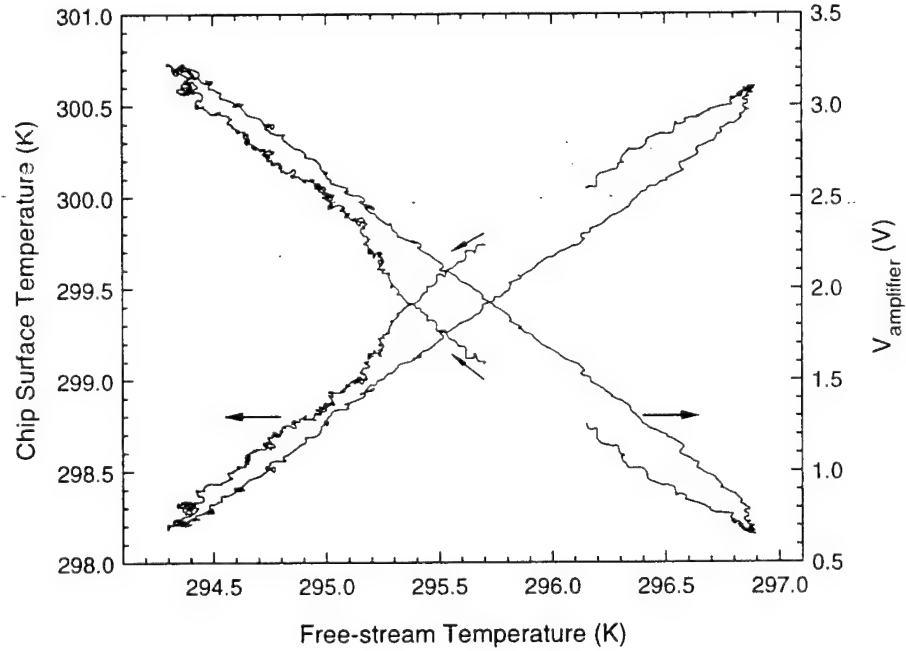


Figure 3.29: Crossplot of sensor output and chip temperature vs. free-stream temperature. The two curves have opposite trends but show the same hysteretic pattern.

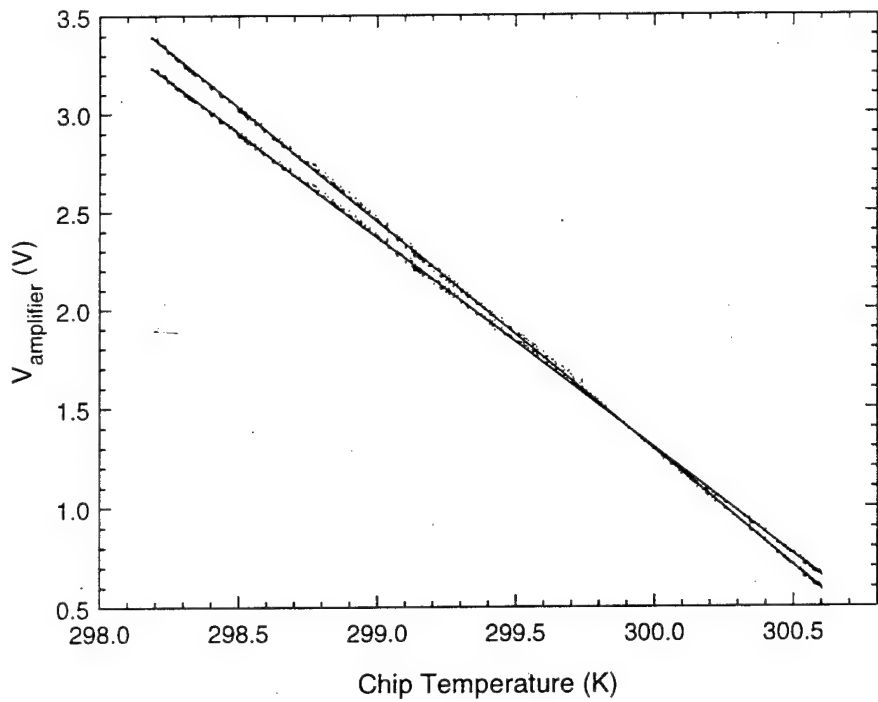


Figure 3.30: Crossplot of sensor output vs. chip temperature. The data collapses with no hysteresis. The two slopes are different as one of the sensors has longer leads.

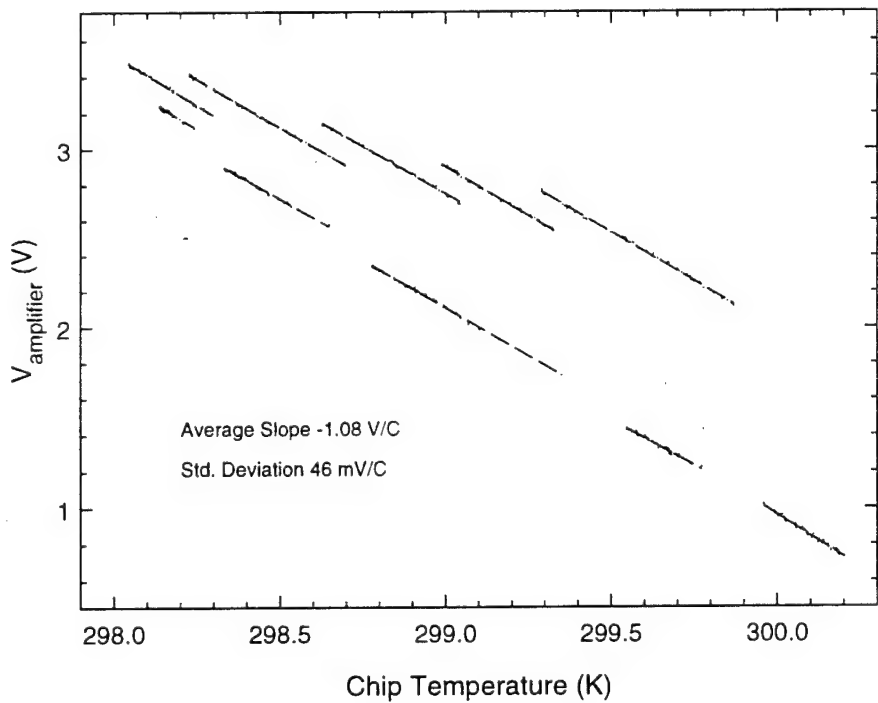


Figure 3.31: Temperature correction coefficient in still air and at nine free-stream velocities (0.5 m/s to 10.8 m/s in increments of 1.3 m/s). Readings were taken every minute and the tunnel speed was changed every 90 min.

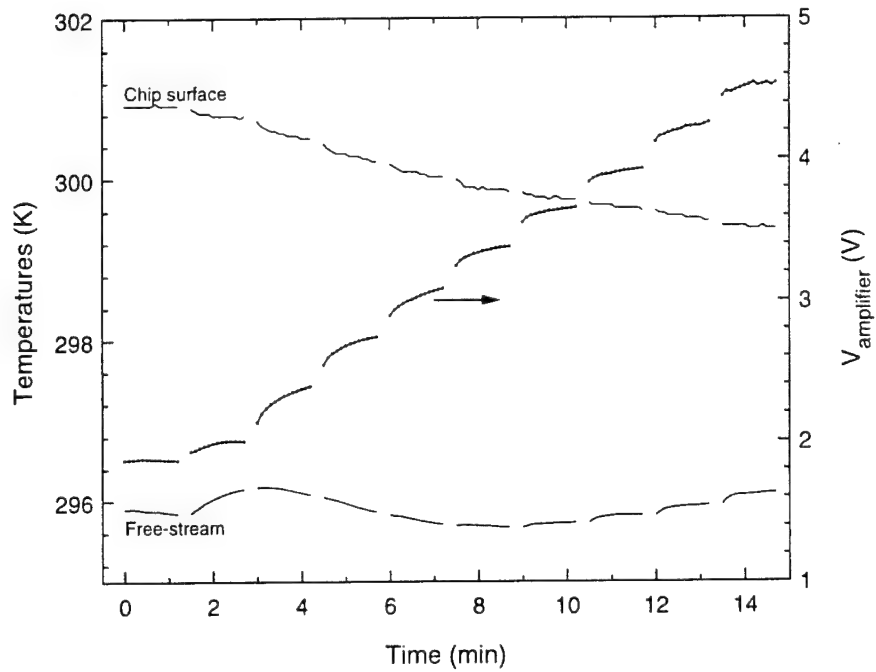


Figure 3.32: Response of a sensor during calibration. Data is taken in still air and at nine free-stream velocities (0.5 m/s to 10.8 m/s in increments of 1.3 m/s). The free-stream velocity is changed every 1.5 min and data is taken every 0.1 min.

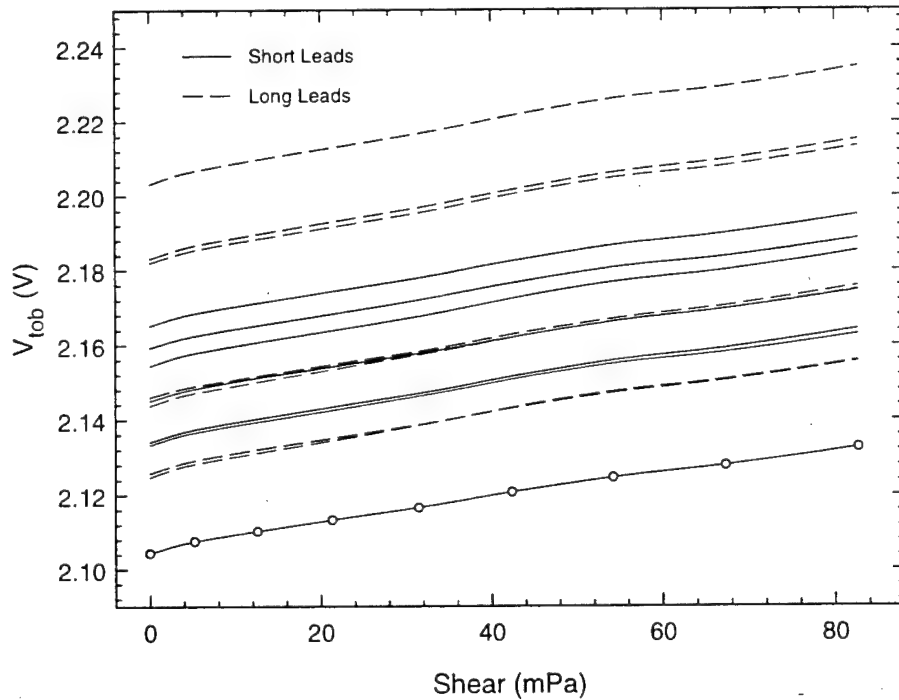


Figure 3.33: Calibration data for shear stress sensor array. The data was taken in quasi-steady mode as in Fig. 3.32.

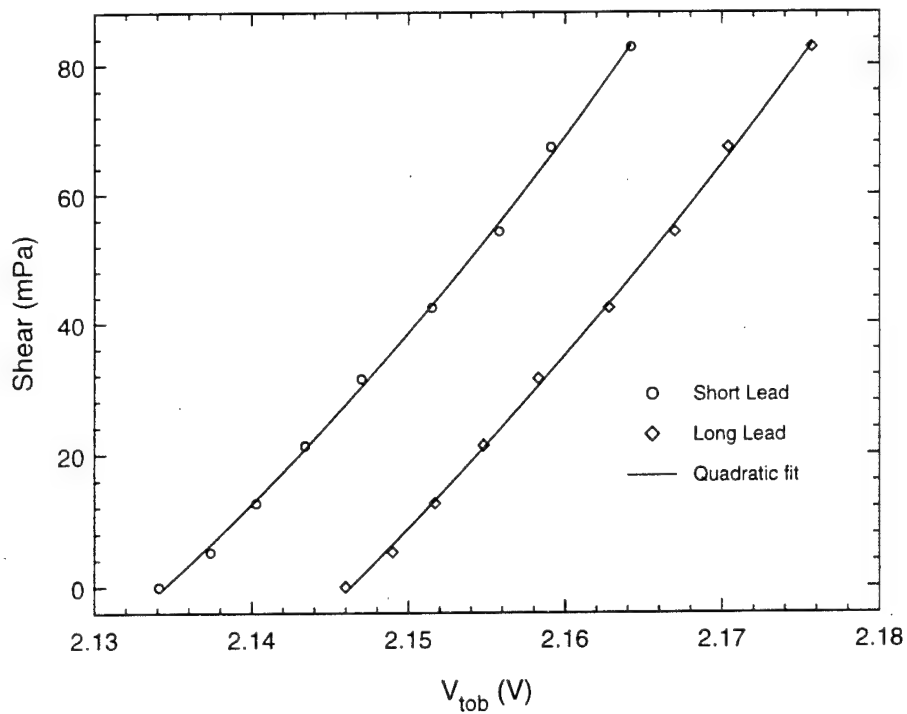


Figure 3.34: Quadratic fit to calibration data.

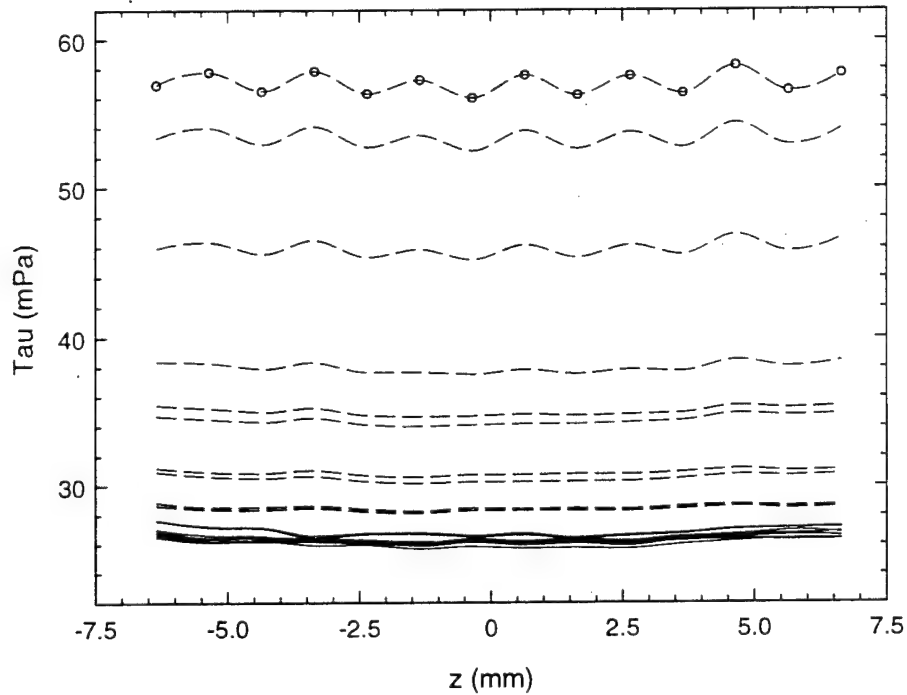


Figure 3.35: Shear stress in a laminar boundary layer with and without temperature correction. Dashed lines are uncorrected values. The ambient temperature drops by  $0.9^{\circ}\text{C}$  for the measurements shown.

## Chapter 4

# Zero Mass Flux Actuators

### 4.1 Introduction

One of the key stumbling blocks for active turbulence control has been the lack of a robust distributed actuation technology. A number of actuation mechanisms and fabrication approaches have been proposed to solve this problem. Coe *et al.* (1995) investigated micro-fabricated synthetic jets. The actuator consisted of an orifice above a cavity bounded by a flexible membrane. Array of microjets with a typical spacing of 4 mm were fabricated both by micromachining and by hybrid assembly. Vibration of the membrane using either electrostatic or piezoelectric drive resulted in the formation of a turbulent jet, with velocities on the order of 10 m/s. Liu *et al.* (1994) and Tsao *et al.* (1997) from the UCLA-Caltech group used surface micromachining to fabricate magnetic flaps with large wall normal displacements (1–2 mm) at low frequencies (< 100 Hz). Their group has also explored an electrostatically driven in-plane actuator with tip deflections of 100  $\mu\text{m}$  and operating frequencies between 500–1200 Hz (Sherman 1998). This device does not suffer from ‘form drag’ losses like the magnetic flaps as it is flush with the flow surface and moves in the spanwise direction.

In general, micromachined actuators have trouble meeting the requirements described in Chapter 1, especially in terms of spanwise spacing and power consumption. Kovacs (1998) discusses a number of actuation mechanisms in terms of their force and deflection capabilities, power density and efficiency. Piezoelectric actuators are attractive for flow control because they can provide large force, stiffness and bandwidth. They also have low power consumption because they act like capacitors and have small parasitic losses.

In this chapter, the development of a robust actuation technology using a hybrid fabrication process is described. The objective was to fabricate arrays of actuators that create substantial disturbances in boundary layers, have a high frequency response, and operate

at low power. Characterization of the actuators in terms of displacement transfer functions, step response and repeatability is presented. The effect of the actuators in a laminar boundary layer is discussed. Finally, scalability of the actuators for use in real boundary layer control applications is discussed.

## 4.2 Piezoelectric Actuator Concept

The actuators are based on the zero mass flux vortex generators developed by Jacobson & Reynolds (1998) and are schematically shown in Fig. 4.1. An array consists of individually addressable piezoceramic-silicon cantilevers with integrated cavities and unequal side gaps. When a potential is applied across the lead zirconate titanate (PZT) piezoceramic, it either expands or contracts in the longitudinal direction. Since the PZT is rigidly bonded to the silicon, the cantilever behaves like a bimetallic strip and moves into or out of the cavity. Each actuator produces a directed jet-like efflux on its downward stroke and a diffuse sink-like influx on its upward stroke. This results in the formation of a pair of counter-rotating vortices. A train of these vortices leads to the formation of a steady jet a few gap distances away from the wall. This jet then creates a pair of control vortices in the crossflow. The actuator is driven at resonance to maximize the tip displacement and thereby its effectiveness. A single dominant vortex pair is obtained by making the gap sizes asymmetrical.

## 4.3 Actuator Design

### 4.3.1 Optimization of Static Deflection

The deflection due to piezoelectric forcing can be analyzed as a variant of the bimetallic strip problem (Timoshenko 1955). The static tip deflection is given by:

$$y_{\text{forcing}} = \frac{p_1 p_2 (h_1 + h_2)}{4(p_1 + p_2)} \frac{d_{31} V}{h_2} \frac{l^2}{EI_{\text{eff}}} \quad (4.1)$$

where  $p_i = b_i h_i E_i$ ,  $d_{31}$  is the piezoelectric coefficient,  $V$  is the potential difference across the piezoceramic, and  $l$  is the cantilever length (see the schematic in Fig. 4.2 for geometric details). The equivalent  $EI$  product is given by:

$$EI_{\text{eff}} = \frac{p_1^2 h_1^2 + p_1 p_2 (4h_1^2 + 6h_1 h_2 + 4h_2^2) + p_2^2 h_2^2}{12(p_1 + p_2)} \quad (4.2)$$

This expression reduces to the form in Young (1989) when the two materials are of equal width. For a given width ratio, the thickness ratio for maximum deflection is the solution of a fifth-order polynomial equation. The normalized deflection as a function of thickness ratio is shown in Fig. 4.2. The optimum ratio is 0.33 but the curve has a fairly broad maximum. A value of 0.4 was chosen for ease of fabrication. It should be noted that if the two materials have equal widths and the same Young's modulus, the problem reduces to maximizing  $h_1 h_2 / (h_1 + h_2)^3$ . This function has a maximum at  $h_1/h_2 = 0.5$ . For a given thickness ratio, the optimum width ratio is given by:

$$\frac{b_2}{b_1} = \frac{h_1^2 E_1}{h_2^2 E_2} \quad (4.3)$$

This optimum is a weak function of the width ratio as shown in Fig. 4.3. A value of 0.9 was chosen to retain the benefits of increased stiffness without incurring much penalty.

#### 4.3.2 Design Space

Figure 4.4 shows the design space for Si-PZT actuators in air at 10 m/s. The actuators must have tip displacements large enough to introduce significant disturbances into the flow, typically on the order of a few wall units. A nominal static deflection of 10  $\mu\text{m}$  is chosen, this is considerably amplified at resonance as the actuators have quality factors  $Q \approx 20$ . The actuators must achieve sufficient control authority without damaging the PZT (a typical de-poling field for PZT-5H is 0.3 V/ $\mu\text{m}$ ) and at a reasonable voltage (20 V maximum).

Since the actuator is driven at resonance, the resonant frequency must be much higher than frequencies sustained by the flow. Desirable frequencies can then be introduced into the flow simply by amplitude modulation of the carrier waveform, as has been previously shown by Wiltse & Glezer (1993). The resonant frequency is given by:

$$f_n = \frac{a_n}{2\pi} \sqrt{\frac{EI_{eff}}{m_{eff}l^4}} \quad (4.4)$$

where  $m_{eff} = \rho_1 b_1 h_1 + \rho_2 b_2 h_2$  is the mass per unit length and  $a_1 = 3.52$  and  $a_2 = 22.0$  are the constants for the first two modes. The minimum frequency is chosen to be 20 times the burst frequency, following the scaling requirements in Chapter 1.

Finally, actuator arrays introducing perturbations into a boundary layer must be stiff enough to withstand environmental forces. Surface micromachined cantilevers are fragile and sensitive to wind loading (Ho & Tai 1996). The tip deflection due to a distributed load

$w$  per unit length is:

$$y_{tip} = \frac{wl^4}{8EI_{eff}} \quad (4.5)$$

For deflections due to self weight  $w = (\rho_1 h_1 + \rho_2 h_2)g$ . The deflection due to pressure fluctuations is modeled as a distributed load  $w = c\rho_f u_\tau^2$ . The numerical value of  $c$  is not critical and is chosen to be 2.7, following the data of Spalart (1988). These deflections are each limited to 5% of the static deflection. This ensures that the actuators do not perturb the flow when they are turned off. The last constraint is conservative but it is not active over most of the design space. It should be noted that the actuator does not need to withstand the full dynamic pressure  $\rho U^2/2$ . This is because the actuator works as a pump and does not protrude appreciably into the flow (the angular deflection is less than  $2^\circ$  at full amplitude).

The design window has cantilevers about 4–8 mm long with piezo thicknesses between 25–150  $\mu\text{m}$ . These lengths and thicknesses naturally lead to a fabrication process that combines micromachining along with mesoscale assembly. Similar design curves for other piezoelectric materials like zinc oxide (ZnO) and poly-vinylidene fluoride (PVDF) indicate that these materials do not have sufficient drive capability and are not rigid enough for our purposes.

Figure 4.5 shows the spring constant  $K = 3EI_{eff}/l^3$  for two piezo thicknesses. Typical actuator spring constants are between 50–400 N/m for the design points chosen in this study. The cantilevers are much stiffer than those routinely made using micromachining techniques (for example, typical spring constants of cantilevers used in atomic force microscopy are about 1 N/m).

#### 4.4 Fabrication

The fabrication process requires three lithographic steps. A layer of low-stress LPCVD silicon nitride 0.15  $\mu\text{m}$  thick is deposited on <100> silicon wafers. The nitride on the wafer backside is patterned to define the cavities and the backside contacts. A timed anisotropic etch in KOH solution (30% wt, 80 °C) is carried out to thin the silicon in the exposed regions. The nitride is then patterned on the frontside to define the cantilevers. This is followed by a second anisotropic etch to release the 50  $\mu\text{m}$  thick silicon cantilevers (Fig. 4.6a). An isotropic HNA etch is used to fillet sharp corners to reduce stress concentration, especially at the cantilever base. Previous work by Pourahmadi *et al.* (1991) has shown that rounding the sharp corners greatly improves the device strength. The effectiveness of the isotropic etch was tested by deflecting the cantilevers with a micro-manipulator till fracture, as done

by Ericson and Schweitz (1990). The mean deflection increased from 3.7 mm to 5.4 mm, clearly indicating the reduction in stress concentration.

The isotropic etch is followed by a blanket etch of the backside nitride and deposition of the ground electrode layer. Next, 125  $\mu\text{m}$  thick discrete piezoceramic pieces (PSI-5A and PSI-5H from Piezo Systems Inc.) are epoxied to the lower surface of the cantilevers. This ensures that the actuators are flush with the flow surface and also protects the driving elements from the mean flow. A silicone rubber piece cast using a separate silicon mold is used to press down on the actuators (Fig. 4.6b). This procedure gives a thin bond line that reduces parasitic capacitances. A ribbon cable connector is then used to transfer conductive epoxy into the backside contact trenches, as in Chapter 3. An insulating layer of PECVD nitride between the common ground electrode and the positive PZT electrode was used to protect against shorting in an earlier version of the process (Kumar *et al.* 1999). This step was found to be unnecessary and was eliminated. A cover plate is used to complete the cavities for the individual actuators (Fig. 4.6c).

Finally, the actuator die is inserted into a custom designed Plexiglas mount to complete the fabrication process. Two types of actuators were made, batch A actuators had a cavity depth of 150  $\mu\text{m}$  and batch B actuators had a cavity depth of 200  $\mu\text{m}$ . A step-by-step listing of the fabrication process is given in Appendix C.

Figure 4.7 shows a completed actuator die. Each cantilever is 8 mm long with a spanwise spacing of 2 mm. Micromachining allows accurate control of critical dimensions and fabrication of arrays with reproducible geometry. Figure 4.8 shows a close-up view of a single actuator tip. The width of the cantilever is 1 mm. The narrow gap is 50  $\mu\text{m}$  wide. Both the wide gap and the tip gap have a dimension of 150  $\mu\text{m}$ . Compensating structures are used to prevent undercutting at convex corners. In Fig. 4.9, the bonded pieces of PZT and the ribbon cable connector that allows for individual actuator addressing are clearly seen. The backside contacts ensure that the base flow is not disturbed. In combination with shape deposition manufacturing techniques (Weiss *et al.* 1996), they would enable multiple dies to be mounted in a seamless manner.

## 4.5 Mechanical Characterization

### 4.5.1 Transfer Function

The actuator tip displacement as a function of frequency was measured using a laser vibrometer (Polytec OFV 502 fiber interferometer and Polytec OFV 3001 vibrometer controller). A laser beam is bounced off the tip of the actuator and the reflected beam is collected

in backscattering mode. Velocity and displacement information are obtained using interferometric techniques. The vibrometer output is fed to a spectrum analyzer (HP 89410A DC-10 MHz Vector Signal Analyzer) to determine the actuator response at the forcing frequency. The entire transfer function is obtained by measuring the response for a number of frequencies in the range of interest. The system is capable of Å level resolution. The largest source of uncertainty is due to errors in aligning the laser beam with the actuator tip. This uncertainty was experimentally determined by making multiple measurements for a single actuator and is estimated to be in the sub- $\mu\text{m}$  range.

A typical transfer function is plotted in Fig. 4.10. The static tip displacement ( $3.4 \mu\text{m}$ ) and resonant frequencies (1475 and 9975 Hz) match well with one-dimensional beam theory calculations. The average power consumption is given by  $V_{rms} I_{rms} \cos(\theta)$  where  $\theta$  is the phase difference between the voltage and the current. The power consumption at the two resonances are 0.5 mW and 1.5 mW respectively. Further optimization of the actuators should be able to reduce these figures by an order of magnitude. This indicates the potential for use of a large array in a real application within a realistic power budget. A comparison of the transfer functions for PZT-5A and PZT-5H actuators is shown in Fig. 4.11. PZT-5H has a higher piezoelectric coefficient than PZT-5A, 320 pC/N as opposed to 171 pC/N, and therefore a larger static deflection. It also has a lower quality factor indicating that the 5H ceramic has higher dielectric losses. The quality factors obtained here are 4–6 times higher than those obtained by JR. This is because all their experiments were performed in water and therefore their actuators had a higher damping ratio  $\zeta$ .

#### 4.5.2 Repeatability and Crosstalk

The repeatability of the actuators in an array was tested by forcing them with a white noise signal. Fig 4.12 shows that the actuator transfer functions are remarkably similar. The mean resonant frequency is 1906 Hz with a standard deviation of 19 Hz. The resonant frequencies of the different actuators are within  $\pm 2\%$  of each other (Fig. 4.13). This is useful as it allows all the actuators to be driven by the same carrier waveform. The quality factors of the different actuators are within  $\pm 10\%$  of each other. Fig. 4.14 shows the tip displacement repeatability of the actuators when forced at the resonant frequency of actuator 4. The variation in amplitude is less than 20% across the actuator array. These data were used to normalize the drive signals to the actuators during the control experiments. This ensures that all the actuators have the same displacement for a given control signal. All the actuators are on the same silicon substrate and therefore susceptible to mechanical crosstalk. This was estimated by forcing actuator 4 at its resonant frequency and measuring the tip displacements of all the other actuators. The mechanical crosstalk is less than 1%

in all cases. The Plexiglas mount adds stability to the silicon chip and makes the crosstalk issue insignificant.

#### 4.5.3 Behavior at Resonance

For the PZT-5H actuator, the resonant frequency decreases with drive amplitude as shown in Fig. 4.15. The decrease is a linear function of the voltage and has a slope of about -6 Hz/Volt. This trend has been noticed earlier by Kugel *et al.* (1996) and is probably due to reordering of dipole moments within the piezoceramic as the electric field increases.

The dependence of resonance frequency on applied voltage implies that different transfer functions can be obtained depending on the choice of forcing frequency. This is shown in Fig. 4.16 for two different frequencies, 1865 Hz and 1750 Hz. The response at the two frequencies has practically no hysteresis, but is non-linear for the 1750 Hz case. A best response, obtained by always forcing at the resonant frequency, is also shown. The best response is linear with a slope of 9  $\mu\text{m}/\text{Volt}$ . Fixing the forcing frequency causes the actuator to operate at ‘off resonance’ conditions and this accounts for the deviation from the best response.

It is impractical to change the forcing frequency when the actuators are used in flow control experiments. The forcing frequency that gave the best response at the center of the drive amplitude range ( $A = 0.5$ ) was chosen. This corresponds to the 1750 Hz plot in Fig. 4.16. The deviation from linearity does not cause any problems for the control experiments as the displacement is monotonic with drive amplitude and non-linearities can be accounted for in the control algorithm. As will be shown in Section 4.6.2.3, a minimum drive threshold of about  $A = 0.5$  is required to create a flow disturbance. Thus, the main effect of the non-linear displacement response is a decrease in the overall control authority of the actuators.

The response of PZT-5A and PZT-5H actuators are compared in Fig. 4.17. The PZT-5H actuator has a greater deflection, as was seen earlier in Fig. 4.11. The response of the PZT-5A actuator is roughly linear but with some hysteresis. Since both actuators have the same geometry, this again confirms that the non-linear response is a property of the PZT-5H material.

#### 4.5.4 Step Response

The response of the actuator to a step change in voltage is shown in Fig. 4.18. The 10 to 90% rise time is 0.25 ms. This is much smaller than typical turbulent time scales in low speed flows. Figure 4.19 shows the actuator response to a step signal change at the 1<sup>st</sup>

resonant frequency. The amplitude increases linearly at the beginning and then saturates as damping effects become significant. The actuator takes about 11 cycles ( $\approx 6$  ms) to reach 90% of the steady-state amplitude. The actuators have been run continuously for 200 hours (one billion cycles at the first resonant frequency) without failure. This is primarily because piezoelectric materials generate very low strains (less than 0.1%) and the relatively thick cantilevers reduce stresses well below yield values.

## 4.6 Fluid Dynamic Behavior

The actuators were characterized in the laminar boundary layer facility described in Chapter 2. All the fluid mechanic data in this report were obtained using PZT-5H actuators. Figure 4.20 shows the coordinate system for the fluid dynamic characterization of the actuators. The origin of the coordinate system is the tip of actuator 4, which is located 49.5 cm downstream of the tunnel contraction. The coordinate  $\Delta x_a$  represents distances downstream of the cantilever tip. The free-stream velocity  $U_\infty$  was chosen to be 5 m/s. At  $\Delta x_a = 0$ , the momentum thickness Reynolds number  $Re_\theta$  was 310 and the displacement thickness  $\delta^*$  was 2.3 mm. The sensor array is located 20 mm ( $8.6\delta^*$ ) downstream of the actuator array.

### 4.6.1 Behavior in Still Air

The response of the actuators in still air is shown in Figs. 4.21 and 4.22 respectively. The mean spanwise velocity profiles show that most of the actuator effect occurs in a 2 mm region from the tip. At the actuator tip, the maximum effect occurs at the center of the actuator  $z = 0$ . The narrow and wide gap are located at  $z = -0.6$  mm and  $z = 0.6$  mm respectively. Both gaps are active 2 mm upstream of the tip. For batch B actuators, the mean velocity is higher over the wide gap. The wall-normal profile in Fig. 4.22 shows that the velocity reaches a maximum  $\approx 0.8$  mm from the wall. This is followed by a steady reduction similar to that of a two-dimensional jet. This behavior has been documented earlier by Rathnasingham & Breuer (1997b) in their slot actuators.

The behavior of the actuators depends on a number of parameters including the Stokes number and the Keulegan-Carpenter number (Koumoutsakos 1995, Lachowicz *et al.* 1999). Changes in the local geometry can also dramatically effect the flow field created by the actuator. Figure 4.23 shows the mean velocities in still air for batch A and batch B actuators, 2 mm upstream of the actuator tip. For the  $150 \mu\text{m}$  cavity depth, most of the flow is over the narrow gap. The opposite behavior is seen for the  $200 \mu\text{m}$  cavity depth. The behavior at the tip of the actuator in the two cases is qualitatively similar with most of the flow

exiting at the center of the actuator (Fig. 4.24).

Figure 4.25 shows time resolved velocities closer to the wall. The flow profiles are periodic with a frequency equal to the forcing frequency. The higher average velocity for the  $y = 0.6$  mm profile indicates entrainment of fluid into the jet created by the actuator. It is difficult to measure velocity profiles closer to the wall without breaking the hot-wire. However, measurements by Smith & Glezer (1998) in a rectangular synthetic jet have shown negative  $v$  velocities closer to the wall, as is expected to satisfy conservation of mass in the actuator cavity. They also show that the mean wall-normal velocity decreases as the wall is approached. A similar behavior is expected for the cantilever type actuators described here.

#### 4.6.2 Behavior in Laminar Flow

All the fluid mechanic data in this section are for batch A actuators unless otherwise mentioned. The base profile with the actuator turned off matched the Blasius boundary layer solution. This indicates that the actuator does not affect the boundary layer when it is turned off, as desired.

##### 4.6.2.1 Velocity Perturbation Map

Figure 4.26 shows contours of the mean disturbance velocity  $\Delta U = U_{Actuator\ on} - U_{Actuator\ off}$  in a spanwise plane just downstream of the actuator tip. The contours were generated from a  $25 \times 21$  grid of data, spaced non-uniformly in both the spanwise and wall-normal direction for maximum resolution. The disturbance is symmetric and the pattern is consistent with that produced by a single pair of counter-rotating vortices with common flow away from the wall. The actuator generates a substantial disturbance, up to 20% of the free-stream velocity. The maximum disturbance velocity is located over the narrow gap and is due to transport of low momentum fluid away from the wall. Figure 4.27 compares the wall-normal profile at the maximum negative perturbation location with the unperturbed Blasius profile. The maximum effect on the mean velocity occurs at some distance from the wall.

##### 4.6.2.2 Streamwise Evolution of Disturbance

The streamwise evolution of the disturbance is presented in Figs. 4.28 to 4.30. Figure 4.28 shows spanwise profiles for five locations downstream of the actuator. The disturbance is localized over the actuator and diffuses outwards as it travels downstream. Spanwise profiles that are in the linear region of the velocity profile can be interpreted as changes in shear stress. This is shown in Fig. 4.29. The actuator creates an asymmetric disturbance with

a larger positive perturbation aligned with the wide gap. Figure 4.30 shows wall-normal profiles of the velocity disturbance at a spanwise location aligned with the narrow gap. The disturbance is concentrated in a region of about one displacement thickness from the wall. Thus, the actuator modifies only the near-wall velocity profile and does not affect the flow further away from the wall. The peak disturbance velocity is about 25% of the free-stream velocity ( $\Delta x_a/\delta_0^* = 4.3$ ,  $y/\delta^* \approx 0.8$ ). The maximum disturbance location gradually moves away from the wall as the disturbance is convected downstream.

A crossplot of the peak disturbance velocity vs. streamwise distance is shown in Fig. 4.31. The peak disturbance velocity initially grows in amplitude and then decays further downstream. The disturbance persists far downstream of the actuator - the peak disturbance velocity is 13% of the free-stream velocity 30 displacement thicknesses downstream of the actuator.

#### 4.6.2.3 Amplitude Control

The magnitude of the disturbance as a function of the actuator drive amplitude is shown in Fig. 4.32. There is practically no velocity disturbance up to a drive amplitude  $A = 0.5$ , probably due to viscous effects. This dead-band region reduces the mechanical crosstalk among adjacent resonant elements and minimizes the need for decoupling zones. From  $A = 0.5$  to  $A = 1.0$ , the disturbance is a monotonic and nearly linear function of the drive amplitude.

#### 4.6.2.4 Power Spectra

The resonant frequency of the actuator was chosen to be an order of magnitude higher than frequencies sustained by the low speed flows in this project. Thus, the energy at the forcing frequency is expected to decrease rapidly downstream of the actuator. Figure 4.33 shows power spectra measurements of the streamwise velocity at the maximum perturbation location as the flow moves downstream.

The velocity signal was sampled at 8192 Hz for 1 second. The data was multiplied by a Hanning window to reduce leakage between bins and then Fourier transformed to obtain a power spectrum record. The frequency resolution is 1 Hz as the total sampling time is 1 second. 40 independent records were averaged to reduce the variance of the power spectrum estimate (Press *et al.* 1992). The power at each frequency  $f_k$  is  $E_{uu}(f_k)$  as the bin width is 1 Hz.

Close to the actuator, both the forcing frequency and its harmonic are present in the flow. However, the energy at the forcing frequency is only a small fraction of the total energy

and the flow is essentially steady even at  $\Delta x_a/\delta^* = 0$ . The energy at the forcing frequency is close to the noise floor four displacement thicknesses downstream of the actuator. The peak close to 1300 Hz seen in the plots is related to the actuator driver electronics and is not a feature of the flow. The power spectra provide additional confirmation that the primary effect of the actuator is to create a steady disturbance in the boundary layer.

#### 4.6.2.5 Flow Step Response

The flow step response was measured by the shear stress array described in Chapter 3. The sensors were located 20 mm downstream of the actuator tip. Figure 4.34 shows phase averaged contours (256 cycles) of the wall shear stress. The actuator was turned on at  $t = 0$  ms and turned off at  $t = 50$  ms, as indicated in Fig 4.35. After a convective time delay, the flow rapidly adjusts to a new shear stress state. The abscissa can also be interpreted as streamwise distance using Taylor's hypothesis. The shear stress pattern of elongated structures in the streamwise direction and alternating positive and negative bands in the spanwise direction is similar to that seen in turbulent boundary layers.

The flow step response is more clearly seen by examining the temporal response of a single sensor and is shown in Fig. 4.35. The first 15 ms represents the convective time delay from the actuator to the sensor. This corresponds to a convective velocity that is  $\approx 0.25U_\infty$ . The next 6 ms represent the time taken by the actuator to achieve its steady-state tip displacement. This is followed by the flow adjusting to its new state with a 10 to 90% rise time of 9 ms. The flow returns to its unperturbed state when the actuator is turned off with the same time constant. There are three possible scaling parameters for the flow rise time: the fly-over time over the actuator  $l/U_\infty$ , the period of oscillation of the cantilever  $T$  and a Stokes flow time constant  $d_{gap}^2/\nu$ . The values of these three parameters are 1.6 ms, 0.56 ms and 1.5 ms respectively. It appears that the fly-over time is not the limiting parameter as results from two different free-stream velocities (5 and 8 m/s) had the same flow rise time (but different convective delays). This is also reasonable as results in Section 4.6.1 have shown that most of the actuator effect occurs over the last 2 mm of the actuator. Note that this is different from the results of JR who had 20 mm long actuators that were active over a substantial streamwise length. Thus, the Stokes time constant appears to govern the flow response in this specific case.

#### 4.6.2.6 Effect of Multiple Actuators

Figure 4.36 shows the effect of three different actuators on the wall shear stress. These data were obtained using the sensor array. The three actuators create similar disturbances

that are offset in the spanwise direction. The resonant frequency of actuator 4 was used as the forcing frequency. Therefore, actuator 4 shows the strongest perturbation. The disturbances created by actuators 3 and 5 are about 75% and 65% as strong as that created by actuator 4. It is interesting to note that the negative perturbation saturates at the higher amplitudes while the positive perturbation appears to grow linearly with amplitude. Thus, these actuators increase the net shear stress in an unperturbed flow.

## 4.7 Actuator for Operation in Water

Operation in water requires electrical isolation of the individual piezoceramic pieces. This can be done either by embedding the PZT in the silicon or by conformally encapsulating the piezoceramic after it has been bonded to the silicon. This section describes the design and fabrication of actuators with the PZT embedded in the silicon.

### 4.7.1 Design

A polyimide curing at 250 °C was used to bond the PZT and planarize the resulting structure. This implied that only PZT-5A that has a Curie temperature of 350 °C could be used for these actuators. PZT-5H has a Curie temperature of 250 °C and would de-pole during the polyimide curing step. Figure 4.37 shows the design space for PZT-5A actuators in water at 0.5 m/s. The static deflection constraints limit the thickness of the piezoceramic to smaller values than in Fig. 4.4 because PZT-5A has a smaller piezoelectric coefficient. The resonant frequency constraint is not active because burst frequencies in water are considerably lower than that in air as seen from Table 1.1. The design window is broadly similar to that for air but suggests than thinner piezoceramic pieces are needed. Once again, a hybrid fabrication process that combines bulk micromachining along with discrete PZT bonding is needed.

### 4.7.2 Multi-Level Etch Process

Embedding the piezoceramic requires the development of a process that can etch the silicon to different etch depths. The need for different depths is clearly seen in the side section of the actuator in Fig. 4.39. It is difficult to get a conformal coating of photoresist on a wafer with anisotropically etched features using spin coating. The quality of the coating depends on a number of parameters including the Weber number, aspect ratio of features, radial position and material properties of the resist (Stillwagon & Larson 1989). Trenches with depths significantly larger than the photoresist thickness suffer from poor coverage at their

boundaries. Radial streaky patterns starting from trench corners are seen at higher spin speeds. These problems can be circumvented using either electrodeposited or spray resists, but these are areas of active research (Linder *et al.* 1996, Luxbacher & Mirza 1999).

An alternative approach is to complete all the lithography before etching the silicon. This involves the use of multiple masking layers, each of which can be selectively patterned and removed. This technique has been used, among others, by Zdeblick (1988) and is described in Fig. 4.38. First, a layer of thermal oxide is grown on the wafer surface followed by deposition of a layer of silicon nitride. The nitride is patterned by plasma etching and the oxide is patterned using a 6:1 buffered oxide etch (BOE). Both the nitride and oxide are patterned over the features that need to be etched to the deeper depth. Then, only the nitride is patterned over the features with the shallow depth (Fig. 4.38a). This is followed by anisotropic etching of the silicon to a depth equal to the difference between the two levels. The oxide protects the shallow depth features and must be thick enough so that it is not consumed in the first KOH etch step. Next, the oxide over the shallow depth features is etched away, leaving the wafer as in Fig. 4.38b. This is followed by the second KOH etch that takes both features to their desired etch depths.

#### 4.7.3 Fabrication

The fabrication process is described in Fig. 4.39. It requires six masks and five lithographic steps. The process starts with  $<100>$  silicon wafers with a  $0.4 \mu\text{m}$  layer of thermal oxide and a  $0.25 \mu\text{m}$  layer of low-stress LPCVD silicon nitride. Through holes are etched in the wafer for two sided alignment. Both the nitride and oxide are patterned to define the backside contacts and the cantilever. Only the nitride is patterned over the cavity and the PZT recess. This is followed by a KOH etch to a depth of  $50 \mu\text{m}$ , which is the thickness of the silicon cantilever (Fig. 4.39a). The oxide over the PZT recess is removed and the KOH etch is continued to a depth of  $175 \mu\text{m}$ . At this point, the recess for the PZT is complete. The oxide over the cavity is removed and a trilayer of PECVD nitride-metal-PECVD nitride is deposited on the frontside. The  $3000 \text{ \AA}$  thick PECVD nitride layers are deposited over the entire wafer but are shown only in the recess for clarity (Fig. 4.39b). They protect the metal during the KOH etch required for cantilever release. The metal layer is formed by evaporation of Cr:Au ( $200 \text{ \AA} : 1 \mu\text{m}$ ) and functions as the positive electrode. The evaporation is carried out through a shadow mask so that the metal is deposited only on the bottom surface of the PZT recess. The cantilever is released and the wafer is diced into individual dies. The PZT is bonded to the silicon using a low temperature curing polyimide (PIX8144 from Hitachi Chemicals, cure temperature  $250^\circ\text{C}$ ). This is followed by a blanket deposition of the ground electrode, which is then protected by a second layer of polyimide.

Finally, backside contacts were made as in Section 4.4.

Figure 4.40 shows details of the compensation structure used to prevent undercutting at convex corners. The size of the rectangular compensation pattern was chosen following the recommendations of Puers & Sansen (1990). The compensation dimension is linearly related to the desired etch depth and was determined to be 200  $\mu\text{m}$  for the etch depth of 175  $\mu\text{m}$  required here. The picture was taken after the silicon had been etched to a depth of 50  $\mu\text{m}$  (Fig. 4.39a). The undercutting at the convex corners along with the emergence of higher order crystal planes is clearly seen. The outline of the nitride mask is shown by the white line, and remnants of the nitride at the three 90° corners are also seen. The compensation was designed for pure KOH even though the size of the structure is about three times larger than for KOH solutions saturated with isopropyl alcohol (IPA). Pure KOH was the preferred etchant as KOH-IPA solutions cause the formation of hillocks on the etched surfaces resulting in higher surface roughness. The tip of a single actuator before the PZT bonding is shown in Fig. 4.41.

The fabrication process described here did produce functional actuators but with low yields. The primary problems were poor planarization of the top surface and breakage of the metal layer over the backside contacts. This work was not pursued further but a number of suggestions for better yield are listed for future reference. Silicon on insulator (SOI) wafers would allow a better control of the different etch depths. Deep reactive ion etching (DRIE) or other ‘gas phase only’ etching processes that are gentler than wet KOH etching would increase the yield of the backside contacts. Finally, processes for depositing or growing the PZT *in situ* would eliminate many of the problems associated with discrete PZT bonding.

## 4.8 Conclusions

Fabrication of transducer arrays for boundary layer control experiments in low speed air flows using a micromachining based technology has been demonstrated. The dynamic range, bandwidth, robustness, and low-power requirements of the actuators make them viable candidates for flow control applications. The actuators do not incur any drag penalty when not in operation as they are mounted flush with the flow surface. Furthermore, the actuator effect is due to its pumping action and not due to the deflection of the cantilever into the flow. Hence, form drag penalties for this actuator should be minimal. The actuator array can significantly affect the spanwise wall shear stress distribution. Compared to the Jacobson actuators, the spanwise footprint is reduced by 20% while the streamwise footprint is reduced by a factor of 2.5.

#### 4.8.1 Design Improvements

The disturbance generated by the actuator should be largely independent of actuator length once the tip deflection crosses a viscous threshold. This is because the average velocity depends on the product of tip deflection and resonance frequency and the length dependence cancels. This suggests that the actuator can be scaled down in the streamwise direction. The ability to etch vertical sidewalls using deep reactive ion etching and the development of high density through wafer interconnects (Chow *et al.* 1998) should also enable scaling of the actuators in the spanwise direction. Recent developments in the deposition and bonding of thick PZT films (Akedo *et al.* 1997, Tanaka *et al.* 1998) indicate the potential for replacing the discrete PZT bonding step with processes that are either automated or parallel in nature. This would allow for true batch fabrication of actuator arrays.

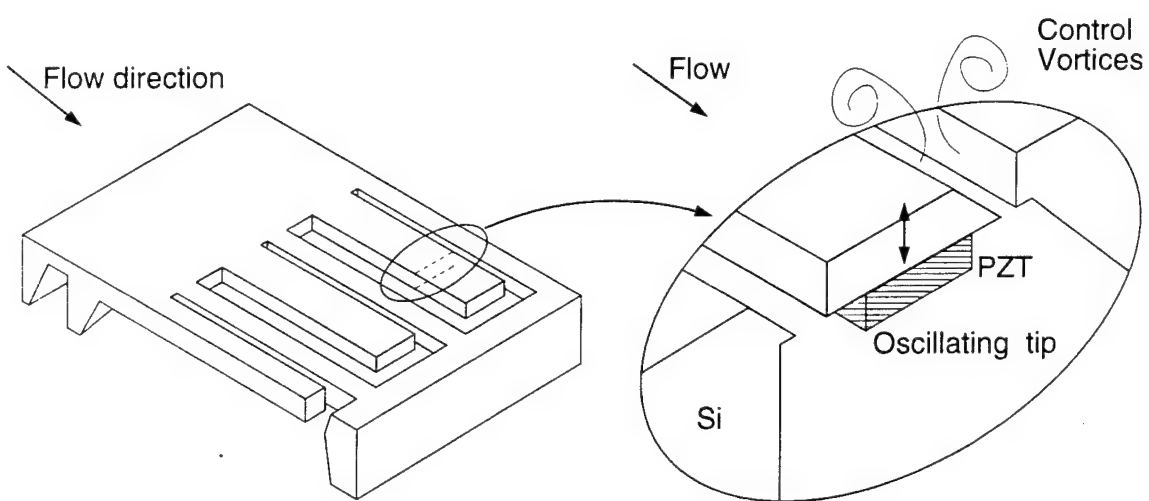


Figure 4.1: Illustration of the actuator concept.

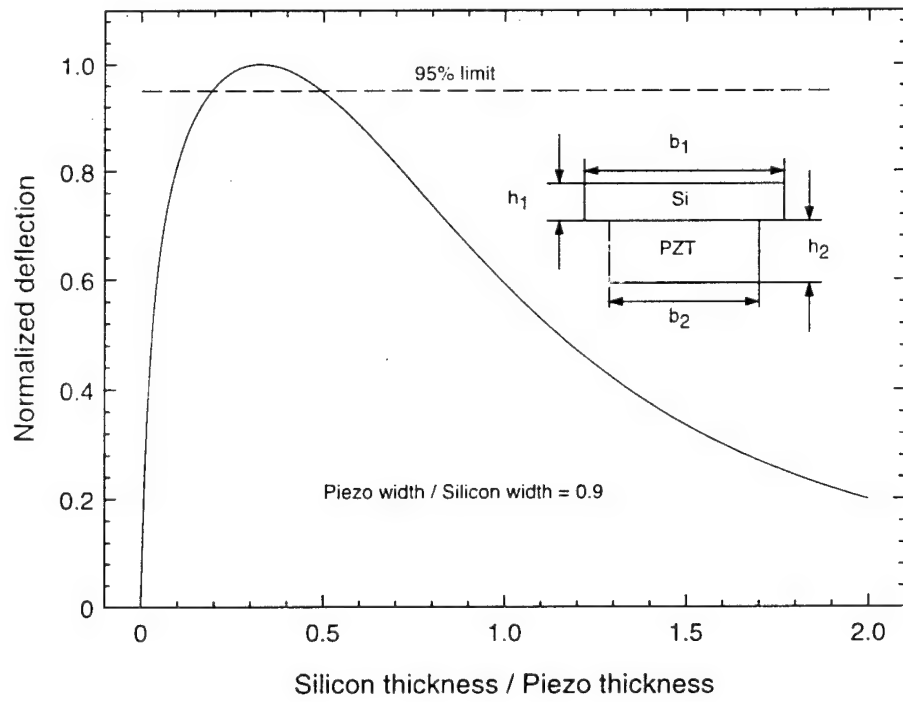


Figure 4.2: Dependence of tip deflection on thickness ratio. The optimum ratio is 0.33 and the 95% limits are 0.2 and 0.5 respectively.

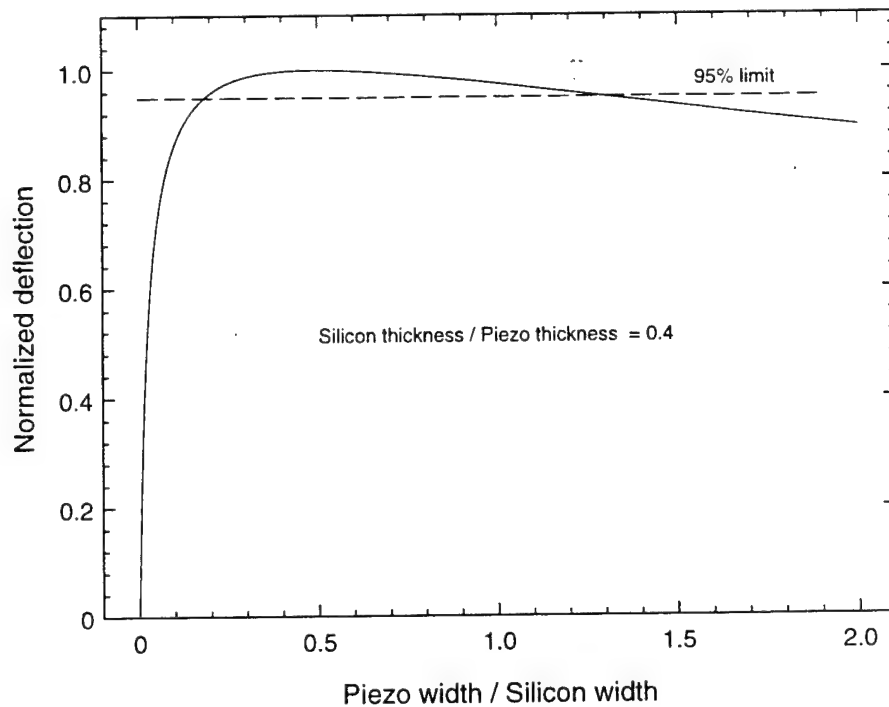


Figure 4.3: Dependence of tip deflection on width ratio. The optimum ratio is 0.49 and the 95% limits are 0.19 and 1.3 respectively.

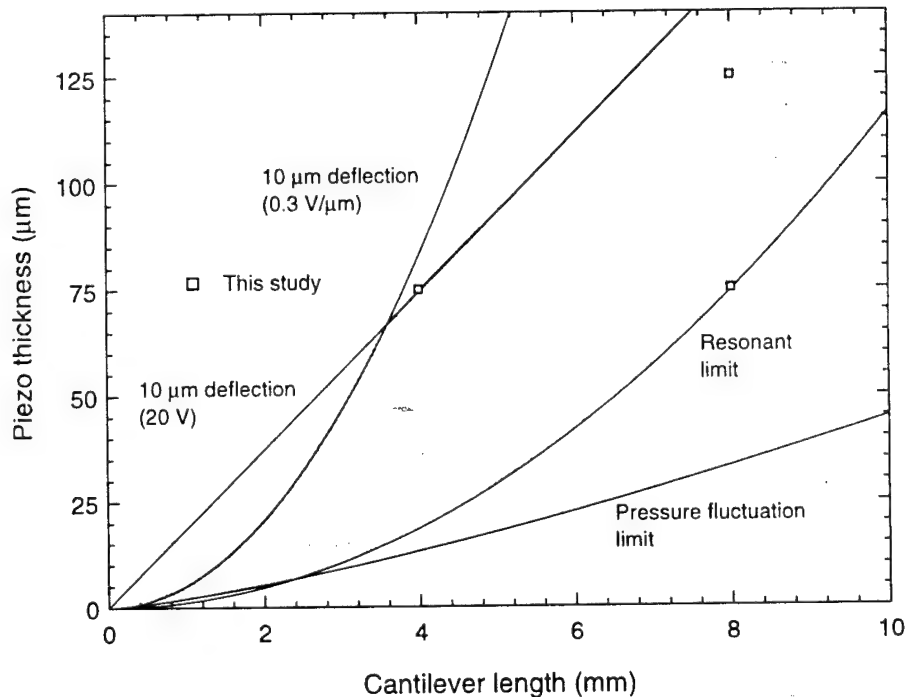


Figure 4.4: Design space for PZT actuator in air at 10 m/s. The optimum thickness ratio was used. Curves are to be interpreted as guidelines and not absolute cutoffs.

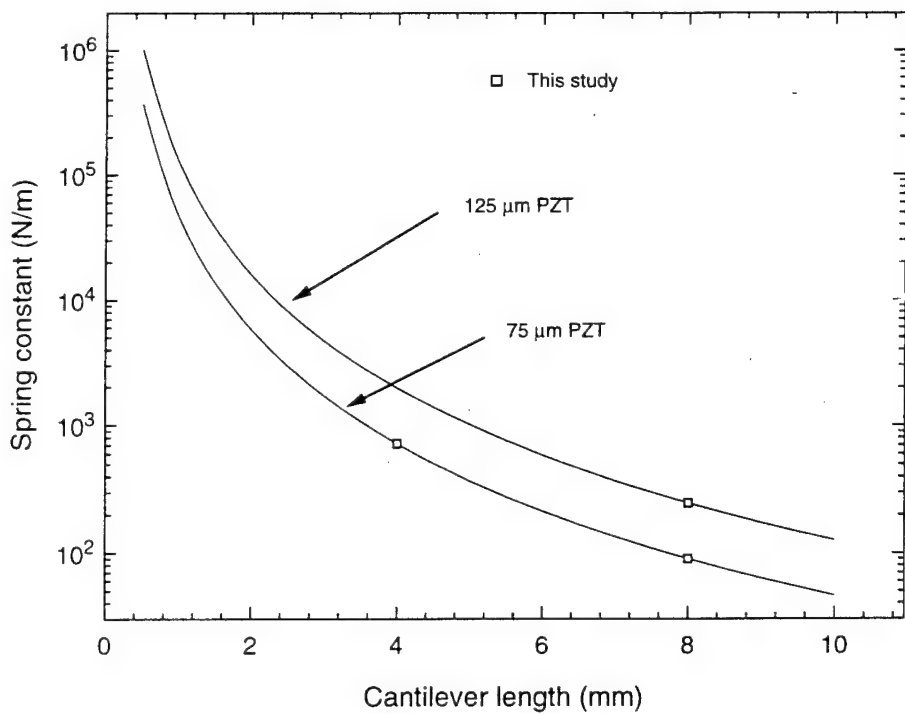


Figure 4.5: Spring constant of actuator (point load at tip).

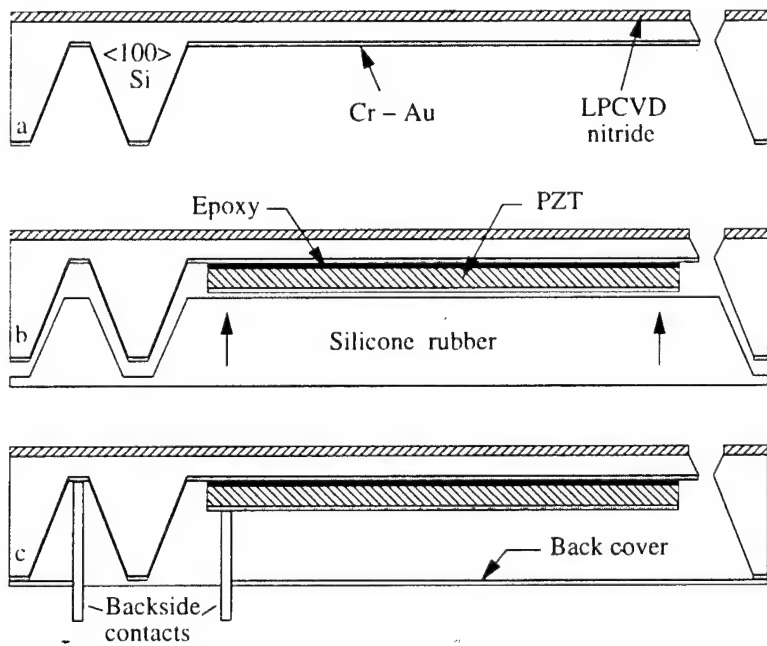


Figure 4.6: Actuator fabrication sequence (not to scale).



Figure 4.7: Top view of an actuator array. For scale, the die has been placed next to a dime.

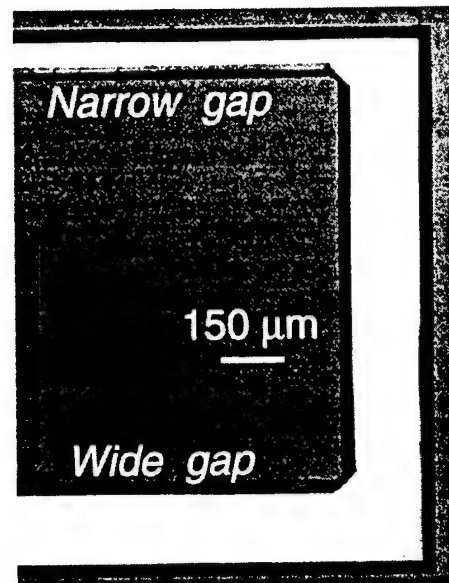


Figure 4.8: Tip of a single actuator.

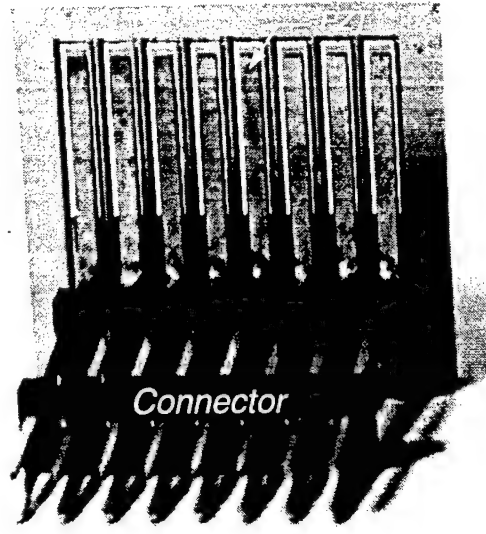


Figure 4.9: Bottom view of array.

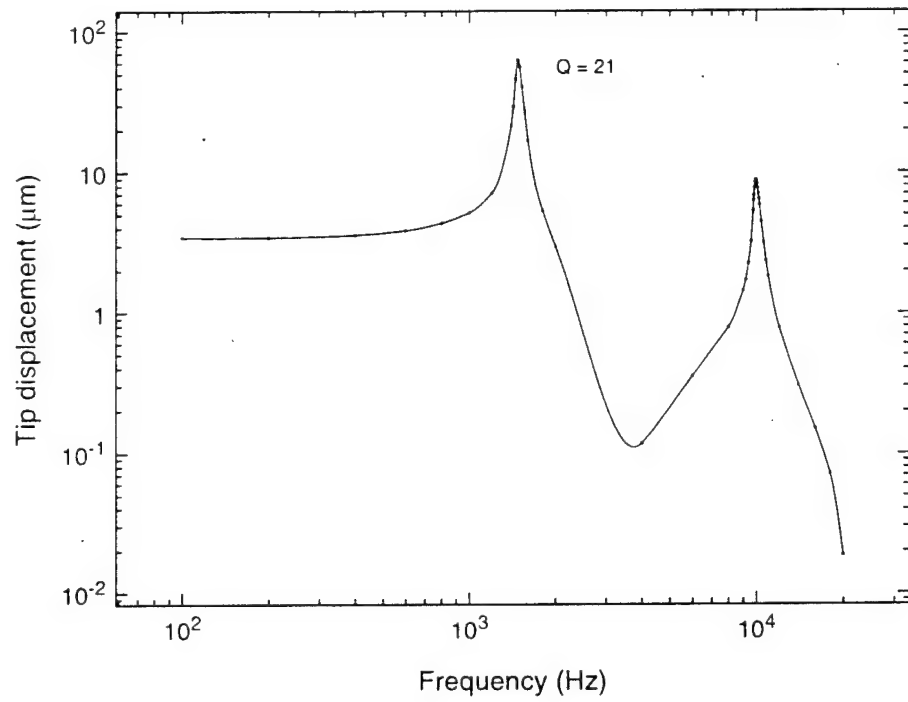


Figure 4.10: Displacement transfer function of PZT-5A actuator (drive amplitude  $A = 0.5$ , actuator is 8 mm long).

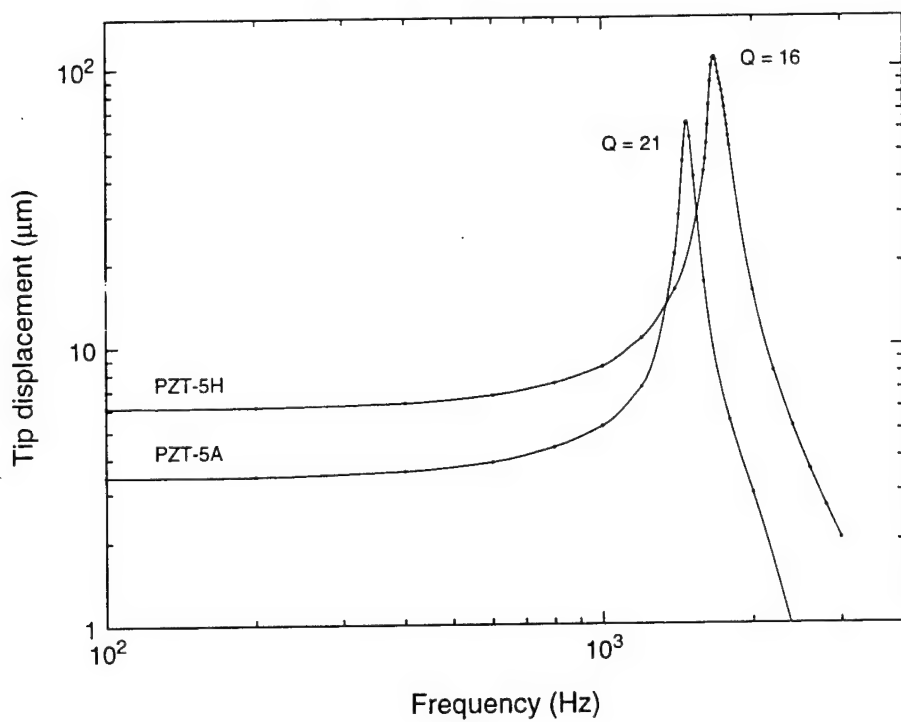


Figure 4.11: Displacement transfer functions of PZT-5A and PZT-5H actuators (drive amplitude  $A = 0.5$ , actuator is 8 mm long).

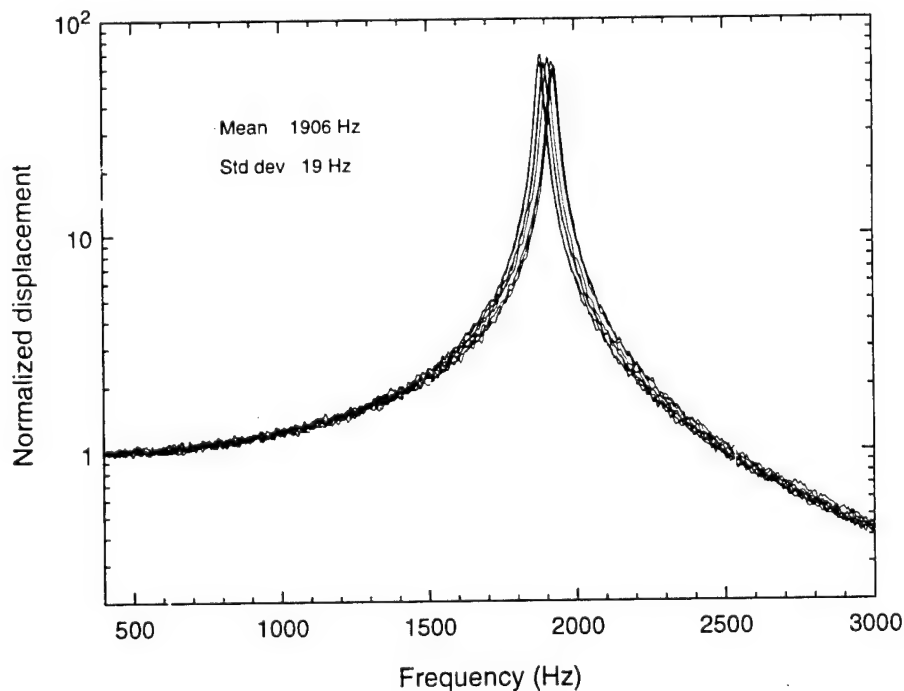


Figure 4.12: Transfer functions of eight different actuators (white noise excitation, peak amplitude = 5 V, 100 Hz - 4 kHz bandwidth).

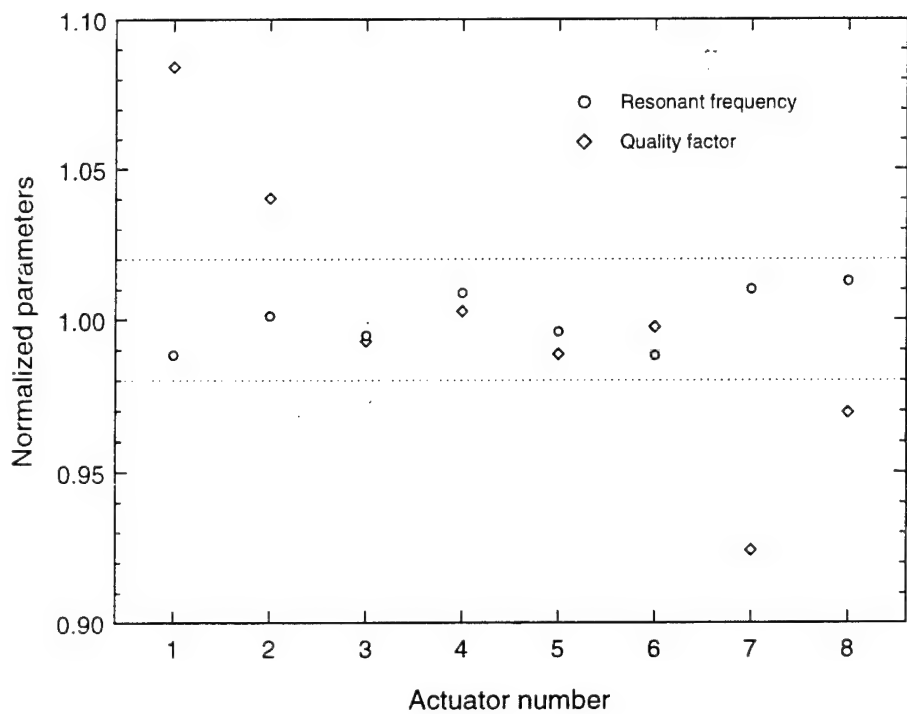


Figure 4.13: Resonant frequencies and quality factors of actuators in Fig. 4.12.

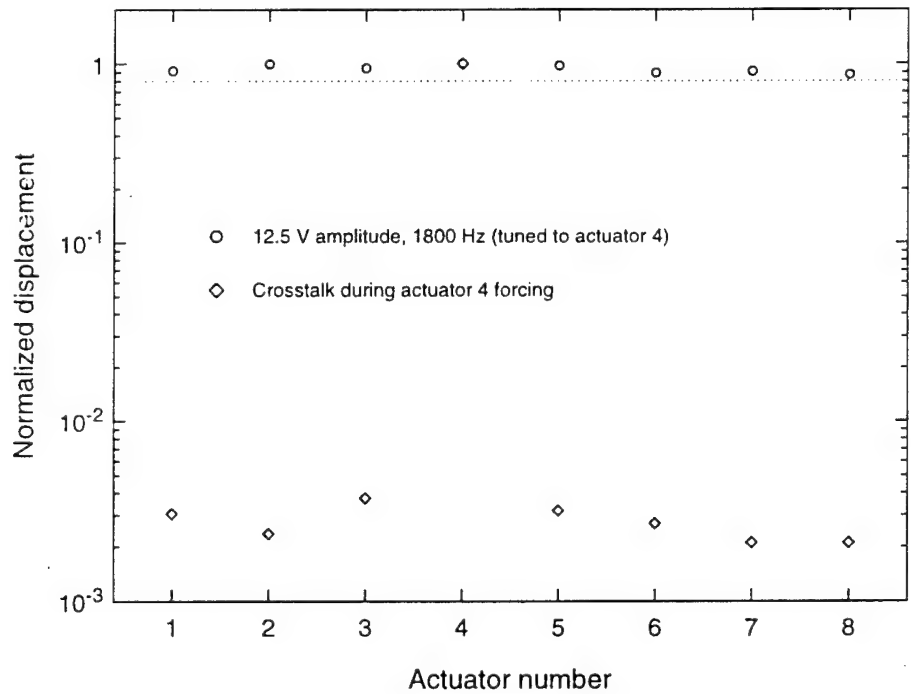


Figure 4.14: Tip displacement repeatability when a single forcing frequency is used and crosstalk when actuator 4 is being driven.

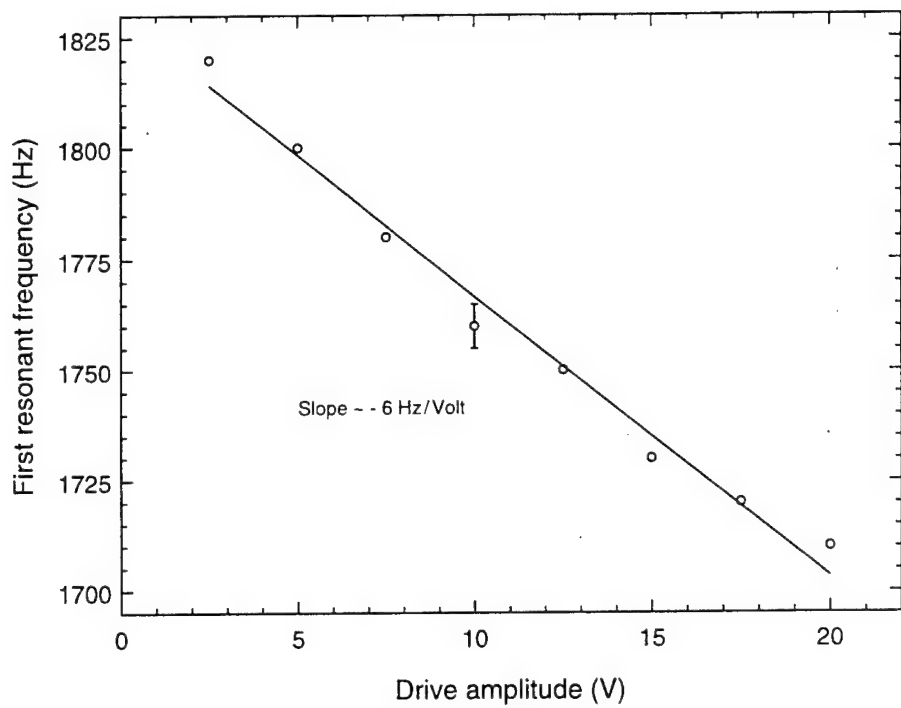


Figure 4.15: Resonant frequency as a function of drive amplitude for PZT-5H actuator.

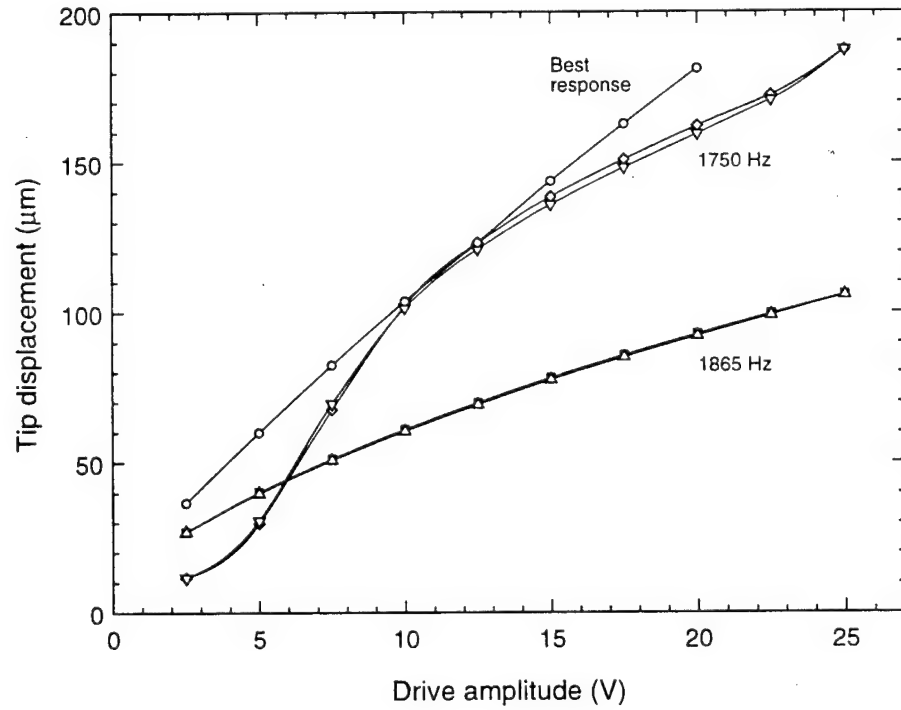


Figure 4.16: PZT-5H actuator tip displacement as a function of drive amplitude.

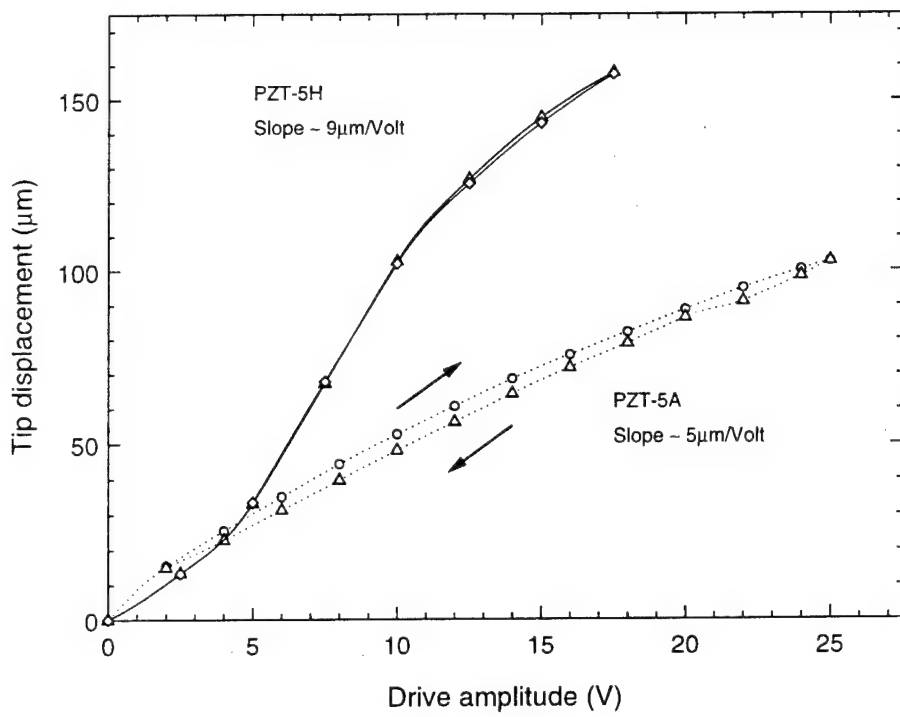


Figure 4.17: Tip displacement of PZT-5A and PZT-5H actuators at 1<sup>st</sup> resonant frequency.

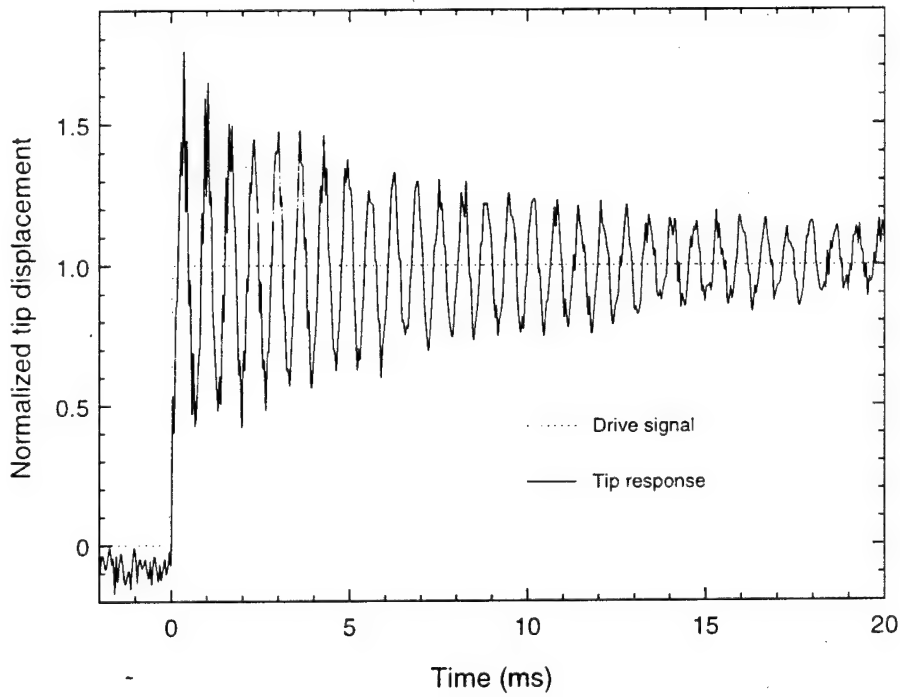


Figure 4.18: Actuator step response (drive amplitude  $A = 0.5$ ).

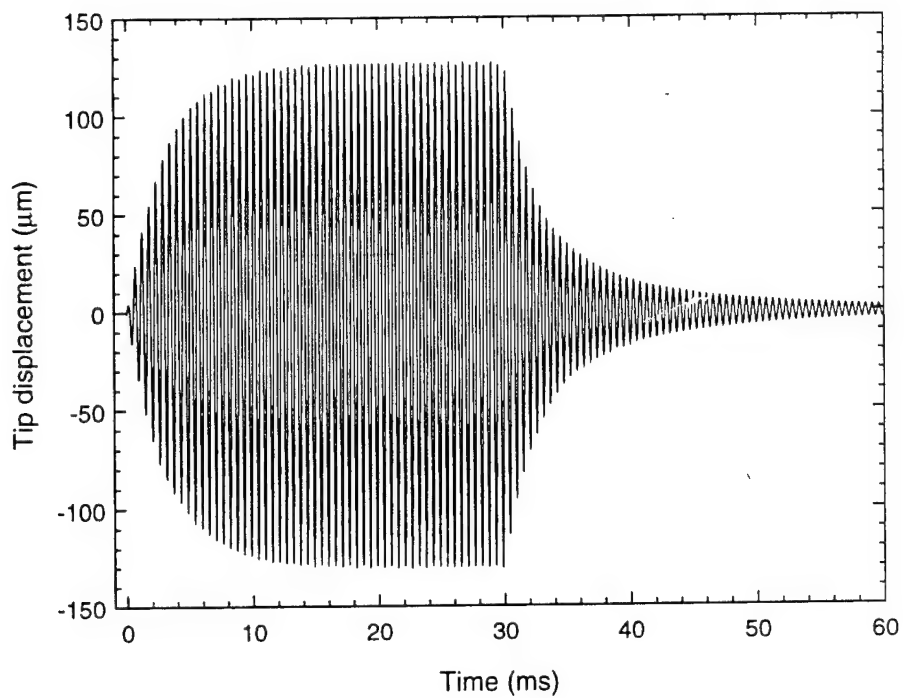


Figure 4.19: Actuator response to step change in driving signal at 1<sup>st</sup> resonant frequency (drive amplitude  $A = 0.625$ ).

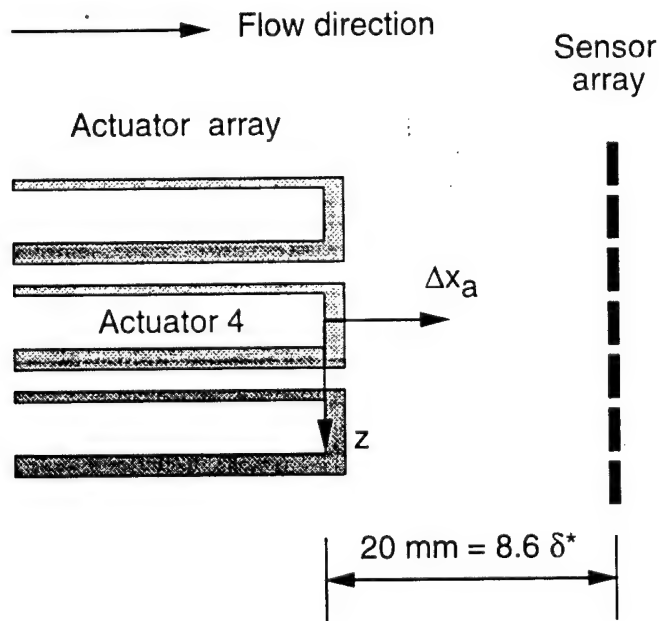


Figure 4.20: Schematic showing coordinate system for actuator characterization experiments.

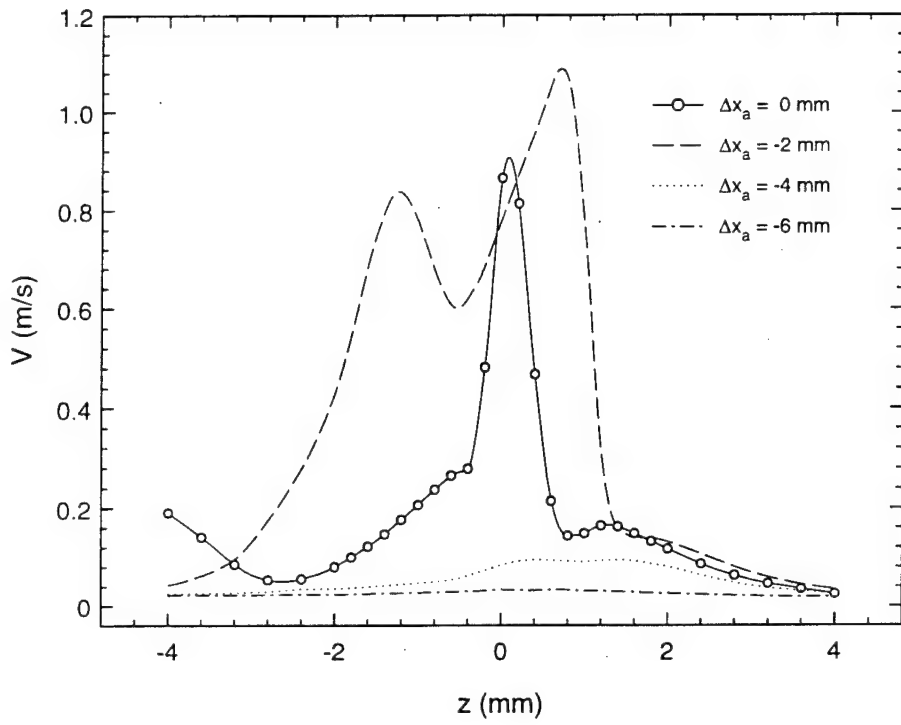


Figure 4.21: Spanwise velocity profiles in still air for different streamwise locations ( $y = 1$  mm, batch B actuator, actuator drive amplitude  $A = 1.0$ ).

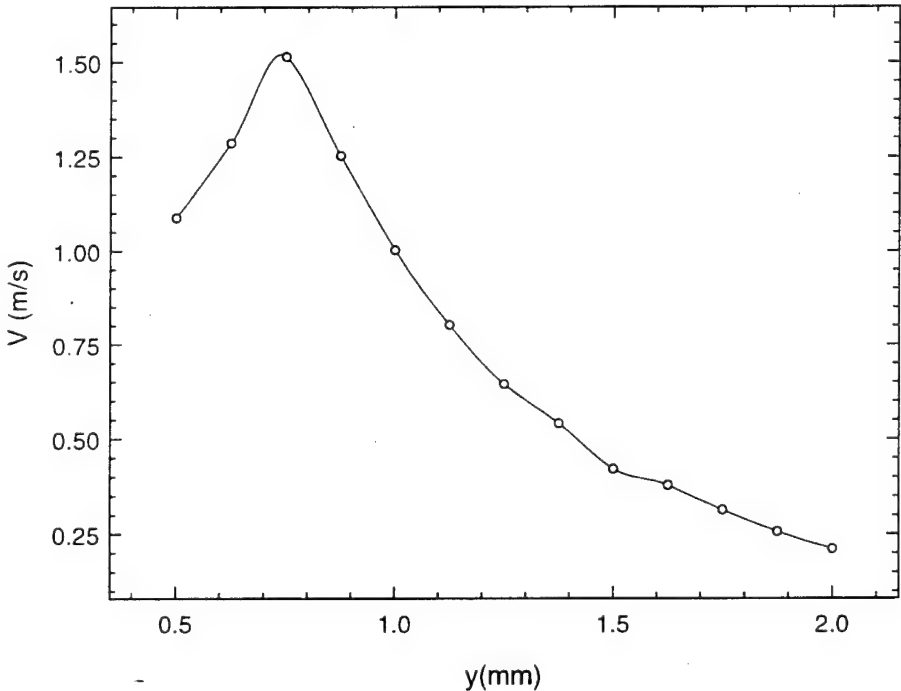
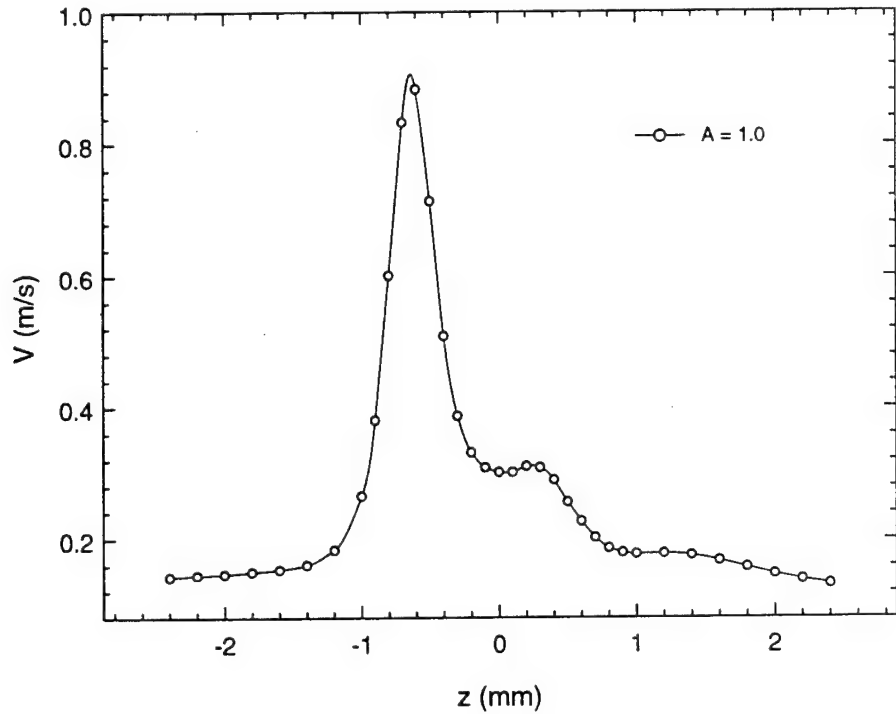
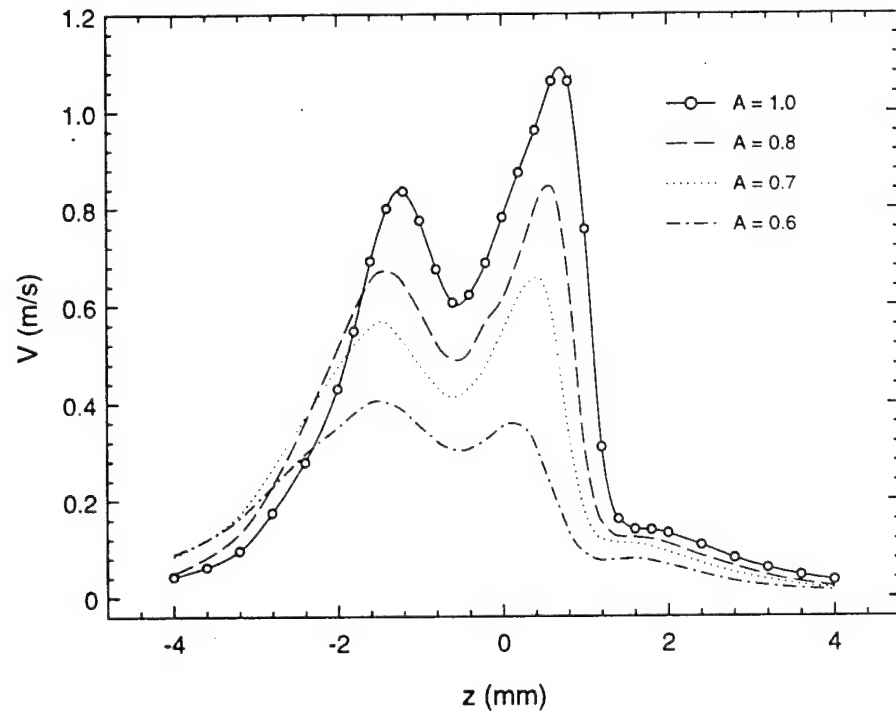


Figure 4.22: Wall-normal velocity profile in still air ( $\Delta x_a = -2$  mm, batch B actuator, actuator drive amplitude  $A = 1.0$ ).

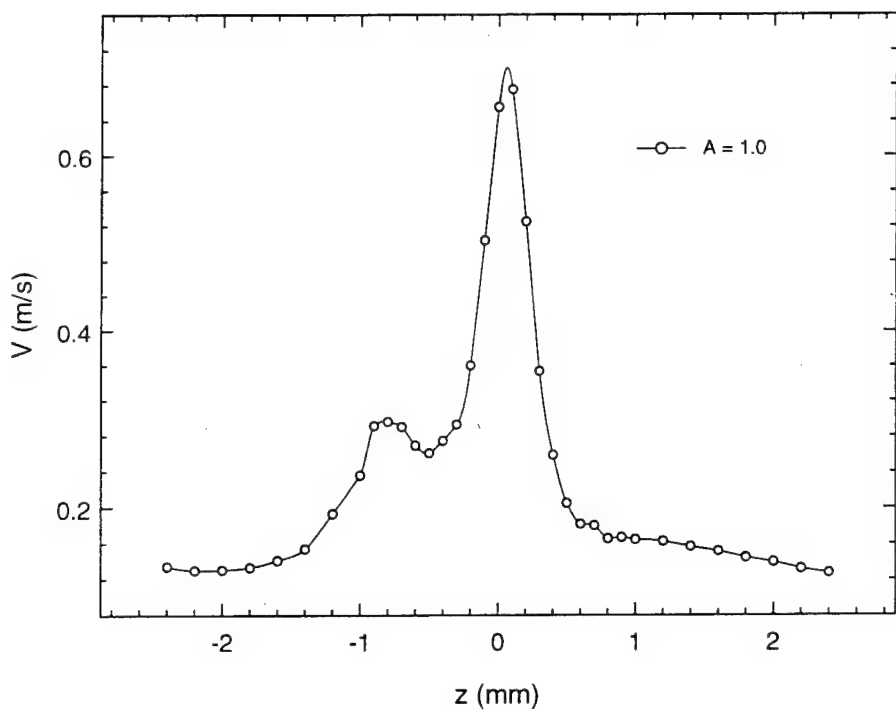


(a) Batch A, cavity depth =  $150 \mu\text{m}$

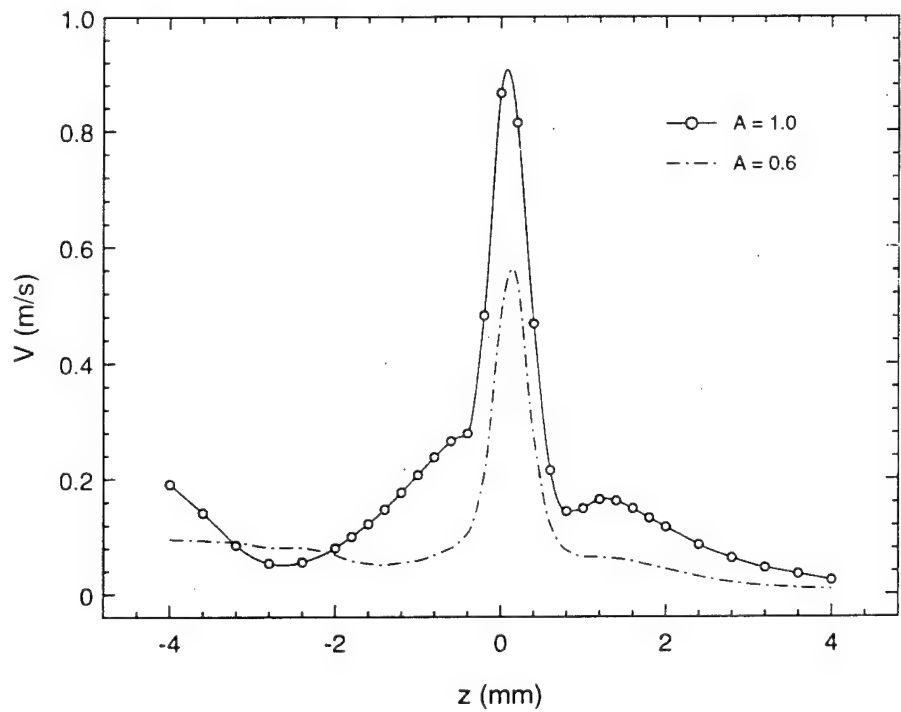


(b) Batch B, cavity depth =  $200 \mu\text{m}$

Figure 4.23: Spanwise velocity profiles in still air at different drive amplitudes ( $\Delta x_a = -2 \text{ mm}$ ).



(a) Batch A, cavity depth =  $150 \mu\text{m}$



(b) Batch B, cavity depth =  $200 \mu\text{m}$

Figure 4.24: Spanwise velocity profiles in still air at different drive amplitudes ( $\Delta x_a = 0 \text{ mm}$ ).

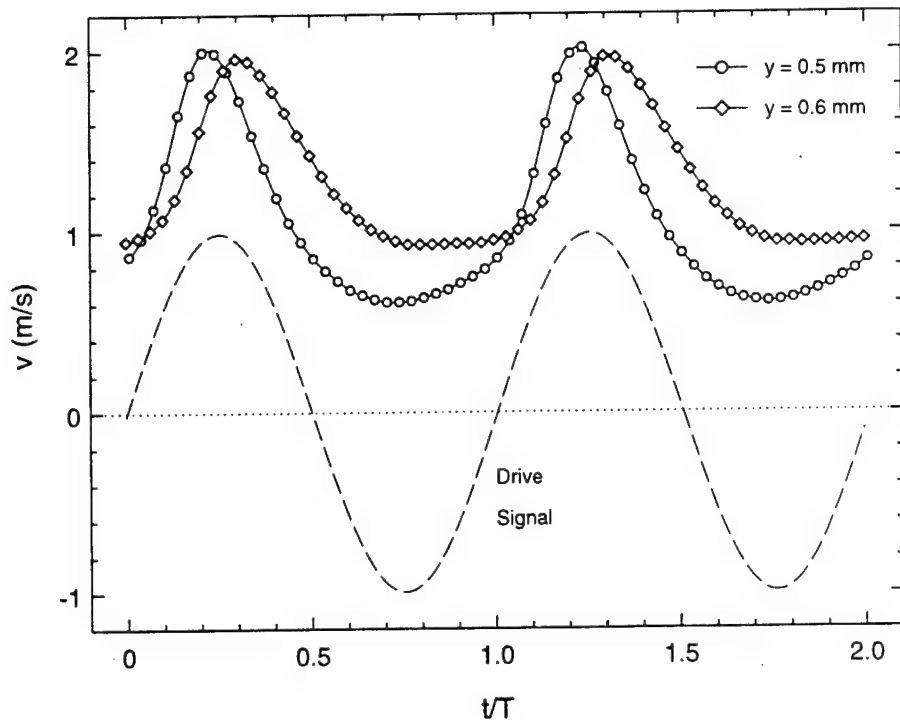


Figure 4.25: Time resolved velocity profiles over wide gap in still air (batch B actuator,  $\Delta x_a = -2$  mm, actuator drive amplitude  $A = 1.0$ ).

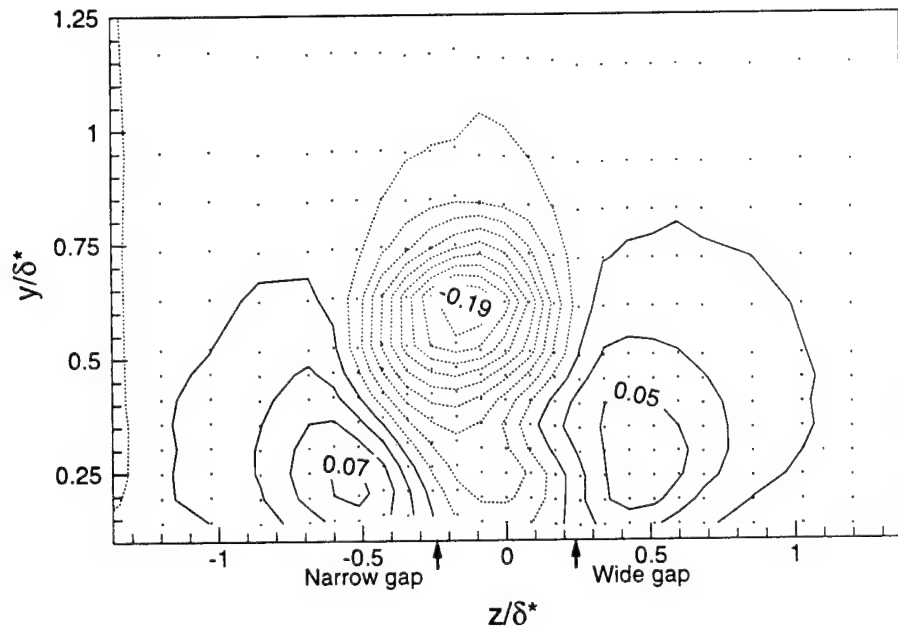


Figure 4.26: Contours of  $\Delta U/U_\infty$  at  $\Delta x_a/\delta^* = 0^+$ . Contours are in increments of  $0.02 U_\infty$ . Negative contours are indicated by dotted lines. Actuator drive amplitude  $A = 0.9$ . Data point locations are shown by dots.

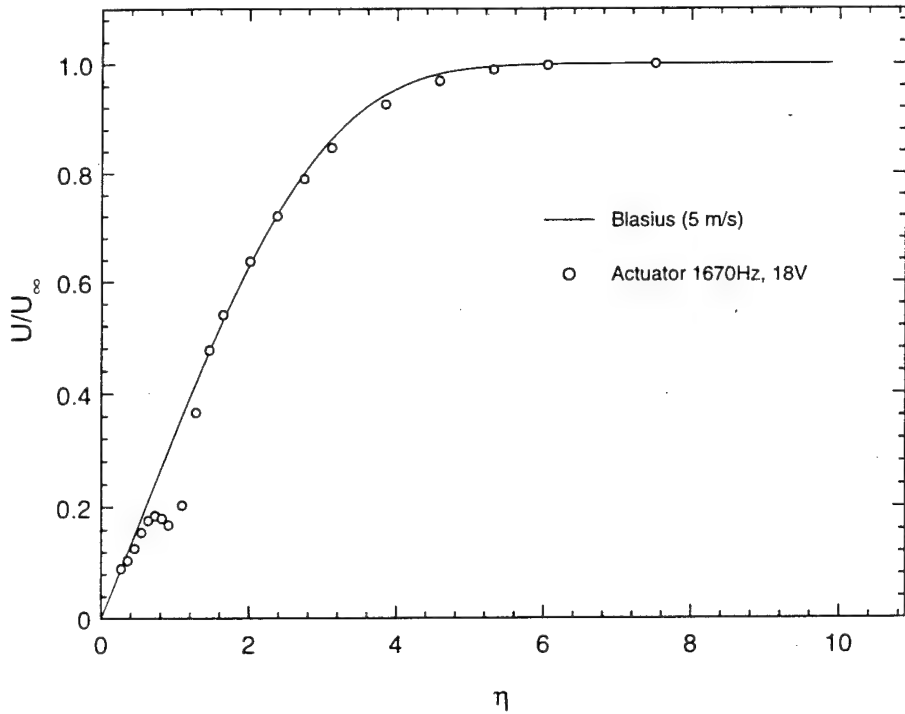


Figure 4.27: Wall-normal velocity profile at maximum negative perturbation location compared to Blasius profile ( $\Delta x_a/\delta^* = 0^+$ , actuator drive amplitude  $A = 0.9$ ).

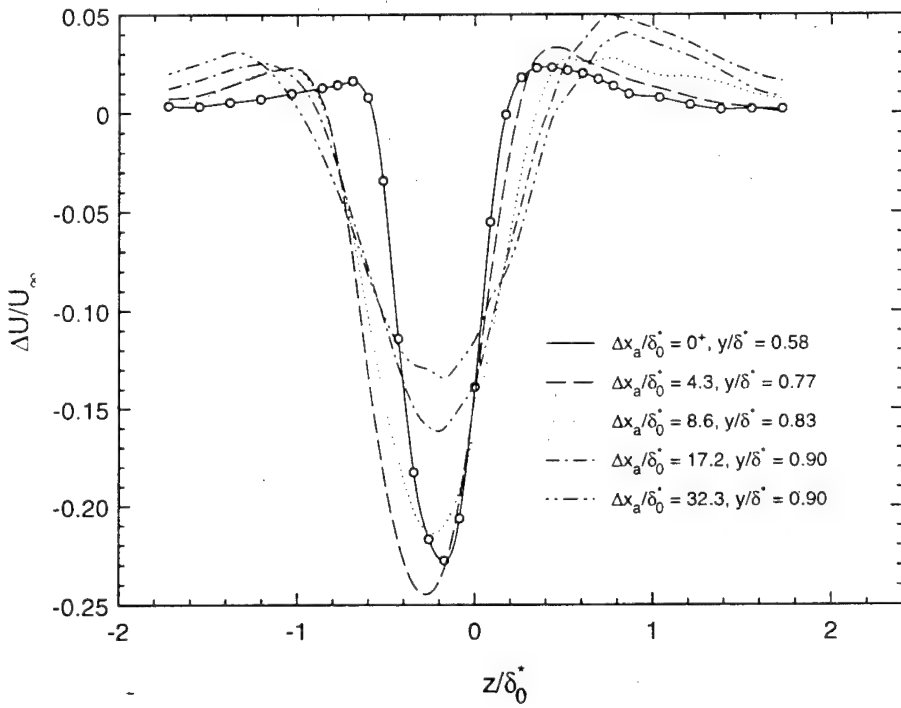


Figure 4.28: Spanwise velocity profiles at maximum negative perturbation location for different streamwise locations. Actuator drive amplitude  $A = 0.9$ .

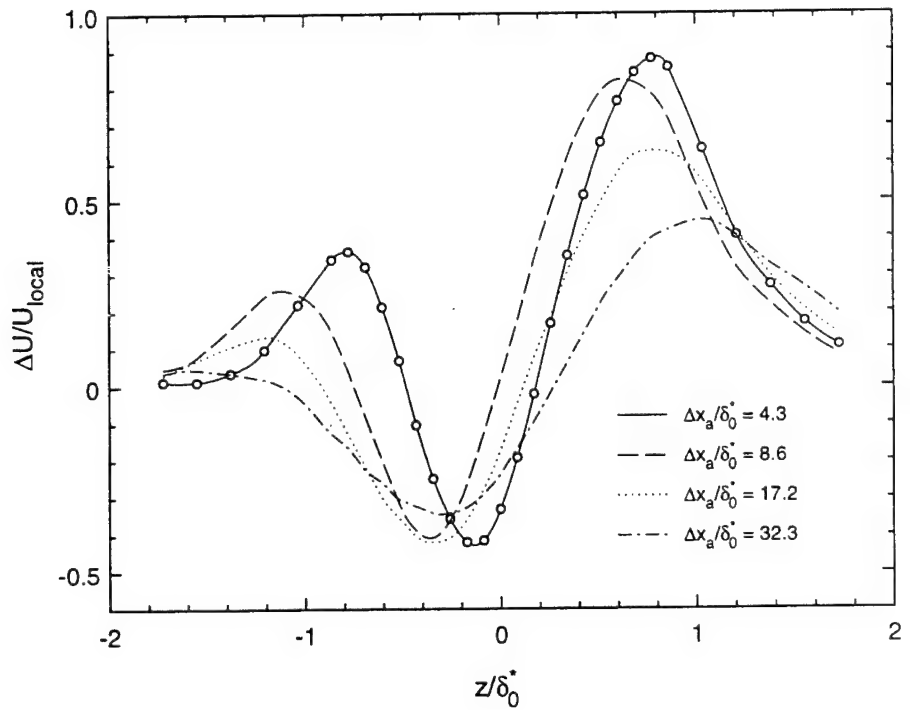


Figure 4.29: Spanwise velocity profiles at  $y = 0.5$  mm for different streamwise locations. Data are for a batch B actuator. Actuator drive amplitude  $A = 0.9$ .

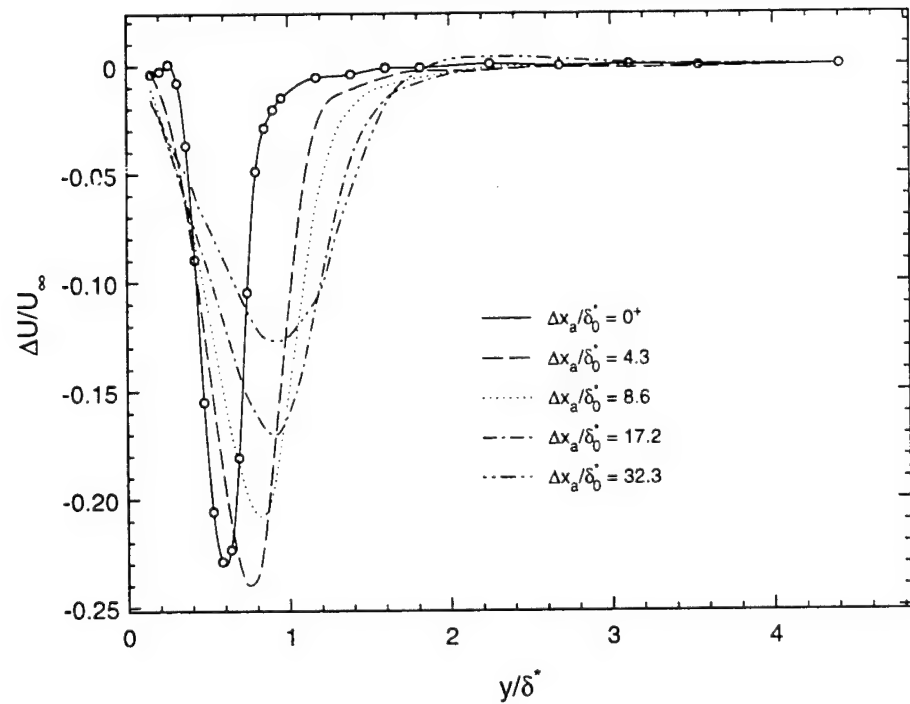


Figure 4.30: Wall-normal disturbance profiles over narrow gap for different streamwise locations. Actuator drive amplitude  $A = 0.9$ .

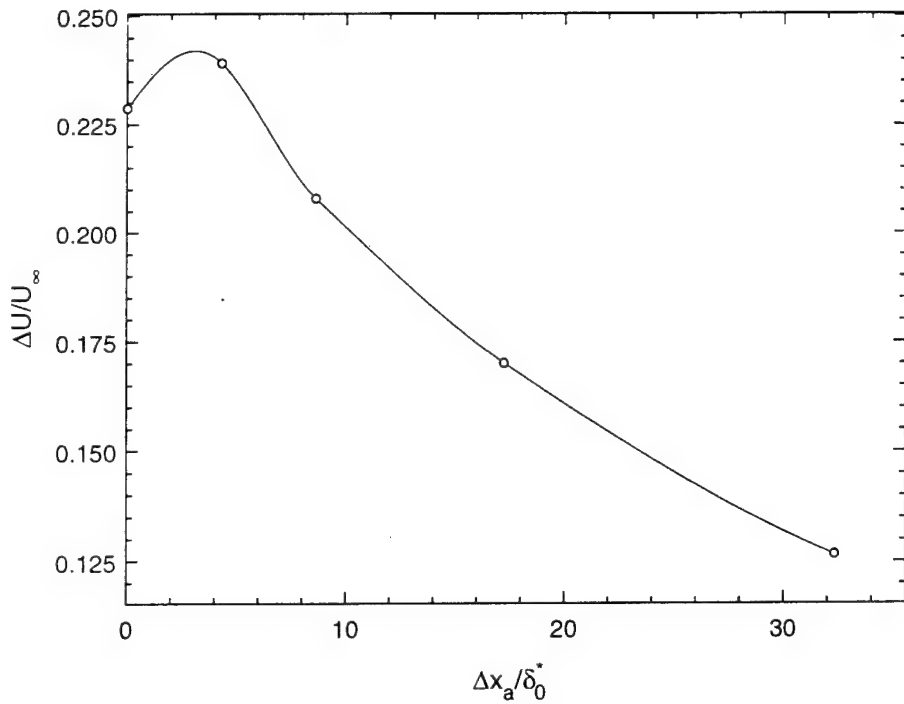


Figure 4.31: Streamwise evolution of peak disturbance amplitude. Actuator drive amplitude  $A = 0.9$ .

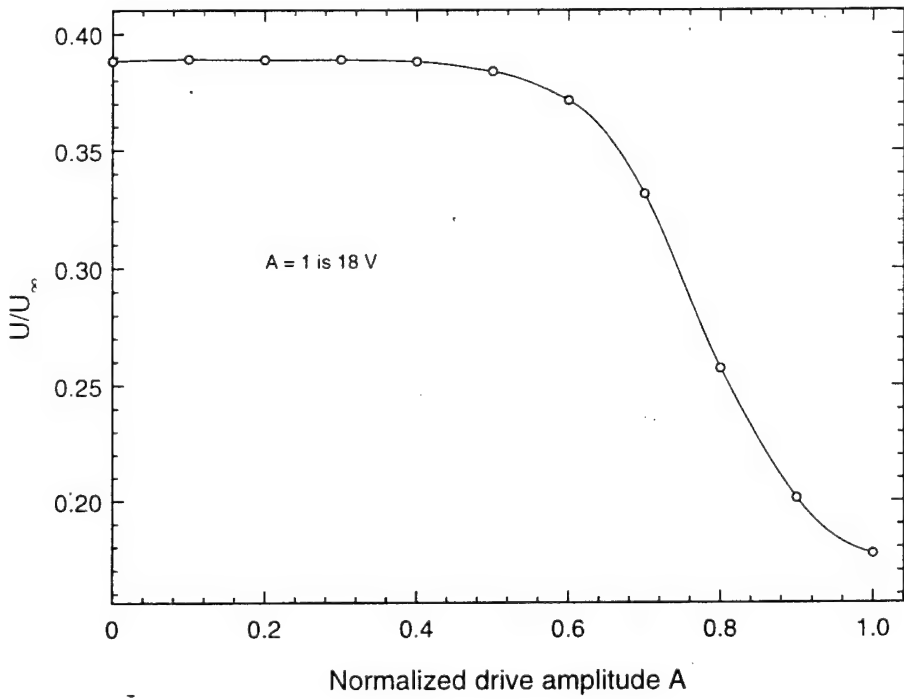


Figure 4.32: Amplitude control of maximum perturbation over narrow gap ( $\Delta x_a/\delta^* = 0^+$ ,  $y/\delta^* = 0.64$ ).

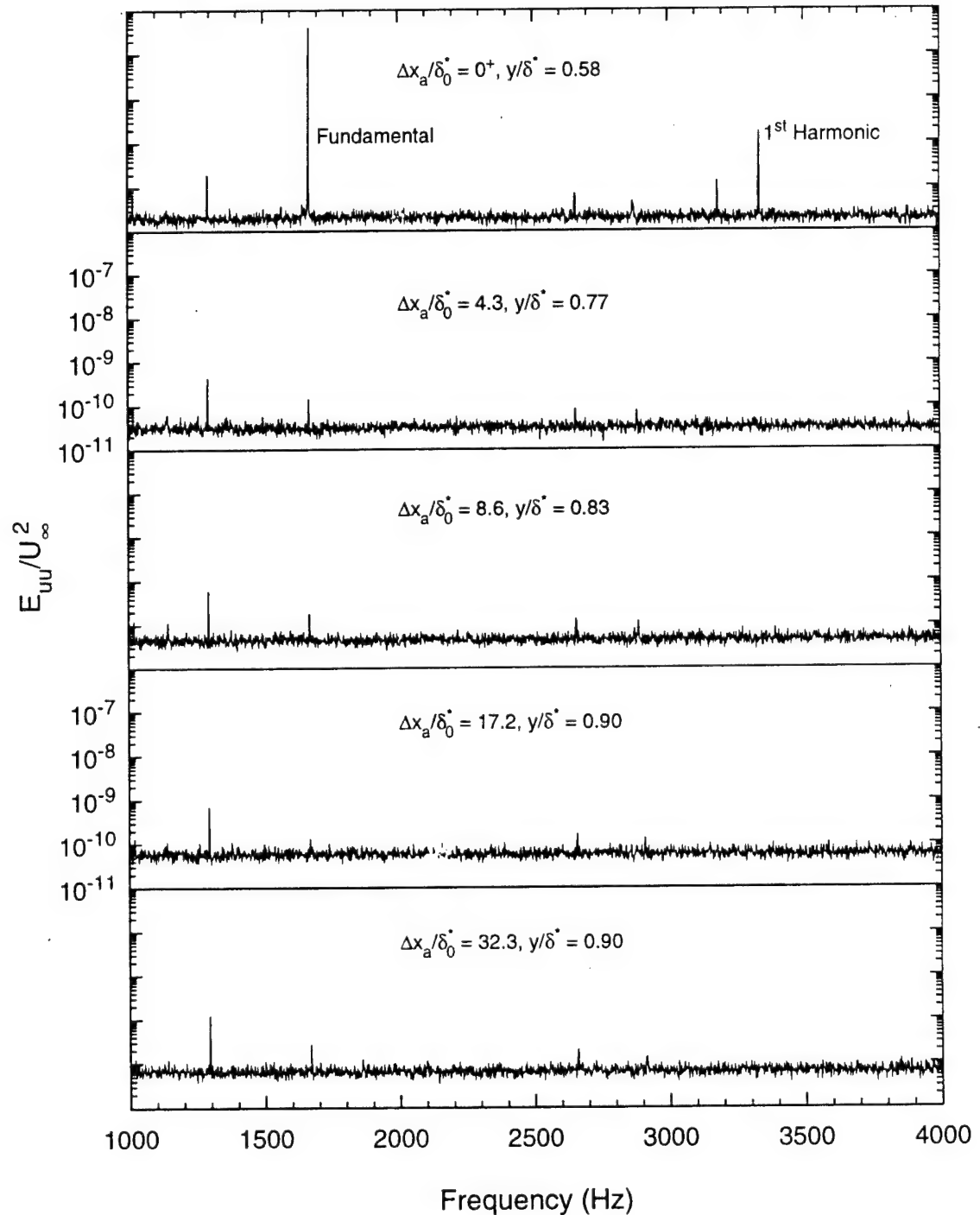


Figure 4.33: Power spectra of velocity disturbance over the narrow gap.

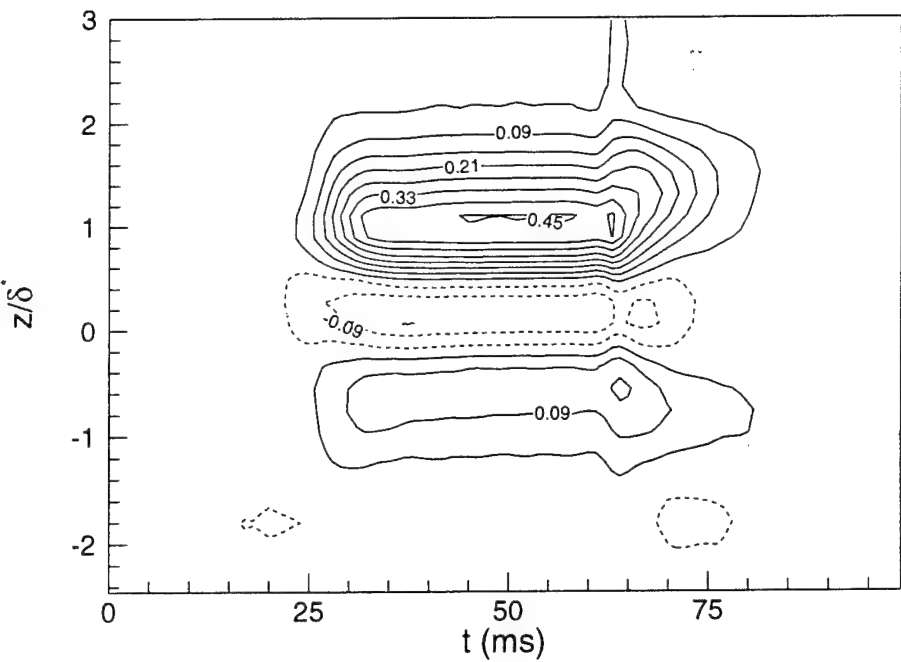


Figure 4.34: Contours of  $\Delta\tau/\tau_{ref}$  measured by sensor array at  $U_\infty = 5$  m/s. Contours are in increments of 0.06  $\tau_{ref}$ . Negative contours are indicated by dotted lines. Data are for a batch B actuator.

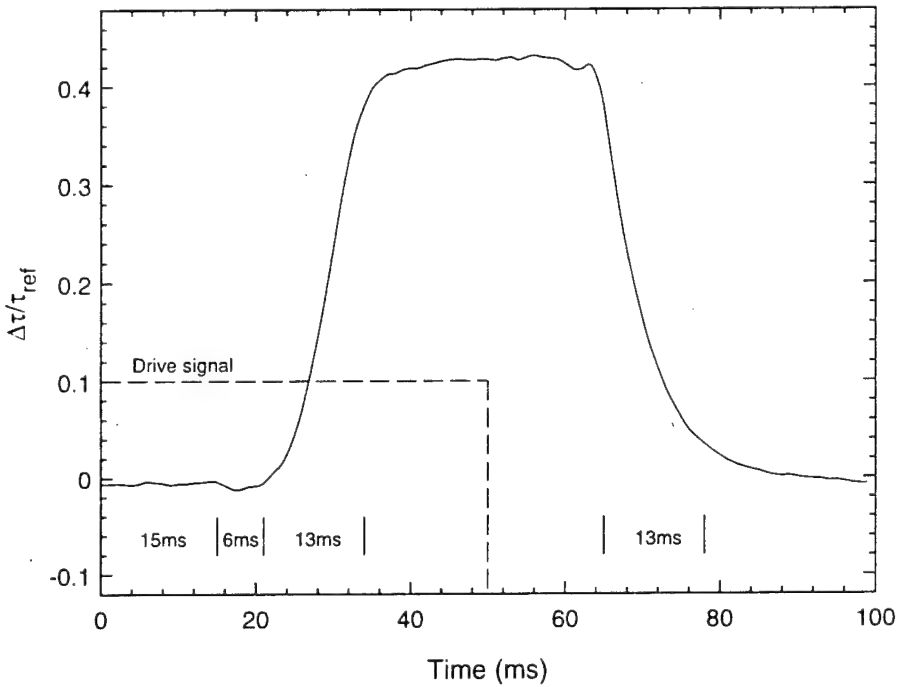


Figure 4.35: Time resolved  $\Delta\tau/\tau_{ref}$  at  $U_\infty = 5$  m/s. The plot is a cross-section through the positive contours of Fig. 4.34. Actuator drive amplitude  $A = 0.9$ .

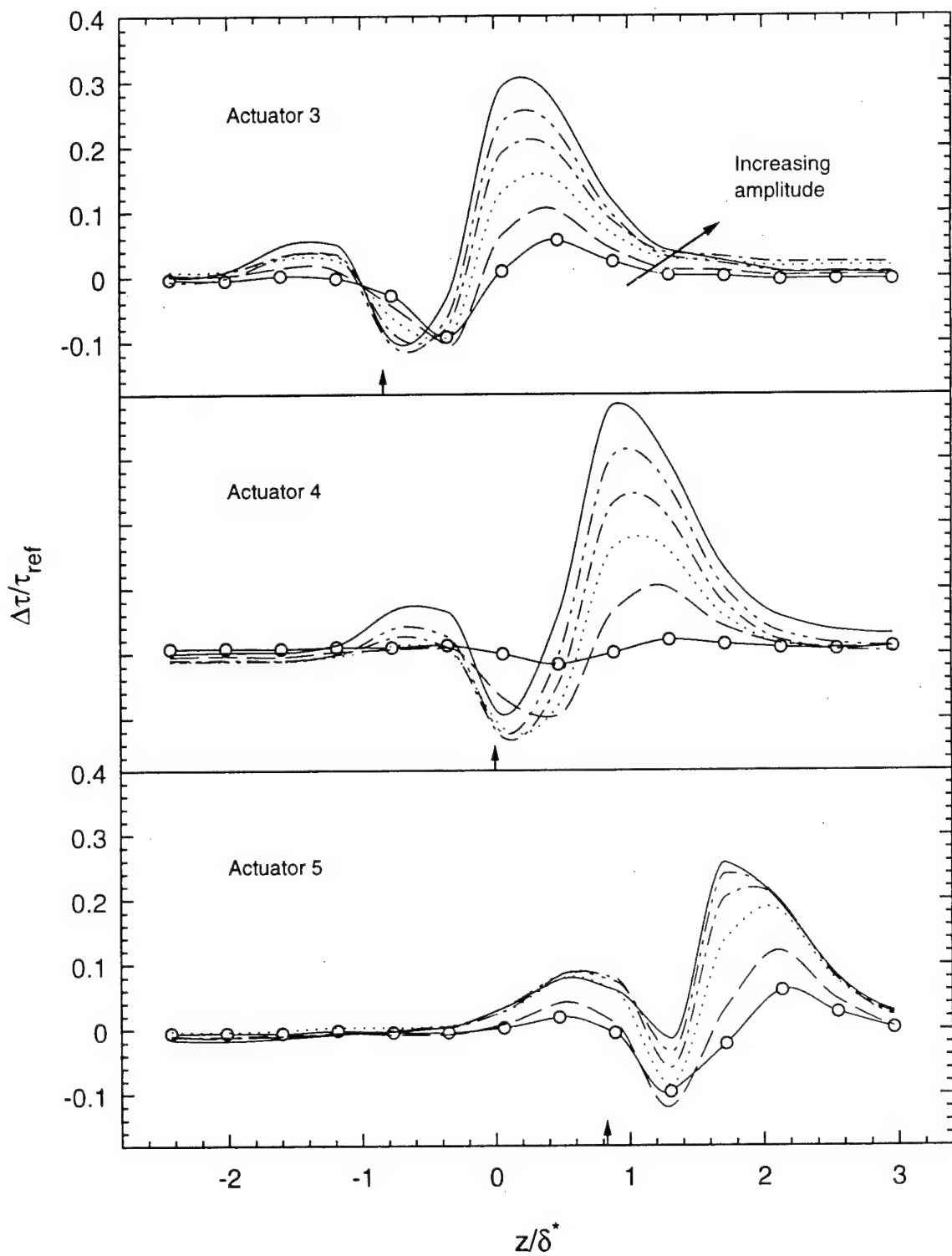


Figure 4.36: Shear stress perturbations introduced by actuators in a laminar boundary layer as measured by sensor array. The amplitude was changed from  $A = 0.5$  to  $A = 1.0$  in steps of 0.1 (batch B actuator,  $\Delta x_a/\delta_0^* = 8.6$ ,  $U_\infty = 5$  m/s).

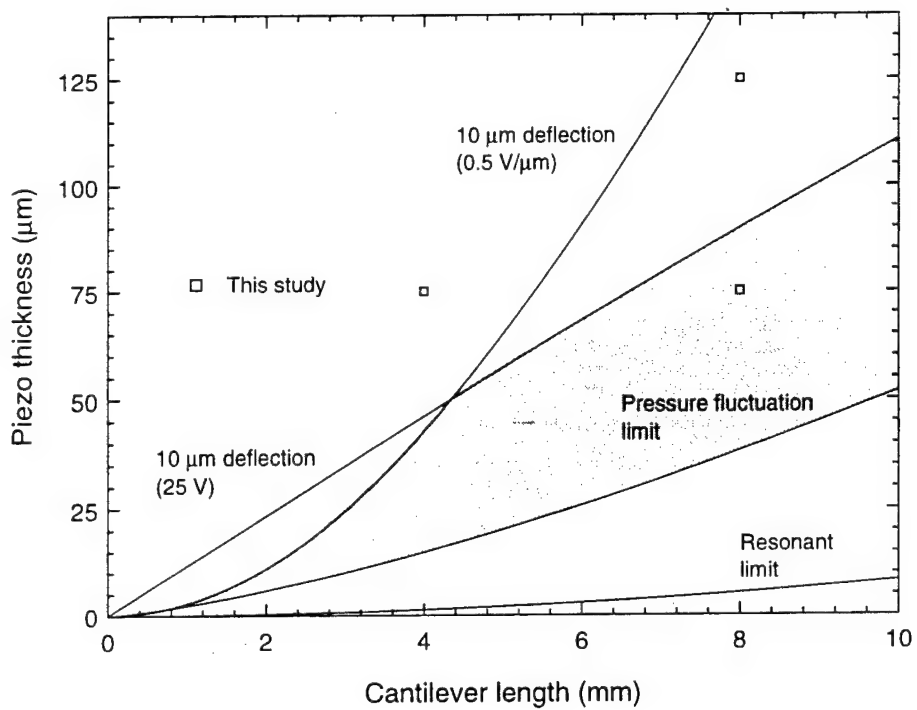


Figure 4.37: Design space for PZT-5A actuator in water at 0.5 m/s.

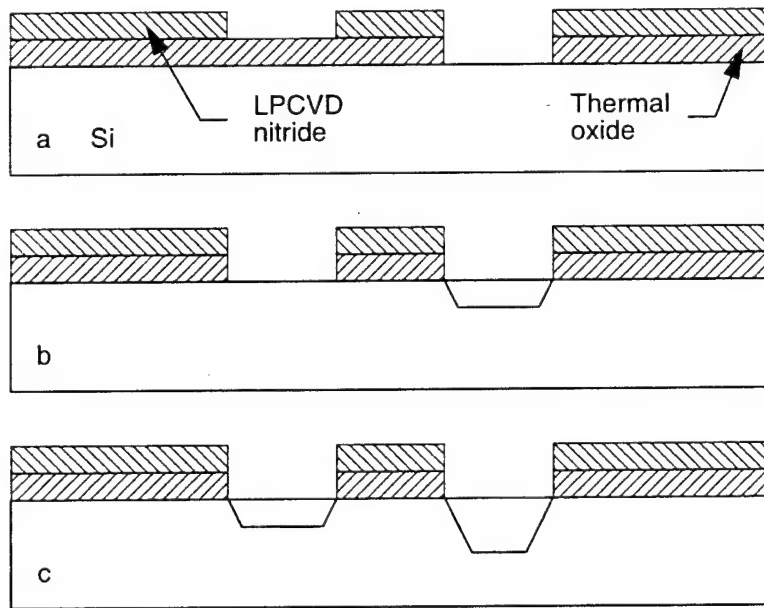


Figure 4.38: Technique for obtaining multiple etch depths.

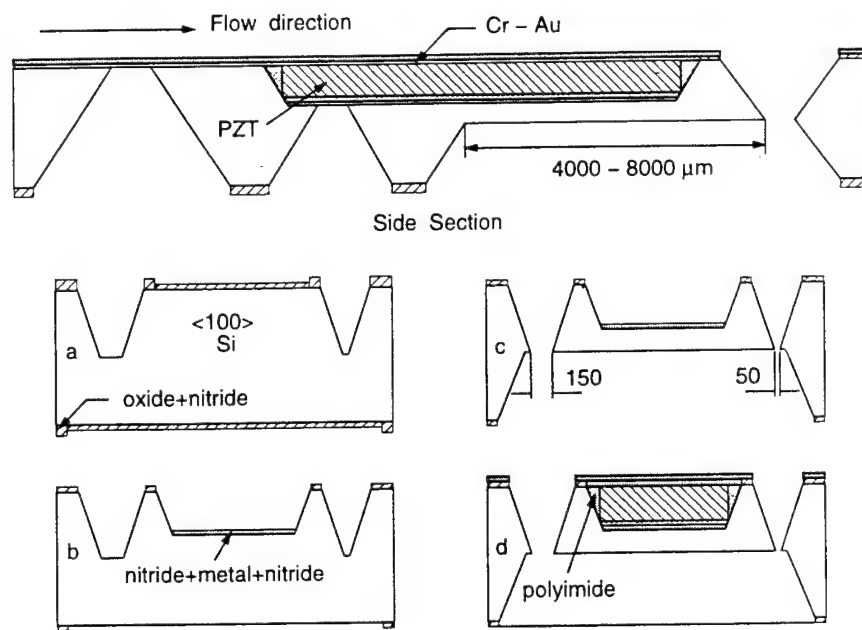


Figure 4.39: Side section and fabrication sequence of actuator designed for operation in water.

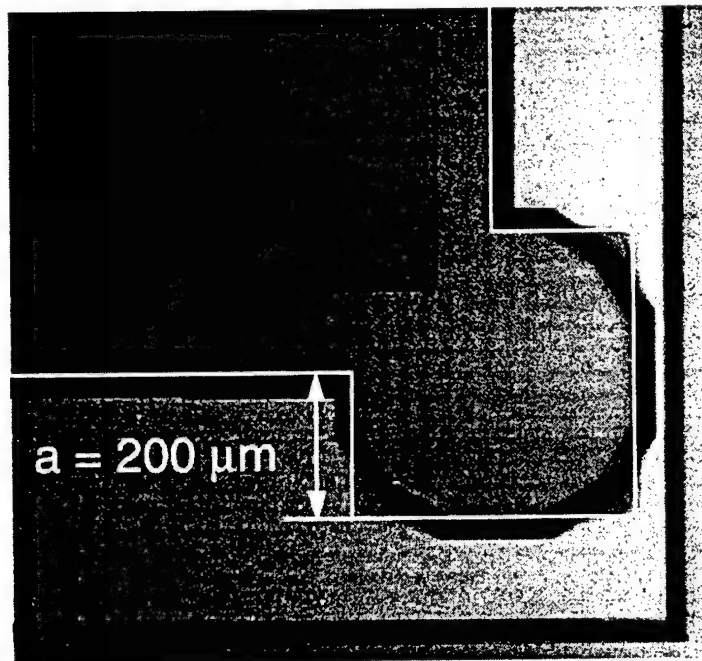


Figure 4.40: Details of convex corner compensation.

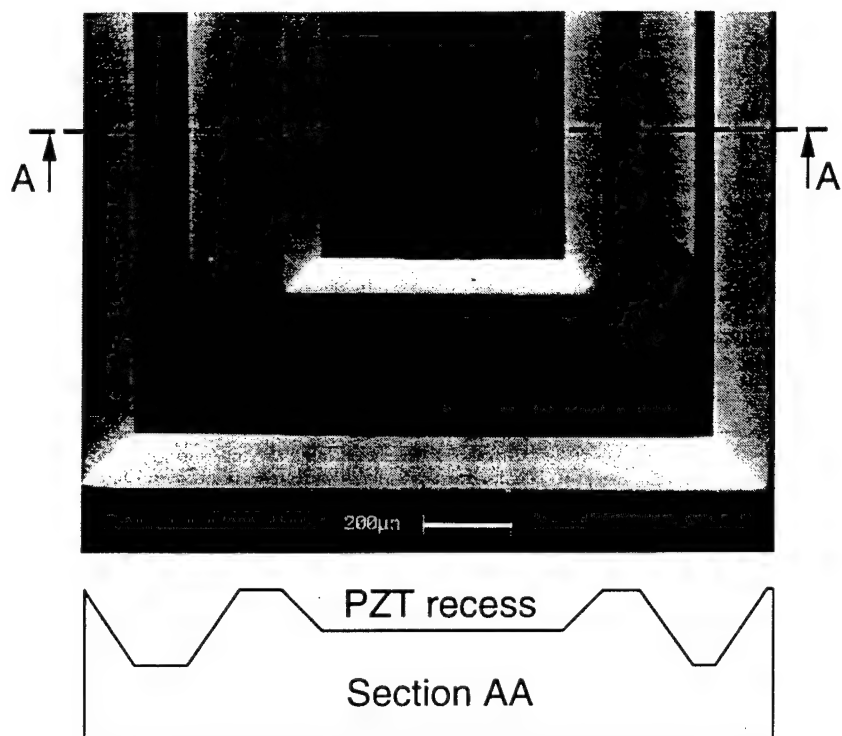


Figure 4.41: Tip of a single actuator designed for operation in water. For orientation, the surfaces with a lighter shade are {111} planes.

# Chapter 5

## Control of the Streamwise Vortex Pair Behind a Cylinder

### 5.1 Introduction

This chapter describes the use of the sensor and actuator arrays in a perturbed laminar boundary layer. Specifically, the system was used to control the streamwise vortex pair behind a cylinder. The objective of the control was to reduce both the drag and the spanwise standard deviation of the shear stress in the perturbed flow. All the experiments in this chapter were performed using batch B actuator arrays.

A schematic of the perturbed flow is shown in Fig. 5.1. The cylinder is introduced at an angle of  $90^\circ$  into the boundary layer of the crossflow. The incoming vortex tubes wrap around the cylinder and are stretched by the flow in the streamwise direction. This results in a pair of counter-rotating vortices with common flow towards the wall. In the downsweep region, the vortices bring high momentum fluid towards the wall and this results in the formation of a high-speed streak. Similarly, low-speed streaks are generated in the upsweep region. This is qualitatively similar to the flow close to the wall in a turbulent boundary layer. One major difference is that the size of the vortices downstream of the cylinder scale with the thickness of the boundary layer rather than being confined to the near-wall region. Nevertheless, considerable insight can be gained from studying the performance of the actuators in this ‘clean’ test flow where results are not contaminated by background turbulence.

A schematic of the experimental setup for the control experiments is shown in Fig. 5.2. A 1.6 mm diameter cylinder was inserted into the boundary layer 25 diameters upstream of the actuator array. The centers of the cylinder and actuator 4 were aligned with each

other. The sensor array was located 12.5 cylinder diameters downstream of the actuator array. The coordinates  $\Delta x_c$  and  $\Delta x_a$  represent distances downstream of the cylinder and the actuator tip respectively. In the discussion that follows, actuator 4 is called the center actuator and actuators 3 and 5 are the left and right actuators respectively.

At 3 m/s, the Reynolds numbers  $Re_x$  and  $Re_{\delta^*}$  are 114,000 and 580 respectively. This matches the flow conditions in the work of JR. The cylinder diameter was chosen instead of the displacement thickness for normalizing the spanwise coordinate. This makes it easier to compare results at different tunnel velocities that have slightly different displacement thicknesses. All wall shear stress data in this chapter are presented normalized by a reference shear stress  $\tau_{ref}$ . The reference shear stress was determined using a hot-wire placed at  $y = 1$  mm, as in Section 3.6.

## 5.2 Evaluation of the Cylinder Disturbance

Figure 5.3 shows the shear stress distribution behind the cylinder at four different insertion depths. The sensor array was calibrated in unsteady mode; this gives results that are closer to the true values as explained in Appendix D. When the insertion depth is increased from 5 to 10 mm, the perturbation strength increases dramatically. The ratio of the cylinder diameter to the displacement thickness  $d/\delta^*$  is 0.66 at  $U_\infty = 5$  m/s, so the cylinder extends through the (unperturbed) boundary layer for  $l/d > 4.4$ . Further increase in the penetration depth causes the peak value of the disturbance to drop but is accompanied by an increase in the shear stress over the entire span. The picture becomes clear when the rms values of the shear stress are examined. Both the peak rms values and the rms level over the span increase as the insertion depth is increased. This indicates that the flow is in the process of transitioning as will also be shown in Fig. 5.5. The insertion depth  $l/d = 6.3$  was chosen to get the benefits of a strong perturbation without the complicating effects of a transitioning flow. The rest of the results in this chapter are for this insertion depth.

Figure 5.4 shows the cylinder disturbances close to the wall for two different flow speeds. The hot-wire is in the linear region of the velocity profile and so the ordinate can also be interpreted as a change in the wall shear stress. The cylinder perturbation is symmetric about the centerline. The extent of the positive perturbation is about two cylinder diameters on either side of the centerline. The positive perturbation peak is at the cylinder centerline, which is aligned with the downsweep of the streamwise vortex pair. The maximum shear stress increases for  $U_\infty = 3$  m/s and 5 m/s are about 200% and 250% respectively. Thus, the perturbations created by the cylinder are strong, finite amplitude and three dimensional.

Spectra in the boundary layer behind the cylinder are presented in Fig. 5.5. The flow

has started transitioning even for a free-stream velocity of 3 m/s. The transition process is well on its way for  $U_\infty = 5$  m/s as seen by the increased energy at higher frequencies (and therefore higher wavenumbers). There are some peaks at sub-harmonics of the shedding frequency. Noise peaks at harmonics of 60 Hz are also seen in the 3 m/s case. Most of the following results are for  $U_\infty = 3$  m/s, in keeping with the philosophy of evaluating the transducers in a perturbed boundary layer that is still largely laminar.

Figure 5.6 shows contours of the mean velocity in a spanwise plane 38 diameters downstream of the cylinder centerline. The contours were generated from a 27 x 26 grid of data, spaced non-uniformly in both the spanwise and wall-normal direction for maximum resolution. The disturbance is nearly symmetric and the pattern is consistent with that produced by a single pair of counter-rotating vortices with common flow towards the wall. A wake region is also seen behind the cylinder in the free stream, for  $y/\delta^* > 3$ . Representative mean and rms profiles in the spanwise and wall-normal directions are presented in Figs. 5.7 and 5.8. The spanwise profiles show that the cylinder creates positive and negative perturbations that are about 30% and 10% of the free-stream velocity respectively. The rms value of the velocity fluctuations in the wake is uniform and is about 5% of the free-stream velocity. Closer to the wall,  $u_{rms}$  shows the beginning of a bimodal distribution (see also Fig. 5.15(a)). The wall-normal profiles are fuller in the downsweep region, leading to an increase in the wall gradient and hence the local shear stress. The maximum value of  $u_{rms}/U_\infty$  is about 0.07 and is located in the wake at  $y/\delta^* \approx 4$ . This is likely due to separation from the top of the cylinder, which is located at  $y/\delta^* = 3.4$ .

### 5.3 System Identification Using Sensor Array

Figures 5.9 and 5.10 show the effect of actuators 3–5 on the cylinder disturbance at  $U_\infty = 3$  m/s and 5 m/s respectively. Only three actuators were used as they cover the spanwise extent of the cylinder disturbance. The data were generated by forcing one actuator at a time with all the other actuators turned off. The ordinate  $(\tau_{ctrl} - \tau_{cyl})/\tau_{ref}$  is the normalized change in the shear stress caused by the actuators. Here  $\tau_{ctrl}$  is the shear stress with the actuators on and  $\tau_{cyl}$  is the shear stress with only the cylinder in the flow. The sensor array was calibrated in quasi-steady mode for this section. This allows multiple runs to be performed without worrying about drift, but results in a considerable underprediction of the peak perturbation magnitudes. The data can be used for control purposes without difficulty as long as the sensors are used to evaluate the effectiveness of the different control runs.

Several interesting observations become apparent on comparing the effect of the actuators at the two free-stream velocities. The perturbation strength introduced by the actuators increases with the amplitude of the control voltage. The center actuator that is aligned with the cylinder is most effective in counteracting the cylinder disturbance (note the different y-axis scales for the 3 actuators). The decrease in the shear stress in the upsweep region of the control vortices tends to saturate at higher amplitudes, while the increase in the downsweep region continues to increase. This implies that the optimal control amplitude will be less than the maximum amplitude. The actuators thus have sufficient control authority for controlling the shear stress distribution. Actuators 3 and 5 actually tend to increase the spanwise averaged shear stress, especially at higher amplitudes. It should be noted that actuator 3 and 5 are not symmetric about the cylinder centerline. Actuator 3 has its wide gap closer to the centerline while actuator 5 has its narrow gap closer to the centerline (see Fig. 5.2). This along with slight misalignments with the cylinder and minor differences in fabrication leads to the observed difference in their effectiveness.

The actuators are more effective at reducing the shear stress for the lower free-stream velocity case. It should be noted that the reference shear stress for the unperturbed boundary layer with  $U_\infty = 5 \text{ m/s}$  is twice that for the boundary layer with  $U_\infty = 3 \text{ m/s}$ . Thus, the perturbation created by the actuators is able to penetrate to a smaller extent into the boundary layer for the higher velocity case. The cylinder disturbance strength for the 5 m/s case is also about 25% greater than the 3 m/s case as shown in Fig. 5.4. A combination of these two factors makes the control less effective. The 5 m/s case is also quite sensitive to small misalignments between the actuators and the cylinder. This is most likely due to the meandering of the streamwise vortex pair behind the cylinder. The 5 m/s case was not pursued further for these reasons and the rest of the results in this chapter are for the 3 m/s case.

## 5.4 Control Strategy

The data in Figs. 5.9 and 5.10 were used to find ‘influence coefficients’ of the actuators on the wall shear stress. This was done by assuming that the relationship between the actuators amplitudes and  $\tau_{ctrl} - \tau_{cyl}$  is linear. This model approximates the behavior of the actuators but does not account for saturation effects. The model works because the effect of the actuators in the *perturbed flow* is approximately linear with actuator amplitude. Influence coefficients obtained by measuring the effect of the actuators in an unperturbed flow would not work. This is because linear superposition of the cylinder and actuator perturbations, both measured in an unperturbed flow, does not accurately describe the

cylinder/actuator interaction. The key is to linearize the effect of the actuators about the *perturbed* flow. The effect of the actuators is assembled into an influence matrix  $C_{ij}$ . The desired response is the inverse of the cylinder perturbation  $\Delta\tau_{des} = -(\tau_{cyl} - \tau_{base})$ . This requires that the actuators return the wall shear stress to the baseline undisturbed value. The optimal amplitudes are then determined by a least squares solution to the system  $CA = \Delta\tau_{des}$ , where  $A$  is now the vector of actuator amplitudes. The advantage of the linear model is that it provides a rational way for combining the effects of the different actuators. If the actuator amplitudes are greater than 1, they exceed the control authority of the actuators (this happens in the higher velocity case). The desired response is then scaled by a gain factor between 0 and 1 so that the maximum amplitude is 1. The procedure returns negative amplitudes for actuator 3 in all cases. The actuators developed here are capable of blowing only and not suction. This rectification of actuator output does not permit negative amplitudes. The reason for the negative amplitude is to assist actuator 4 in counteracting the maximum cylinder disturbance, as is seen from Fig. 5.9. The negative amplitude returned by the procedure was interpreted as a signal to remove the actuator from the optimization procedure. The procedure was repeated with the remaining two actuators and this returned physically realizable answers.

The least squares procedure gives a surprisingly good initial guess for the control amplitudes. This guess was further optimized by performing one-dimensional searches in amplitude space about the initial guess. The sensor array was used for monitoring the flow response. This allowed multiple candidates to be evaluated quickly. An example of such a one-dimensional search is shown in Fig. 5.11. The amplitude of the center actuator is fixed at 0.95 and that of the right actuator is increased from 0.5 to 0.75. The effect of the center actuator is partially cancelled by the right actuator. This results in a drop in the shear stress perturbation between  $z/d = 1$  and  $z/d = 3$ . However, as the vortices created by the center actuator are weakened, there is also an increase in the shear stress from  $z/d = -2$  to  $z/d = 0$ . Furthermore, the vortices generated by the right actuator also cause their own increase in shear stress for  $z/d > 3$ . The optimum control was determined by evaluating the decrease in the spanwise standard deviation of the wall shear. The standard deviation is much more sensitive to changes in amplitude than the mean shear stress and is therefore a better function to minimize. Reduction of the standard deviation also leads to a reduction in the mean shear stress, as has been found previously by JR. The minimum standard deviation was obtained with the right actuator at an amplitude of 0.7. The effect of the left actuator was also investigated about the optimum found by the one-dimensional search procedure. Turning on the left actuator reduced the control effectiveness in all cases. This is because the left actuator partially cancels the beneficial effects of the center actuator.

## 5.5 Control Performance

Figure 5.12 shows spanwise profiles for two optimal forcing situations (the hot-wire is in the linear region of the velocity profile). Both cases lead to a 18% reduction in the spanwise averaged shear stress  $\tau^z$  with a 68% reduction in the spanwise standard deviation  $\sigma^z$ . The lower amplitude forcing is preferred as it causes a smaller increase in the rms values of the velocity fluctuations. Wall-normal profiles at the cylinder centerline in Fig. 5.13 show that the control is effective to about one displacement thickness within the flow. The wall velocity gradient of the controlled profile is reduced but is still above baseline. The control does not affect the flow above  $y/\delta^* = 2$  and in particular leaves the wake behind the cylinder untouched. This is expected as the actuators were designed to affect the flow close to the wall only and are being used at ‘off design’ conditions to counteract a disturbance that extends through the entire boundary layer.

### 5.5.1 Spanwise Flow Maps

Figure 5.14 shows contours of the mean disturbance velocity with and without control. The spanwise plane is located just downstream of the sensor array. The contours were generated from a  $27 \times 15$  grid of data as in Fig. 5.6. The disturbance velocity was obtained by subtracting out the baseline velocity without the cylinder in the flow. The location of the positive peak is much closer to the wall than the location of the negative peaks ( $0.35 \delta^*$  compared to  $0.75 \delta^*$ ). Care must therefore be taken not to miss the positive peak in spanwise traverses and in interpreting hot-wire data as wall shear stress data as explained in Appendix D. When the optimal control is applied, the strength of the cylinder disturbance reduces considerably. The peak disturbance magnitude decreases by 47% from 32% to 17% of the free-stream velocity. The negative peak is also reduced for  $z/d > 2$ . The control does not result in a symmetric distribution about the centerline because of the asymmetry of the side actuators discussed earlier. Note that as actuator 3 is turned off, the cylinder disturbance is largely unaffected for  $z/d < -2$ . The contour plots of  $u_{rms}$  in Fig. 5.15(a) are nearly symmetric about the centerline and show a bimodal distribution associated with the streamwise vortex pair. The peak value of  $u_{rms}$  is about 4% of the free-stream velocity. It is located at a distance of one displacement thickness from the wall and is a good indicator of the center of the streamwise vortices. This also confirms that the vortices created by the cylinder scale with the boundary layer thickness. The actuators do not change  $u_{rms}$  significantly. The peaks at  $y/\delta^* = 1$  decrease slightly in magnitude. The rms velocity also increases slightly along the cylinder centerline above actuator 4. This is due to the control vortices introduced by that actuator.

### 5.5.2 Streamwise Evolution of Controlled Flow

The effect of the control was also measured at five streamwise locations downstream of the actuator. The difference between the control and the cylinder velocity field  $U_{ctrl} - U_{cyl}$  is shown in Figs. 5.16 and 5.17. The control produces both positive and negative perturbations in the spanwise direction to counter the effect of the cylinder. The effect of the control starts diminishing as the flow moves downstream. This is due to incomplete cancellation of the cylinder disturbance especially in the region  $1 < y/\delta^* < 2$ . The profiles in the wall-normal direction also show that the penetration of the control into the flow decreases with streamwise distance. The profile just downstream of the actuator tip has two peaks because of the inflection point in the velocity profile caused by the actuator, as shown in Fig. 4.27. The spanwise profile at  $\Delta x_a/\delta^* = 0.3$  (not shown) also has large gradients. The flow quickly readjusts and by  $\Delta x_a/\delta^* = 4$ , there is a single dominant peak. This has important implications in terms of the placement of downstream sensors for use either as control sensors or as a diagnostic. The distance between the actuators and the downstream sensors should be at least a couple of displacement thicknesses so as to allow the flow to readjust to the control. Sensors placed closer would either completely miss the effect of the actuators or would provide a misleading picture of the flow field. Similar conclusions were reached by JR in their experiments.

### 5.5.3 Figures of Merit

The net reduction in the shear stress is obtained by integrating the profiles of  $(U_{ctrl} - U_{cyl})/U_{local}$  across the span and is shown in Fig. 5.18. The peak reduction in the shear stress is 18% and this occurs at the location of the sensor array. This is also accompanied by a 68% reduction in the spanwise standard deviation of the shear stress. These numbers are about a factor of 2 better than those achieved in JR. There are two reasons for this difference. The actuators act on the cylinder disturbance considerably sooner than in JR, 25 diameters downstream as opposed to 41 diameters downstream. Secondly, two actuators were used as opposed to a single actuator in their case. For comparison, if only actuator 4 was run at its optimal amplitude of 0.8 (see Fig. 5.9), the standard deviation is reduced by 31%. A better figure of merit is the net reduction in the shear stress  $(U_{cyl} - U_{ctrl})^z$  normalized by the net increase caused by the cylinder  $(U_{cyl} - U_{base})^z$ , where the superscript  $z$  denotes spanwise averaged values. This figure of merit has a value of zero when no control is applied and would achieve a value of 1 if the control succeeded in returning the wall shear stress to the unperturbed baseline value. Thus  $(U_{cyl} - U_{ctrl})^z / (U_{cyl} - U_{base})^z$  can be interpreted as the reduction in the strength of the disturbance, *as measured by the wall*

*shear stress.* The maximum reduction is about 85% at the location of the sensor array. The reduction in the strength of the disturbance decreases as one moves downstream beyond the sensor array. The control is still effective 25 displacement thicknesses downstream of the actuator array with a reduction of 44% in the strength of the disturbance.

## 5.6 Conclusions

Actuator and sensor arrays were evaluated by controlling the streamwise vortex pair behind a cylinder in a laminar boundary layer. The sensors were used to optimize actuator amplitudes for reducing the drag in the perturbed flow. The strength of the disturbance, as measured by the wall shear stress, was reduced by 85% at the sensor array location. The effect of the control persisted greater than 25 displacement thicknesses downstream of the actuator array.

An array of sensors serves as an extremely useful diagnostic. The sensors average the shear stress over a shorter spanwise length as compared to hot-wires, and so give a better estimate of the local shear stress distribution. They also provide an immediate spanwise picture of the shear stress (as compared to traversing a hot-wire across the boundary layer). This allows multiple runs with different actuator amplitudes and is useful in optimizing control amplitudes. Algorithms developed using such sensors use wall information only and can therefore be implemented in a practical setting. It should be noted that the sensors provide only a limited amount of information about the flow and spanwise maps of the entire flow field are invaluable in understanding the details of the interaction between the disturbance created by the cylinder and the actuators. Attempts to draw conclusions based on sensor results only are likely to be incomplete and misleading.

Nonlinear effects in the flow make prediction of the effect of multiple actuators (running simultaneously) a difficult task. Extensive characterization is required to understand the interactions between adjacent actuators. Attempts have been made by other researchers to optimize actuator amplitudes using control heuristics like genetic searches and the simplex method. These methods are slow and are likely to have convergence problems in a real-time situation. The solution appears to be either to deploy actuators only one at a time or to design them so that their effects are largely independent of each other.

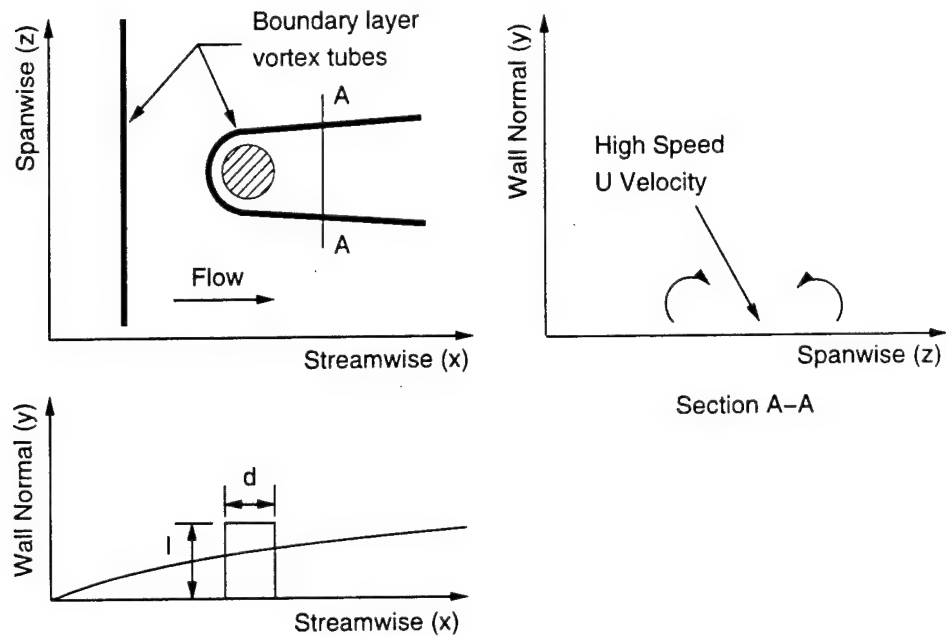


Figure 5.1: Schematic of flow behind a cylinder.

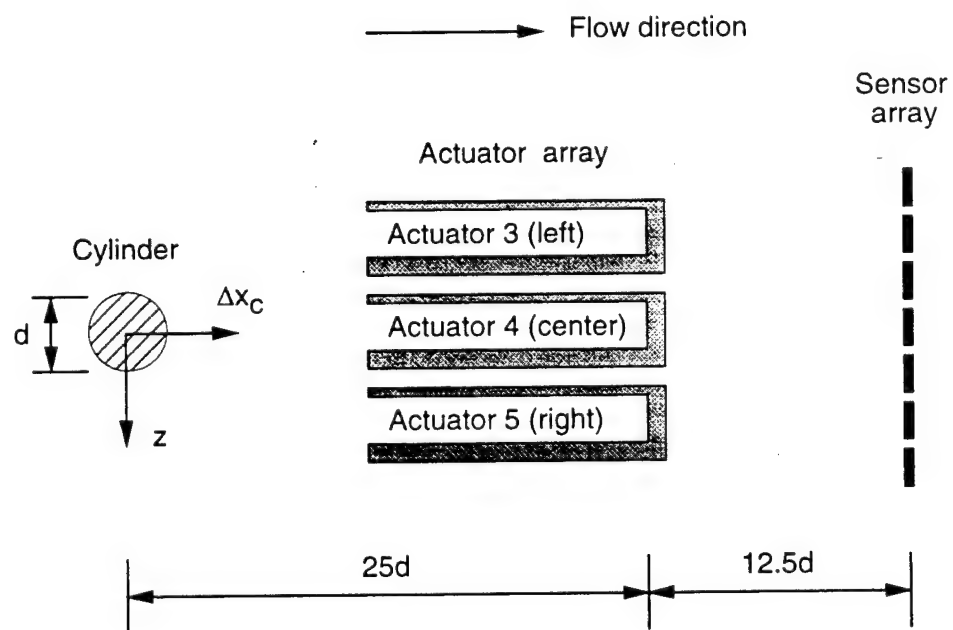
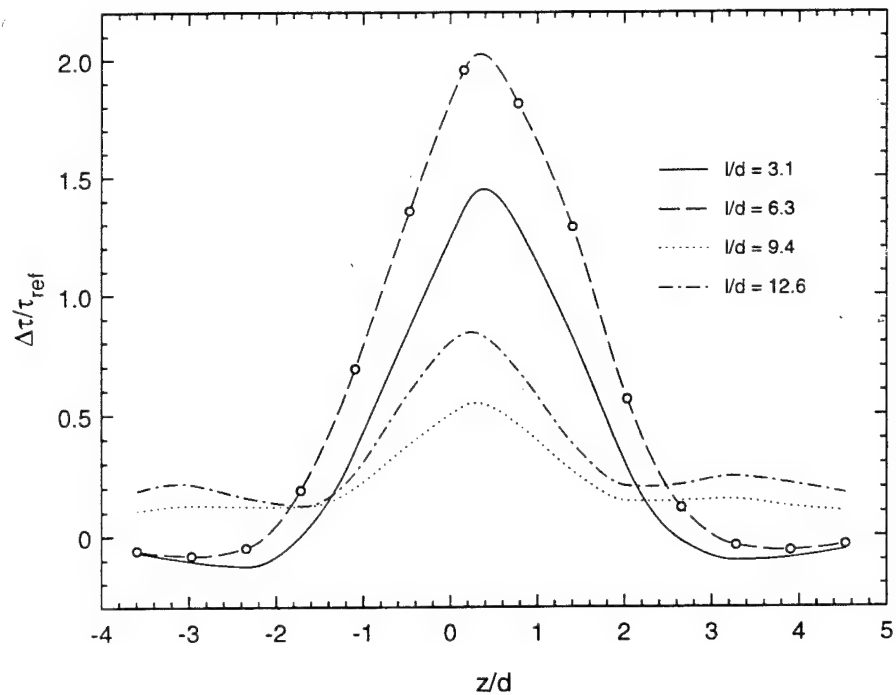
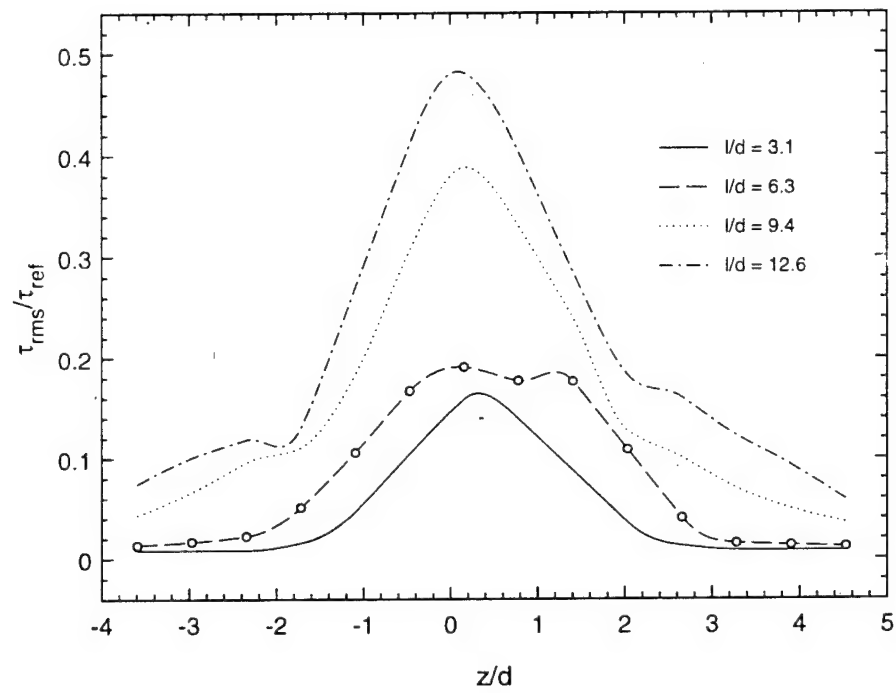


Figure 5.2: Schematic of control experiment setup showing locations of cylinder, actuator array, and sensor array.



(a) Mean profiles



(b) Rms profiles

Figure 5.3: Disturbance profiles behind cylinder at different insertion depths as measured by sensor array ( $\Delta x_c/d = 38$ ,  $U_\infty = 5$  m/s).

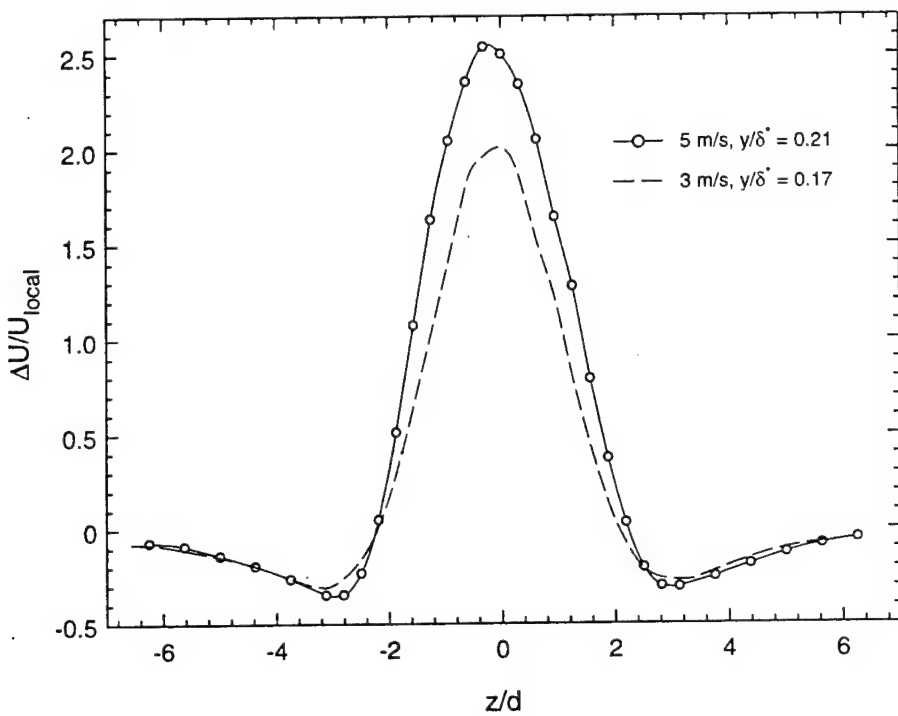


Figure 5.4: Disturbance profiles behind cylinder at two free-stream velocities as measured by a hot-wire ( $y = 0.5$  mm,  $\Delta x_c/d = 38$ ,  $z/d = 0$ ).

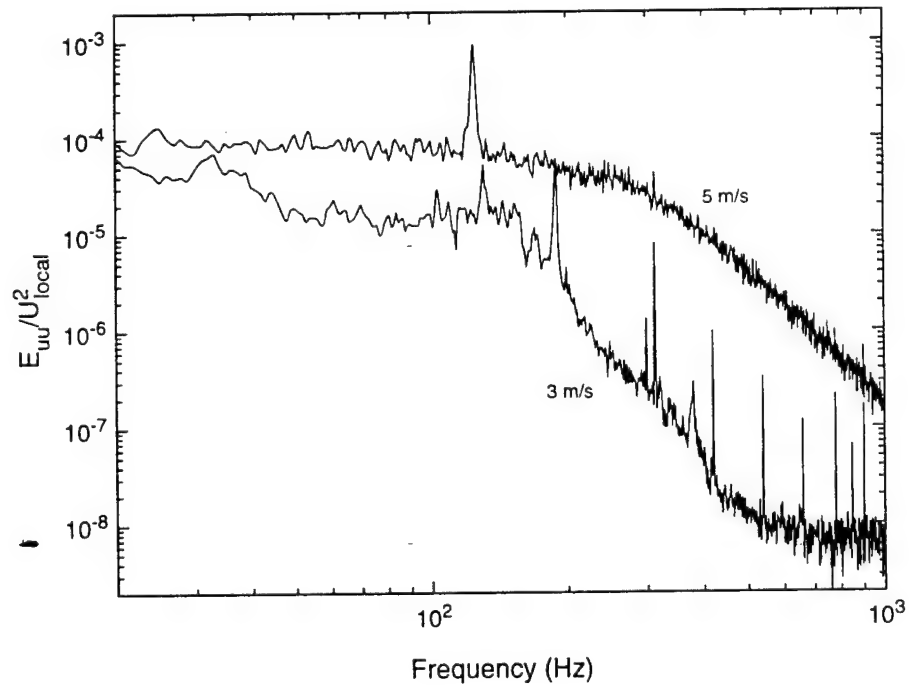


Figure 5.5: Power spectra in boundary layer behind cylinder at two free-stream velocities ( $y = 1$  mm,  $\Delta x_c/d = 38$ ,  $z/d = 0$ ).

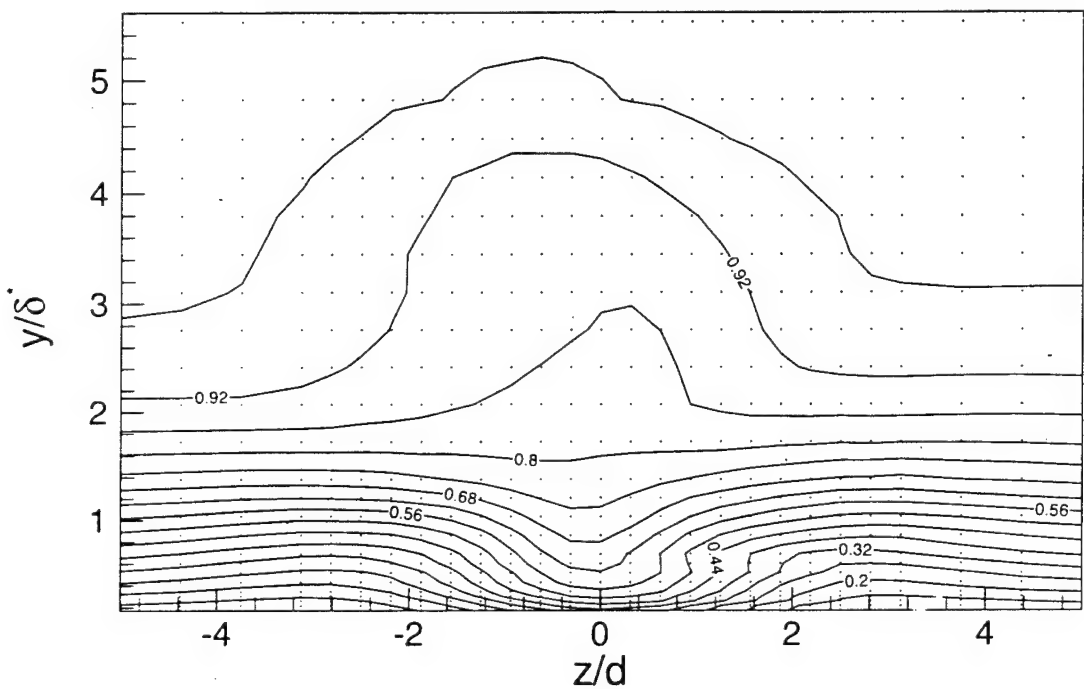
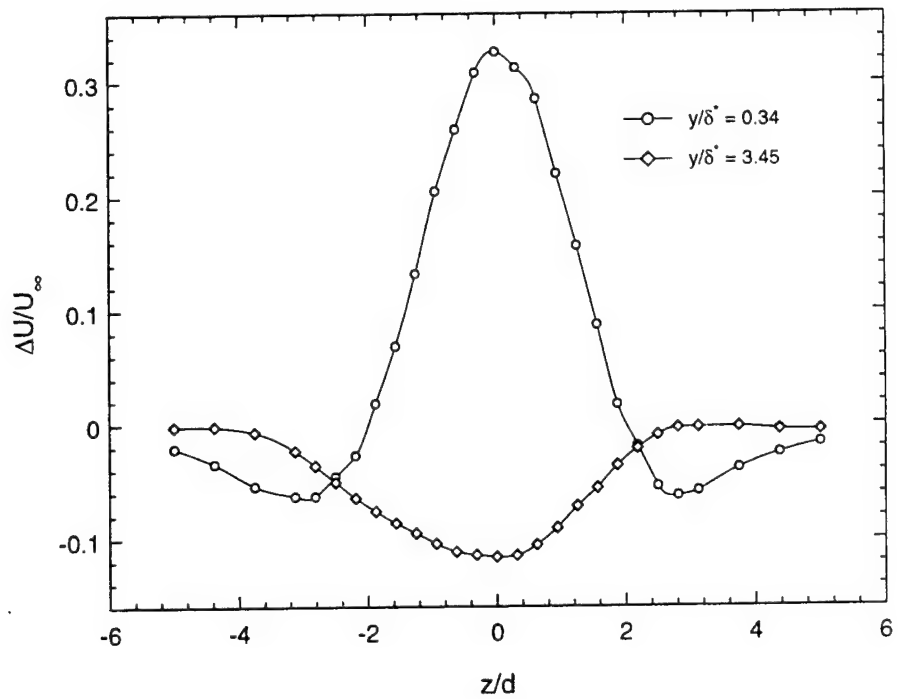
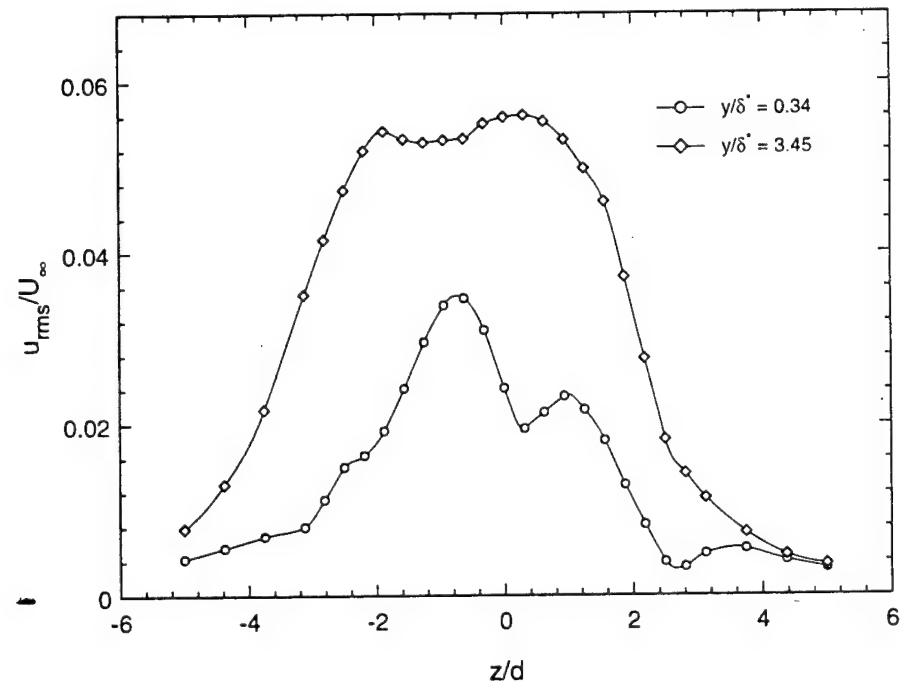


Figure 5.6: Contours of  $U/U_\infty$  behind cylinder ( $\Delta x_c/d = 38$ ,  $U_\infty = 3$  m/s). Contours are in increments of 0.06  $U_\infty$ . Data point locations are shown by dots.

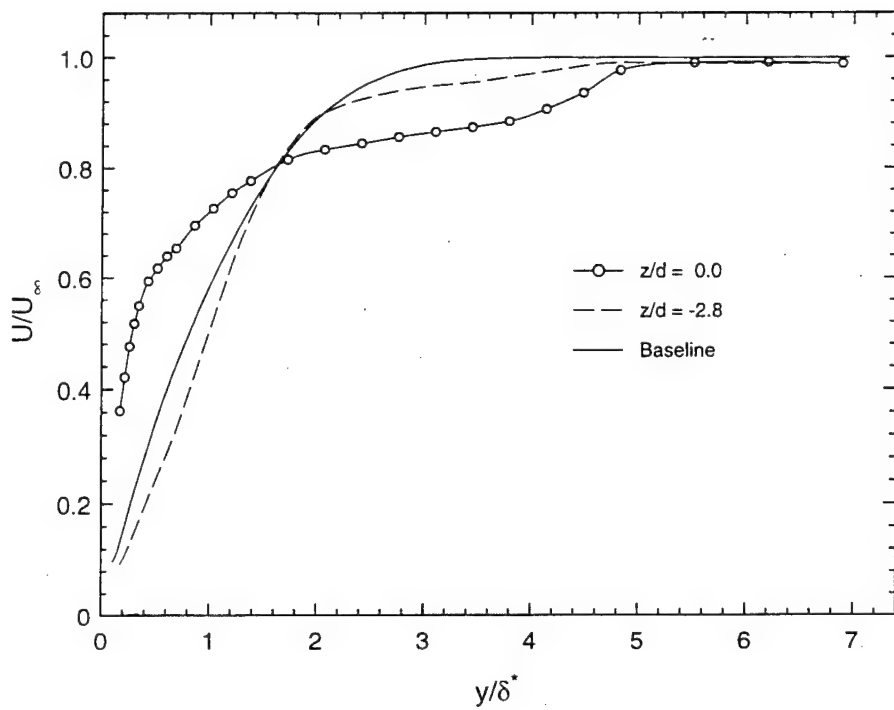


(a) Mean profiles

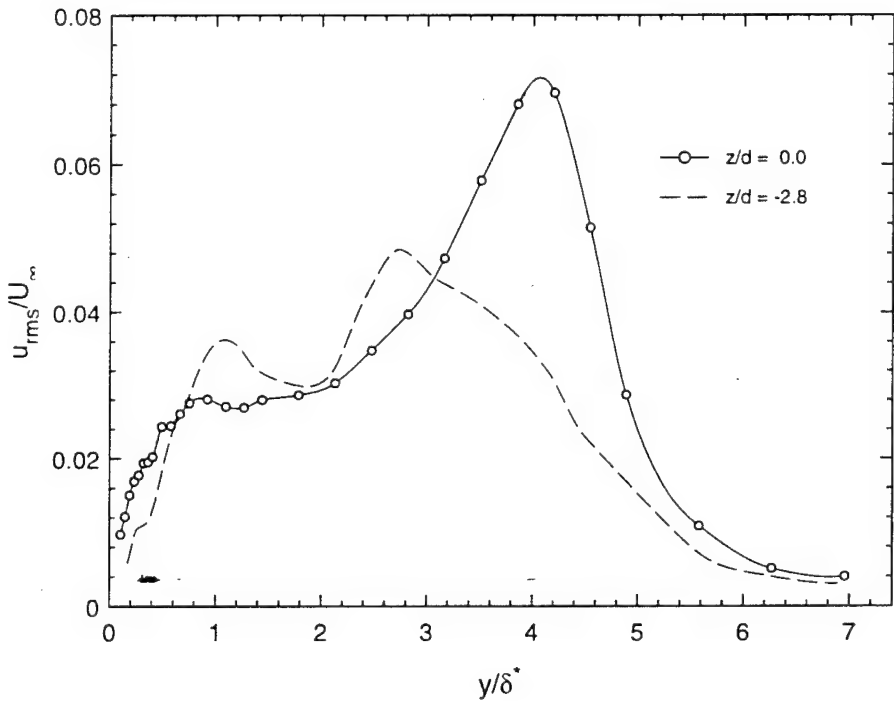


(b) Rms profiles

Figure 5.7: Spanwise disturbance profiles in boundary layer and wake behind cylinder ( $\Delta x_c/d = 38$ ,  $U_\infty = 3$  m/s).



(a) Mean profiles



(b) Rms profiles

Figure 5.8: Wall-normal velocity profiles in upsweep and downsweep regions behind cylinder ( $\Delta x_c/d = 38$ ,  $U_\infty = 3$  m/s).

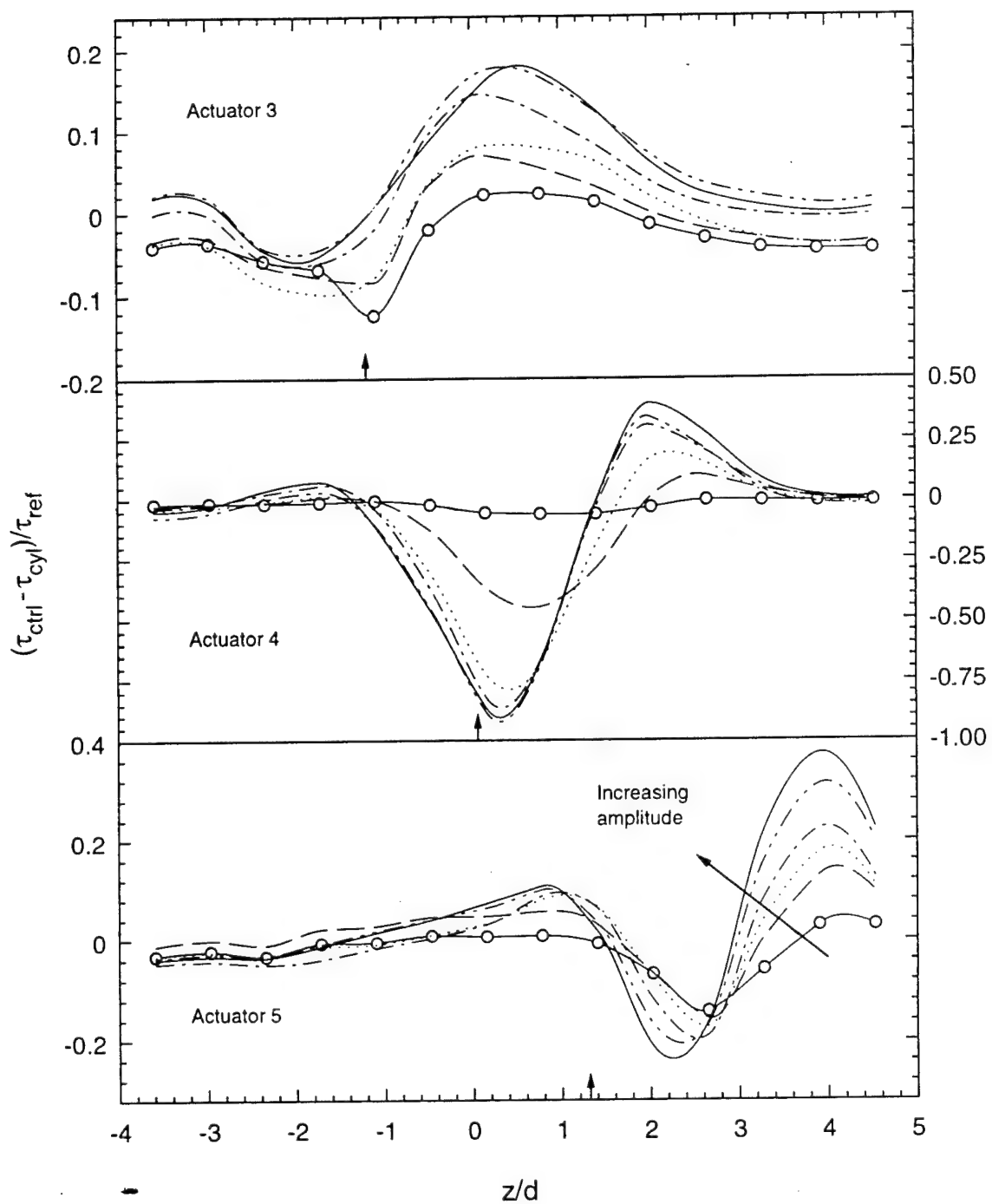


Figure 5.9: Effect of actuators on the disturbance created by the cylinder as measured by the shear-stress sensor array. The amplitude was changed from  $A = 0.5$  to  $A = 1.0$  in steps of 0.1. The arrows on the abscissa indicate the centerline of the corresponding actuators. ( $\Delta x_a/d = 12.5$ ,  $U_\infty = 3$  m/s).

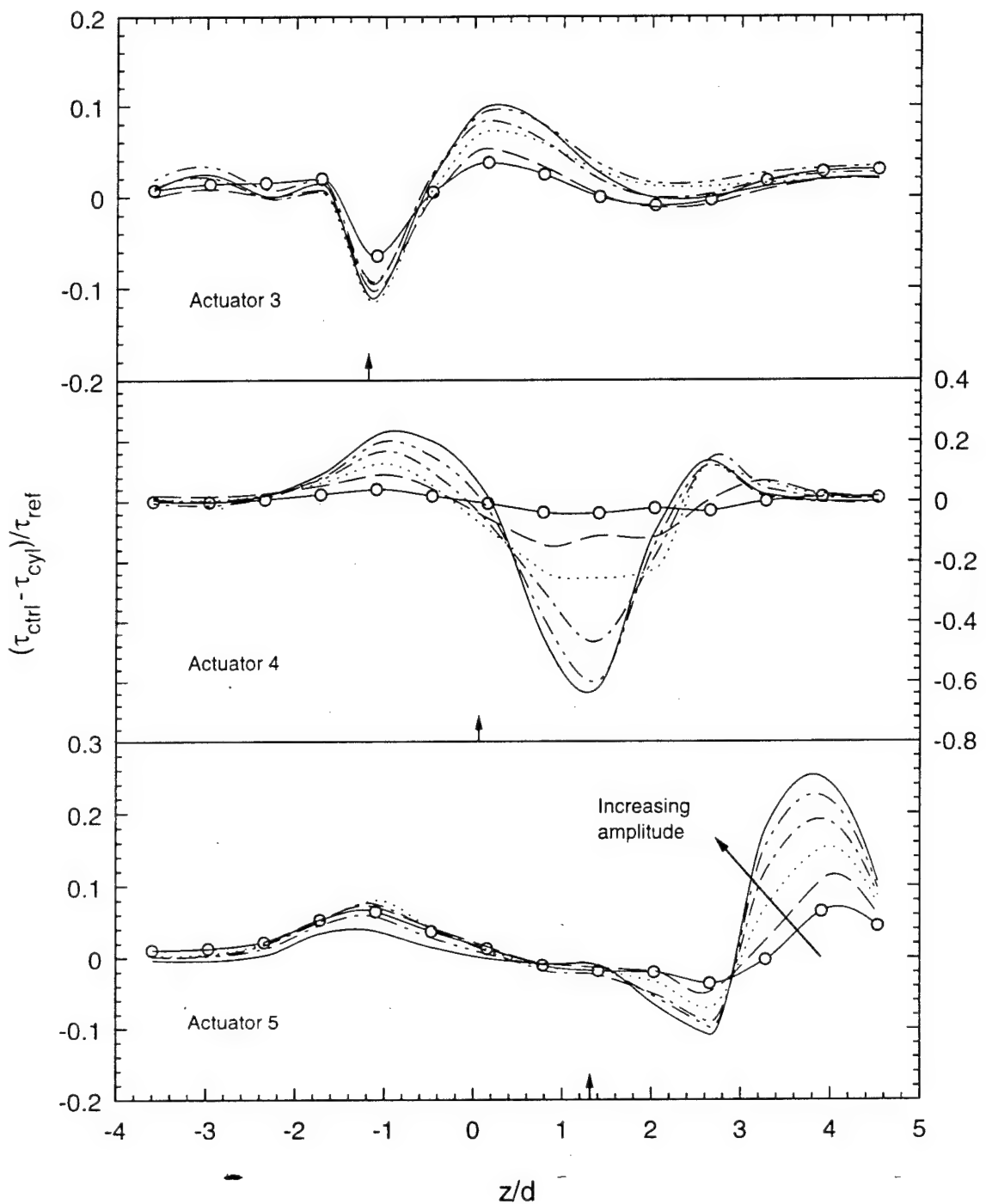


Figure 5.10: Effect of actuators on the disturbance created by the cylinder as measured by the shear-stress sensor array. The amplitude was changed from  $A = 0.5$  to  $A = 1.0$  in steps of 0.1. The arrows on the abscissa indicate the centerline of the corresponding actuators. ( $\Delta x_a/d = 12.5$ ,  $U_\infty = 5$  m/s).

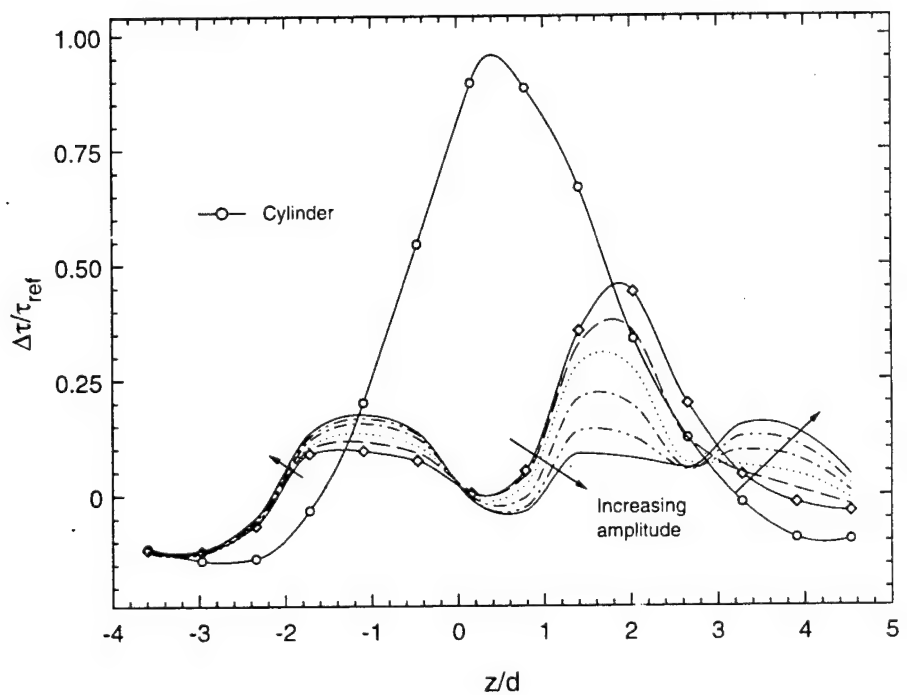


Figure 5.11: Example of optimization by one dimensional search about initial guess, data from sensor array ( $\Delta x_a/d = 12.5$ ,  $A_4 = 0.95$ ,  $A_5$  varied from 0.5 to 0.75 in steps of 0.05).

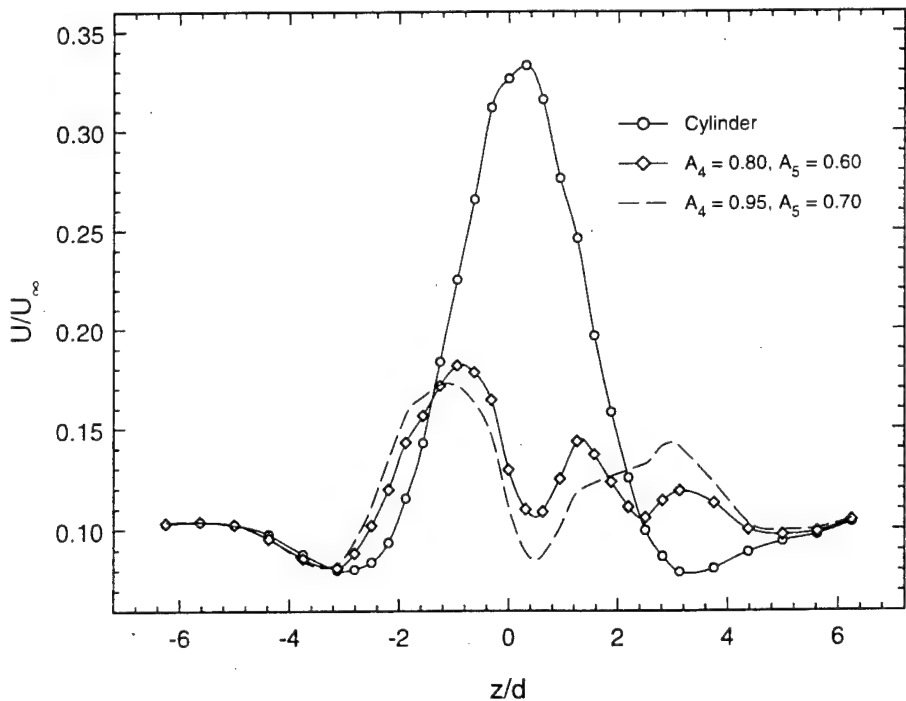


Figure 5.12: Spanwise velocity profiles in boundary layer behind cylinder with and without control ( $\Delta x_a/d = 13.1$ ,  $y/\delta^* = 0.17$ ).

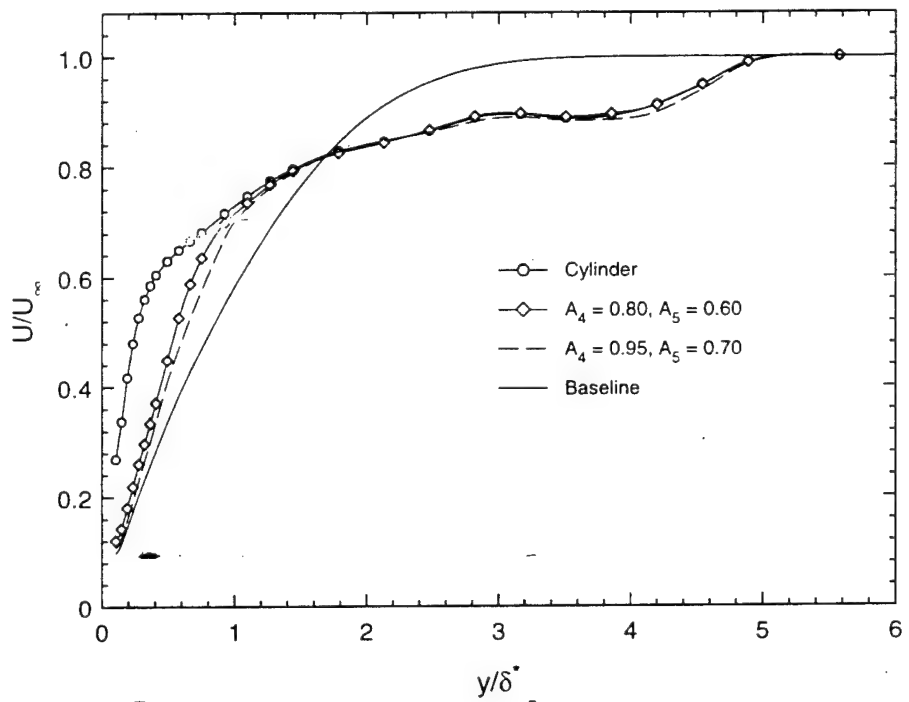
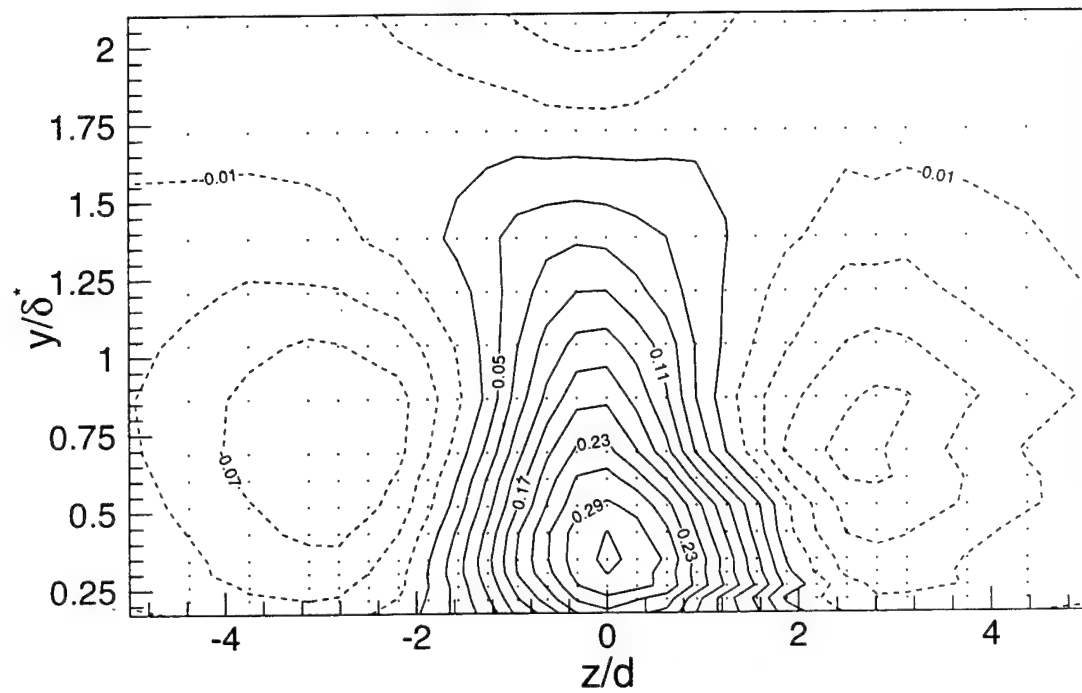
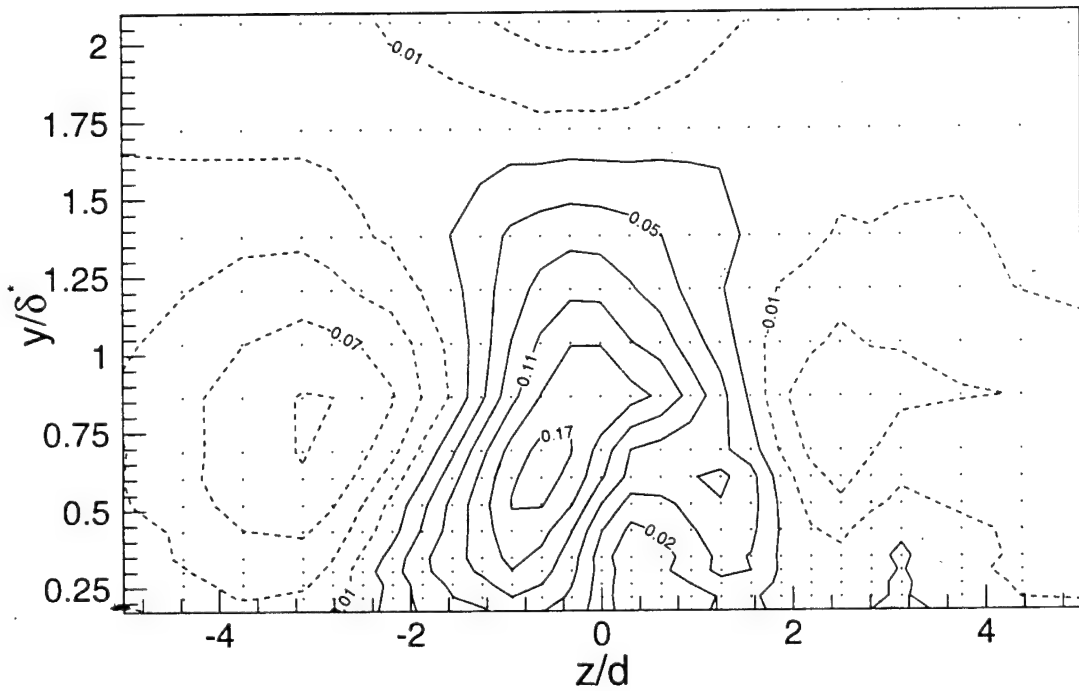


Figure 5.13: Wall-normal velocity profiles behind cylinder with and without control ( $\Delta x_a/d = 13.1$ ,  $z/d = 0.0$ ).

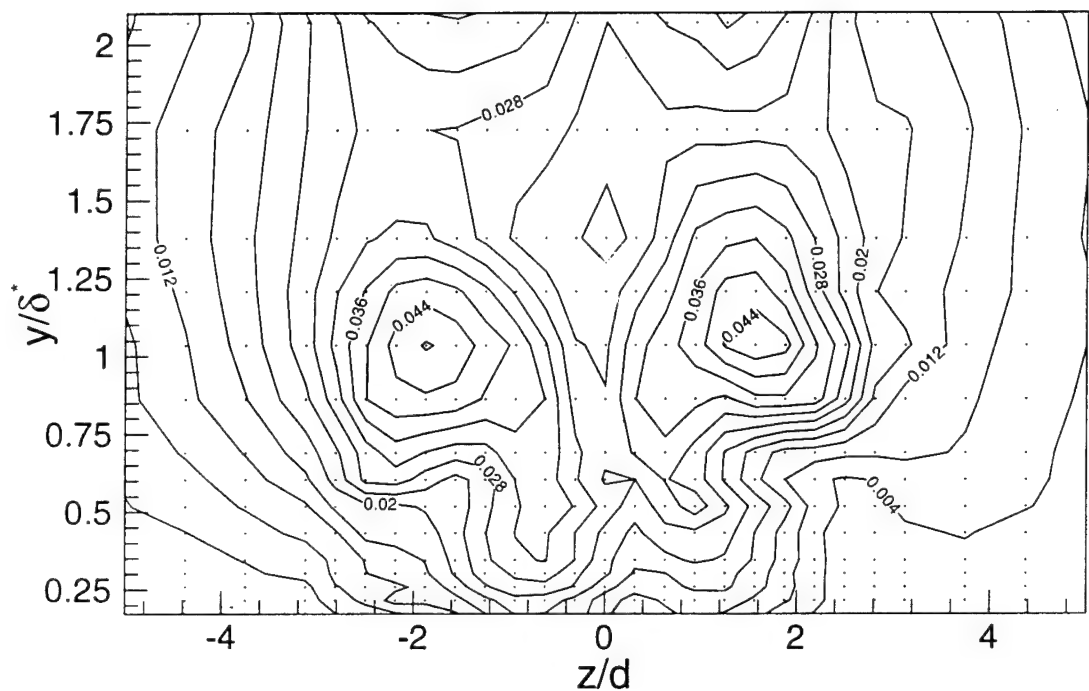


(a) Cylinder

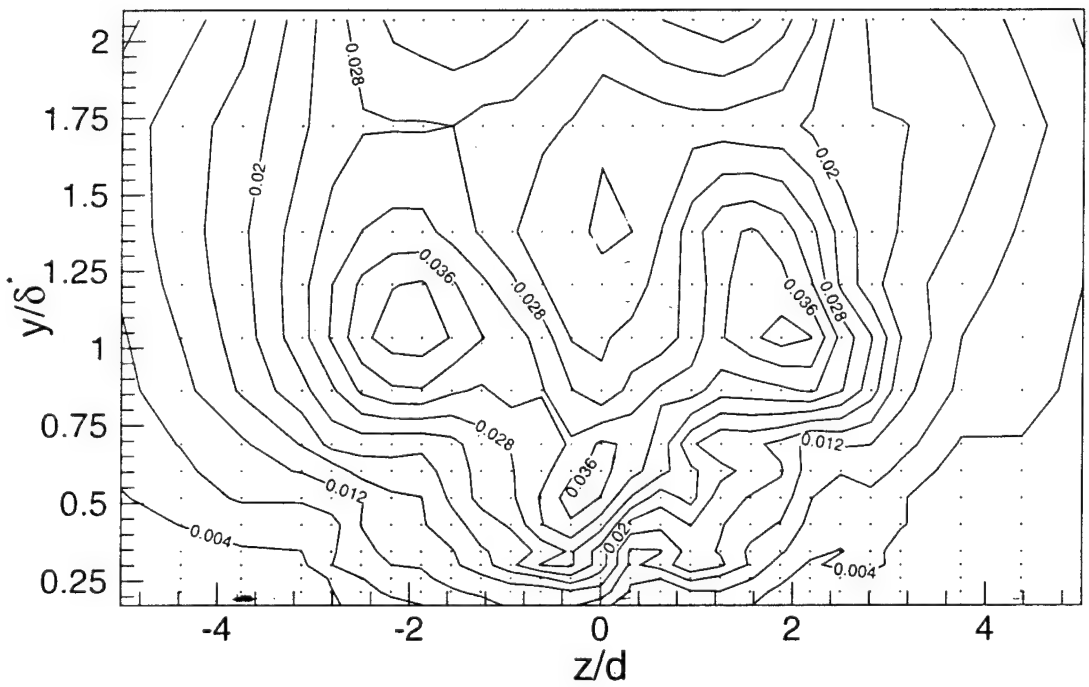


(b) Control

Figure 5.14: Contours of  $\Delta U/U_\infty$  behind cylinder at  $\Delta x_a/d = 13.1$ . Contours are in increments of  $0.03 U_\infty$ . Negative contours are indicated by dashed lines.



(a) Cylinder



(b) Control

Figure 5.15: Contours of  $u_{rms}/U_\infty$  behind cylinder at  $\Delta x_a/d = 13.1$ . Contours are in increments of  $0.004 U_\infty$ .

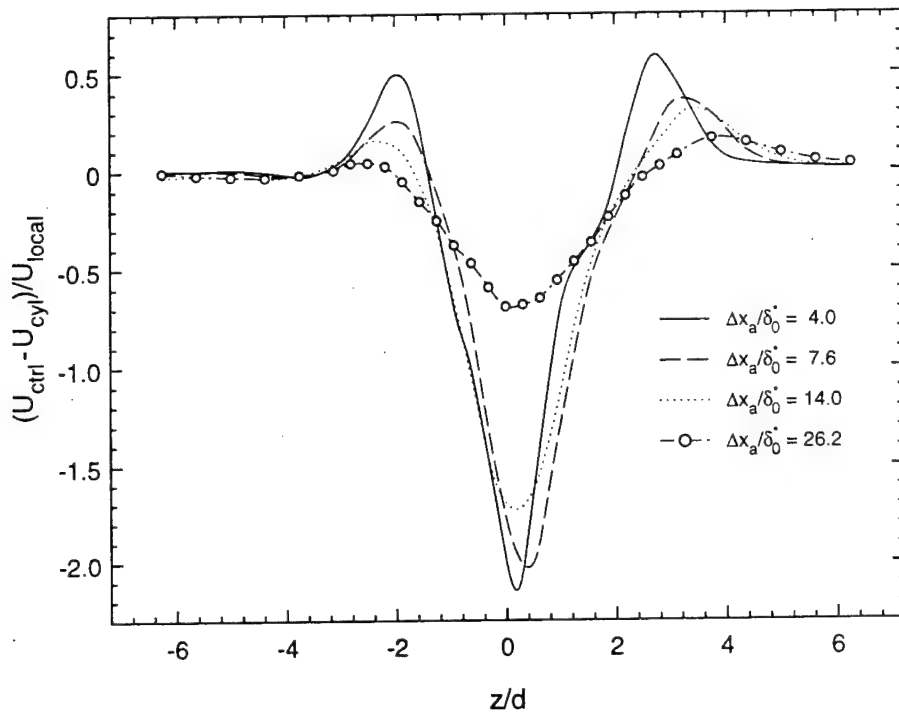


Figure 5.16: Spanwise velocity difference profiles for different streamwise locations ( $y/\delta^* = 0.17$ ).

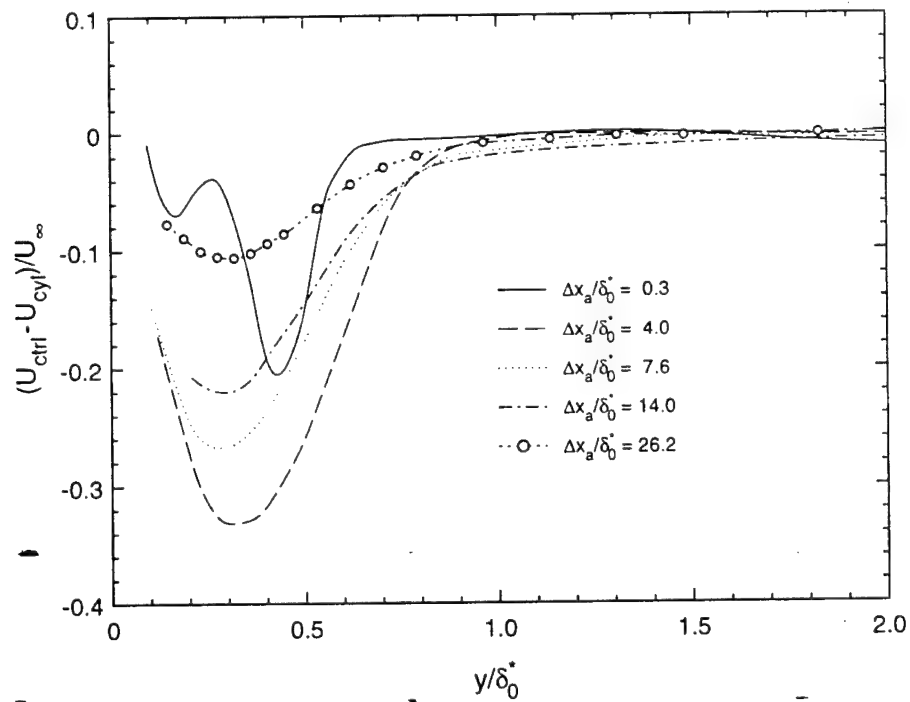


Figure 5.17: Wall-normal velocity difference profiles for different streamwise locations ( $z/d = 0.0$ ).

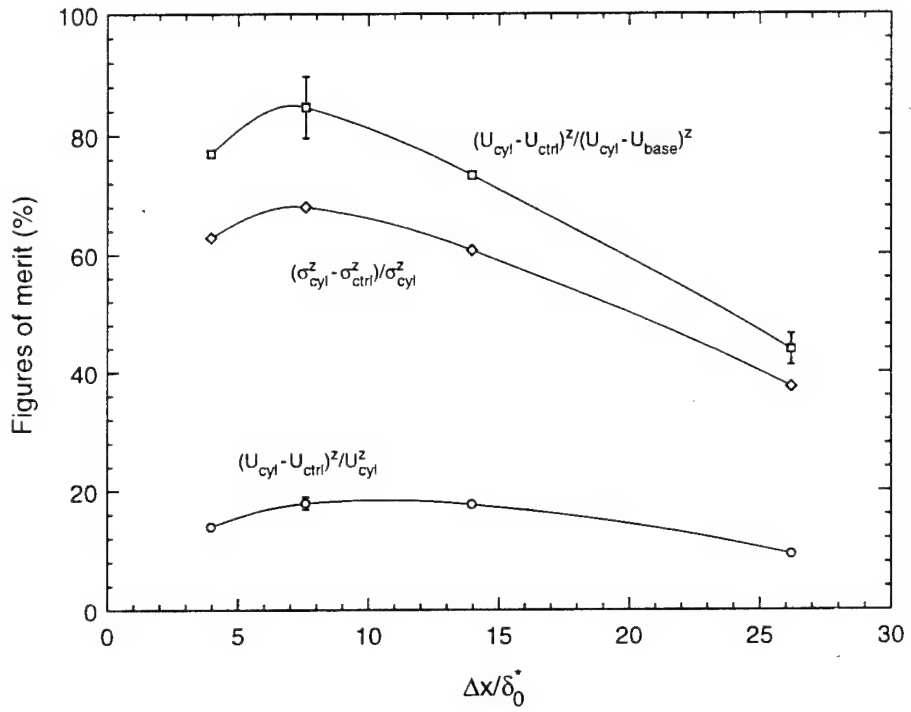


Figure 5.18: Figures of merit as a function of streamwise location. The superscript z indicates averaging in the spanwise direction.

# Chapter 6

## Conclusions

This project focused on the design, fabrication and characterization of MEMS-based arrays of sensors and actuators for boundary layer control. These transducers provide a testbed for the evaluation and development of control strategies in a controlled environment. Care was taken to ensure that the transducers were flush with the flow surface and did not affect the flow when not in operation. This required the development of a novel and robust back-side contact technology. The next sections summarize the main results from the previous chapters. Finally, recommendations for future work in this area are provided.

### 6.1 Sensors

The sensors are arrays of hot-films that provide snapshots of the spanwise wall shear stress distribution. Their key features are summarized below:

- Modules of eight and sixteen sensors with a spanwise spacing of 2 and 1 mm respectively have been fabricated. The active elements are thermally isolated metal resistors embedded in polyimide diaphragms. Nominal sensor resistances are between 5–6  $\Omega$  making them compatible with standard anemometry equipment.
- The sensors have a frequency response of 16 kHz when operated as constant temperature hot-film anemometers at an overheat ratio of 1.5 (about 90 °C above ambient). Individual sensors have a power consumption of about 10 mW at this overheat ratio. The sensor response in a laminar flow is nearly linear over the range of 0–80 mPa and has a slope of 0.3 mV/mPa (with a 50  $\Omega$  resistance in series in the Wheatstone bridge).
- The sensors were used to characterize the effect of multiple actuators in an unperturbed laminar boundary layer. The array was also used to study the disturbance

created by a cylinder and its interaction with actuator counter-disturbances.

## 6.2 Actuators

Arrays of Jacobson actuators were fabricated using a combination of micromachining techniques along with mesoscale assembly. The salient characteristics of the actuators are listed below:

- The actuators retained all the desirable features of the Jacobson actuators. They are fast with millisecond rise times, have power consumption in the milliwatt range, and incur no drag penalty when not in operation. Compared to the Jacobson actuators, the spanwise footprint is reduced by 20% while the streamwise footprint is reduced by a factor of 2.5.
- A single actuator creates a substantial disturbance, up to 25% of the free stream velocity, in a laminar boundary layer ( $U_\infty = 5$  m/s,  $Re_\theta = 310$ ). The disturbance is concentrated in a region of about one displacement thickness from the wall. It persists far downstream - the peak disturbance velocity is greater than 10% of the free stream velocity 30 displacement thicknesses downstream of the actuator. This is comparable to the perturbations created by the Jacobson actuator. Thus, micromachined actuators can be used to successfully alter the characteristics of low speed flows.
- Fabrication of arrays of reproducible actuators has been demonstrated. The actuators have similar mechanical transfer functions. Arrays of actuators allow considerable control of the spanwise velocity distribution in low speed flows.

## 6.3 Control of a Streamwise Vortex Pair

A cylinder introduced at an angle of  $90^\circ$  into the boundary layer of a crossflow creates a pair of streamwise vortices with alternating high and low speed regions close to the wall. The disturbance is steady but it allows an evaluation of the complete transducer system. The objective of the control was to reduce both the drag and the spanwise standard deviation of the shear stress in the perturbed flow.

- The sensors were used to determine 'influence coefficients' of the actuators on the wall shear stress. A least squares procedure was then used to determine a starting guess for the optimal actuator amplitudes. The amplitudes were further optimized by performing one-dimensional searches about the starting guess and using the sensors to monitor the flow response.

- Hot-wire velocity measurements were used to evaluate the effect of the actuators at several streamwise locations. A maximum drag reduction of 18% occurred at the location of the sensor array. This was accompanied by a reduction of 68% in the spanwise standard deviation. The strength of the disturbance, as measured by the spanwise averaged wall shear stress, was reduced by 85% at the sensor location. The effect of the control persisted greater than 25 displacement thicknesses downstream of the actuator array.

## 6.4 Recommendations

- Future sensor designs should focus on improving performance by reducing conduction heat loss to the substrate. Chevron sensors that can measure  $(\partial w / \partial y)_w$  should also be considered.
- Hot-film sensors dissipate a lot of power and exceed realistic power budgets in high-speed flows. The development of other shear stress sensors is necessary for active feed-forward or feedback control. One possibility is to use thin piezoelectric polymer films, generally made from poly-vinylidene fluoride (PVDF). Polymer sensors are attractive as they can be conformally coated over curved surfaces. Pressure or shear forces deform the film and generate an electric charge on the surface that can be measured using a charge amplifier (Nitsche *et al.* 1989). Alternatively, a surface acoustic wave (SAW) can be sent along a sensor with interdigitated electrodes. The SAW velocity change is proportional to the pressure and shear loading and can be measured either as a phase shift or a frequency shift (Varadan *et al.* 1990, Varadan *et al.* 1989). In both methods, a differential arrangement is necessary to separate the pressure and shear signals. The sensors are relatively insensitive to the shear stress and are also very susceptible to capacitive pickup. Thus, they would benefit considerably from on-chip signal amplification. Micromachined versions of these sensors should be investigated further.
- The flow close to the actuator and in the actuator cavity is complicated and three dimensional. Numerical simulations of the three dimensional flow are also difficult because the flow is in a complex geometry, has moving boundaries, and is quite sensitive to changes in geometry (Walther and Koumoutsakos 1999). An experimental determination of the velocity field created by the actuator in still air, perhaps with techniques like micro-PIV, would go a long way in improving understanding of the flow disturbance and in developing appropriate scaling laws.

- Different gap geometries can be easily fabricated using micromachining as a ‘rapid prototyping’ tool. Figure 6.1 shows a wafer level view of the actuator arrays. Here a single gap geometry was chosen for all the arrays, but multiple geometries could be created by changing a single mask in the fabrication process. In particular, the behavior of an actuator with narrow side gaps and a wide tip gap should be studied. Here most of the displaced fluid should exit through the tip gap. This should create a disturbance that is symmetric about the centerline of the actuator. This would be a useful reference point in evaluating the effectiveness of other geometries.
- Improvements in the properties of piezoelectric materials should be kept in mind in designing the next version of actuators. Park and Shrout (1997) have grown single crystal materials that have piezoelectric coefficients  $> 2500$  pC/N. These materials can achieve strains up to 1.7%. This is an order of magnitude larger than conventional piezoceramics and may make it possible to perturb the flow without breaking the flow surface. Different actuation mechanisms should also be considered. However, their scalability in high speed flows in terms of power consumption and frequency response should be carefully evaluated. In this regard, electrokinetic pumps show some promise.
- Active open loop control schemes should be investigated both numerically and experimentally. Recent developments such as spanwise wall oscillations and colliding wall jets point to a different paradigm for controlling wall turbulence. Spanwise periodic disturbances can easily be synthesized with the actuator arrays fabricated in this project. The effect of the array for periods close to the burst frequency should be especially interesting. Insights from optimal control and ‘what if’ simulations should be used to guide the development of experimentally feasible control strategies.

The following passage is an excerpt from a work of science fiction set in the sixth decade of the 21<sup>st</sup> century (Bear 1997, pg. 322):

The plane is an ingenious deltoid with a central bulge of passenger compartment smoothly curving to razor wing tips. Along the upper and lower wing surfaces, tens of thousands of tiny nano-controlled bumps hint at its radical design. The bumps can form tiny vanes or dips in the wing’s surface to control the coefficient of friction of air passing over and under the wing ...

It is hoped that the work in this project brings that vision a little closer to reality.

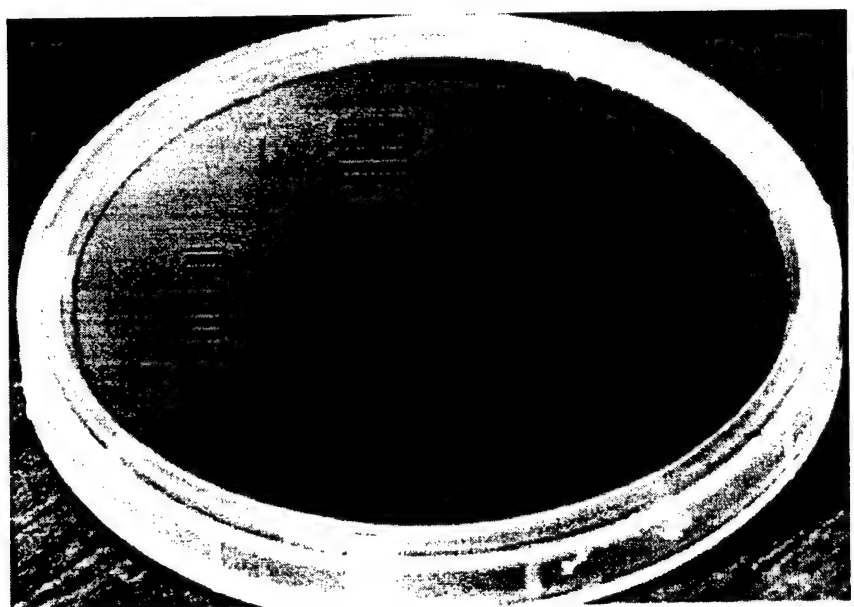


Figure 6.1: Wafer level view of 4 and 8 mm actuator arrays.



## Appendix A

# Common Fabrication Processes

All fabrication work except deposition of dielectrics was done at the Ginzton Microstructures Laboratory. Deposition of dielectrics like silicon nitride and oxide was done at the Center for Integrated Systems. The Ginzton facility offered more flexibility in using materials that were not CMOS compatible. The lab temperature was maintained between 20-22 °C, with a relative humidity of 70%. 3" wafers with a nominal thickness of 375  $\mu\text{m}$  were used as the starting material. The wafers are thinner than 4" wafers (550  $\mu\text{m}$  nominal thickness) and hence have considerably less flare out during wet anisotropic etching. However, if dry anisotropic etches like deep reactive ion etching (DRIE) that etch vertically downward are used, the processes developed here can be migrated to 4" wafers. Details of common procedures that were repeated several times are listed below.

### A.1 Mask Design and Fabrication

Masks for various processing steps were designed in AutoCAD. They were then printed onto linotronic film at ASSU Type and Design (Press Building, Stanford University). The resolution was 3200 dpi, which gives a spot size of 8  $\mu\text{m}$  and a minimum feature size of about 25  $\mu\text{m}$ . This was adequate for most of the work in this project. The patterns were transferred from linotronic film to 4 inch square, 1.5 mm thick iron oxide masks (Towne Technologies Inc., Somerville, NJ 08876). The steps in this procedure are listed below:

1. Spin on photoresist (Shipley 1400-27 or 1813) at 2500 rpm for 40 sec on iron oxide side.
2. Prebake at 90 °C for 30 min in convection oven.
3. Place the linotronic film face down on the mask. Place a dummy glass mask over the film to ensure good planarity. Expose in the Kasper for 90 sec.

4. Develop in a 1:1 mixture of Microposit developer concentrate and de-ionized (DI) water for 1 min. Rinse in DI water for 1 min and blow dry.
5. Etch in a hydrochloric acid solution ( $\text{FeCl}_2$  : HCl :  $\text{H}_2\text{O}$  in ratio 150 g : 575 cc : 285 cc) for 30-45 sec. The pattern will turn bright twice before etching through.
6. Strip the photoresist off in acetone, rinse and blow dry.

High resolution masks for sensor definition ( $\pm 1 \mu\text{m}$  accuracy) were fabricated at Photosciences Inc., Torrance, CA 90505.

## A.2 Lithography

Both the sensors and actuators were bulk micromachined. Both sides of the wafer needed to be protected during plasma etches. Shipley 1813 was used as the standard photoresist. The steps in a typical lithography run are listed below:

1. Presinge wafer  $90^\circ\text{C}$  for 10 min. This is especially important during liftoff lithography and promotes better adhesion to the surface.
2. Spin on photoresist at 3000 rpm for 40 sec on non-lithography side. The thickness of the photoresist is  $1.6 \mu\text{m}$ .
3. Prebake at  $90^\circ\text{C}$  for 15 min. This hardens the photoresist sufficiently to enable processing on the reverse side.
4. Repeat step 2 on the lithography side.
5. Prebake at  $90^\circ\text{C}$  for 30 min.
6. Align in the Kasper and expose for 45 sec. The Kasper intensity is  $5 \text{ mW/cm}^2$  and this gives a dose of  $225 \text{ mJ/cm}^2$ . The first mask was aligned to the wafer flat, subsequent masks used alignment marks on the wafer.
7. Develop in a 1:1 mixture of Microposit developer concentrate and DI water for 1 min. Rinse in DI water for 1 min and blow dry.

### A.2.1 Liftoff Process

The sensor and its leads were patterned using liftoff lithography. Photoresist was needed only on the lithography side and the first two steps in Section A.2 were omitted here. Shipley 1813 photoresist was used for thin film liftoff ( $2500 \text{ \AA Ni}$ ) and was prebaked at

75 °C instead of 90 °C. Hoechst AZ4620 photoresist was used for thick film liftoff (1  $\mu\text{m}$  Au). The AZ4620 was exposed for 150 sec and was developed in a 1:4 mixture of AZ400K developer and DI water for 4 min. Any residual photoresist traces were removed in a 15 sec oxygen plasma etch before metal deposition.

### A.3 Plasma Etching

The plasma ash (Phlegmatron Deluxe MkII from Plasma Technology, Sunnyvale CA 94086) was used for all thin film etching in this work. Two main recipes were used:

- Nitride etch: This is Process 2 on the plasma etcher. The settings are 1% O<sub>2</sub>, 24% CF<sub>4</sub>, 50% RF power. The actual power is 150 W and the pressure is 90 mtorr. The nominal nitride etch rate is 700 Å/min.
- Photoresist etch: This is Process 5 on the plasma etcher and is used for etching organic materials. The settings are 100% O<sub>2</sub>, 0% CF<sub>4</sub>, 50% RF power. The actual power is 150 W and the pressure is 290 mtorr. The nominal photoresist etch rate is 0.2  $\mu\text{m}/\text{min}$ . Polyimides also etch in an oxygen plasma at the rate of 0.1–0.2  $\mu\text{m}/\text{min}$ .

A plasma etch is typically followed by stripping the photoresist off in acetone. If the wafer has not been metallized, it is also cleaned with a piranha etch (9:1 H<sub>2</sub>SO<sub>4</sub> : H<sub>2</sub>O<sub>2</sub> at  $\approx 100^\circ\text{C}$ ) for about 5 min to remove any residual photoresist.

### A.4 Wet Anisotropic Etching

Wet etching of silicon was carried out in a potassium hydroxide (KOH) solution. The etchant is anisotropic as it stops on {111} crystal planes. A 30% wt. in water solution was used as it causes the least surface roughness (Findler *et al.* 1992). An electronic grade KOH solution (46.2% from J. T. Baker) was used. KOH pellets (Mallinckrodt Chemicals) are only 87.8% KOH and add impurities to the solution. The solution was stirred at 500 rpm to prevent temperature and concentration gradients. For through wafer etches, the endpoint was determined by shining a flashlight on the etching side and monitoring the color of the transmitted light. The color changes progressively from dark red to orange and yellow as the silicon membrane is thinned below 8  $\mu\text{m}$  (Smits & Tilmans 1984). A very dilute hydrochloric acid (HCl) solution was used during the cleaning cycle to neutralize the KOH. The wafer was then rinsed in running DI water for  $\approx 5$  min.

Typical etch rates for a 30% solution are given in Table A.1. A least squares fit was carried out on raw etch-rate data between 69 °C and 85 °C assuming an  $\exp(-E/RT)$

Temperature (°C)	Etch rate (μm/min)
70	0.64
72	0.71
74	0.78
76	0.86
78	0.95
80	1.05
82	1.15
84	1.27

Table A.1: Etch rate for a 30% KOH solution as a function of temperature.

Arrhenius temperature dependence. The fit was used to generate the data in Table A.1. This data was used to estimate the endpoint for timed etches. The etch depth was measured using an Alpha-Step 200 profilometer (Tencor Instruments, San Jose, CA 95134). An optical microscope with a calibrated stage (least count  $\pm 2 \mu\text{m}$ ) was used to measure etch depths greater than  $150 \mu\text{m}$ . The microscope was focused first on the top surface of the wafer and then on the etched surface; the difference in the readings of the stage gave the etch depth. This was cross-checked by measuring the flare-out of the {111} crystal planes using a calibrated eye-piece. This method is accurate to  $\pm 3.5 \mu\text{m}$  under 20x magnification (least count of eye-piece under this magnification is  $\pm 2.5 \mu\text{m}$ ).

## A.5 Backside Contact Formation

The backside contacts were made using 2 mm spacing ribbon cable connectors (Part TW-08-08-G-D-435-120 from Samtec Inc., New Albany, IN 47151). A two row connector was used to transfer conductive epoxy (H20E-PFC from Epoxy Technology Inc., Billerica, MA 01821) into the contact trenches on the silicon dies. The steps in this process are listed below:

1. Mix equal amounts of part A and part B. The pot life of the epoxy is 3 days at room temperature. Make a uniform layer of epoxy  $375 \mu\text{m}$  thick using a shimstock jig of the same thickness.
2. Check that the connector slides easily into the transducer Plexiglas mount (Figs. B.1, B.2 and C.1). Sand the bands on the connector if necessary. Dip the connector in epoxy, remove and spot on a glass slide. This removes the excess epoxy and the spots confirm that the individual pins are level with each other.
3. Insert the epoxy end of the connector carefully into the contact trenches. Push gently

till the connector settles in. Remove the connector and inspect the epoxy transfer. A uniform film of epoxy should have been transferred into all the trenches and the underlying gold contact should be fully covered with epoxy. Reload the connector with epoxy, spot on a glass slide, and make the final contacts. The two rows of the connector ensure that it remains in position without toppling over.

4. Cure at 120 °C for 30 min (sensors) or 90 °C for 90 min (actuators).



## Appendix B

# Sensor Fabrication Process

Starting material: 3", 375  $\mu\text{m}$  thick, p-type (boron doped), double side polished <100> silicon wafers with resistivity  $> 20 \Omega\text{-cm}$ . The dopant density is less than  $10^{15}/\text{cm}^3$ .

Step No	Process	Thickness	Recipe/ Mask	Time/ Settings	Equipment/ Chemical	Remarks
1	Nitride growth	0.2 $\mu\text{m}$	Nitride1	45 min	Tylan Nitride	Low stress nitride
2	Backside lithography	1.6 $\mu\text{m}$ resist	ALIGN	225 mJ/cm <sup>2</sup>	Kasper	Through wafer alignment marks
3	Nitride etch	0.2 $\mu\text{m}$	Std. nitride etch	3 min	Plasma asher	
4	Backside KOH etch	100 $\mu\text{m}$	80 °C	$\approx$ 100 min	KOH 30% soln.	
5	Backside lithography	1.6 $\mu\text{m}$ resist	SIETCH	225 mJ/cm <sup>2</sup>	Kasper	Contacts and thermal isolation
6	Nitride etch	0.2 $\mu\text{m}$	Std. nitride etch	3 min	Plasma asher	
7	Backside KOH etch	$\approx$ 275 $\mu\text{m}$	80 °C	$\approx$ 275 min	KOH 30% soln.	Etch till alignment marks seen from frontside. Contacts supported by 100 $\mu\text{m}$ Si.
8	Liftoff lithography	1.6 $\mu\text{m}$ resist	NI	225 mJ/cm <sup>2</sup>	Kasper	Sensor definition on frontside
9	- Metallization	200 Å : 0.25 $\mu\text{m}$	-	-	Evaporator/ Cr:Ni	Cr is adhesion layer -

10	Liftoff	-	In wafer boat, metal side down	30 min	Acetone	Ni film over photoresist has micro-cracks and lifts off very easily
11	Liftoff lithography	8 $\mu\text{m}$ resist	AU	2.5 min	Kasper/AZ4620	Sensor leads, thick photoresist overexposed for Au liftoff
12	Metallization	200 $\text{\AA}$ : 1 $\mu\text{m}$	-	-	Evaporator/ Cr:Au	
13	Liftoff	-	In wafer boat, metal side down	24 hrs	Acetone	5 sec ultrasound bursts help
14	Polyimide coupler	-	3000 rpm	40 sec	PIQ coupler 3	Adhesion promoter for polyimide
15	Coupler cure	-	350 $^{\circ}\text{C}$	1 hr	Sunk heater	Done under petri dish, time includes ramp and soak
16	Polyimide	7 $\mu\text{m}$	3000 rpm	40 sec	PIQ3600	Bring to room temperature before use
17	Polyimide cure	-	160 $^{\circ}\text{C}$ , 250 $^{\circ}\text{C}$ , 350 $^{\circ}\text{C}$	30 min, 30 min, 1 hr	Sunk heater	Done under petri dish, time includes ramp and soak
18	Frontside protection	-	See Section B.1	-	-	Protects metal and imide from KOH etch
19	Backside KOH etch	$\approx$ 100 $\mu\text{m}$	80 $^{\circ}\text{C}$	$\approx$ 100 min	KOH 30% soln.	Etch till contacts and sensor released
20	Wafer clean	-	Soak	10 min each	Borothene, isopropanol, acetone	Use hot solution and multiple cycles if necessary
21	Backside nitride etch	0.2 $\mu\text{m}$	Blanket nitride etch	3.5 min	Plasma ashер	Expose contacts, remove nitride under sensor
22	Dicing	-	-	-	Ginzton Crystal Shop	Protect backside with photoresist and mount on blue tape
23	Contact formation	-	See Appendix A	120 $^{\circ}\text{C}$ , 30 min	H20E-PFC	-
24	Sensor mount	-	See Figs. B.1 and B.2	-	Devcon 2-Ton epoxy	No epoxy should enter thermal isolation cavity

Table B.1: Steps in sensor fabrication process.

## B.1 Frontside Wax Protection

It is important to get a uniform coating of wax so that the KOH solution does not attack the top surface during the one-sided release step. The edges of the wafer are especially important as the KOH solution tends to seep in through any cracks in the wax. The procedure below gives reliable results.

1. Use a 4" wafer as the substrate. This allows space for getting a good wax seal around the edges.
2. Melt wax powder at 165 °C on both wafers. Take wafers off the hotplate. The wax solidifies quickly.
3. Place the two waxed surfaces together. Center the 3" wafer on the 4" wafer. Place on the hotplate again to re-melt the wax.
4. Allow wax to melt quickly while holding the 3" wafer in position with a Q tip. Carefully remove the sandwich from the hotplate. The wax solidifies with an increase in volume and this gives a uniform edge bead that seals in the edges of the 3" wafer.
5. To separate the sandwich and remove the wax, heat again on the hotplate. Wax residue is removed by multiple solvent cleans.

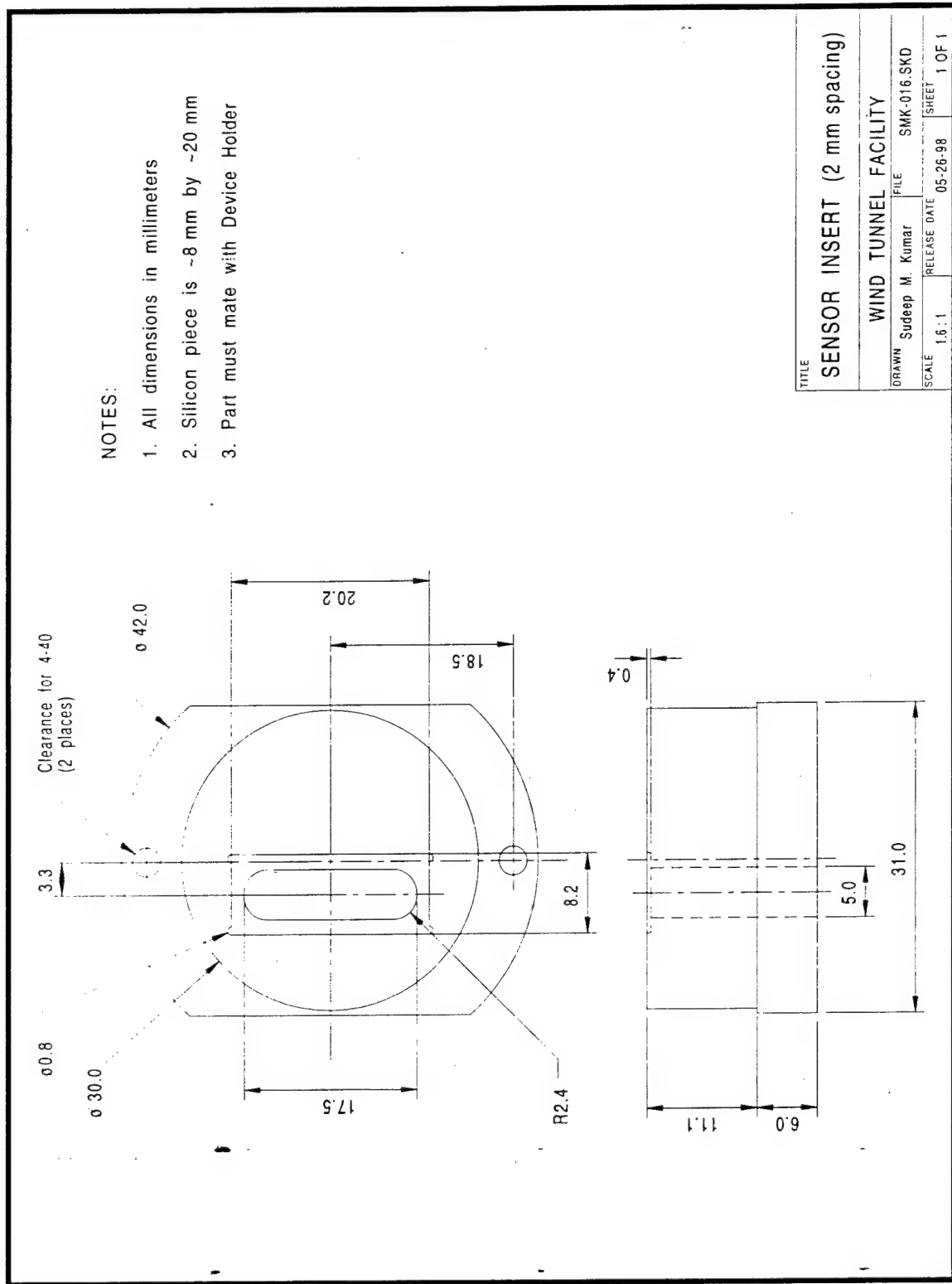
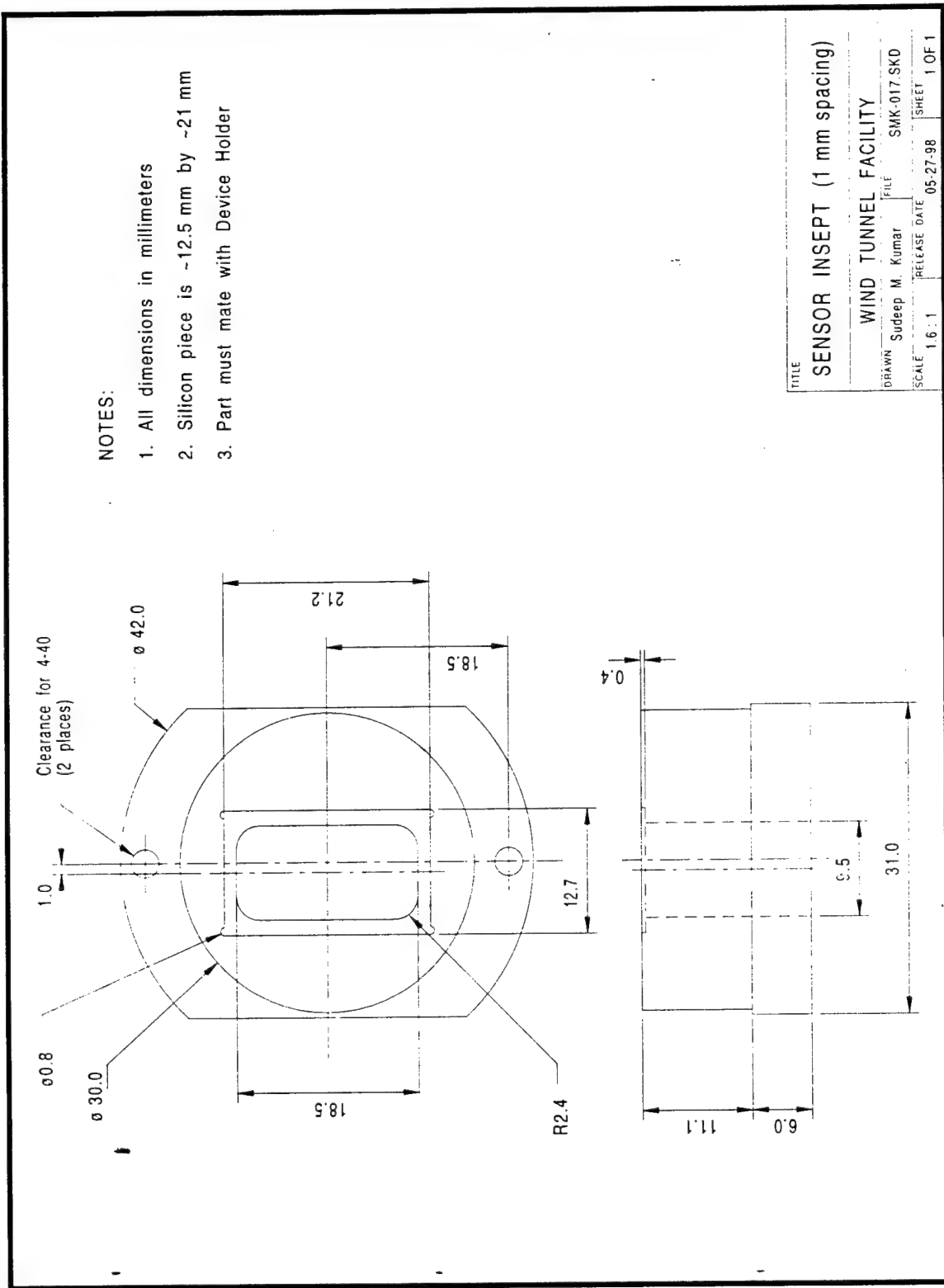


Figure B.1: Sensor mount for 8 sensor die (2 mm spacing).





## Appendix C

# Actuator Fabrication Process

Starting material: 3", 375  $\mu\text{m}$  thick, p-type (boron doped), double side polished <100> silicon wafers with resistivity  $> 20 \Omega\text{-cm}$ . The dopant density is less than  $10^{15}/\text{cm}^3$ . The PZT is a 125  $\mu\text{m}$  thick sheet of 5H material from Piezo Systems Inc., Cambridge, MA 02139. An additional gold layer is deposited on the negative polarity side to serve as the positive electrode. The PZT is then diced into  $900 \mu\text{m} \times 1100 \mu\text{m}$  pieces at the Ginzton Crystal Shop.

Step No	Process	Thickness	Recipe/ Mask	Time/ Settings	Equipment/ Chemical	Remarks
1	Nitride growth	0.2 $\mu\text{m}$	Nitride1	45 min	Tylan Nitride	Low stress nitride
2	Backside lithography	1.6 $\mu\text{m}$ resist	ALIGN	225 mJ/cm <sup>2</sup>	Kasper	Through wafer alignment marks
3	Nitride etch	0.2 $\mu\text{m}$	Std. nitride etch	3 min	Plasma ash	
4	Backside KOH etch	150 $\mu\text{m}$	80 °C	≈ 150 min	KOH 30% soln.	
5	Cavity lithography	1.6 $\mu\text{m}$ resist	SICAV	225 mJ/cm <sup>2</sup>	Kasper	Definition of integrated cavities
6	Nitride etch	0.2 $\mu\text{m}$	Std. nitride etch	3 min	Plasma ash	
7	Backside KOH etch	255 $\mu\text{m}$	80 °C	≈ 255 min	KOH 30% soln.	≈ 30 $\mu\text{m}$ etch left when alignment marks seen from frontside

8	Cantilever lithography	$1.6 \mu\text{m}$ resist	SICANT	$225 \text{ mJ/cm}^2$	Kasper	Lithography on frontside
9	Nitride etch	$0.2 \mu\text{m}$	Std. nitride etch	3 min	Plasma ashер	
10	Two-sided KOH etch	$60 \mu\text{m}$	$80^\circ\text{C}$	$\approx 60 \text{ min}$	KOH 30% soln.	Etch till all cantilevers released
11	Fillet etch	few $\mu\text{m}$	HNA etch (Henning 1997)	1 min, 600 rpm	3:30:10 HF:HNO <sub>3</sub> : CH <sub>3</sub> COOH	Reduces stress concentration at cantilever base
12	Backside nitride etch	$0.2 \mu\text{m}$	Blanket nitride etch	3 min	Plasma ashер	Remove overhanging nitride before electrode deposition
13	Metallization	$200 \text{ \AA} : 1 \mu\text{m}$	-	-	Evaporator/ Cr:Au	Deposition of ground electrode
14	Dicing	-	-	-	Ginzton Crystal Shop	Mount backside on blue tape
15	PZT bonding	-	See Section C.2	-	Devcon 2-Ton epoxy	
16	Contact formation	-	See Appendix A	$90^\circ\text{C}, 90 \text{ min}$	H20E-PFC	
17	Back cover bonding	$\approx 10 \mu\text{m}$	3000 rpm	40 sec	Epotek 301 epoxy	Optical epoxy
18	Actuator mount	-	See Fig. C.1	-	Devcon 2-Ton epoxy	

Table C.1: Steps in actuator fabrication process.

## C.1 RTV Mold and Casting Fabrication

A RTV rubber piece is used to press down on the PZT during the bonding step. The RTV casting process is detailed below.

1. Use a 4" wafer coated with LPCVD nitride for making the mold. Pattern the polished side with the SICAV mask used in the actuator fabrication process. Place the wafer horizontally in the KOH solution with the patterned side up. This allows the bubbles generated during the etching process to escape and improves etch-depth uniformity over the wafer. A variation of  $\pm 0.3 \mu\text{m}$  per  $100 \mu\text{m}$  of etch depth was measured experimentally. Etch to a depth of  $300 \mu\text{m}$ . This gives a clearance of  $100 \mu\text{m}$  between the silicon die surface and the RTV when the casting is used to press down on the PZT. Etch the LPCVD nitride masking layer to remove any overhanging nitride. Both

silicon and LPCVD nitride surfaces behave in a similar manner with respect to release of the RTV casting.

2. The silicone rubber used is RTV664 from GE Silicones, Waterford, NY 12188. It has a work time of 3 hours and cures in 24 hours. Use 30 ml of the base and 3 ml of the hardener (ratio 10:1). Mix thoroughly with a glass stirring rod.
3. Degas under 29" of vacuum for about 9 minutes. The mixture will expand to 4-5 times its original size and then recede. Dissolved and trapped air bubbles are removed during this process.
4. Use Tygon tubing to create a dam on the 4" wafer mold. Buna-N O rings were also tried, but the RTV reacts with the O rings and does not cure at the edges. Mount the wafer on a teflon block on a level surface. Pour the RTV into the mold, starting from the center and moving outward.
5. The RTV will form a smooth surface in a few minutes. Allow to cure for about 24 hrs at room temperature.
6. Remove the dam from the wafer mold. Gently loosen all sides of the RTV casting. Remove the casting using a slow, continuous pulling motion.
7. Soak the casting in a 6% soap solution (3 ml MICRO detergent from International Products Corporation, Burlington, NJ 08016 in 50 ml water). This improves the RTV release in the PZT bonding step.
8. Cut the RTV casting into individual dies.

## C.2 PZT Bonding

1. Clean the actuator die and the PZT pieces. Place the die in the PZT bonding jig to prevent the die from moving (Fig. C.2).
2. Spin Devcon 2-Ton epoxy (Devcon Corp., Danvers MA 01923) on a coverslip at 5000 rpm for 40 sec. This gives an epoxy film about 40  $\mu\text{m}$  thick. The epoxy sets in 30 min and has a tensile strength of 15 MPa.
3. Place PZT pieces in the epoxy with the gold side up. Slide the PZT pieces to the edge of the coverslip, this thins out the epoxy further.
4. Carefully place the PZT on the cantilevers using a small pair of tweezers. Move the die onto a glass slide.

5. Align the RTV rubber piece with the cavities in the die. When properly aligned, the RTV piece mates with the silicon die and there is very little clearance ( $\approx 100 \mu\text{m}$ ) between the two pieces.
6. Place a brass deadweight on the assembly. The nominal pressure is 0.36 bar (295 g deadweight on eight 11.2 mm  $\times$  0.9 mm PZT pieces). Remove the deadweight and the RTV piece after 30 min. The epoxy reaches full strength in about 8 hrs.

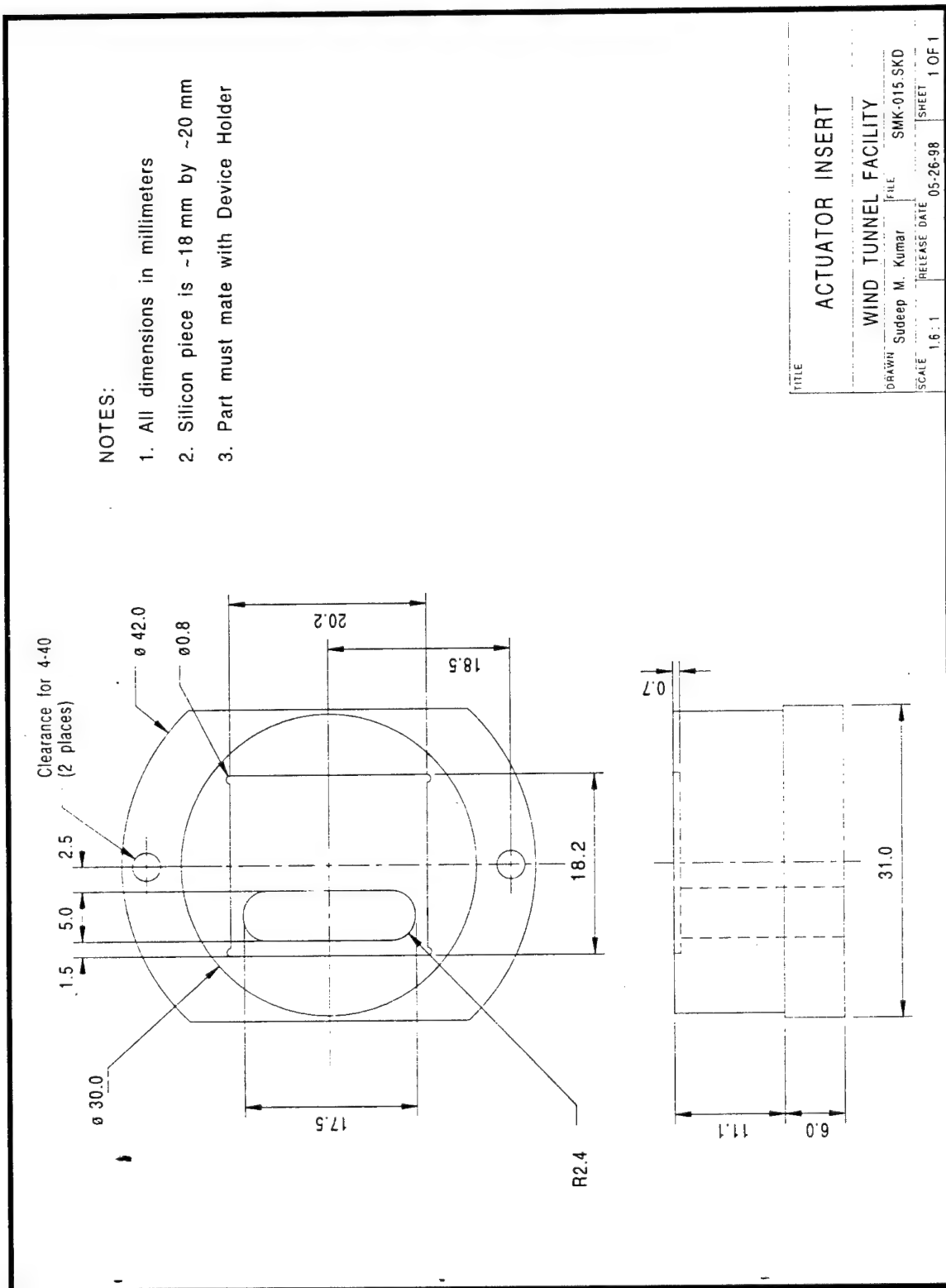


Figure C.1: Actuator mount.

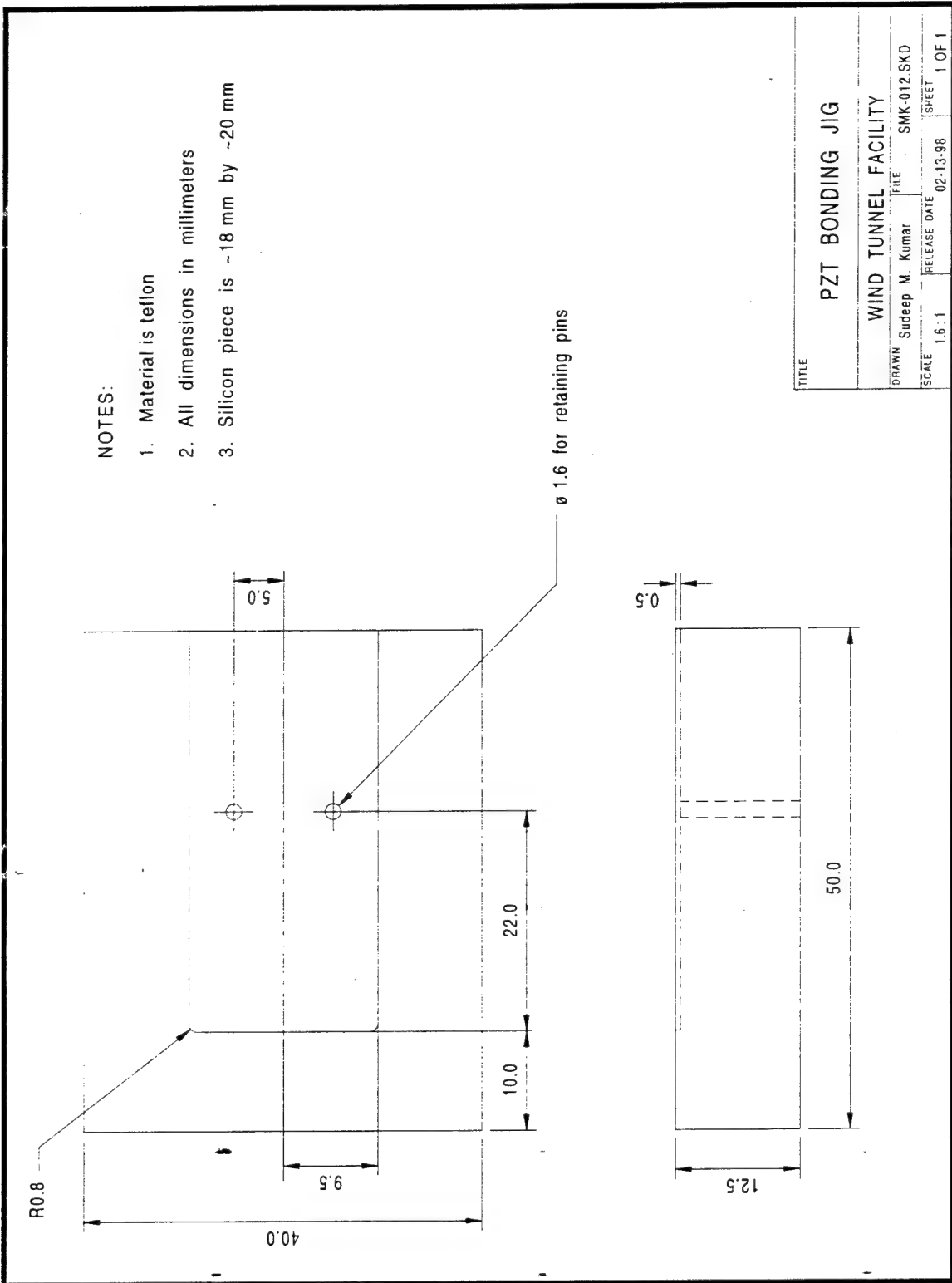


Figure C.2: PZT bonding jig.

## Appendix D

# Uncertainty Analysis

Uncertainties of experimentally determined quantities were computed following the guidelines of Kline and McClintock (1953) and Moffat (1988). All uncertainties are reported at a 95% confidence level (19:1 odds). The errors are classified as fixed systematic errors and random statistical errors. The errors are assumed to be independent of each other; this allows the total uncertainty to be determined as the root sum square of the individual uncertainties. Both the hot-wire and the shear stress sensors also had bias errors as they were calibrated in spanwise uniform flows but used in flows with large spanwise gradients. The uncertainties in position, velocity and wall shear stress are summarized in the following sections.

### D.1 Position

The traverse could be moved in increments of 5 mm in the streamwise direction. The uncertainty in the streamwise position was determined by checking the position of the hot-wire against fiducial marks in the opposing wall, and is estimated to be  $\pm 1$  mm. The major source of uncertainty for the wall-normal position was the error in determining the location of the wall. This error was quantified by changing the offset till the shear close to the wall varied by more than  $\pm 5\%$  (see Fig. D.2). The uncertainty in  $y$  determined by this method is  $\pm 25 \mu\text{m}$ . The uncertainty in the spanwise position  $z$  was primarily due to the fact that the two traverses were not precisely perpendicular to each other. For a wall-normal traverse of 10 mm, the uncertainty in  $z$  is  $\pm 50 \mu\text{m}$ .

## D.2 Velocity

### D.2.1 Fixed Errors

The major sources of fixed errors are uncertainties in the calibration fit, drifts of the bridge voltage due to temperature variations, and discretization errors in the 12 bit data acquisition system. Guidance for estimating these errors was obtained from earlier research programs in the same flow facility (Westphal *et al.* 1984, Anderson & Eaton 1987). The errors in the mean and rms velocities are estimated to be  $\pm 2\%$  of local values.

### D.2.2 Random Errors

Confidence intervals for the mean and rms velocities can be obtained using standard statistical techniques as described in Bendat & Piersol (2000). For the mean velocity  $U$ , the 95% confidence interval is given by:

$$U \pm t_{n-1}(\alpha/2) \frac{s}{\sqrt{n}} = U \pm t(0.025) \frac{s}{\sqrt{n}} = \pm 1.96 \frac{s}{\sqrt{n}} \quad (\text{D.1})$$

where  $s$  is the estimated standard deviation,  $n$  is the number of samples, and  $\alpha = 0.05$  for a 95% confidence interval. All hot-wire statistics were obtained using 20,000 samples at a sampling rate of 1000 Hz. The maximum rms velocities are about 7% of the mean in the wake of the cylinder. This corresponds to a statistical uncertainty of  $\pm 0.1\%$  that is insignificant compared to the fixed error uncertainty.

If the velocity has a normal distribution, its variance will have a  $\chi^2$  distribution. The confidence interval is:

$$\frac{(n-1)s^2}{\chi_{n-1}^2(\alpha/2)} \leq \sigma^2 \leq \frac{(n-1)s^2}{\chi_{n-1}^2(1-\alpha/2)} \quad (\text{D.2})$$

where  $\sigma^2$  is the true variance. For  $(n-1) > 120$ ,  $\chi^2(\alpha)$  can be evaluated using the following formula:

$$\chi_{n-1}^2(\alpha) \approx (n-1) \left( 1 - \frac{2}{9(n-1)} + z(\alpha) \sqrt{\frac{2}{9(n-1)}} \right)^3 \quad (\text{D.3})$$

where  $z(0.025) = 1.96$  and  $z(0.975) = -1.96$ . For 20,000 samples, the uncertainty in the variance is  $\pm 2\%$ . This corresponds to a statistical uncertainty of  $\pm 1\%$  for  $u_{rms}$ . Thus, the total uncertainty in the rms velocity, including both fixed and random errors is  $\approx \pm 2.5\%$  of local values.

### D.2.3 Bias Errors

The bias error in the velocity measurements is because the hot-wire averages the velocity field over its length. An estimate of this was obtained by measuring the wall-normal velocity over an actuator in still air with the hot-wire aligned with and perpendicular to the narrow gap. These results are shown in Fig. D.1 and show that the averaging decreases the peak value of the velocity and broadens the distribution in the spanwise direction. Thus, the velocity disturbance magnitudes in Chapters 4 and 5 are conservative; the disturbances created by the actuator are likely to be stronger and more localized. The mean velocities for wires with spanwise lengths of  $640 \mu\text{m}$  and  $1270 \mu\text{m}$  are within a few percent of each other. However, the shorter wire captures the rms profiles with better accuracy. Note that a simple running average of the true velocity field as suggested by Suzuki & Kasagi (1992) is too conservative. The running average overestimates both the drop in the peak velocity and the transverse spread. This is expected because even though the energy equation governing the hot-wire heat transfer is linear, the velocity  $U$  appears as a non-constant coefficient in the equation.

## D.3 Wall Shear Stress Using Hot-Wire

The wall shear is measured independently by placing a hot-wire in the linear region of the velocity profile. This is shown in Fig. D.2 for a Blasius boundary layer. The shear is constant over the first 20% of the boundary layer within an experimental uncertainty of  $\pm 5\%$ . However, once the cylinder is introduced into the flow, this is no longer true in the downsweep region of the streamwise vortex pair. The gradient decreases rapidly in the wall-normal direction and measurements made with  $y/\delta^* > 0.25$  severely underpredict the wall shear stress. This is seen clearly in Fig. D.3 where spanwise profiles behind the cylinder are shown for three  $y$  locations. The peak positive perturbation is increasingly underpredicted as one moves further from the wall. The curves collapse in the negative perturbation region. This is because the negative perturbation peaks are located considerably further from the wall (see Fig. 5.14). The velocity profile is therefore linear up to a greater distance from the wall, as is also seen in Fig. 5.8.

The wall-normal location  $y = 0.5 \text{ mm}$  was chosen for estimating the wall shear. This location was always in the linear region of the velocity profile, both in the Blasius boundary layer and in the perturbed flow. The remaining sources of uncertainty are errors in the wall-normal location  $y$  and in the mean velocity  $U$ . These uncertainties are  $\pm 5\%$  and  $\pm 2\%$  respectively. The resulting net uncertainty in the wall shear is  $\approx \pm 6\%$ .

## D.4 Wall Shear Stress Using Sensor Array

### D.4.1 Fixed Errors

The sensor were calibrated against a hot-wire located at  $y = 1$  mm, assuming spanwise uniformity in the base flow. Major sources of uncertainty include errors in the absolute location of the hot-wire from the wall, uncertainties in the calibration fit, and uncertainties in the temperature correction coefficients of the sensors. This uncertainty was shown to be  $\approx \pm 1$  mPa in Chapter 3. This corresponds to uncertainties of  $\pm 7.5\%$  and  $\pm 4\%$  for the flows with  $U_\infty = 3$  and 5 m/s respectively. Random errors are insignificant as shown in Section D.2.

### D.4.2 Bias Errors

Bias errors arise when the chip temperature during calibration cannot be matched to that during data acquisition. The chip temperature is a function of the *average shear* over the entire sensor array. In the perturbed flows studied here, the average shear is much lower than the peak shear and therefore deviations from the baseline are always underpredicted by the array. This is shown in Fig. D.4. An ideal sensor responds only to the shear stress and will therefore have a smaller slope. The sensors in this study have a larger slope because of conduction loss to the substrate. Thus, a given change in output voltage is interpreted as a smaller change in the shear stress. Note that sensors calibrated in unsteady mode would have calibration curves that fall between the two extremes shown. Such calibrations give the incorrect baseline shear but capture deviations from the baseline more accurately. Since the silicon chip is almost isothermal, a single guard heater would not be able to correct for this effect. The only viable solution is to minimize the heat loss by conduction to the silicon chip.

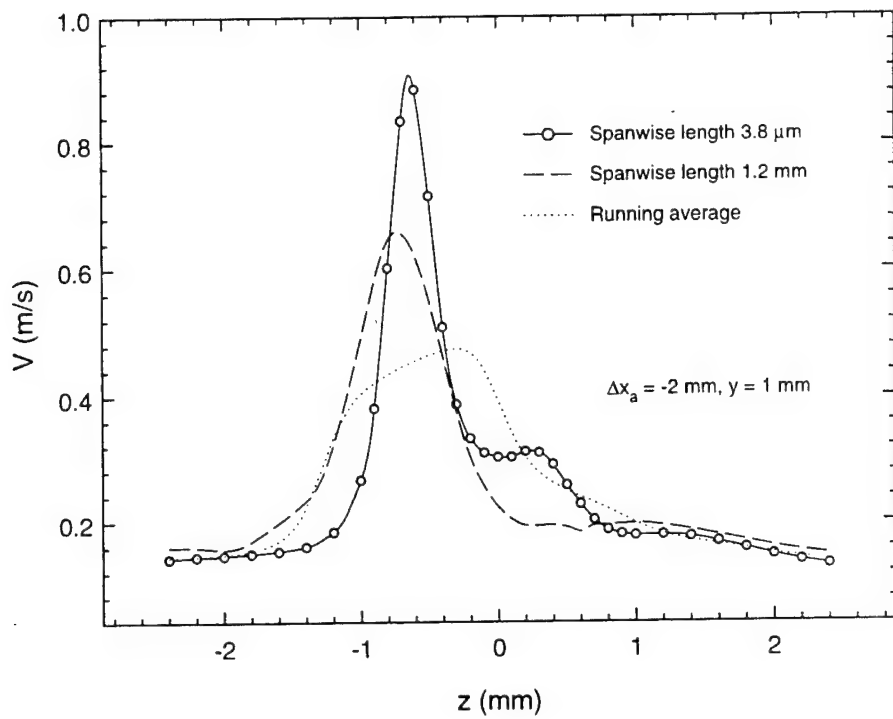


Figure D.1: Error due to averaging over hot-wire length. Data is for actuator in still air as in Fig. 4.23.

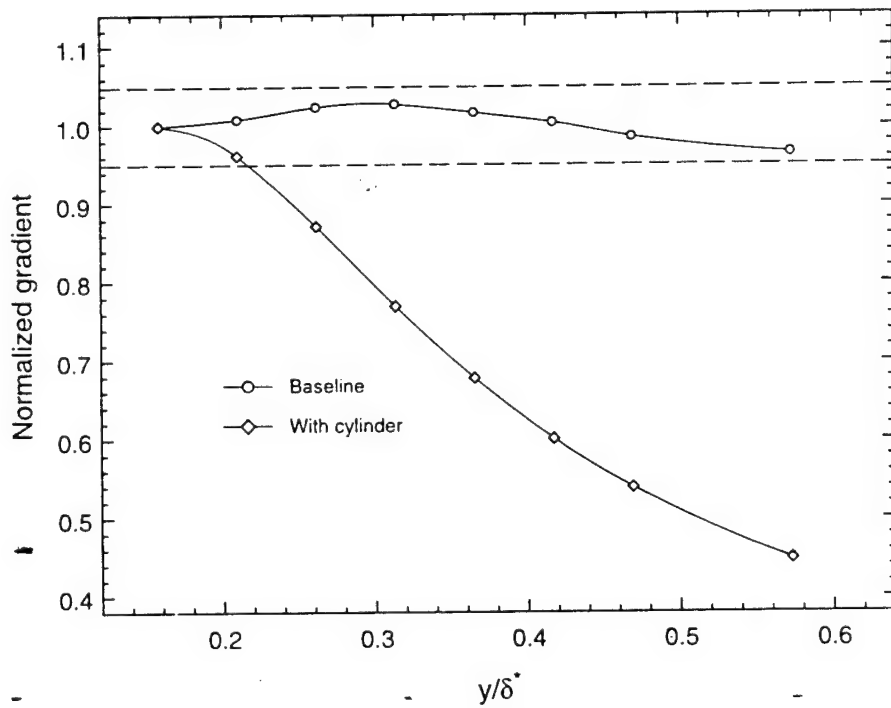


Figure D.2: Error in determining the streamwise velocity gradient assuming a linear profile close to the wall ( $\Delta x_a/\delta_0^* = 9.4$ ,  $z/d = 0$ ,  $U_\infty = 5 \text{ m/s}$ ).

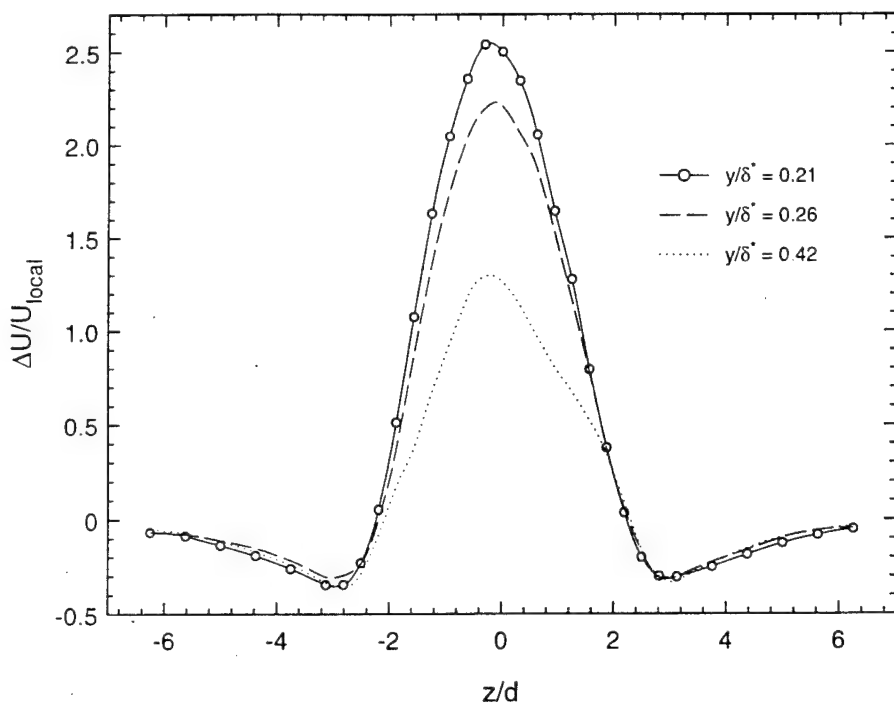


Figure D.3: Spanwise profiles behind cylinder at three different  $y$  locations from wall ( $\Delta r_a/\delta_0^* = 9.4$ ,  $U_\infty = 5$  m/s).

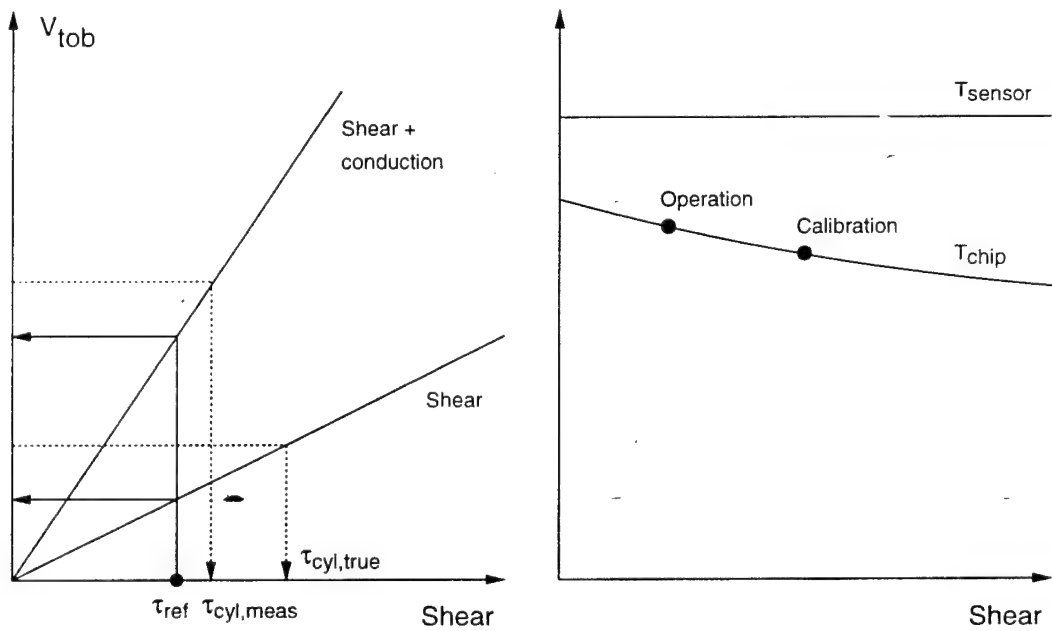


Figure D.4: Schematic explaining sensor bias error due to substrate conduction in flows with spanwise variation of wall shear.

# Bibliography

AKEDO, J., ICHIKI, M., KIKUCHI, K., & MAEDA, R. 1997 Fabrication of three dimensional micro structure composed of different materials using excimer laser ablation and jet molding. *Proceedings IEEE Micro Electro Mechanical Systems*, 135-140.

AKHAVAN, R., JUNG, W. J., & MANGIABACCHI, N. 1993 Turbulence control in wall-bounded flows by spanwise oscillations. *Applied Scientific Research* **51**, 299-303.

ALFREDSSON, P. H., & JOHANSSON, A. V. 1988 The fluctuating wall-shear stress and the velocity field in the viscous sublayer. *Phys. Fluids* **31**, 1026-1033.

ANDERSON, S. D., & EATON, J. K. 1987 An experimental investigation of pressure driven three-dimensional turbulent boundary layers. *Stanford University Thermosciences Division Rep.* MD-49.

BANDYOPADHYAY, P. R. 1986 Review - mean flow in turbulent boundary layers disturbed to alter skin friction. *J. Fluids Eng.* **108**, 127-139.

BARON, A., & QUADRI, M. 1996 Turbulent drag reduction by spanwise-wall oscillations. *Applied Scientific Research* **55**, 311-326.

BARTH, P. W., BERNARD, S. L., & ANGELL, J. B. 1985 Flexible circuit and sensor arrays fabricated by monolithic silicon technology. *IEEE Transactions on Electron Devices* **ED-32**, 1202-1205.

BEAR, G. 1997 *Slant. Tor.*

BEARMAN, P. W. 1971 Corrections for the effect of ambient temperature drift on hot-wire measurements in incompressible flow. *DISA Information* **11**, 25-30.

BENDAT, J. S., & PIERSOL, A. G. 2000 *Random Data : Analysis and Measurement Procedures*, 3<sup>rd</sup> ed. Wiley-Interscience.

BERGER, T. W., KIM, J., LEE, C., & LIM, J. 2000 Turbulent boundary layer control utilizing the Lorentz force. *Phys. Fluids* **12**, 631-649.

BEWLEY, T. R., & LIU, S. 1998 Optimal and robust control and estimation of linear paths to transition. *J. Fluid Mech.* **365**, 305–349.

BEWLEY, T. R., & MOIN, P. 1999 Optimal and robust control and estimation of transition, convection, and turbulence. *Stanford University Flow Physics and Computation Division Rep.* TF-76.

BLACKWELDER, R. F. 1997 An experimental model for near wall structure. In *Self-Sustaining Mechanisms of Wall Turbulence; Advances in Fluid Mechanics v. 15* (ed. R. L. Panton), pp. 49–64. Computational Mechanics Publications.

BLACKWELDER, R. F., & ECKELMANN, H. 1979 Streamwise vortices associated with the bursting phenomenon. *J. Fluid Mech.* **94**, 577–594.

BLACKWELDER, R. F., & HARITONIDIS, J. H. 1983 Scaling of the bursting frequency in turbulent layers. *J. Fluid Mech.* **132**, 87–103.

BLACKWELDER, R. F., LIU, D., & JEON, W. 1998 Velocity perturbations produced by oscillating delta wing actuators in the wall region. *Experimental Thermal Fluid Sci.* **16**, 32–40.

BREUER, K. S., HARITONIDIS, J. H., & LANDAHL, M. T. 1989 The control of transient disturbances in a flat plate boundary layer through active wall motion. *Phys. Fluids A* **1**, 574–582.

BRUUN, H. H. 1995 *Hot-wire Anemometry : Principles and Signal Analysis*. Oxford University Press.

BUICE, C. U., & EATON, J. K. 1997 Experimental investigation of flow through an asymmetric plane diffuser. *Stanford University Thermosciences Division Rep.* TSD-107.

BURGER, G. J., SMULDERS, E. J. T., BERENSCHOT, J. W., LAMMERINK, T. S. J., FLUITMAN, J. H. J., & IMAI, S. 1995 High resolution shadow mask patterning in deep holes and its application to an electrical wafer feed-through. *International Conference on Solid-State Sensors and Actuators (Transducers '95)*, 573–576.

BUSHNELL, D. M., & HEFNER, EDS., J. N. 1990 *Viscous Drag Reduction in Boundary Layers*, vol. 123 of *Progress in Astronautics and Aeronautics*. AIAA.

BUSHNELL, D. M., & MCGINLEY, C. B. 1989 Turbulence control in wall flows. *Ann. Rev. Fluid Mech.* **21**, 1–20.

CAHILL, D. G. 1990 Thermal conductivity measurement from 30 to 750 K : the  $3\omega$  method. *Rev. Sci. Instrum.* **61**, 802–808.

CHOI, H., MOIN, P., & KIM, J. 1993 Direct numerical simulation of turbulent flow over riblets. *J. Fluid Mech.* **255**, 503–539.

CHOI, H., MOIN, P., & KIM, J. 1994 Active turbulence control for drag reduction in wall-bounded flows. *J. Fluid Mech.* **262**, 75–110.

CHOI, K.-S., DEBISSCHOP, J.-R., & CLAYTON, B. R. 1998 Turbulent boundary-layer control by means of spanwise-wall oscillation. *AIAA Journal* **36**, 1157–1163.

CHOW, E. M., SOH, H. T., PARTRIDGE, A., HARLEY, J. A., KENNY, T. W., & QUATE, C. F. 1998 Fabrication of high-density cantilever arrays and through-wafer interconnects. *IEEE Solid State Sensor and Actuator Workshop*, 220–224.

COE, D. J., ALLEN, M. G., SMITH, B. L., & GLEZER, A. 1995 Addressable micromachined jet arrays. *International Conference on Solid-State Sensors and Actuators (Transducers '95)*, 329–332.

COLE, K. D., & BECK, J. V. 1987 Conjugated heat transfer from a strip heater with the unsteady surface element method. *J. Thermophys. Heat Transfer* **1**, 348–354.

COLE, K. D., & BECK, J. V. 1988 Conjugated heat transfer from a hot-film probe for transient air flow. *J. Heat Transfer* **110**, 290–296.

ERICSON, F., & SCHWEITZ, J.-A. 1990 Micromechanical fracture strength of silicon. *Journal of Applied Physics* **68**, 5840–5844.

FINDLER, G., MUCHOW, J., KOCH, M., & MÜNZEL, H. 1992 Temporal evolution of silicon surface roughness during anisotropic etching process. *Proceedings IEEE Micro Electro Mechanical Systems*, 62–66.

GAD-EL-HAK, M. 1994 Interactive control of turbulent boundary layers: A futuristic overview. *AIAA Journal* **32**, 1753–1765.

GOLDBERG, H. D., BREUER, K. S., & SCHMIDT, M. A. 1994 A silicon wafer-bonding technology for microfabricated shear-stress sensors with backside contacts. *IEEE Solid State Sensor and Actuator Workshop*, 111–115.

HAMMOND, E. P., BEWLEY, T. R., & MOIN, P. 1998 Observed mechanisms for turbulence attenuation and enhancement in opposition-controlled wall-bounded flows. *Phys. Fluids* **10**, 2421–2423.

HANRATTY, T. J., & CAMPBELL, J. A. 1996 Measurement of wall shear stress. In *Fluid Mechanics Measurements, 2<sup>nd</sup> ed.* (ed. R. J. Goldstein), pp. 575–648. Taylor and Francis.

HARITONIDIS, J. H. 1988 The measurement of wall shear stress. In *Advances in Fluid Mechanics Measurements* (ed. M. Gad-el-Hak), pp. 229–261. Springer Verlag.

HENNING, A. K. 1997. Redwood Microsystems, personal communication.

HO, C.-M., & TAI, Y.-C. 1996 Review : MEMS and its applications for flow control. *J. Fluids Eng.* **118**, 437–447.

HO, C.-M., & TAI, Y.-C. 1998 Micro-Electro-Mechanical-Systems (MEMS) and fluid flows. *Ann. Rev. Fluid Mech.* **30**, 579–612.

HOCENES, J. H. A., & HANRATTY, T. J. 1982 The use of multiple wall probes to identify coherent flow patterns in the viscous wall region. *J. Fluid Mech.* **124**, 363–390.

JACOBSON, S. A., & REYNOLDS, W. C. 1993 Active control of boundary layer wall shear stress using self-learning neural networks. *AIAA Paper 93-3272*. AIAA Shear Flow Conference, July 6-9.

JACOBSON, S. A., & REYNOLDS, W. C. 1995 An experimental investigation towards the active control of turbulent boundary layers. *Stanford University Thermosciences Division Rep.* TF-64 (referred to herein as JR).

JACOBSON, S. A., & REYNOLDS, W. C. 1998 Active control of streamwise vortices and streaks in boundary layers. *J. Fluid Mech.* **360**, 179–211.

JIANG, F., TAI, Y.-C., GUPTA, B., GOODMAN, R., TUNG, S., HUANG, J.-B., & HO, C.-M. 1996 A surface micromachined shear stress imager. *Proceedings IEEE Micro Electro Mechanical Systems*, 110–115.

JIMÉNEZ, J. 1994 On the structure and control of near wall turbulence. *Phys. Fluids* **6**, 944–953.

JOSHI, S. S., SPEYER, J. L., & KIM, J. 1997 A systems theory approach to the feedback stabilization of infinitesimal and finite-amplitude disturbances in plane poiseuille flow. *J. Fluid Mech.* **332**, 157–184.

JOSLIN, R. D. 1998 Aircraft laminar flow control. *Ann. Rev. Fluid Mech.* **30**, 1–29.

KAYS, W. M., & CRAWFORD, M. E. 1993 *Convective Heat and Mass Transfer*, 3<sup>rd</sup> ed. McGraw-Hill.

KEEFE, L. R. Method and apparatus for reducing the drag of flows over surfaces. U. S. Patent number 5,803,409, Sept. 1998.

KLINE, S. J., & MCCLINTOCK, F. A. 1953 Describing uncertainties in single-sample experiments. *Mech. Engr.* **75**, 3–8.

KLINE, S. J., REYNOLDS, W. C., SCHRAUB, F. A., & RUNSTADLER, P. W. 1967 The structure of turbulent boundary layers. *J. Fluid Mech.* **30**, 741–773.

KOUMOUTSAKOS, P. 1995 Simulations of vortex generators. *Center for Turbulence Research, Annual Research Briefs*, 233–240.

KOUMOUTSAKOS, P. 1999 Vorticity flux control for a turbulent channel flow. *Phys. Fluids* **11**, 248–250.

KOVACS, G. T. A. 1998 *Micromachined Transducers Sourcebook*. McGraw-Hill.

KRAVCHENKO, A. G., CHOI, H., & MOIN, P. 1993 On the relation of the near-wall streamwise vortices to wall skin friction in turbulent boundary layers. *Phys. Fluids A* **5**, 3307–3309.

KUGEL, V. D., ZHANG, Q. M., XU, B., MING WANG, Q., CHANDRAN, S., & CROSS, L. E. 1996 Behavior of piezoelectric actuators under high electric field. In *Proceedings of the 10th International Symposium on Applications of Ferroelectrics* (eds. B. M. Kulwicki, A. Amin, & A. Safari), pp. 655–658. IEEE.

KUMAR, S. M., REYNOLDS, W. C., & KENNY, T. W. 1999 MEMS based transducers for boundary layer control. *Proceedings IEEE Micro Electro Mechanical Systems*, 135–140.

KURABAYASHI, K. 1999. Stanford University, personal communication.

LAADHARI, F., SKANDAJI, L., & MOREL, R. 1994 Turbulent reduction in a boundary layer by a local spanwise oscillating surface. *Phys. Fluids* **6**, 3218–3220.

LACHOWICZ, J. T., YAO, C., & WLEZIEN, R. W. 1999 Flow field characterization of a jet and vortex actuator. *Experiments in Fluids* **27**, 12–20.

LEE, C., KIM, J., BABCOCK, D., & GOODMAN, R. 1997 Application of neural networks to turbulence control for drag reduction. *Phys. Fluids* **9**, 1740–1747.

LEE, C., KIM, J., & CHOI, H. 1998 Suboptimal control of turbulent channel flow for drag reduction. *J. Fluid Mech.* **358**, 245–258.

LIANG, P. W., & COLE, K. D. 1992 Transient conjugated heat transfer from a rectangular hot film. *J. Thermophys. Heat Transfer* **6**, 349–355.

LIEPMANN, H. W., & NOSENCHUCK, D. M. 1982 Active control of laminar-turbulent transition. *J. Fluid Mech.* **118**, 201–204.

LINDER, S., BALTES, H., GNAEDINGER, F., & DOERING, E. 1994 Fabrication technology for wafer through-hole interconnections and three-dimensional stacks of chips and wafers. *Proceedings IEEE Micro Electro Mechanical Systems*, 349–354.

LINDER, S., BALTES, H., GNAEDINGER, F., & DOERING, E. 1996 Photolithography in anisotropically etched grooves. *Proceedings IEEE Micro Electro Mechanical Systems*, 38-43.

LIU, C., TSAO, T., TAI, Y.-C., & HO, C.-M. 1994 Surface micromachined magnetic actuators. *Proceedings IEEE Micro Electro Mechanical Systems*, 57-62.

LUMLEY, J., & BLOSSEY, P. 1998 Control of turbulence. *Ann. Rev. Fluid Mech.* **30**, 311-327.

LUXBACHER, T., & MIRZA, A. 1999 Spray coating for MEMS, interconnects, and advanced packaging applications. *Sensors* **16**, 61-65.

MATHEWS, J., & POLL, D. I. A. 1985 The theory and application of heated films for the measurement of skin friction. *College of Aeronautics, Cranfield Institute of Technology Rep.* 8515.

McMICHAEL, J. M. 1996 Progress and prospects for active flow control using Microfabricated Electro-Mechanical Systems (MEMS). *AIAA Paper 96-0306*. AIAA 34st Aerospace Sciences Meeting, January 15-18.

MOFFAT, R. J. 1988 Describing the uncertainties in experimental results. *Experimental Thermal and Fluid Science* **1**, 3-17.

MOIN, P., & BEWLEY, T. 1994 Feedback control of turbulence. *Appl. Mech. Rev.* **47**, S3-S13.

MOIN, P., & KIM, J. 1997 Tackling turbulence with supercomputers. *Scientific American* **276**, 62-68.

NITSCHE, W., MIROW, P., & SZODRUCH, J. 1989 Piezo-electric foils as a means of sensing unsteady surface forces. *Experiments in Fluids* **7**, 111-118.

NOSENCHUCK, D. M., & BROWN, G. L. 1993 Discrete spatial control of wall shear stress in turbulent boundary layers. In *Near-Wall Turbulent Flows* (eds. R. M. C. So, C. G. Speziale, & B. E. Launder), pp. 689-698. Elsevier Science Publishers.

NOSENCHUCK, D. M., & BROWN, G. L. Multiple electromagnetic tiles for boundary layer control. U. S. Patent number 5,437,421, Aug. 1995.

PADMANABHAN, A., GOLDBERG, H., BREUER, K. S., & SCHMIDT, M. A. 1996 Wafer-bonded floating-element shear stress microsensor with optical position sensing by photodiodes. *Journal of Microelectromechanical Systems* **5**, 307-315.

PADMANABHAN, A., SHEPLAK, M., BREUER, K. S., & SCHMIDT, M. A. 1997 Micromachined sensors for static and dynamic shear-stress measurements in aero-dynamic flows. *International Conference on Solid-State Sensors and Actuators (Transducers '97)* **1**, 137–140.

PARK, S.-E., & SHROUT, T. R. 1997 Ultrahigh strain and piezoelectric behavior in relaxor based ferroelectric single crystals. *Journal of Applied Physics* **82**, 1804–1811.

PERRY, A. E. 1982 *Hot-wire Anemometry*. Oxford University Press.

PETERSEN, K. E. 1982 Silicon as a mechanical material. *Proc. IEEE* **70**, 420–457.

PISANO, A. P. 1998 MEMS 2003 and beyond - A DARPA vision of the future of MEMS. <<http://www.darpa.mil/MTO/MEMS/2003/index.html>>.

PODVIN, B., & LUMLEY, J. 1998 Reconstructing the flow in the wall region from wall sensors. *Phys. Fluids* **10**, 1182–1190.

POURAHMADI, F., GEE, D., & PETERSEN, K. 1991 The effect of corner radius of curvature on the mechanical strength of micromachined single-crystal silicon structures. *International Conference on Solid-State Sensors and Actuators (Transducers '91)*, 197–200.

PRESS, W. H., TEUKOLSKY, S. A., VETTERLING, W. T., & FLANNERY, B. P. 1992 *Numerical Recipes in Fortran*. 2<sup>nd</sup> ed. Cambridge University Press.

PUERS, B., & SANSEN, W. 1990 Compensation structures for convex corner micro-machining in silicon. *Sensors and Actuators A: Physical* **23**, 1036–1041.

RATHNASINGHAM, R., & BREUER, K. S. 1997a System identification and control of a turbulent boundary layer. *Phys. Fluids* **9**, 1867–9.

RATHNASINGHAM, R., & BREUER, K. S. 1997b Coupled fluid-structural characteristics of actuators for flow control. *AIAA Journal* **35**, 832–837.

SCHOPPA, W., & HUSSAIN, F. 1998 A large-scale control strategy for drag reduction in turbulent boundary layers. *Phys. Fluids* **10**, 1049–1051.

SHAHI, J., NG, K.-Y., & SCHMIDT, M. A. 1992 A microfabricated floating-element shear stress sensor using wafer-bonding technology. *Journal of Microelectromechanical Systems* **1**, 89–94.

SHERMAN, F., TUNG, S., KIM, C.-J., HO, C.-M., & WOO, J. 1998 In-plane microactuator for fluid control application. *Proceedings IEEE Micro Electro Mechanical Systems*, 454–459.

SIMONICH, J. C., & MOFFAT, R. J. 1982 Local measurements of turbulent boundary layer heat transfer on a concave surface using liquid crystals. *Stanford University Thermosciences Division Rep.* HMT-35.

SIRKAR, K. K., & HANRATTY, T. J. 1970 The limiting behaviour of the turbulent transverse velocity component close to a wall. *J. Fluid Mech.* **44**, 605–614.

SIROVICH, L., & KARLSSON, S. 1997 Turbulent drag reduction by passive mechanisms. *Nature* **388**, 753–755.

SIROVICH, L., LEVICH, E., & BRONICKI, L. Y. Method and apparatus for controlling turbulence in boundary layer and other wall-bounded fluid flow fields. U. S. Patent number 5,797,414, Aug. 1998.

SMITH, B. L., & GLEZER, A. 1998 The formation and evolution of synthetic jets. *Phys. Fluids* **10**, 2281–2297.

SMITS, J. G., & TILMANS, H. A. C. 1984 Pressure dependance of resonant diaphragm transfer function. In *Sensors and Actuators : Research, Development and Application* (ed. P. Bergveld), pp. 117–122. Twente University of Technology.

SPALART, P. R. 1988 Direct simulation of a turbulent boundary layer up to  $Re_\theta = 1410$ . *J. Fluid Mech.* **187**, 61–98.

STILLWAGON, L. E., & LARSON, R. G. 1989 Topographic substrate leveling during spin coating. In *Proceedings of the Symposium on Patterning Science and Technology* (eds. R. Gleason, G. J. Heffron, & L. K. White), pp. 230–238. The Electrochemical Society.

SUZUKI, Y., & KASAGI, N. 1992 Evaluation of hot-wire measurements in wall shear turbulence using a direct numerical simulation database. *Experimental Thermal Fluid Sci.* **5**, 69–77.

TAN-ATICHAT, J., NAGIB, H. M., & LOEHRKE, R. I. 1982 Interaction of free-stream turbulence with screens and grids: A balance between turbulence scales. *J. Fluid Mech.* **114**, 501–528.

TANAKA, K., TAKATA, E., & OHWADA, K. 1998 Anodic bonding of lead zirconate titanate ceramics to silicon with intermediate glass layer. *Sensors and Actuators A: Physical* **69**, 199–203.

TIMOSHENKO, S. 1955 *Strength of Materials - Part 1*, 3<sup>rd</sup> ed. D. Van Nostrand.

TSAO, T., JIANG, F., MILLER, R., TAI, Y.-C., GUPTA, B., GOODMAN, R., TUNG, S., & HO, C.-M. 1997 An integrated MEMS system for turbulent boundary layer

control. *International Conference on Solid-State Sensors and Actuators (Transducers '97)*, 315–318.

VARADAN, V. V., ROH, Y. R., SHANKAR, B., & VARADAN, V. K. 1990 Measurement of the skin friction associated with turbulent flows in air and water using saw devices. *IEEE Ultrasonics Symposium* 1, 303–306.

VARADAN, V. V., ROH, Y. R., & VARADAN, V. K. 1989 Local/global saw sensors for turbulence. *IEEE Ultrasonics Symposium* 1, 591–594.

WALTHER, J., & KOUMOUTSAKOS, P. 1999. Institute of Fluid Dynamics, ETH Zürich, personal communication.

WANG, X.-Q., HAN, Z., JIANG, F., TSAO, T., LIN, Q., TAI, Y.-C., KOOSH, V., GOODMAN, R., LEW, J., & HO, C.-M. 1999 A fully integrated shear stress sensor. *International Conference on Solid-State Sensors and Actuators (Transducers '99)*, 1074–1077.

WEISS, F., PRINZ, F., NEPOTNIK, G., PADMANABHAN, K., SCHULTZ, L., & MERZ, R. 1996 Shape deposition manufacturing of wearable computers. *Proceedings Solid Freeform Fabrication Symposium*, 31–38.

WESTPHAL, R. V., JOHNSTON, J. P., & EATON, J. K. 1984 Experimental study of flow reattachment in a single-sided sudden expansion. *Stanford University Thermosciences Division Rep.* MD-41.

WILTSE, J. M., & GLEZER, A. 1993 Manipulation of free shear flows using piezoelectric actuators. *J. Fluid Mech.* 249, 261–285.

YOUNG, W. C. 1989 *Roark's Formulas for Stress and Strain*, 6<sup>th</sup> ed. McGraw-Hill.

ZDEBLICK, M. J. 1988 A planar process for an electric-to-fluidic valve. *Ph.D. Thesis*, Department of Electrical Engineering. Stanford University, Stanford, CA.